DISSERTATION

A COMPUTATIONAL AND EXPERIMENTAL STUDY ON COMBUSTION PROCESSES IN NATURAL GAS/DIESEL DUAL FUEL ENGINES

Submitted by

Andrew Hockett

Department of Mechanical Engineering

In partial fulfillment of the requirements

For the Degree of Doctor of Philosophy

Colorado State University

Fort Collins, Colorado

Fall 2015

Doctoral Committee:

Advisor: Anthony J. Marchese

Greg Hampson
Daniel B. Olsen
Xinfeng Gao
Peter Young

ABSTRACT

A COMPUTATIONAL AND EXPERIMENTAL STUDY ON COMBUSTION PROCESSES IN NATURAL GAS/DIESEL DUAL FUEL ENGINES

Natural gas/diesel dual fuel engines offer a path towards meeting current and future emissions standards with lower fuel cost. However, numerous technical challenges remain that require a greater understanding of the in-cylinder combustion physics. For example, due to the high compression ratio of diesel engines, substitution of natural gas for diesel fuel at high load is often limited by engine knock and pre-ignition. Additionally, increasing the natural gas percentage in a dual fuel engine often results in decreasing maximum load. These problems limit the substitution percentage of natural gas in high compression ratio diesel engines and therefore reduce the fuel cost savings. Furthermore, when operating at part load dual fuel engines can suffer from excessive emissions of unburned natural gas. Computational fluid dynamics (CFD) is a multi-dimensional modeling tool that can provide new information about the in-cylinder combustion processes causing these issues.

In this work a multi-dimensional CFD model has been developed for dual fuel natural gas/diesel combustion and validated across a wide range of engine loads, natural gas substitution percentages, and natural gas compositions. The model utilizes reduced chemical kinetics and a RANS based turbulence model. A new reduced chemical kinetic mechanism consisting of 141 species and 709 reactions was generated from multiple detailed mechanisms, and has been validated against ignition delay, laminar flame speed, diesel spray experiments, and dual fuel engine experiments using two different natural gas compositions. Engine experiments were

conducted using a GM 1.9 liter turbocharged 4-cylinder common rail diesel engine, which was modified to accommodate port injection of natural gas and propane. A combination of experiments and simulations were used to explore the performance limitations of the light duty dual fuel engine including natural gas substitution percentage limits due to fast combustion or engine knock, pre-ignition, emissions, and maximum load. In particular, comparisons between detailed computations and experimental engine data resulted in an explanation of combustion phenomena leading to engine knock in dual fuel engines.

In addition to conventional dual fuel operation, a low temperature combustion strategy known as reactivity controlled compression ignition (RCCI) was explored using experiments and computations. RCCI uses early diesel injection to create a reactivity gradient leading to staged auto-ignition from the highest reactivity region to the lowest. Natural gas/diesel RCCI has proven to yield high efficiency and low emissions at moderate load, but has not been realized at the high loads possible in conventional diesel engines. Previous attempts to model natural gas/diesel RCCI using a RANS based turbulence model and a single component diesel fuel surrogate have shown much larger combustion rates than seen in experimental heat release rate profiles, because the reactivity gradient of real diesel fuel is not well captured. To obtain better agreement with experiments, a reduced dual fuel mechanism was constructed using a two component diesel surrogate. A sensitivity study was then performed on various model parameters resulting in improved agreement with experimental pressure and heat release rate.

ACKNOWLEDGEMENTS

Thank you to my advisor for introducing me to the world of combustion, guiding me through the Ph.D., and providing career advice. Thank you to Woodward for sponsoring this project. Thank you to Greg Hampson for offering me access to his many years of engine experience and providing career advice. Thank you to Jason Barta for all his help with installing the engine, writing engine control code, and generally being available to help with experimental data.

DEDICATION

This dissertation is dedicated to my wife, Jessie, for supporting my decision to pursue a doctorate degree and being patient with the time it took.

TABLE OF CONTENTS

LIST OF TABLES

LIST OF FIGURES

CHAPTER 1: INTRODUCTION

The incentive to power internal combustion engines with natural gas continues to increase due to both economic and emissions advantages of natural gas in comparison to traditional gasoline and diesel fuels. According to projections from the U.S. Energy Information Administration (EIA), energy consumption from the transportation sector is expected to remain at approximately 25% of total U.S. energy use through 2040 and nearly all of the energy consumption from this sector will be accomplished using internal combustion engines [1]. During this same time period, the EIA reference case shows that natural gas is expected to remain less expensive than petroleum fuels on an energy equivalent basis. For many applications the fuel cost savings is sufficient to offset the initial capital investment of converting equipment to operate on natural gas. These economic conditions have created a strong incentive for natural gas engine conversions in numerous applications.

Additionally, pollutants from the combustion of petroleum based fuels continue to adversely impact environment, climate, and human health, specifically with regards to emissions of carbon dioxide, carbon monoxide, unburned hydrocarbons (UHC), particulate matter (PM), and oxides of nitrogen (NO_X). Lean premixed combustion of natural gas can generate lower combustion temperatures and therefore less NO_X than diesel combustion. Additionally, lean premixed combustion avoids rich regions within sprays where soot is formed. Furthermore, the U.S. Environmental Protection Agency (EPA) initiated regulations on greenhouse gas emissions (GHG) and fuel efficiency standards for light duty vehicles by 2018 and heavy duty vehicles by 2025 [2] [3]. A substantial part of these regulations can be met by using alternative fuels that produce less carbon than gasoline or diesel for the same energy output. Natural gas is one such

fuel because it is composed primarily of methane, which has higher hydrogen to carbon ratio than diesel or gasoline and a higher heating value. Therefore, natural gas can produce the same amount of energy with about 25% less carbon dioxide emissions in comparison to producing the same energy by burning diesel or gasoline [4]. However, the reduction in total GHG emissions can be compromised if the natural gas does not burn to completion throughout the cylinder, since methane has a global warming potential that is 25 times greater than carbon dioxide over a 100 year period [5]. Therefore, converting from gasoline and diesel to natural gas offers a path towards meeting emissions regulations at lower fuel cost.

The EIA projects that the use of natural gas engines in the transportation sector will increase substantially by 2040 with the largest increases occurring in heavy duty applications, such as on-highway freight trucks (semi-trucks), large buses, locomotives, marine shipping tankers, construction equipment, mining equipment, and agricultural equipment [1]. Such heavy duty applications utilize diesel engines rather than spark ignited gasoline engines, because of the higher power density needed to minimize engine weight and the larger transient load capability required to accelerate large masses from rest. Therefore the use of natural gas as a substitute for diesel fuel in high compression ratio, heavy-duty engines is expected to increase significantly.

Diesel engines can be readily converted to natural gas/diesel dual fuel engines by fumigating the intake manifold or intake runners with natural gas and using the injected diesel mass as an ignition source, which then subsequently initiates combustion of the premixed natural gas air mixture near the diesel flame. In a typical dual fuel retrofit, the stock diesel engine control unit (ECU) is still in use and, as more energy from natural gas is added, the ECU reduces the injected diesel mass to maintain the commanded engine torque. The amount of natural gas that has been substituted for diesel can be defined on an energy basis in terms of the substitution rate,

$$z = \frac{m_{NG} Q_{NG}}{m_{NG} Q_{NG} + m_d Q_d}, \tag{1.1}$$

where m_{NG} is the mass of natural gas in the charge mixture, m_d the mass of injected diesel, Q_{NG} the mass based lower heating value of natural gas, and Q_d the lower heating value of diesel. In more advanced dual fuel engines, the ECU is calibrated to operate in dual fuel mode and an optimal substitution rate and injection strategy is used at different engine loads and speeds.

The fuel cost savings of the dual fuel engine increases as the substitution rate of natural gas increases. However, operating a high compression ratio diesel engine with a premixed fuel will eventually lead to problems with engine knock and pre-ignition as the natural gas mass is increased. As a result the natural gas substitution rate in a high compression ratio dual fuel engine is limited and therefore the fuel cost savings is also limited. Knock and pre-ignition occur at high load where the flame temperatures are exceptionally high. Additionally, at part load conditions, the substitution rate can be limited by emissions regulations. Because wall temperatures are lower at part load, the natural gas flame can quench before reaching the walls. This causes a large mass of unburned natural gas to be exhausted. A significant amount of the unburned natural gas has also been attributed to incomplete combustion in the piston crevices. Regulations on unburned hydrocarbons can limit the substitution rate or the load range of a dual fuel engine.

Engine knock is caused by uncontrolled fast combustion in which a large amount of energy is released in a short period of time. This creates an increase in pressure rise rate followed by high frequency pressure oscillations. The strong pressure waves create unacceptable engine noise, impose high stresses on engine structural components, and dramatically increase heat transfer rates ultimately leading to damage of engine surfaces. Karim [6] has reported that dual fuel

engines can experience both spark ignited (SI) and compression ignition (CI) knock characteristics, which should be expected since they operate with both a premixed propagating flame and diesel spray ignition. The common explanation for uncontrolled fast combustion in an SI engine is that a turbulent premixed flame propagating across the combustion chamber raises the pressure and temperature of the unburned fuel air mixture in front of the flame, known as the end gas, until the end gas experiences a volumetric energy release or auto-ignition. In contrast, diesel CI engines experience a sudden spike in combustion rate when the spray head ignites via a premixed, fuel rich auto-ignition. If the energy released during ignition of the spray is excessive, then the pressure waves generated can cause many of the same problems as with end gas knocking in SI engines. Consequently, there is a strong demand among many dual fuel applications to overcome these knock limits and further increase the substitution rate at high load so that the economic and emissions benefits of natural gas can be maximized.

Pre-ignition is typically associated with SI engines and is characterized by start of combustion occurring before spark timing. In a dual fuel engine where the diesel fuel is the combustion initiator, pre-ignition is characterized by start of combustion occurring before the start of injection. Pre-ignition events do not occur every cycle, but are intermittent events that cause much higher peak pressure and often induce engine knocking during that cycle. In addition to damage from induced engine knock, pre-ignitions that occur too early in the cycle create excessive peak pressure that can be much greater than the allowable design pressure, which can lead to structural failure of engine components. There have been many proposed causes for pre-ignition including ignition of lubricating oil droplets released from the cylinder liner, surface hot spots from deposits, and particles that flake off from deposits [7] [8].

One technique to increase the natural gas substitution percentage that has received considerable investigation is the use of a small diesel pilot injected at advanced timing (typically ~25° BTDC) to ignite the natural gas. This "liquid spark" method has been shown to avoid the formation of a non-premixed diesel jet flame and instead ignites after the end of injection via rich premixed auto-ignition. However, with a very small injected diesel mass the engine begins to behave similarly to a SI engine with a high compression ratio and additional techniques become necessary to avoid knock at high load. For example, Singh et al. [9] was able to achieve 95% natural gas substitution using early pilot injections, but these results were obtained at a mid-load condition and with a reduced compression ratio. For dual fuel engines with a high compression ratio and large bore diameter typical of a heavy duty diesel engine, the same maximum load achievable in conventional diesel mode cannot be achieved in dual fuel mode using substitution rates greater than roughly 70% due to knocking [10] [11]. At such lower substitution rates, injection timings near TDC would be necessary to avoid excessive pressure rise. Therefore, it should be expected that at lower substitution rates a non-premixed diesel jet flame is established in the presence of a natural gas/air mixture.

Lower substitution rates are necessary in many dual fuel applications. For instance, heavy duty on-road trucks require the capability to handle large load transients. Large cycle-to-cycle load transients cannot be achieved with greater fumigation of natural gas into the manifold and instead require a large change in direct injected diesel mass, creating periods of low substitution rate. Additionally, Mittal et al. [10] demonstrated that at low load the emissions of unburned hydrocarbons (UHC) can be significantly reduced by using a lower substitution percentage. Furthermore, in many mobile dual fuel applications, the supply of natural gas is often limited and

so there is a desire to have the option to use a lower substitution percentage in order to conserve natural gas.

Computational modeling of in-cylinder combustion processes has proven to be a valuable tool for designing engine components and combustion control strategies, because it can help explain causes for observed changes in engine performance and emissions. For example, computational modeling of dual fuel combustion can yield valuable information about how knock occurs in dual fuel engines and where incomplete combustion of natural gas is prominent. For this reason, dual fuel engine manufacturers are in need of a multi-dimensional modeling tool that can predict combustion behavior, such as knock, over a wide range of substitution rates, loads, and natural gas compositions. While a number of authors have performed computational modeling of high substitution rates using early pilot injection [12] [13] [14], there has been little work done on validating an engine CFD model from low to moderate substitution percentages. The combustion at these lower substitution rates is different than that in the liquid spark method because a non-premixed diesel jet flame occurs and initiates a premixed propagating natural gas flame. Additionally, the modeling that has been done previously often involved a significant simplification of either the chemical kinetics or the turbulent flow field. A major goal of this work is the development of a computational tool that incorporates sufficiently detailed chemical kinetics and can predict pressure, heat release rate, engine knock, pre-ignitions, and emissions within a 24-hour computation time using a computational hardware package that industry has access to. This model must be validated for different natural gas compositions, loads, and substitution percentages.

In the process of developing a computational tool for dual fuel engines it is also necessary to develop an accurate chemical kinetic model to describe diesel jet flames, diesel ignition,

premixed propagating natural gas flames, and natural gas auto-ignition. Large detailed chemical kinetic mechanisms describing the combustion of diesel and natural gas surrogates exist, but they are impractical for use in an engineering application because the computational cost is prohibitively high. Therefore, reduced mechanisms are used in the diesel/natural gas CFD simulations presented in this work. Chemical mechanism reduction techniques begin with a large mechanism and use an algorithm to automatically remove chemical species and reactions that do not have a substantial impact on specified combustion behavior (e.g. ignition delay, laminar flame speed) across a chosen set of initial pressure, temperature, and reactant composition. This procedure results in a reduced chemical mechanism (as defined by a lower number of species and reactions) that retains similar behavior of the original mechanism at those chosen conditions.

Prior to the work described in this thesis, there was not a sufficient reduced chemical kinetic mechanism available for simulating natural gas/diesel dual fuel combustion in a CFD simulation that accounted for the variation in the ethane and propane concentrations in the natural gas mixture. Some previous modeling work used pure methane to represent the chemistry of natural gas [15] [16]. However, Bourque et al. [17] found that ignition delay periods and flame speeds for typical pipeline natural gas compositions with small concentrations of heavier hydrocarbons can be quite shorter compared with pure methane. As such, one of the primary accomplishments of this work was the development of a reduced chemical kinetic mechanism for natural gas/diesel dual fuel combustion that can simulate varying natural gas reactivity using a multi-component natural gas surrogate mixture. This mechanism has been validated across a wide range of conditions relevant to dual fuel combustion using comparisons with ignition delay computations from detailed mechanisms, laminar flame speed experiments of methane at high pressure, experimental data from a diesel spray injected into a constant volume chamber, and experimental

engine data from a light duty turbocharged diesel engine outfitted with natural gas port injection. The engine experiments encompassed a wide range of substitution rates, loads, and natural gas compositions including a case where engine knock occurred.

In addition to conventional dual fuel combustion, another dual fuel strategy that has received considerable attention in recent years is reactivity controlled compression ignition (RCCI). RCCI is a low temperature combustion (LTC) method whereby compression heating of a lean premixed fuel air mixture in a high compression ratio engine initiates ignition reactions throughout the chamber. Lean premixed combustion results in lower flame temperatures compared to stoichiometric SI engines and diesel non-premixed flames. If combustion temperatures can be kept low enough then NOx formation rates can be significantly reduced. For many decades researchers have pursued homogenous charge compression ignition (HCCI), which ideally begins with a homogenous mixture of fuel and air during the compression stroke and ignition occurs at all locations nearly simultaneously. At moderate loads, HCCI has demonstrated significant efficiency gains, large reductions in NOx emissions, and virtually zero soot [18]. However, HCCI engines suffer from very fast and large heat release rates at high loads, which create such high pressure rise rate and peak pressures that HCCI operation is not able to achieve similar maximum loads as in traditional SI and CI engines. Conversely, at low loads the mixture becomes sufficiently lean such that misfire occurs.

RCCI is a dual fuel extension to HCCI whereby a low reactivity fuel such as gasoline or natural gas is premixed with the intake air and a higher reactivity fuel such as diesel is direct injected part way through the compression stroke. This results in a stratification of the high reactivity fuel and therefore a gradient in mixture reactivity. Due to the reactivity gradient, ignition proceeds from areas of high mixture reactivity to areas of low reactivity, which

lengthens the combustion duration, lowers the pressure rise rate and peak pressure, and allows for high loads to be achieved. Additionally, the load range can be extended by using a greater percentage of high reactivity fuel at low load and a greater percentage of low reactivity fuel at high load. Splitter et al. [19] were able to achieve high efficiency RCCI operation using gasoline and diesel in a heavy duty single cylinder engine between 4 and 14.5 bar IMEP while meeting EPA emission standards for NO_X without aftertreatment. Despite the improvements to the load range over HCCI, RCCI is still not able to achieve high enough loads that are comparable to the loads achievable with traditional SI and diesel engines. For this reason and due to sensitive combustion phasing, RCCI has still not been introduced commercially.

The use of natural gas for RCCI operation is advantageous because the difference in reactivity between natural gas and diesel is wider in comparison to that between gasoline and diesel. This allows for further lengthening of the combustion duration, which consequently allows for lower pressure rise rate, lower peak pressures, and extension to higher engine loads [15]. Also as explained previously, natural gas has economic advantages over gasoline and can produce less carbon dioxide emissions.

Greater understanding of RCCI from multi-dimensional modeling is necessary to explore emissions formation and find optimal control strategies that can overcome the difficulties of combustion phasing and excessive pressure rise rate. Previous attempts to model natural gas/diesel RCCI are limited and have demonstrated additional modeling challenges due to the wider reactivity difference between diesel and natural gas and accurately modeling the mixing of the injected fuel [15] [16]. Previous attempts have demonstrated overly fast combustion rate increase and pauses in combustion rate. These previous works used a single component surrogate for diesel fuel. The work presented in this thesis includes the development of a new reduced

chemical kinetic mechanism for RCCI whereby diesel fuel is represented with two components (n-dodecane and p-xylene) in an attempt to more accurately represent the reactivity gradient. Usaing the new RCCI chemical kinetic mechanism, a sensitivity study is presented on the model inputs that identifies, which modeling methods result in improved agreement with the experimental heat release profiles.

In addition to computational work, experimental work was done to assess the performance of the engine in comparison to conventional diesel operation. These experiments were conducted by recording the maximum load for diesel operation, dual fuel operation with a substitution rate of 65%, and dual fuel operation with the minimum diesel injection and therefore maximum substitution rate. By comparing these load curves the reduction in maximum load with substitution rate could be quantified. Also the best performance at high load using dual fuel operation could be characterized in terms of the substitution rate, the maximum load, emissions, and efficiency. This procedure helped identify performance limitations unique to a light duty engine operating in dual fuel mode. Future work is planned to use the newly developed dual fuel model to explore strategies to overcome the limitations on this specific engine and then test those strategies experimentally.

The work presented in this thesis has been disseminated via the submission of three different manuscripts (to date) and an additional study. The first submitted manuscript describes the development of a reduced natural gas/diesel dual fuel mechanism, which has been validated against ignition delay computations of detailed mechanisms, adiabatic HCCI simulations of detailed mechanisms, experimental premixed laminar flame speeds of CH4/O2/He mixtures at 40 and 60 atm, ignition delay and lift-off length from a diesel spray experiment in a constant volume chamber, and finally against dual fuel engine experiments using multi-dimensional CFD

simulations. The engine simulations were calculated for natural gas/diesel dual fuel engine experiments at varying injection timings, engine loads, substitution percentages, and natural gas compositions. The second manuscript utilizes the developed dual fuel model to explore the in-cylinder combustion physics and formulate a conceptual explanation of dual fuel combustion. The model is then used to simulate an experiment where knocking occurred and a discussion on knock in dual fuel engines is made. An additional section has been added on simulations of a spray into a constant volume chamber where air and natural gas are present at varying equivalence ratios. The third manuscript concerns a sensitivity study on RCCI modeling and includes the construction of multi-component dual fuel mechanism where diesel fuel is represented using two components. Finally, a study is presented comparing the maximum load curves between diesel and dual fuel operation and the associated performance and emissions differences.

CHAPTER 2: COMPUTATIONAL METHOD FOR ENGINE SIMULATIONS

2.1. CONVERGE and Numerical Scheme

Computational modeling of the in-cylinder physics was performed using the commercial CONVERGE™ version 2.2.0 code. The CONVERGE™ code uses a fixed and uniform Cartesian grid and a cut cell method at the boundaries. A cell-centered finite volume method was used where the cell-face fluxes for mass, momentum, and energy transport was found from 2nd order central differencing. An implicit time marching method was used to find the transient solution. The governing equations were solved using the conservative form. The transient solver used the pressure implicit with splitting of operators (PISO) method of Issa et al. [20] for the velocity-pressure coupling. The PISO method is a predictor-corrector technique that first solves the velocity field implicitly and then iteratively updates the velocity field using implicit pressure solutions.

The governing equations in CONVERGE include conservation of mass, momentum, energy, and chemical species. When a turbulence model is active, additional transport equations include the transport of turbulent kinetic energy and turbulent dissipation rate, which are explained in greater detail in section 2.3. The partial differential equations (PDE) for mass, momentum, and energy are solved simultaneously to ensure the correct pressure gradient. Using Einstein notation, the compressible form of the mass and momentum PDE's are respectively,

$$\frac{\partial \rho}{\partial t} + \frac{\partial \rho u_i}{\partial x_i} = 0, \tag{2.1}$$

and,

$$\frac{\partial \rho u_i}{\partial t} + \frac{\partial \rho u_i u_j}{\partial x_j} = -\frac{\partial P}{\partial x_i} + \frac{\partial \sigma_{ij}}{\partial x_j} + \rho g_i + S_i, \tag{2.2}$$

where the viscous stress tensor, σ_{ij}, is given by,

$$\sigma_{ij} = \mu\left(\frac{\partial u_i}{\partial x_j} + \frac{\partial u_j}{\partial x_i}\right) + \left(\mu' - \frac{2}{3}\mu\right)\frac{\partial u_k}{\partial x_k}\delta_{ij}. \tag{2.3}$$

In the above equations, ρ is the density, u_i the velocity component, P the pressure, S_i the source term, μ the dynamic viscosity, μ' the dilation viscosity (assumed to be zero), g_i the acceleration component of a body force, and δ_{ij} is the Kronecker delta. The energy equation is,

$$\frac{\partial \rho e}{\partial t} + \frac{\partial u_j \rho e}{\partial x_j} = -P\frac{\partial u_j}{\partial x_j} + \sigma_{ij}\frac{\partial u_i}{\partial x_j} + \frac{\partial}{\partial x_j}\left(K\frac{\partial T}{\partial x_j}\right) + \frac{\partial}{\partial x_j}\left(\rho D\sum_m h_m\frac{\partial Y_m}{\partial x_j}\right) + S, \tag{2.4}$$

where e is the specific internal energy, K is the thermal conductivity, T is the temperature, D is the mass diffusivity, h_m is the specific enthalpy of species m, Y_m is the mass fraction of species m, and S is an energy source term. The species transport equation is solved separately and is defined as,

$$\frac{\partial \rho_m}{\partial t} + \frac{\partial \rho_m u_j}{\partial x_j} = \frac{\partial}{\partial x_j}\left(\rho D\frac{\partial Y_m}{\partial x_j}\right) + S_m, \tag{2.5}$$

where ρ_m is the density of species m (i.e. $\rho_m = \rho Y_m$) and S_m is the source term for species m due to chemical reaction. The molecular mass diffusivity is calculated based on a user supplied Schmidt number, Sc, according to,

$$D = \frac{\nu}{Sc}. \tag{2.6}$$

Finally, an equation of state is needed for the compressible transport equations to couple pressure, density, and temperature. For the simulations in this work, the Redlich-Kwong equation of state was employed using the critical pressure and temperature of air, as explained in the CONVERGE™ theory manual [21].

The diffusive terms in the momentum and energy equations require the gas phase viscosity and thermal conductivity of the mixture. Rather than calculating mixture averaged values, these properties were given the values for air as a function of temperature. This is a reasonable assumption for engine simulations as typically over 90% of the charge mass consists of air. The gas phase properties are defined in the input file *gas.dat*, which lists dynamic viscosity, μ, and thermal conductivity, k, as functions of temperature from 0 K to 5000 K.

A variable time step was employed where the size of the time step is limited by a variety of stability and accuracy constraints. For example, three different Courant-Friedrichs-Lewy (CFL) numbers were used to control the time step, which include the convection based CFL number, the diffusion based CFL number, and the Mach number based CFL number, defined respectively as,

$$CFL_u = u\frac{\Delta t}{\Delta x}, \tag{2.7}$$

$$CFL_\nu = \nu\frac{\Delta t}{\Delta x^2}, \tag{2.8}$$

$$CFL_{mach} = a\frac{\Delta t}{\Delta x}, \tag{2.9}$$

where u is the velocity, ν is the kinematic viscosity, a is the speed of sound, Δx is the cell width, and Δt is the time step size. If CFL_u =1, then the time step is limited such that a massless particle

anywhere in the simulation cannot travel a distance greater than one cell width. In addition, the time step was restricted based the spray model and the chemistry. When the spray model was active, the maximum time step allowed was,

$$\Delta t_{spray} = \min\left[\frac{\Delta x}{parcel\ velocity}\right] \times mult\_dt\_spray, \tag{2.10}$$

where *mult_dt_spray* is a user specified input. Thus if *mult_dt_spray* = 1, then the time step is restricted such that a spray parcel can only travel the distance of one cell width. When the chemistry solver was active, the maximum allowable time step was,

$$\Delta t_{chem} = \Delta t_{prev} \times \min\left[\frac{T}{\Delta T}\right] \times mult\_dt\_chem, \tag{2.11}$$

where Δt_{prev} is the previous time step, T is the initial cell temperature, ΔT is the temperature change due to chemical reaction, and *mult_dt_chem* is a user specified input. Thus if *mult_dt_chem* = 0.5, then the time step is restricted such that the change in temperature of any cell is less than 50% of the initial cell temperature. Specific values for the CFL numbers and other time step control parameters are given throughout the chapters where specific computation method is described.

Details of the PISO algorithm can be found in the CONVERGE™ theory manual. During each PISO loop, the discretized form of the transport equations are solved using iterations of the point-wise selective over-relaxation method until the iteration error for each solution variable has converged within a specified tolerance. The iteration error is defined as,

$$error_{\varphi} = \frac{\Delta\varphi}{norm}, \tag{2.12}$$

where φ is a solution variable, $\Delta\varphi$ is the change in the solution variables between successive SOR iterations, and *norm* is a normalization value for φ. The convergence tolerances used for each of the solution variables is given in the appendix. Once the PISO algorithm has converged, a final iteration is performed using a point-wise Jacobi method to ensure strict conservation of the variables. Finally, the turbulence equations are solved for using the new solution variables.

2.2. Geometry

All engine combustion simulations in this work utilized a 1/7th sector of the cylinder geometry, wherein each sector included one of the injector's seven nozzles as depicted in Figure 2.1(a). A 2 mm base cell size was used for the sector simulations. Adaptive mesh refinement (AMR) was used to refine the grid based on temperature and velocity gradients with the minimum cell size being 0.25 mm. Fixed embedding using a cone with 0.25 mm cells was used in the near nozzle region. The choice of a minimum cell width of 0.25 mm is based on the recommendations from Senecal et al. [22], who demonstrated grid convergence spray behavior with the same spray models at 0.25 mm and significant increases in computational cost with further refinement. Additionally, the full cylinder geometry with intake runners and valve motions as depicted in Figure 2.1(b) was used for preliminary simulations of the intake stroke for the purpose of obtaining a mapping file at IVC. The mapping file was then used to initialize the velocity and turbulence fields in the sector simulations. The base cell size in the intake stroke simulations was 4 mm and the minimum cell size for AMR was 0.5 mm. The intake stroke simulations also used fixed boundary embedding of 0.5 mm along the cylinder head, liner, and piston. Fixed boundary embedding was used along the valve surfaces where the velocity is high to aid with stability.

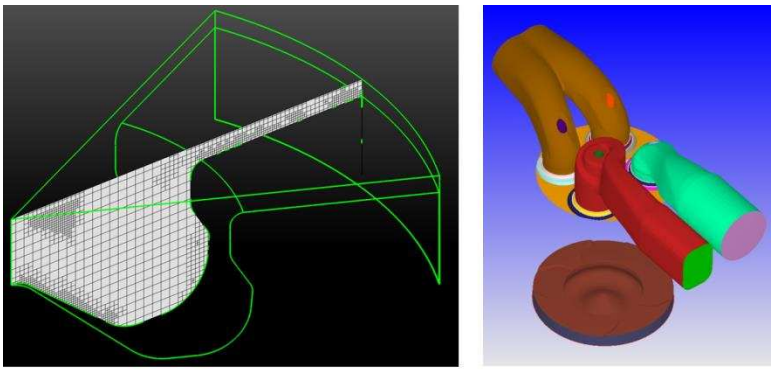

(a) (b)

Figure 2.1. (a) Sector geometry used for engine combustion simulations. (b) Cylinder and port geometry used to obtain the velocity and turbulence fields at IVC for use in the sector simulations. The cylinder liner is hidden to show the piston geometry.

In addition to engine simulations, spray validation studies were used to evaluate the performance of the spray models and the reduced chemical mechanisms. These spray models were validated against spray experiments in a constant volume chamber. Therefore, the spray simulations were carried out in a constant volume cube geometry. The spray is injected at the center of one of the cube faces. Similar to the engine simulations the base cell size in the constant volume chamber geometry was 2 mm and the minimum cell size was 0.25 mm. Also a cone of fixed embedding with 0.25 mm was used in the near nozzle region.

2.3. Turbulence model

The presence of turbulence significantly increases the diffusion rates of mass, momentum, energy, and chemical species. Accurate representation of the higher diffusion rates is important for capturing the chemical reaction rates in premixed and non-premixed combustion. The turbulence model utilized for the simulations herein was a Reynolds Averaged Navier-Stokes (RANS) model. In a RANS model the actual velocity, u_i, is decomposed into an ensemble

averaged velocity component, $\bar{u}_i$, and a fluctuating velocity component, u'_i, which is known as the Reynolds decomposition,

$$u_i = \bar{u}_i + u'_i. \tag{2.13}$$

For constant density flows, substitution of the Reynolds decomposition into the governing equations yields an equivalent form with ensemble averaged quantities plus additional turbulent terms which need to be modeled. However, for high speed flows, such as those occurring in engines, the density is not constant and therefore density weighted flow quantities are more appropriate for describing the turbulent governing equations. This density weighting is accomplished using Favre averaging, which is denoted with a tilde. The Favre averaged velocity is defined as,

$$\tilde{u}_i = \frac{\overline{\rho u_i}}{\bar{\rho}}. \tag{2.14}$$

The Reynolds decomposition is then redefined using Favre averaged quantities according to,

$$u_i = \tilde{u}_i + u''_i, \tag{2.15}$$

where u''_i is the fluctuating velocity component with respect to the Favre averaged velocity.

Applying ensemble averaging to the Navier-Stokes equations and substituting in the Favre averaged decomposition to simplify terms results in a form analogous to the laminar form, but with Favre averaged quantities for solution variables and an additional term to describe the effects of turbulence. The ensemble averaged form of the continuity, momentum, energy, and species conservation equations are respectively,

$$\frac{\partial \bar{\rho}}{\partial t} + \frac{\partial \bar{\rho}\tilde{u}_i}{\partial x_i} = 0 \tag{2.16}$$

$$\frac{\partial \bar{\rho}\tilde{u}_i}{\partial t} + \frac{\partial \bar{\rho}\tilde{u}_i\tilde{u}_j}{\partial x_i} = -\frac{\partial \bar{P}}{\partial x_i} + \frac{\partial}{\partial x_i}\left[\mu\left(\frac{\partial \tilde{u}_i}{\partial x_j} + \frac{\partial \tilde{u}_j}{\partial x_i}\right) - \frac{2}{3}\mu\frac{\partial \tilde{u}_k}{\partial x_k}\delta_{ij}\right] + \frac{\partial}{\partial x_j}\left(-\bar{\rho}\widetilde{u_i''u_j''}\right), \tag{2.17}$$

$$\frac{\partial \bar{\rho}\tilde{e}}{\partial t} + \frac{\partial \bar{\rho}\tilde{u}_i\tilde{e}}{\partial x_i} = -\bar{P}\frac{\partial \tilde{u}_j}{\partial x_j} + \bar{\sigma}_{ij}\frac{\partial \tilde{u}_i}{\partial x_j} + \frac{\partial}{\partial x_j}\left(K\frac{\partial \bar{T}}{\partial x_j}\right) + \frac{\partial}{\partial x_j}\left(\rho D\sum_m \tilde{h}_m\frac{\partial \tilde{Y}_m}{\partial x_j}\right) + \frac{\partial}{\partial x_j}\left(-\bar{\rho}\widetilde{u_i''e''}\right), \tag{2.18}$$

$$\frac{\partial \bar{\rho}_m}{\partial t} + \frac{\partial \bar{\rho}_m\tilde{u}_j}{\partial x_j} = \frac{\partial}{\partial x_j}\left(\bar{\rho}D\frac{\partial \tilde{Y}_m}{\partial x_j}\right) + \frac{\partial}{\partial x_j}\left(-\bar{\rho}\widetilde{u_i''Y_m''}\right). \tag{2.19}$$

Comparison of the ensemble averaged form of the momentum equation in Equation (2.17) with the laminar form in Equation (2.2) shows that each ensemble averaged term has an analogous laminar term. However, the ensemble averaged momentum equation also has an additional term, known as the Reynolds stress tensor,

$$\tau_{ij,t} = -\bar{\rho}\widetilde{u_i''u_j''} \tag{2.20}$$

The ensemble averaged energy and species equations also have additional Reynolds turbulence terms, which are respectively,

$$q_t = -\bar{\rho}\widetilde{u_i''e''}\,, \tag{2.21}$$

$$\dot{m}_{m,t} = -\bar{\rho}\widetilde{u_i''Y_m''}\,. \tag{2.22}$$

Here q_t is represents additional heat flux in the energy equation and $\dot{m}_{m,t}$ represents an additional mass flux in the species equation for species *m*. Because there are no readily available equations for the Reynolds terms, the system cannot be solved.

To close the system of equations, additional theory for the Reynolds fluctuating terms needs to be introduced. This is typically done using the gradient approximation, which uses an analogy between increased diffusion rates due to turbulence and molecular diffusion rates, which are proportional to the spatial gradient of the quantity being transported. This can stated formally as,

$$-\bar{\rho}\widetilde{u_i''\varphi''} = \frac{\mu_t}{\sigma_\varphi}\frac{\partial\bar{\varphi}}{\partial x_i}, \tag{2.23}$$

where φ is the scalar quantity being transported, μ_t is a turbulent viscosity, and σ_φ is a turbulent non-dimensional number relating μ_t to the turbulent proportionality coefficient for φ. By applying the gradient approximation of equation (2.23), the Reynolds fluctuating terms in equations (2.20) through (2.22) can be expressed respectively as,

$$-\bar{\rho}\widetilde{u_i''u_j''} = \mu_t\left(\frac{\partial\tilde{u}_i}{\partial x_j}+\frac{\partial\tilde{u}_j}{\partial x_i}-\frac{2}{3}\frac{\partial\tilde{u}_k}{\partial x_k}\delta_{ij}\right)-\frac{2}{3}\mu_t k\delta_{ij}, \tag{2.24}$$

$$-\bar{\rho}\widetilde{u_i''e''} = \bar{\rho}\alpha_t\frac{\partial\tilde{e}}{\partial x_i} = \frac{\mu_t}{\mathrm{Pr}_t}\frac{\partial\tilde{e}}{\partial x_i}, \tag{2.25}$$

$$-\bar{\rho}\widetilde{u_i''Y_m''} = \bar{\rho}D_t\frac{\partial\tilde{Y}_m}{\partial x_i} = \frac{\mu_t}{\mathrm{Sc}_t}\frac{\partial\tilde{Y}_m}{\partial x_i}. \tag{2.26}$$

where α_t is a turbulent thermal diffusivity, D_t is a turbulent species diffusivity, and k is the turbulent kinetic energy, which is explained below. In equation (2.25) Pr_t is a turbulent Prandtl number, i.e.,

$$\mathrm{Pr}_t = \frac{\mu_t}{\bar{\rho}\alpha_t}, \tag{2.27}$$

and Sc_t is a turbulent Schmidt number, i.e.,

$$\mathrm{Sc}_t = \frac{\mu_t}{\bar{\rho} D_t}. \tag{2.28}$$

For all simulations presented herein, constant values of Pr_t = 0.9 and Sc_t = 0.78 were assumed, which are typical values of air. Therefore, RANS models use increased viscosity, thermal diffusivity, and species diffusivity to represent the effects of turbulent eddies. The solution from a RANS simulation will produce the ensemble averaged flow and does not resolve any of the turbulent eddy structure observed experimentally. Often the average behavior is sufficient to produce useful simulation results.

By assuming constant turbulent Prandlt and Schmidt numbers, the turbulent viscosity is the last remaining quantity needed to close the system of governing equations. There are a number of methods used to model turbulent viscosity. The most common approach, which is also used in this work, is a two equation model. In a two equation RANS model, two additional transport equations for turbulent kinetic energy, *k*, and turbulent dissipation rate, ε, are solved for and used to define the turbulent viscosity and turbulent conductivity for each computational cell. The turbulent kinetic energy is defined as,

$$k = \frac{1}{2}\widetilde{u_i'' u_i''}. \tag{2.29}$$

The turbulent dissipation rate is the rate that turbulent kinetic energy of the smallest eddies is transformed into molecular thermal energy. The turbulent viscosity is then found using the values for *k* and ε at each cell center using,

$$\mu_t = C_\mu \rho \frac{k^2}{\varepsilon} \tag{2.30}$$

where C_μ is a model constant. The Reynolds turbulent stress term in equation (2.24) then can be expressed using the definition for *k*,

$$\tau_{ij} = \mu_t \left(\frac{\partial \tilde{u}_i}{\partial x_j} + \frac{\partial \tilde{u}_j}{\partial x_i} - \frac{2}{3}\delta_{ij} \frac{\partial \tilde{u}_i}{\partial x_i} \right) - \frac{2}{3}\mu_t k \delta_{ij}, \tag{2.31}$$

For the simulations in this work, the RNG turbulence model used was the renormalization group (RNG) *k*-*ε* from Han and Reitz [23]. The transport equation for *k* is,

$$\frac{\partial \rho k}{\partial t} + \frac{\partial \rho u_i k}{\partial x_i} = \sigma_{ij} \frac{\partial u_i}{\partial x_j} + \frac{\partial}{\partial x_i} \frac{\mu}{\mathrm{Pr}_k} \frac{\partial k}{\partial x_j} - \rho\varepsilon + S_s, \tag{2.32}$$

where Pr_k is a Prandtl number describing the ratio of viscous diffusion to diffusion of *k* and S_s is a source term used by the spray model to represent turbulent kinetic energy transferred from the gas phase to the liquid parcels. The transport equation for *ε* is,

$$\frac{\partial \rho \varepsilon}{\partial t} + \frac{\partial (\rho u_i \varepsilon)}{\partial x_i} = \frac{\partial}{\partial x_j} \left(\frac{\mu}{\mathrm{Pr}_\varepsilon} \frac{\partial \varepsilon}{\partial x_j} \right) + c_{\varepsilon 3} \rho \varepsilon \frac{\partial u_i}{\partial x_i} + \left(c_{\varepsilon 1} \frac{\partial u_i}{\partial x_j} \tau_{ij} - c_{\varepsilon 2} \rho \varepsilon + c_s S_s \right) \frac{\varepsilon}{k} - \rho R, \tag{2.33}$$

where for the RNG model the *R* term is,

$$R = \frac{C_\mu \eta^3 (1 - \eta/\eta_0)}{(1 + \beta \eta^3)} \frac{\varepsilon^2}{k}. \tag{2.34}$$

The η term in equation (2.34) is,

$$\eta = \frac{k}{\varepsilon} |S_{ij}| = \frac{k}{\varepsilon} \sqrt{2 S_{ij} S_{ij}}. \tag{2.35}$$

In the *ε* equation Pr_ε describes the ratio of viscous diffusion to the diffusion of *ε* and $c_{\varepsilon 1}$, $c_{\varepsilon 3}$, and $c_{\varepsilon 1}$ are model constants. The RNG model is an improvement over the standard *k*-*ε* model (*R* = 0)

because the model constants can be derived analytically from iso-tropic turbulence correlations and therefore does not require tuning of model constants.

For RANS based turbulence models, a turbulent length scale can be defined to aid in determining if the grid is properly resolved to represent turbulent diffusion rates, which is defined as,

$$le = {C_\mu}^{3/4} \frac{k^{3/2}}{\varepsilon}, \tag{2.36}$$

where C_μ is a model constant. The cell width should be less than *le* in areas where combustion is occurring to ensure accuracy in combustion rate. It was found that a cell spacing of 0.25 mm is able to accomplish this in most situations.

The assumption of a well stirred reactor in each cell was made. Even though RANS models account for increased diffusion rates from sub-grid turbulence, there is still commutation error between the cell centered temperature and averaged reaction rate. There were no sub-grid models used to correct the cell centered mean reaction rate for turbulence-chemistry interactions (TCI). However, Pomraning et al. [24] found that the well-stirred reactor assumption with a RANS turbulence model is able to achieve grid convergence for premixed and non-premixed combustion at cell sizes of 0.25 mm and smaller using AMR and that the converged solution agreed well with experimental measurements of premixed and non-premixed flames. Pomraning et al. also concluded that while the TCI commutation error in the cell-average reaction rate is not accounted for with the well-stirred reactor assumption, in a well-resolved RANS simulation the magnitude of this error must not be significant in comparison to other sources of uncertainty.

2.4. Sector initial conditions

The initial conditions in the engine sector simulations used a homogenous temperature, pressure, and composition. As explained previously, the initial velocity and turbulence fields in the sector simulations were mapped from an intake stroke simulation using the complete cylinder geometry. An intake simulation was performed once for each engine speed and boost pressure as the charge motion is most strongly dependent upon those parameters as opposed to the fuel air ratio of natural gas. The mapping file was then used for cases with different diesel injection timings and natural gas/air ratio as long as the engine speed and boost pressure were the same.

A single cylinder GT-POWER model was used to find the trapped mass at (intake valve closure) IVC, the exhaust residual mass, the IVC pressure, and the IVC bulk temperature. The values for IVC temperature and pressure obtained from the GT-POWER simulation were close to the values obtained from the intake stroke simulation, but small differences in initial pressure and temperature can lead to larger differences in the TDC pressure and temperature, which affects the ignition delay of the spray and the flame speed. It was found that using the GT-POWER results for IVC pressure and temperature in the sector simulations gave closer agreement with the experimental compression curve in comparison to the conditions found from the CONVERGE intake stroke simulation. This closer agreement could be due to the multiple cycles used in the GT-POWER solution. Even though the agreement was close using the GT-POWER initial conditions, some tuning of the initial pressure and corresponding initial temperature was necessary for the sector simulations to more closely match the pressure curve during the compression stroke. Also some final tuning of wall temperatures was used to match the TDC pressure as the heat transfer has the most significant impact on cylinder pressure near TDC.

2.5. Boundary Conditions

For the sector simulations, periodic boundary conditions were used where mass, momentum, and energy could translate from one side of the sector to the other. The walls of the cylinder used homogenous Neumann conditions for pressure, species, passives, and turbulent kinetic energy. The turbulent dissipation rate used a zero Dirichlet condition. The surface roughness of all surfaces was set to zero. Turbulent law of the wall functions where used for the velocity and temperature boundary conditions. Law of the wall functions are logarithmic fits of a turbulent boundary layer and are necessary at high Reynolds number flows, because resolving the viscous sub-layer would require very small cells that would be computationally expensive. When using a κ-ε turbulence model, CONVERGE uses the velocity law of the wall from Launder and Spalding [25], which uses a Von Karmen constant of 0.42. For temperature, the turbulent heat transfer model of Amsden [26] was used. These wall functions are described in further detail within the CONVERGE™ theory manual [21].

2.6. Spray Model

The spray model considered in this study was that of the Lagrangian drop Eulerian fluid type. Unless otherwise stated, the liquid phase was modeled as a single component with the thermodynamic properties of diesel fuel obtained from the CONVERGE™ liquids property library (known as "DIESEL2"). These properties include the vapor pressure, density, heat capacity, and surface tension as functions of temperature. These properties are close to those for tetradecane. The dynamics of the spray droplets were modeled using a statistical approach where Lagrangian particles called parcels are used to represent a group of identical droplets. The blob

injection method was used in which parcels are initialized at a random location within the nozzle diameter with a drop radius equal to the nozzle radius. These initial parcels are referred to as parent parcels and represent the intact liquid core of the spray. Droplet breakup was modeled using the modified KH-RT droplet breakup model, in which the Kelvin-Helmholtz (KH) breakup mechanism initially strips off smaller droplets from the parent parcels due to surfaces waves from viscous aerodynamic forces. These smaller drops are represented by adding child parcels having a breakup droplet radius and reducing the mass of the parent parcel such that mass is conserved. Thereafter the breakup of child parcels occurs as a competition between the KH mechanism and Rayleigh-Taylor (RT) mechanism due to droplet deceleration, which causes child parcels to split into a greater number of parcels all having a smaller RT breakup radius. Because the parent parcels are only broken up by the KH mechanism, the hybrid model does not use a defined breakup length to model primary breakup. More details of the modified KH-RT breakup mechanism is contained in the CONVERGE™ theory manual [21]. The magnitude and wavelength of the initial liquid surface disturbances responsible for the primary KH breakup were modeled using the KH-ACT method of Som and Aggarwal [27], which includes effects for aerodynamics, cavitation, and turbulence within the nozzle.

Droplet collisions can also cause droplets to break apart as well as cause them to merge into larger droplets. Collision and coalescence were modeled using the no time counter (NTC) collision model of Schmidt and Rutland [28]. Collision outcomes included reflexive and stretching separation as described by Post and Abraham [29]. The droplet distribution throughout the spray is highly dependent upon the collision model and a convergent outcome requires a sufficient number of injected parcels. The number of parcels chosen is based on validation against experiment spray data as described in Chapter 4. Droplet/wall interactions were modeled

using the CONVERGE™ hybrid film model, which uses both particle and film height quantities to model wall impingement [21]. The Frossling correlation was used to model droplet vaporization, which assumes a homogeneous droplet temperature.

Modeling of momentum coupling between the liquid and gas phases is a challenging problem for high pressure sprays and is well known to produce grid dependent results. One reason for this is because much of the exchange of momentum occurs in the boundary layer surrounding the droplets as they travel through the gas. However, the droplet boundary layers are of such a small scale that resolving them in a CFD simulation is far too computationally expensive. Therefore, sub-grid models are required to exchange momentum between the parcels and the cell centered nodes. One example of grid size dependence that arises from a sub-grid approach is when the parcel velocity becomes close to the cell velocity such that the relative velocity is nearly zero. The relative velocity is responsible for determining breakup time in the KH and RT breakup mechanisms. With zero relative velocity the breakup time in the KH and RT mechanisms becomes goes to infinity and very long liquid penetrations are the result. This non-physical result is due to grid size and can lead to highly inaccurate combustion results. CONVERGE™ uses a nearest node approach to for the exchange of momentum from liquid parcels to the gas phase and an interpolation method to exchange momentum from the gas phase to the liquid parcels, which significantly helps prevent the relative velocity from going to zero. Nevertheless, sufficient grid resolution is required. As described previously, Senecal et al. [22] performed grid convergence studies for sprays using the same models in the CONVERGE code and found that a cell width of 0.25 mm resulted in grid convergent spray behavior. The computational cost increased greatly with further refinement. Therefore, the 0.25 mm cell width is used for the sprays in this study.

To model the diesel injection, CONVERGE™ first calculates the injected mass flow rate as a function of time, $\dot{m}(t)$, from user supplied measurements of the total injected mass, the injection duration, and the rate of injection profile or rate shape. Using $\dot{m}(t)$, the mass injected during during a time step is determined and this mass is divided evenly among the number of parcels injected during that time step, which is determined by evenly distributing the total number of injected parcels across the injection duration. The injection velocity v_{inj} of the parcels is related to the injected mass flow rate according to,

$$\dot{m} = \rho_l A_{eff} v_{inj} \tag{2.37}$$

where ρ_l is the liquid density and A_{eff} is the effective area of the jet due to area contraction from a vena contracta. However, the effective area is unknown and therefore the injection velocity must be related to the geometric area of the nozzle orifice, A_n. Prior to area contraction, the mass flow rate is defined as,

$$\dot{m} = \rho_l A_n v_{old} \tag{2.38}$$

where v_{old} is the average velocity before area contraction. With $\dot{m}$ known v_{old} can be solved for directly. Therefore, a relation is needed between v_{old} and v_{inj} to complete the spray parcel initialization.

The two definitions for mass flow rate in equations (2.37) and (2.38) can be related using a discharge coefficient model,

$$\dot{m} = C_d \rho_l A_n v_{ideal} \tag{2.39}$$

where ρ_l is the liquid density, A_n is the nozzle's orifice area, C_d is the discharge coefficient, and v_{ideal} is the ideal velocity. The ideal velocity is found from the Bernoulli relation for inviscid flow according to,

$$v_{ideal} = \sqrt{\frac{2\,\Delta P_{inj}}{\rho_l}}, \tag{2.40}$$

where ΔP_{inj} is the pressure difference across the injector nozzle. When the flow is steady ΔP_{inj} should be equal to the difference between the measured rail pressure, P_{rail}, and the measured cylinder pressure, P_{cyl}. CONVERGE™ first calculates v_{old} using the known mass flow rate and equation (2.38). Equating equations (2.38) and (2.39), the injection pressure is then calculated according to,

$$\Delta P_{inj} = \tfrac{1}{2}\rho_l \left(\frac{v_{old}}{C_d}\right)^2 \tag{2.41}$$

The discharge coefficient is a user supplied quantity that and is typically measured under steady flow conditions. The discharge coefficient accounts for the effects of viscid flow and the vena contracta via,

$$C_d = C_a C_v \tag{2.42}$$

where C_a is the contraction coefficient,

$$C_a = \frac{A_{eff}}{A_n}, \tag{2.43}$$

and C_v is the velocity coefficient,

$$C_v = \frac{v_{inj}}{v_{ideal}}. \tag{2.44}$$

For the simulations performed in this study CONVERGE™ uses the varying injection pressure, $\Delta P_{inj}(t)$, to calculate a dynamic velocity coefficient, $C_v(t)$. The relation between velocity coefficient and injection pressure is not publicly shared by Convergent Science. Using C_d and $C_v(t)$, $C_a(t)$ is then calculated from equation (2.42). Finally, the initial velocity of the injected parcels is found from,

$$v_{inj} = \frac{v_{old}}{C_a} \tag{2.45}$$

2.7. Chemistry model

Reduced chemical kinetic mechanisms were used to solve for the chemical reaction rates at each cell center in all of the simulations presented in this work. A chemical kinetic mechanism is a set of elementary reactions and associated rate constant information, which when solved as a system of equations can describe the overall chemical reaction rates that occur during combustion. These kinetic mechanisms were reduced from detailed mechanisms, which are too large to yield run times less than 24 hours in multi-dimensional CFD simulations. To limit the compute time, a goal of the reduction was to keep the size of the reduced mechanism under 150 species. CONVERGE™ uses a preconditioned iterative solver for mechanisms over 100 species, which significantly reduces the compute time. To further reduce computational cost, a multi-zone chemistry model was employed where the chemistry for cells similar in temperature, progress equivalence ratio, and mass fraction of the fuel species are solved simultaneously. The

multi-zone method of Babajimopoulos et al. [30] was used. The mechanisms were written in the CHEMKIN® format, which uses the Arrhenius form for the reaction rate constants.

For most of the simulations, diesel fuel was represented as n-heptane due to the similar ignition delay properties with diesel fuel [22] and similar heating value. Natural gas was represented as a mixture of methane, ethane, and propane with the composition matched to a gas sample measurement. While pipeline quality natural gas is predominantly methane, its reactivity is greatly influenced by the presence of ethane and propane, which are typically present in low concentrations, but have much higher reactivity than methane. The measured natural gas compositions in this work had negligible levels of hydrocarbons heavier than propane and therefore the assumption of a methane through propane surrogate is an accurate one.

The direct relation graph with error propagation and sensitivity analysis (DRGEPSA) method [21], was used to reduce the base mechanisms. Direct relation graph methods are automatic reduction algorithms that remove unimportant species by comparing reaction rates from zero dimensional ignition delay calculations. To do this a set of important species or target species is selected and a range of initial temperatures, pressures, and equivalence ratios is used to initialize the ignition delay calculations. Species that do not change the ignition delay more than a specified tolerance are removed and a smaller mechanism is produced which has similar ignition delay behavior as the original mechanism. The predictive capability of the reduced mechanism when used to simulate real engine data is dependent upon the range of temperatures, pressure, and compositions used in the reduction procedure. A more detailed description of the DRGEPSA algorithm is provided in the CONVERGE™ theory manual [21].

In addition to solving combustion chemistry, the extended Zeldovich mechanism for NO formation was included in the simulations. This is three reaction mechanism which uses quasi-

steady state assumptions and equilibrium constants to solve for thermal NO formation. The NO mass is converted to NO_2 mass using a factor of 1.533.

2.8. Computational Hardware

The majority of the simulations were performed on the CSU's ISTeC Cray High Performance Computing System. This is a Cray XE6 model which contains 54 nodes, 2 processors per node, and 16 cores per processor. Each node contains 32 GB of RAM. Each processor is a 64 bit, 1.9 GHz AMD Magny Cours. Sector simulations typically used 48 to 64 cores and the intake stroke simulations used over 300 cores. OpenMPI was used for the parallel processing, which on a Cray system required the use of the cluster compatibility mode (CCM).

There was also a small local cluster that was used in some of the spray simulations and some of the early engine sector simulations. This was a system of HP processors with each node having 16 cores and 32 MB of RAM. CONVERGE™ was run using HPMPI to handle the parallel processing. Sector simulations utilized either one or two nodes.

CHAPTER 3: EXPERIMENTAL SETUP

3.1. Conversion of Light Duty Diesel Engine to Dual Fuel Engine

Engine experiments were conducted using a four cylinder light-duty General Motors (GM) 1.9 L common rail, turbo-charged diesel engine. The specifications of the engine are listed in Table 3.1 and the diesel injector specifications are listed in Table 3.2. For the experiments described herein, the engine was modified to allow multi-port injection of natural gas. This modification was accomplished by building a natural gas rail with Woodward natural gas injectors attached to the rail and connecting tubing from each injector to the intake manifold runners as shown in Figure 3.1, such that the gas was injected perpendicular to the air flow direction. To ensure that all natural gas mass was introduced when the air flow rate into the cylinders was high, injections were timed such that the end of injection was no less than 10 degrees before intake valve closure (IVC) and the start of injection was just after intake valve opening (IVO). This minimized cylinder to cylinder exchange of natural gas, which leads to cylinder load imbalances and introduces uncertainty as to how much natural gas to use as a model input. The maximum natural gas injection pressure was limited by the injector characterization table to 7 bar. Therefore, the amount of natural gas that could be injected was limited.

A propane injection system was installed to mix additional propane with natural gas for port injection into cylinder 2, as indicated by the ‘T’ connector in Figure 3.1, for two reasons. Firstly, the presence of end gas auto-ignition is more prevalent in large bore engines because the premixed natural gas flame must travel a further distance to consume all the gas in the cylinder, giving the end gas a longer residence time to undergo auto-ignition reactions. This can make it

Table 3.1. Engine specifications.

GM engine code	Z19DTH
Cylinder arrangement	4 Inline
Displacement volume	1.9 L
Bore	82 mm
Stroke	90.4 mm
Connecting rod length	161 mm
Compression ratio	17.5
Injection system	Bosch Common Rail
Max injection pressure	1600 bar
Valves per cylinder	4 DOHC
Rated power	110 kW (147.5 hp) @ 4000 RPM
Rated torque	315 Nm (232 ft-lbf) @ 2000 RPM

Table 3.2. Diesel injector specifications.

Name	Bosch CRIP 2-MI
Nozzles	7
Nozzle orifice diameter	141 micron
Included spray angle	148
Flow specification	440 mm^3/30 sec
Discharge coefficient	0.86

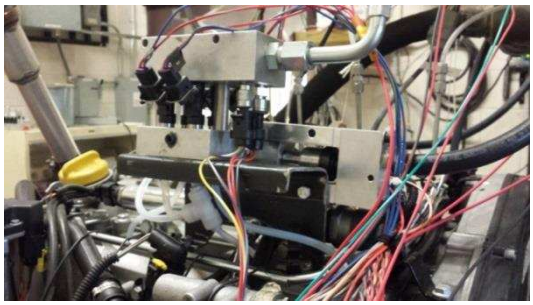

Figure 3.1. Natural gas and propane port injection installation. Note that the propane injection tube tees into the natural gas tube for cylinder 2.

difficult to induce knocking in small bore engines, such as the one used in this study. However, by adding a small amount of propane to make the natural gas more reactive, the ratio of flame travel time to end gas ignition delay time in a small bore engine can be made more similar to that in a large bore engine. Additionally, the reactivity of natural gas, as characterized by methane number, can vary greatly worldwide and therefore the presence of end gas knocking in a dual fuel engine can be dependent upon the concentration of higher hydrocarbon species than

methane. Propane is often added to simulate fuels with lower methane number and higher knock tendency. For both of these reasons, propane addition to cylinder 2 was used in some experiments.

The engine and injectors were controlled by a Woodward Engine Control Module (ECM), which enabled control over diesel injection pressure, boost pressure, swirl level, EGR rate, and individual cylinder control of diesel and natural gas injection timing and duration. The diesel fuel consumption was measured using Micro Motion CMF025 Coriolis mass flow meters on the supply and return of the fuel tank, which have an accuracy of ±0.1% of the measured rate. Natural gas consumption was measured using a Micro Motion CMF010 Coriolis mass flow meter, which has an accuracy of ±0.35% of the measured rate. The air mass flow rate was measured with an automotive hot wire anemometer, which has an accuracy of ±3%. In-cylinder pressure transducers (Kistler 6058A) were installed in the glow plug hole of each cylinder and pressure data was acquired on a National Instruments data acquisition system. Diesel Rail pressure was controlled using a pressure regulator, an inlet metering valve on the high pressure pump, and a Bosch pressure transducer on the rail. Fuel temperature was measured prior to the high pressure pump. Crank angle data was acquired with a resolution of 0.25 crank angle degrees. Apparent heat release rates (AHRR) were calculated based on 100 cycle averaged pressure and assuming a constant ratio of specific heats of 1.3. A 5-point moving average was applied to smooth out the AHRR profiles. The simulated AHRR profiles were calculated by applying the same algorithm to the simulated pressure curves.

NOx emissions analyzers were installed in each of the exhaust ports. The make and model for these analyzers were ECM NOx 5210. Thermocouples were also installed in each of the

exhaust ports so that exhaust temperature could be compared with the exhaust temperature from the GT-POWER cycle simulations.

3.2. Rate of Injection Meter and Injector Characterization

The rate shape and injection duration strongly determine the velocity of injected parcels, which has a significant effect on the rate of droplet break up and vaporization. A Bosch type rate of injection meter was used to measure the rate shape, the injection duration, the delay period between application of the electric current profile and the start of injection, and the injected mass as functions of electronic pulse width and injection pressure. Figure 3.2 shows a schematic layout of the apparatus used in the rate of injection measurements. When the injector fires pressure waves travel down the passageway in the housing and through the 11 meter rate tube. An orifice at the end of the rate tube is used to dampen the reflected pressure wave. A pressure transducer is placed in a static port in the housing near the injector tip is used to record the pressure wave.

The shape of the pressure versus time profile of the wave is directly proportional to the rate of volume flow through the injector. This can be expressed as,

$$P = \rho_f a u_t, \tag{3.1}$$

where a is the speed of sound of the fluid, ρ_f the fuel density, and u_t the average flow velocity in the tube. This can then be combined with the continuity equation to give the volume flow rate as a function of the pressure,

$$\dot{q} = \frac{A_t}{a\rho_f} P, \tag{3.2}$$

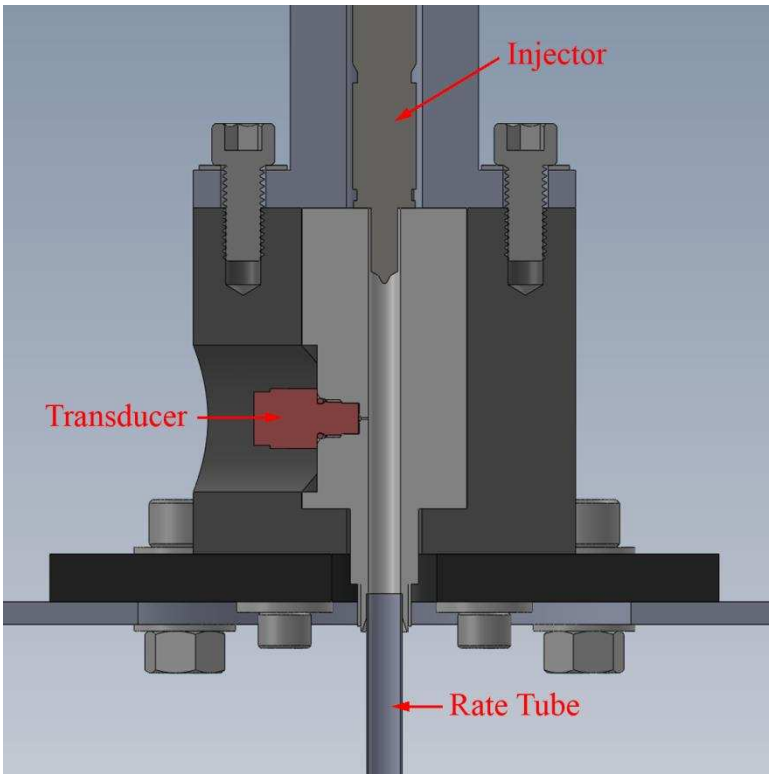

Figure 3.2. Internals of the apparatus used to hold injector and measure the pressure wave.

where A_t is the cross sectional area of the tube. In addition to rate shape, the mass flow rate was measured using an AVL flow meter. A function for density versus temperature was used to convert the mass flow rate into volume flow rate, because the injected volume is independent of fuel density. This allowed for volume injected as a function of injection pressure and electronic injection duration to be tabulated, which are known as injector characterization tables. The characterization tables could then be used in a feed forward torque based control scheme where the ECU can predict the amount of necessary fuel to inject in order to deliver a commanded engine torque. The fuel temperature on the engine was used to determine the fuel density in real time, convert the desired fuel mass into volume per injection, and determine the electronic pulse width. This rate of injection data was gathered for each of the four injectors used in the engine experiments. Figure 3.3 shows an example of this data for one of the injectors. A comparison

between the curves for all four injectors at a single injection pressure of 600 bar is shown in Figure 3.4, which demonstrates quantitatively similar behavior from injector to injector.

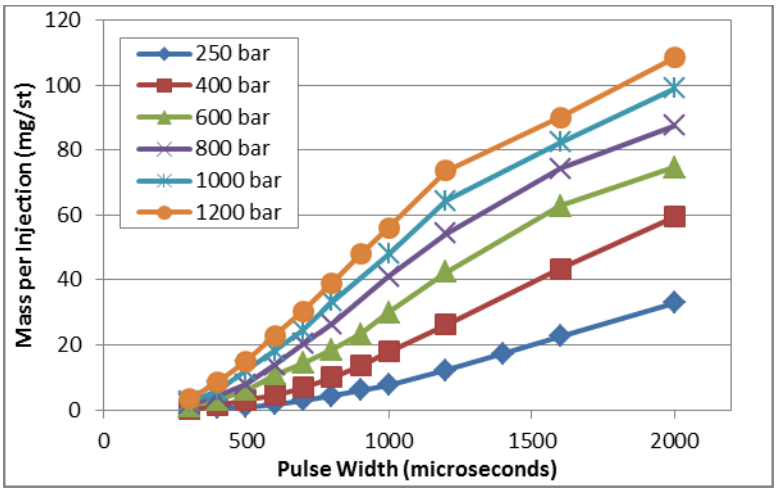

Figure 3.3. Example of injector characterization data for one of the four injectors.

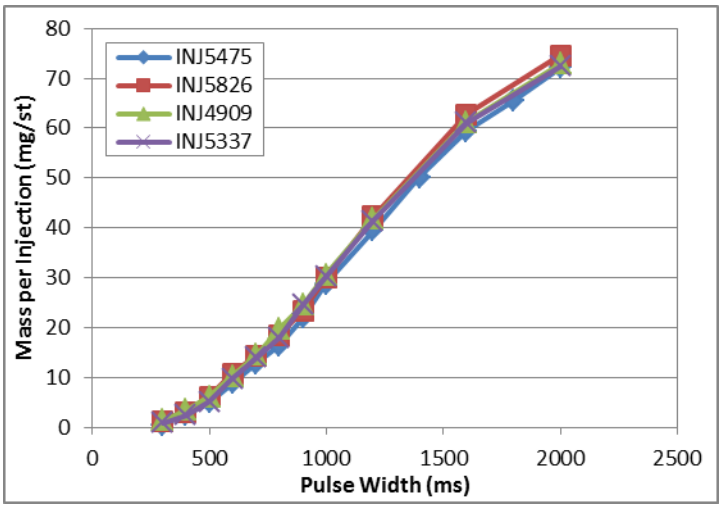

Figure 3.4. Comparison of an injector characterization curve between all four injectors at 600 bar injection pressure.

The ROI data provided an injection duration and shape to model the injection velocity with. As described in the computational section, there is a predicted injection pressure. For long injection durations the steady state rate should result in a maximum injection pressure close to the experimentally measured rail pressure. However, for short injection durations the steady state

rate is never reached. In these cases the maximum injection pressure can be checked by comparing the short duration rate shape with a long injection rate shape at the same injection pressure. An example is depicted in Figure 3.5. The peak injection pressure for the short duration case should scale with the ratio of peak injection rate to the steady state rate for the long injection duration. In this case the predicted peak injection pressure should therefore be close to 530 bar rather than the experimentally measured 700 bar. For such short injection durations it was found that a slightly lower discharge coefficient was necessary to achieve the 530 bar. This can be attributed to the fact that discharge coefficients are measured with the injector needle fully open and only describes the behavior at steady state injection rate. Therefore, the transient behavior of the needle can be accounted for by reducing the discharge coefficient until the expected peak injection pressure is attained.

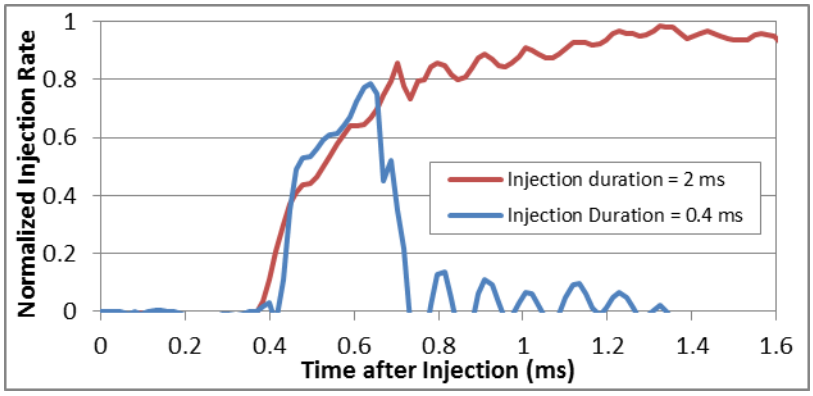

Figure 3.5. Comparison of a short injection rate shape with another one at the same injection pressure but with a much longer injection duration.

CHAPTER 4: SPRAY MODEL VALIDATION

4.1. Engine Combustion Network Experiments

The spray model was validated against spray experiments done by the Engine Combustion Network (ECN) at Sandia National Laboratories [31], which consisted of a vaporizing, but non-reacting spray injected into a constant volume chamber at typical TDC temperature and pressure conditions. Measurements of liquid penetration, vapor penetration, and fuel mixture fraction were made using various optical imaging and laser diagnostic techniques. A detailed explanation of the experimental techniques can be found on the ECN website [31]. Spray simulations were performed for the 500 bar injection pressure Spray A condition [32] and the 1500 bar injection pressure Spray H condition [33]. Specific details about these two experimental conditions are listed in Table 4.1. Rate of injection profiles were available for each of these injections. The injected mass was not provided in the experimental data for Spray A. Therefore, the injected mass used in the model for Spray A was increased until the predicted injection pressure was equal to the experimentally measured injection pressure.

Table 4.1. Experimental conditions of two ECN sprays used for model validation.

ECN spray name	Spray H	Spray A
Fuel	n-heptane	n-dodecane
Injection Pressure (bar)	1543	539
Injected mass (mg)	17.8	7.8
Injection duration (ms)	6.8	5.65
Ambient Temperature (K)	967	893
Ambient Pressure (bar)	43.3	60.7
Oxygen %	0	0
Nozzle Orifice diameter (mm)	0.100	0.090
Discharge coefficient	0.8	0.86
Fuel temperature (K)	373	373

The geometry used for the spray simulations consisted of a cube with a side length equal to that of the experimental chamber. A base cell width of 4 mm was used and adaptive mesh refinement was used to refine the grid down to 0.25 mm cells based on velocity, temperature, and fuel mass fraction gradients. Fixed embedding of 0.25 mm cells was used in the near nozzle region. The choice for a minimum cell size of 0.25 mm is based on the grid convergence studies performed by Senecal et al. for diesel sprays [22].

Comparisons of liquid and vapor penetration between the simulations and the experiments are shown in Figure 4.1. The vapor penetration in the simulations was defined as the maximum axial distance where the fuel mass fraction was 0.1%. The liquid penetration in the simulations was defined as the maximum axial distance where the liquid volume fraction within a cell was 0.1%. The spray model demonstrates excellent agreement within the first millisecond, which is longer than typical ignition delays periods for the particular diesel engine used in this thesis. Therefore, the breakup and vaporization physics is well represented using the current spray model at both a low and high injection pressure.

The Spray H dataset also includes the spatial distribution of the ensemble averaged fuel mixture fraction at various times after start of injection. Comparisons between experimental and simulated fuel mass fraction were made at 1.13 ms after start of injection. Figure 4.2 presents the fuel mass fraction profile down the centerline of the spray axis, in which the uncertainty in the experimental measurement is represented by the vertical thickness of the line. The simulated centerline fuel mass fraction shows that the axial penetration is about 3 mm shorter than the experimental. The simulated fuel mass fraction is higher than experimental at the most upstream position, but the agreement is within 25% relative error for most of the vapor penetration length. The degree of qualitative and quantitative agreement in Figure 4.2 demonstrates that the coupling

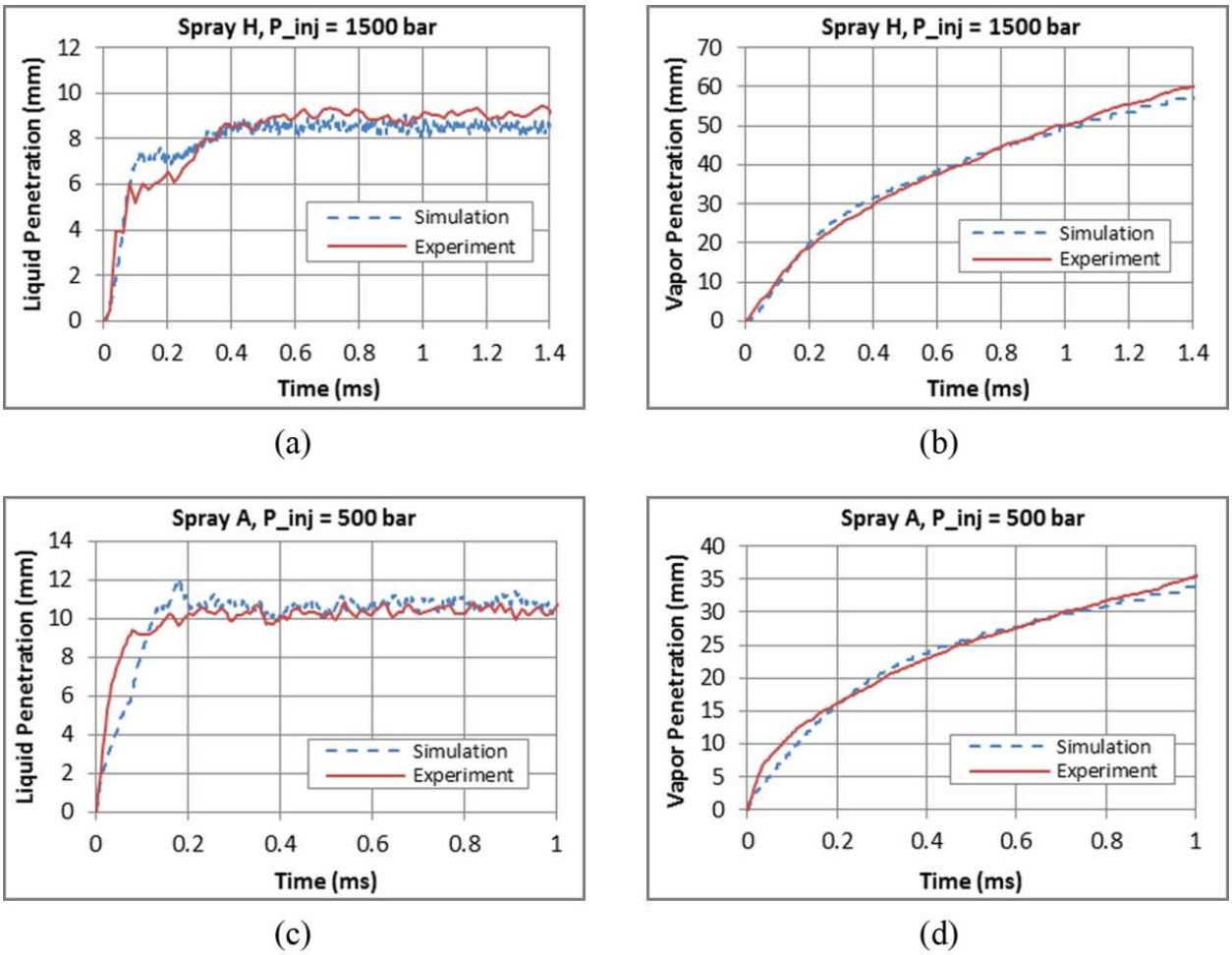

Figure 4.1. Comparisons between spray simulations and ECN experiments. (a) Liquid penetration for 1500 bar injection pressure Spray H. (b) Vapor penetration for 1500 bar injection pressure Spray H. (c) Liquid penetration for 500 bar injection pressure Spray A. (d) Vapor penetration for 500 bar injection pressure Spray A.

of the spray models and the turbulence model is able to reproduce with sufficient accuracy the fuel air mixtures in a real diesel spray at engine conditions that control the ignition delay.

Figure 4.3(a) and (b) present a similar comparison for radial fuel mass fraction profiles made at 25 mm and 45 mm downstream of the injector. Throughout most of the interior of the spray the fuel mass fraction is well captured by the model. For the 25 mm location, there is some small discrepancy at the periphery of the vapor boundary. At the 45 mm location, the centerline fuel

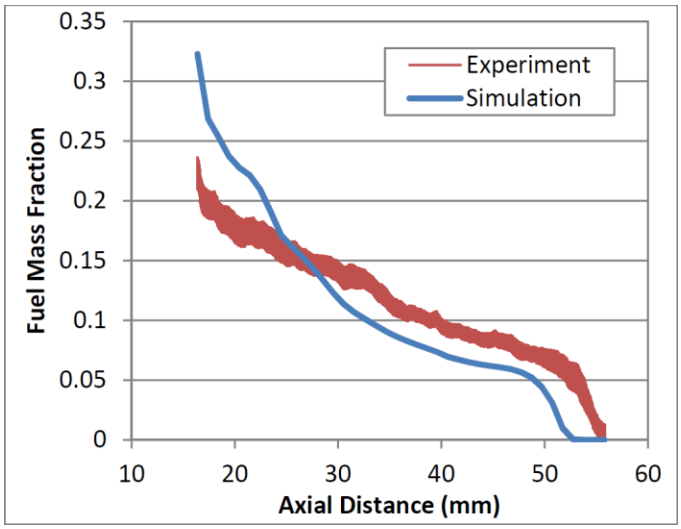

Figure 4.2. Experimental and simulated centerline fuel mass fraction for the Spray H condition.

mass fraction is under predicted by approximately 25%, which is consistent with the results in Figure 4.2. However, the level of agreement throughout the majority of the spray cross section at both locations indicates that the model can sufficiently predict the diffusion rates of fuel into air, which has a significant impact on ignition delay and flame location in diesel sprays.

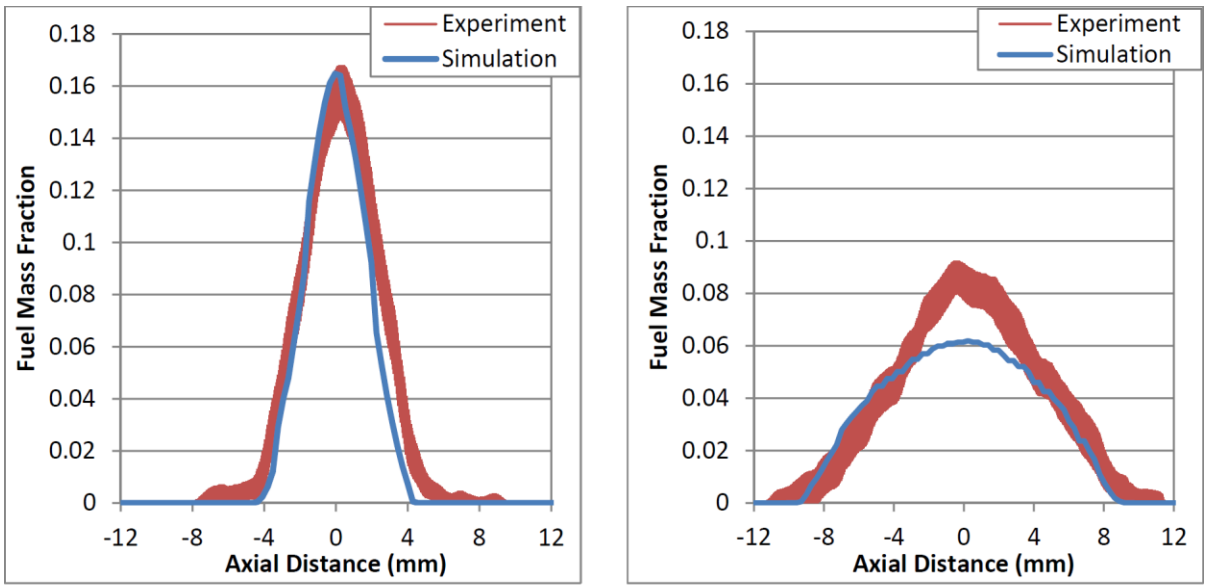

Figure 4.3. Radial profiles of experimental and simulated fuel mass fraction for the Spray H condition at (a) 25 mm and (b) 45 mm downstream of the injector.

CHAPTER 5: A REDUCED CHEMICAL KINETIC MECHANISM FOR CFD SIMULATIONS OF NATURAL GAS/DISEL DUAL FUEL ENGINES

5.1. Introduction

To date there is still not a sufficient chemical kinetic mechanism for simulating natural gas/diesel dual fuel combustion that can account for the variation in chemical reactivity of the natural gas source. Niemann et al. [15] used pure methane as a natural gas surrogate in a multi-dimensional model KIVA model for natural gas/diesel reactivity controlled compression ignition (RCCI) under the assumption that a natural gas mixture with high methane content should behave similarly to pure methane. However, Bourque et al. [17] found that ignition delay periods and flame speeds for typical pipeline natural gas compositions with small concentrations of heavier hydrocarbons can be quite shorter compared with pure methane. Rahimi et al. [34] presented a 76 species reduced chemical kinetic mechanism for natural gas/diesel homogeneous charge compression ignition (HCCI) engines by combining a reduced n-heptane mechanism with the GRI-Mech 3.0 natural gas mechanism and then using a genetic optimization algorithm to adjust rate constants for three different engine operating conditions consisting of different natural gas percentage, total equivalence ratio, exhaust gas recirculation (EGR), and compression ratio. However, only one natural gas composition was validated in the study by Rahimi et al. and therefore a rate constant optimization and validation study is necessary before it can be applied to a different natural gas composition. Also, the validation simulations used a five zone model rather than a multi-dimensional CFD simulation, meaning the rate constant optimization could be compensating for errors from the simplified spatial resolution. Furthermore, the mechanism of Rahimi et al. was validated for HCCI simulations and not for simulations of premixed

propagating natural gas flames or non-premixed diesel spray flames, which are present in dual fuel engines and should be validated using a multi-dimensional simulation with sufficient spatial resolution.

The objective of the present study is to develop a reduced chemical kinetic mechanism from highly detailed base mechanisms for use in multi-dimensional CFD simulations of natural gas/diesel dual fuel engines where premixed propagating natural gas flames and non-premixed diesel spray flames are present. The developed mechanism does not utilize rate constant tuning and can model a wide variation in natural gas composition while yielding compute times of less than 24 hours. Validation studies for the present reduced mechanism include comparisons with detailed mechanisms using calculated ignition delay sweeps and HCCI simulations, experimental methane laminar flame speeds at high pressure, optical experiments for a reacting diesel spray in a constant volume chamber, and dual fuel engine experiments for two different natural gas compositions including a case where engine knocking occurred.

5.2. CSU141 Reduced Mechanism

The new reduced dual fuel chemical mechanism was constructed from previously published detailed mechanisms. Diesel fuel was modeled using n-heptane due to similar Cetane number and heating value with diesel fuel [22]. Natural gas was modeled using mixtures of methane, ethane, and propane as a surrogate. While pipeline quality natural gas is predominantly methane, its reactivity is greatly influenced by the presence of ethane and propane, which are typically present in low concentrations (< 10% by volume combined), but have much higher reactivity than methane. Larger hydrocarbons such as butane and pentane were not included in the natural gas surrogate mixture, because they typically have a very low concentration in pipeline natural

gas mixtures and have been shown not to have a significant impact on the combustion behavior when present in such low concentration [35] [36].

A reduced methane/ethane/propane mechanism was formulated from the detailed methane through n-pentane mechanism (293 species, 1588 reactions) from Healy et al. [37] at the National University of Ireland Galway, hereafter referred to in this paper as the NUIGIII mechanism. This detailed natural gas mechanism has been previously validated against experimental ignition delay data from rapid compression machine and shock tube experiments at temperatures between 630 and 1550 K, pressures up to 30 bar, and at lean, stoichiometric, and rich conditions. A reduced n-heptane mechanism was formulated from the detailed n-heptane mechanism from Curran et al. [38] [39] at Lawrence Livermore National Laboratories (LLNL) with 561 species and 2539 reactions, hereafter referred to as the LLNL mechanism. The detailed LLNL mechanism has previously been validated against experimental ignition delay data from rapid compression machine and shock tube experiments for temperatures between 550 and 1700 K, pressures between 1 to 42 atm, and equivalence ratios from 0.3 to 1.5.

The direct relation graph with error propagation and sensitivity analysis (DRGEPSA) method [40] was used reduce the detailed base mechanisms, which is an automatic mechanism reduction algorithm included within the CONVERGE™ software package. The NUIGIII mechanism was reduced based on ignition delay calculations of two different natural gas mixtures in air as described in Table 5.1. The target species included helium and argon to retain the third body efficiency information, because these inert species are often used in laminar flame experiments at high pressure. The 85% methane composition was chosen to be similar to the composition measured in the engine experiments. This reduction resulted in a 49 species skeletal mechanism for methane, ethane, and propane mixtures. A preliminary study of this reduced mechanism

found that ignition delay for pure propane in air did not agree well with the NUIGIII mechanism. Therefore, another reduction was performed for a composition with higher propane content than ethane content, which resulted in a 46 species skeletal natural gas mechanism. Next, DRGEPSA was used to reduce the LLNL n-heptane mechanism to a 131 species and 656 reactions skeletal mechanism. The three reduced mechanisms were then combined to form the final 141 species and 709 reactions reduced chemical kinetic mechanism for mixtures of methane, ethane, propane, and n-heptane, which is hereafter referred to as the CSU141 mechanism. An illustration of the reduction procedure is given in Figure 5.1.

Table 5.1. Conditions used for reducing the base mechanisms using DRGEPSA.

Base Detailed Mechanism	LLNL n-heptane	NUIGIII Natural Gas	NUIGIII Natural Gas
Target species	n-C_7H_{16}, O_2, OH, HO_2, CH_4, C_2H_6, C_3H_8, He, Ar, N_2	CH_4, C_2H_6, C_3H_8, O_2, OH, HO_2, CO_2, H_2O, Ar, He, N_2	CH_4, C_2H_6, C_3H_8, O_2, OH, HO_2, CO_2, H_2O, Ar, He, N_2
Fuel composition (mole frac.)	$X_{nC7H16} = 1.0$	$X_{CH4} = 0.85$, $X_{C2H6} = 0.1$, $X_{C3H8} = 0.05$	$X_{CH4} = 0.93$, $X_{C2H6} = 0.02$, $X_{C3H8} = 0.05$
Temperature (K)	700, 750, 800, 850, 900, 950, 1000, 1050, 1100, 1150, 1200	750, 800, 850, 900, 950, 1000, 1050, 1100, 1150, 1200	750, 800, 850, 900, 950, 1000, 1050, 1100, 1150, 1200
Pressure (bar)	10, 30, 80	10, 30, 80	10, 30, 80
Equivalence ratio, φ	0.2, 0.5, 1.0, 1.5, 2.0	0.2, 0.4, 0.6, 0.8, 1.0, 1.2, 1.4	0.2, 0.4, 0.6, 0.8, 1.0, 1.2, 1.4
Ignition delay error (%)	0.1	0.5	0.5
Sensitivity analysis fraction	0.75	0.75	0.75

Any duplicate reactions between the three reduced mechanisms were given the rate constant values from the reduced natural gas mechanisms to ensure that engine knocking from natural gas auto-ignition is accurately represented. Care was taken to find and add reactions from the detailed base mechanisms that were not in any of the individual reduced mechanisms, but whose species were all present after combining the reduced mechanisms. For laminar flame speed

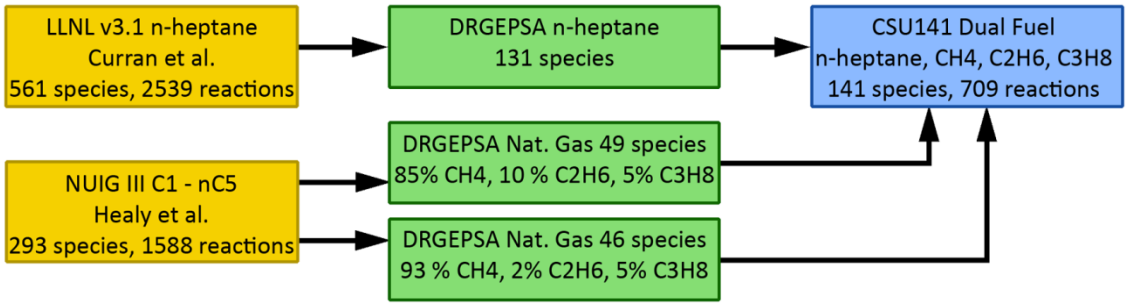

Figure 5.1. Diagram showing the reduction of detailed mechanisms and combination of reduced mechanisms.

calculations, the natural gas transport data from Bourque et al. [17] was combined with the transport data from the LLNL n-heptane mechanism, whereby any duplicate species were given the transport data from the natural gas data file. The CSU141 mechanism (species, reactions) is provided in appendix A.

Ignition delay and zero dimensional HCCI engine calculations were performed using CHEMKIN®. The ignition delay period was defined by a 400 K increase in temperature, because this is the definition built into the DRGEPSA algorithm. The 400 K increase definition was compared with the maximum temperature derivative definition and good agreement between the two definitions was observed at all conditions. The present CSU141 mechanism is not compared against experimental ignition delay data, because a heat loss model would need to be added in the calculations and this would introduce additional error making it difficult to assess the accuracy of the reduction method. The reader should refer to the detailed mechanisms for comparisons with experimental ignition delay periods.

5.3. Engine Experiments

The experimental operating conditions are listed in Table 5.2. The nomenclature for referring to the different operating conditions in Table 5 uses a ‘D’ to designate diesel followed by the

Table 5.2. Experimental operating conditions.

Fuel case name	D25G17		D12G22		D11G8	D11G18	D12G22P2
Engine Speed (RPM)	2200		2200		2000	2000	2200
Injected diesel per cylinder (mg)	25.4		12.1 ± 3		10.6	10.6	11.7 ± 3
Natural gas per cylinder (mg)	16.5		21.8		8.0	17.9	22.1
Propane per cylinder (mg)	0		0		0	0	2.3
Natural gas substitution, z (%)	43.3		67.9		47.6	67.1	71.9
Natural Gas Composition	Lower Reactivity		Lower Reactivity		Higher Reactivity	Higher Reactivity	Lower Reactivity
Diesel injection pressure (bar)	700		700		700	700	700
Injection Duration (CAD)	13.4		6.2		5.9	5.9	5.3
Electronic SOI (°ATDC)	-8.8	-13	-8	-14	-12	-12	-10
Boost pressure (kPa abs)	169.3	167.2	168.2	163.6	120	120	163
Manifold temperature (°C)	43.6	43.5	44.6	44.4	39.6	38.6	48.2
Net IMEP (bar)	15.0	15.6	10.9	10.7	7.0	11.7	11.7
Natural gas equivalence ratio, φ_{NG}	0.357	0.362	0.479	0.512	0.25	0.55	0.600
Total equivalence ratio, φ_T	0.845	0.856	0.712	0.765	0.55	0.74	0.824

mass of diesel injected per cylinder per cycle in units of milligrams rounded to the nearest integer. In a similar manner, the letter ‘G’ signifies the mass of natural gas in milligrams and ‘P’ signifies the mass of propane in milligrams. Start of injection (SOI) timing sweeps were performed for two different fuel combinations at 2200 RPM and the highest boost pressure attainable at this engine speed. The D25G17 SOI sweep had a moderate substitution rate of about 43% natural gas by energy and the D12G22 sweep had a higher substitution rate of about 68%. Additionally, a load sweep was performed at 2000 RPM and a lower boost pressure by increasing the natural gas mass while keeping the diesel injection constant. The load sweep used a higher reactivity natural gas composition while the SOI sweeps used a lower reactivity natural gas composition as described in **Error! Reference source not found.**. The variation in natural gas composition is due to moving the location of the engine from one facility to another and conducting the experiments at different times of the year. Additionally, in the D12G22P2 experiment, an additional 2 mg of propane was added to a case from the D12G22 SOI sweep to

induce engine knocking and assess whether the model could predict natural gas auto-ignition. Therefore, these experiments encompass a wide range of substitution percentages, engine loads, natural gas equivalence ratios, natural gas reactivity, and TDC conditions for validation of the reduced mechanism.

Table 5.3. Measured natural gas composition at two different facilities.

Species	Low Reactivity (mole fraction)	High Reactivity (mole fraction)
CH_4	0.9461	0.8812
C_2H_6	0.0285	0.0823
C_3H_8	0.0031	0.0075
CO_2	0.0125	0.0167
N_2	0.0093	0.0123

5.4. Results

5.4.1. n-Heptane Ignition Delay Calculations

Figure 5.2 shows comparisons of adiabatic zero dimensional ignition delay periods between the detailed LLNL n-heptane mechanism and the CSU141 reduced dual fuel mechanism. Comparisons are made for n-heptane/air mixtures at pressures of 10, 30, and 80 bar, temperatures between 700 to 1300 K, and equivalence ratios between very lean, $\varphi = 0.2$, and rich, $\varphi = 2.0$. These temperatures and pressures are relevant to diesel sprays at engine TDC conditions. The reduced CSU141 mechanism has excellent agreement with the detailed base mechanism across all conditions presented in Figure 5.2 and in particular captures the negative temperature coefficient (NTC) region resulting from the two stage ignition process for n-heptane. Figure 5.2(d) shows excellent agreement at rich mixtures between 700 and 1000 K where diesel sprays are known to undergo auto-ignition. Therefore diesel spray auto-ignition should be well captured by the CSU141 mechanism.

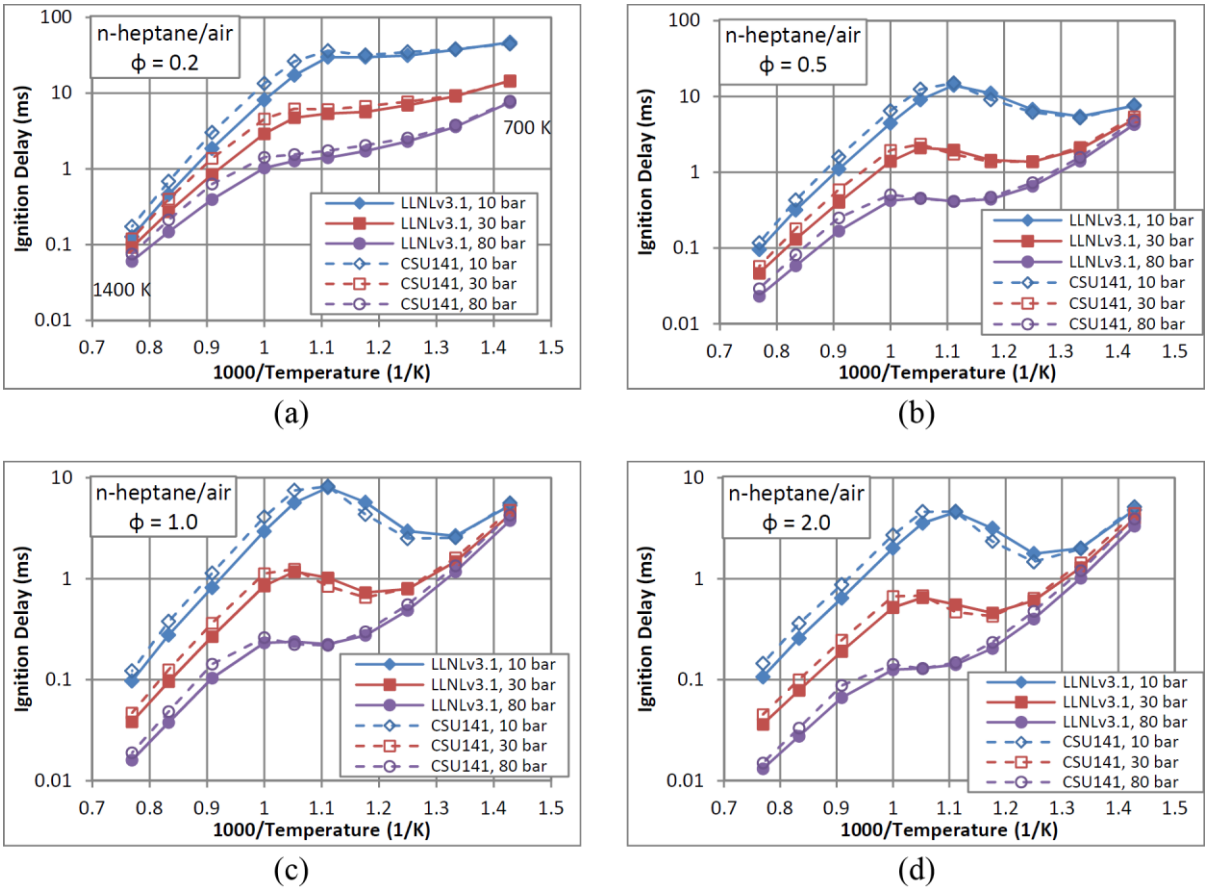

Figure 5.2. Ignition delay plots for n-heptane/air mixtures comparing the CSU141 reduced mechanism with the detailed LLNL mechanism for (a) very lean φ = 0.2, (b) lean φ = 0.5, (c) stoichiometric φ = 1.0, and (d) rich φ = 2.0 mixtures.

In addition to conventional dual fuel combustion, early injection schemes such as RCCI require accurate modeling of the chemical kinetics of diesel fuel over a wider range of equivalence ratios. Fuel air mixtures in RCCI engines can be anywhere between slightly rich to very lean and begin at temperatures lower than peak compression temperatures. Figure 5.2(a), (b), and (c) show excellent agreement for CSU141 at lower temperatures for very lean to stoichiometric conditions.

5.4.2. Natural Gas Ignition Delay Calculations

Comparisons of ignition delay between the detailed NUIGIII mechanism and the reduced CSU141 mechanism for two different natural gas/air mixtures consisting of methane, ethane, propane, and air are shown in Figure 5.3. The 90/6.7/3.3 mixture consisted of 90% methane, 6.7% ethane, and 3.3% propane by mole. The 70/20/10 mixture consisted of 70% methane, 20% ethane, and 10% propane by mole. The ignition delay plots show that the reduced CSU141 mechanism captures with excellent accuracy the behavior of the detailed mechanism for both mixtures across the range of pressures, temperatures, and equivalence ratios. Therefore, it is expected that the CSU141 mechanism should be able to predict auto-ignition in natural gas/diesel dual fuel engine simulations. It should be noted that the NUIGIII mechanism has not been validated for these mixtures above 30 atm. However, the 80 bar calculations were of interest because typical turbocharged light-duty diesel engines can have TDC compression pressures near 80 bar.

5.4.3. Adiabatic HCCI Simulations

The ignition delay calculations presented thus far were conducted at constant volume and fixed initial temperature/pressure. The performance of the mechanism was further validated for the effects of varying temperature and pressure from the compression and expansion strokes in an engine by performing zero-dimensional adiabatic HCCI engine simulations using CHEMKIN®. The engine geometry for these calculations was identical to that of the experimental engine described previously. The engine speed was chosen to be 2000 RPM, which is close to the speed used in the engine experiments.

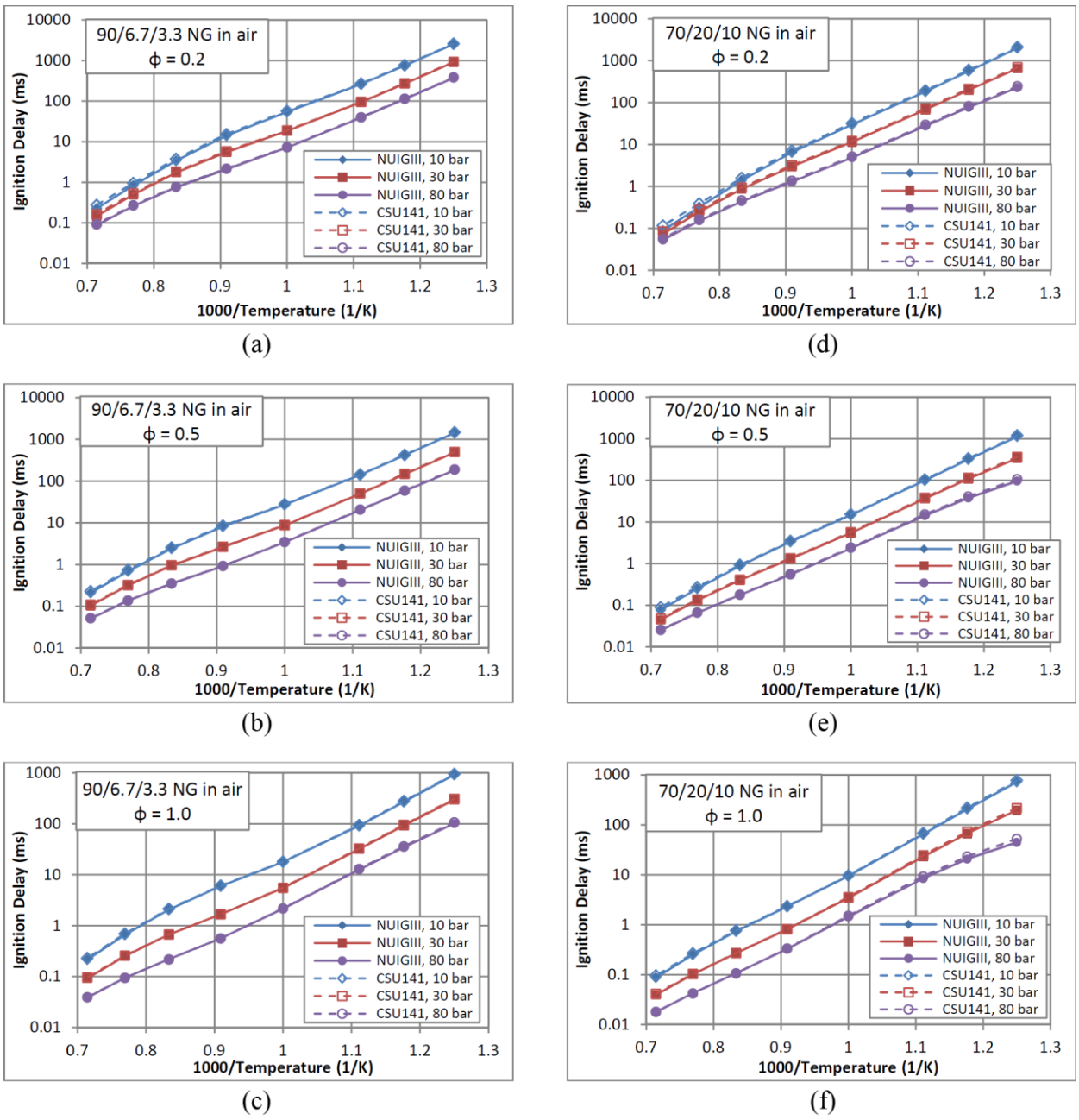

Figure 5.3. Comparisons of natural gas/air ignition delay calculations between the reduced CSU141 mechanism and the detailed NUIGIII mechanism. The 90/6.7/3.3 mixture is shown in the left column for (a) very lean φ = 0.2, (b) lean φ = 0.5, and (c) stoichiometric φ = 1.0 mixtures. The right column shows the 70/20/10 mixture at (d) very lean φ = 0.2, (e) lean φ = 0.5, and (f) stoichiometric φ = 1.0 mixtures.

Figure 5.4 shows computational comparisons between the detailed LLNL n-heptane mechanism and the CSU141 mechanism for n-heptane/air mixtures at φ = 0.5 and φ = 2.0. For

these computations, the initial pressure was fixed at 1.7 bar and the initial temperature was varied. The CSU141 and the LLNL mechanisms exhibited excellent agreement in terms of start of combustion timing for the low temperature heat release, high temperature ignition, and pressure rise. The agreement tends to diverge slightly as the start of combustion retards past TDC. However, the results of Figure 5.4 strongly suggest that the CSU141 mechanism can predict start of combustion behavior of diesel sprays and auto-ignition in HCCI or RCCI engines to the same level of accuracy as the detailed LLNL n-heptane mechanism.

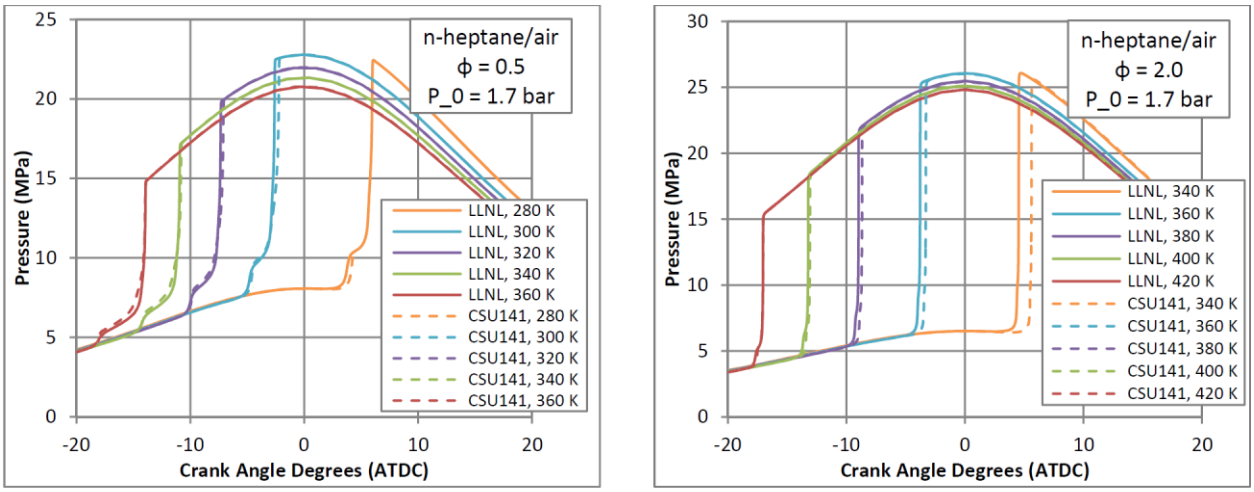

(a) (b)

Figure 5.4. Zero-dimensional adiabatic HCCI engine simulation comparisons between the detailed LLNL and reduced CSU141 mechanism for varying initial temperatures of n-heptane/air mixtures at (a) φ = 0.5 and (b) φ = 2.0.

Figure 5.5(a) shows calculated HCCI pressure curves for the 90/6.7/3.3 natural gas mixture in air at φ = 0.5 for both the detailed NUIGIII mechanism and the reduced CSU141 mechanism for various initial temperatures at a fixed initial pressure of 1.7 bar. Figure 5.5(b) shows a similar comparison for the 70/20/10 natural gas mixture. As shown, the reduced mechanism captures the ignition behavior of the detailed mechanism for these natural gas mixtures. At lower initial temperature when the start of combustion begins to retard past TDC, the reduced mechanism

begins to predict earlier start of combustion than the detailed mechanism. However, the results of Figure 5.5 strongly suggest that the CSU141 will predict the end gas auto-ignition of natural gas to the same level of accuracy as the detailed NUIGIII mechanism.

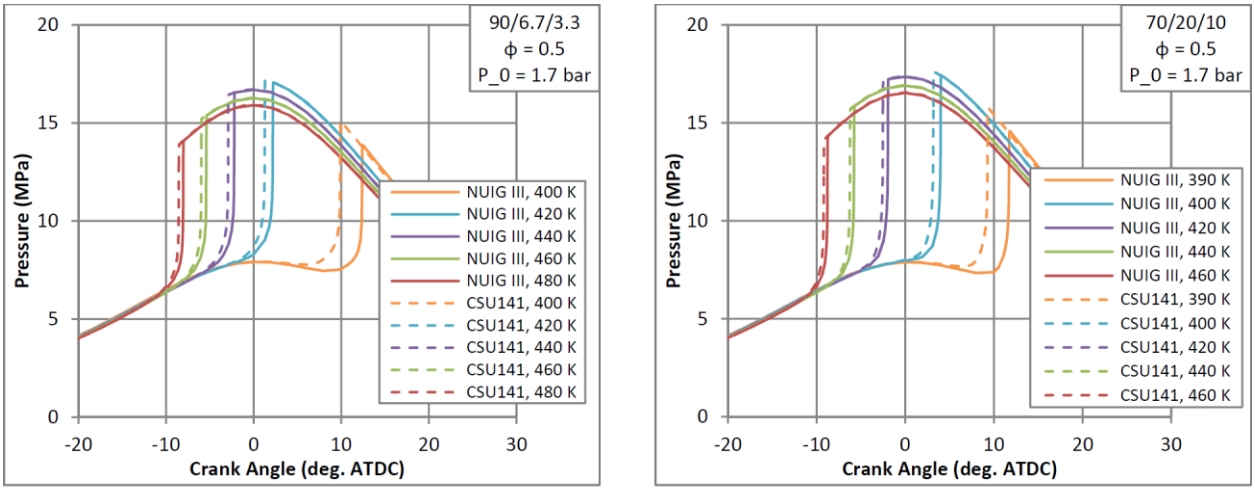

(a) (b)

Figure 5.5. Zero-dimensional adiabatic HCCI engine simulation comparisons between the detailed NUIGIII and reduced CSU141 mechanism for varying initial temperatures at ϕ = 0.5 for (a) the 90/6.7/3.3 natural gas mixture in air and (b) the 70/20/10 natural gas mixture in air.

5.4.4. Laminar Flame Speed Calculations of Methane at High Pressures

High pressure methane laminar flame speed measurements using spherically propagating flames in a constant volume chamber were conducted by Rozenchan et al. [41] at 40 and 60 atm. These high pressure experiments were conducted with helium as the inert and with reduced oxygen concentration to prevent flow instabilities and maintain laminar behavior. Specifically, laminar flame speed measurements in CH4/O2/He mixtures at various equivalence ratios were conducted at 40 atm using an oxidizing gas consisting of 17 % O2 and 83% He by volume and at 60 atm using an oxidizing gas with 15% O2 and 85% He by volume. For these experiments, the unburned gas temperature was held fixed at 298 K.

Figure 5.6 compares the experimental and calculated results using the reduced mechanism at both 40 and 60 atm. In the 40 atm case, the CSU141 mechanism agrees with experiments to within 6% at lean to stoichiometric conditions and slightly over predicts the flame speed at rich conditions. For the 60 atm case, the reduced CSU141 mechanism over predicts the flame speed across the range of equivalence ratios investigated, but the deviation diminishes as the mixture becomes leaner. The relative error in flame speed at the leanest condition, $\varphi = 0.85$, is only 8% and at $\varphi = 0.9$ is 16%.

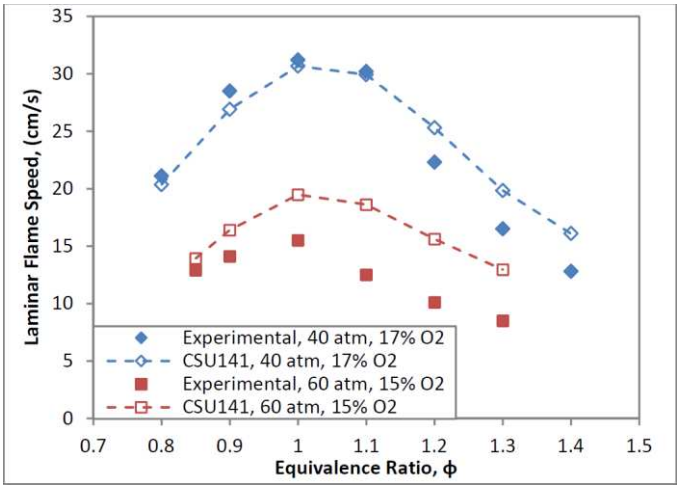

Figure 5.6. Comparisons of experimental laminar flame speeds with CSU141 computations for CH_4/O_2/He mixtures at (a) 40 atm and (b) 60 atm. The experimental data is from Rozenchan et al. [41]. The indicated O_2 % refers to the molar composition in the O_2/He oxidizer gas.

Martinez et al. [42] compared a variety of natural gas mechanisms to experimental laminar flame speeds for methane/air mixtures at 20 atm and different equivalence ratios. At $\varphi = 0.9$ they found a wide spread in predictions with most mechanisms over predicting the flame speed by 20% to 100%. Because the agreement between the simulations and experiments for methane laminar flame speed at high pressure had less than 20% error, CSU141 is as effective as any of the natural gas mechanisms evaluated by Martinez et al. Because the natural gas/air mixtures in

dual fuel engines are usually lean and contain mostly methane, the results in Figure 5.6 are encouraging and suggest that the reduced CSU141 mechanism can be used to predict flame speed for lean natural gas mixtures at high pressures in dual fuel engines.

5.4.5. Combusting Diesel Spray

The ECN spray database includes a set of data for a diesel spray at an injection pressure of 1400 bar into a chamber filled with 21% oxygen at a nominal temperature of 1000 K and density of 30 kg/m^3 [31], which are typical TDC conditions for high compression ratio diesel engines. This data set was used to validate the combined capabilities of the spray, turbulence, and reduced chemical kinetic mechanism to simulate reacting diesel sprays. Table 5.4 lists some of the important experimental conditions for this spray, while more information can be found on the ECN website [31].

Table 5.4. Experimental conditions for the ECN combusting diesel spray used for model validation [23].

ECN spray name	Spray D2
Fuel	Diesel #2
Injection pressure (bar)	1400
Injected mass (mg)	14.3
Injection duration (ms)	5.1
Nominal ambient temperature (K)	1000
Nominal ambient density (kg/m^3)	30
Oxygen % volume	21
Nozzle orifice diameter (mm)	0.100
Discharge coefficient	0.8
Fuel temperature (K)	436

Experimental ignition delay and flame lift-off length are used as benchmarks for validating the simulations. The experimental ignition delay is based on the time between start of injection and the time of rapid pressure rise. In the simulations, the ignition delay is the elapsed time when the temperature derivative reaches a local maximum that corresponds with the largest

temperature rise. The experimental lift-off length is the axial distance from the nozzle to the flame as measured by OH chemiluminescence. The simulated lift-off length is indicated by the location where the OH mass fraction becomes larger than 2% of the maximum in the domain. The simulated lift-off length was measured at 2 ms, which is well after steady state behavior is established. For these simulations, the liquid properties of diesel were represented using the properties of n-tetradecane.

Figure 5.7 shows the simulation results using a plane through the center of the spray colored by the simulated mass fraction of OH and also indicates the lift-off length. Table 5.5 presents a comparison of the simulated and experimental ignition delay and lift-off length. The simulated ignition delay is within 14% error of the experimental. When the ignition delay periods are converted to crank angle degrees at an engine speed of 2000 rpm, the simulated ignition delay is longer than the experimental by only 0.4 crank angle degrees. The simulated lift-off length is within 20% error of the experimental. This degree of agreement demonstrates that the coupling of the reduced chemistry, turbulence, and spray models can give reasonably accurate predictions of non-premixed diesel jet flames.

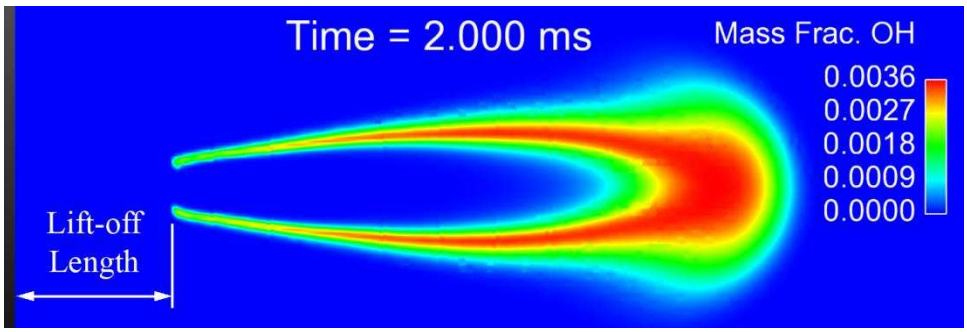

Figure 5.7. Simulation result for OH mass fraction at 2 ms. The lift-off length is defined as 2% of the maximum OH mass fraction.

Table 5.5. Comparison of experimental and simulated ignition delay and lift-off length.

	Ignition delay (ms)	Lift-off length (mm)
Experiment	0.24	9.5
Simulation	0.273	11.4

5.4.6. Multi-dimensional Engine Simulations

The experimental and computational pressure and heat release rates for the D25G17 and D12G22 SOI timing sweeps are compared in Figure 5.8(a) and (b) respectively. Each simulation took approximately 12 hours to compute using 48 cores. As shown in Figure 5.8, excellent agreement between model and experiment was obtained for the start of combustion phasing, pressure rise rate, peak pressure, CA10 to CA90 combustion duration, and shape of heat release rate as injection timing changed. There is some over prediction of the AHRR during the premixed ignition of the spray, as indicated by the peak in AHRR at start of combustion. For dual fuel combustion, the first peak in the AHRR curve includes heat release from the premixed burn of the diesel vapors and entrained natural gas in the head of the spray. The slight discrepancy in AHRR between model and experiment during spray ignition could be the result of using a single component fuel surrogate for the diesel chemistry, a single component liquid surrogate for the vaporization model, error in measurement method for the injector rate shape, experimental uncertainty in the mass of diesel fuel injected, and using a sector simulation, which assumes perfect symmetrical behavior for each spray. Overall, the model has effectively captured the general trends in pressure and AHRR behavior for the two injection timings. The model predictions are particularly noteworthy given the fact that no adjustments (i.e. tuning) of model constants was done between different injection timing cases. The only differences made between the input files other than injection timing included accounting for small variations in manifold

pressure and the ingested air mass as these parameters varied slightly in the experiments as injection timing was advanced.

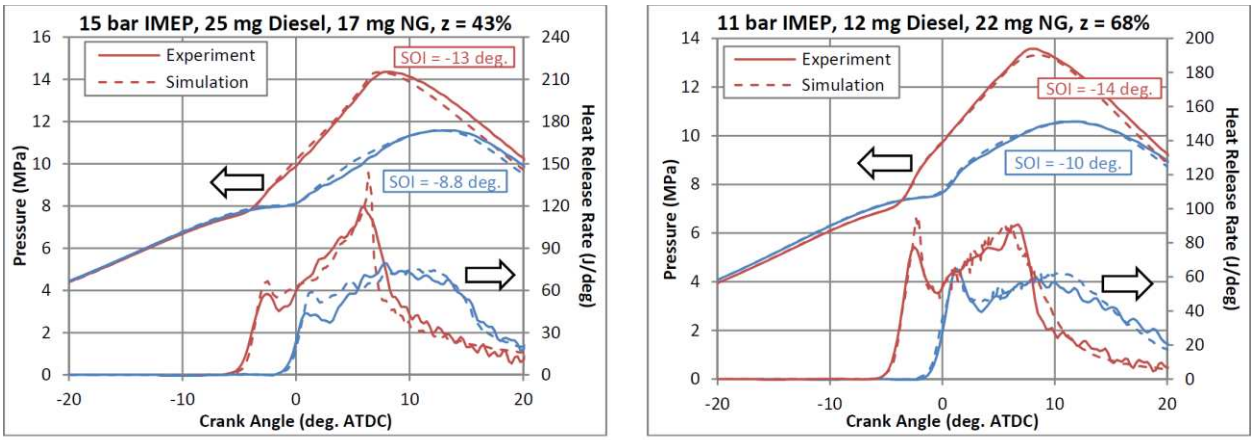

(a) (b)

Figure 5.8. Comparisons of experimental and computational pressure and AHRR for (a) the D25G17 SOI sweep and (b) the D12G22 SOI sweep.

Figure 5.9 presents comparisons between the experiments and simulations for the natural gas load sweep using a fixed boost pressure and fixed diesel injection mass and timing. This load sweep therefore provides validation with variation in natural gas equivalence ratio. As previously explained, these experiments were conducted with a higher reactivity natural gas mixture due to greater ethane and propane content. Additionally, the boost pressure used for the load sweep was appreciably lower than that used in the SOI sweeps. The simulations were able to capture the start of combustion timing, the pressure rise rate, the shape and magnitude of the AHRR profile, and the combustion duration. Again, some over prediction was observed for the heat release rates during spray ignition, which can be attributed to the same sources of error discussed above for the SOI timing sweep. The peak pressure was somewhat under predicted and as a result the expansion pressure was also lower. Examination of the experimental AHRR for the D11G18 case near the timing of peak pressure shows a small increase in the AHRR that is not captured by the simulations. This discrepancy could be due to sources of error that are not specifically due to

the accuracy of the chemistry in the reduced chemical mechanism, such as uncertainty in air and fuel mass flow measurements, the assumptions of a RANS based turbulence model, assuming constant wall temperatures, assuming homogenous composition and temperature at IVC, and the symmetry assumption from using a sector simulation. In general, the agreement in Figure 5.9 demonstrates the ability of the reduced mechanism to predict the combustion behavior responsible for the observed AHRR curves at two widely different natural gas equivalence ratios, natural gas substitution percentages, and total fuel mass. In particular, the CSU141 mechanism is able to capture the observed AHRR curves from a higher reactivity natural gas mixture than the previous mixture used in the SOI sweeps.

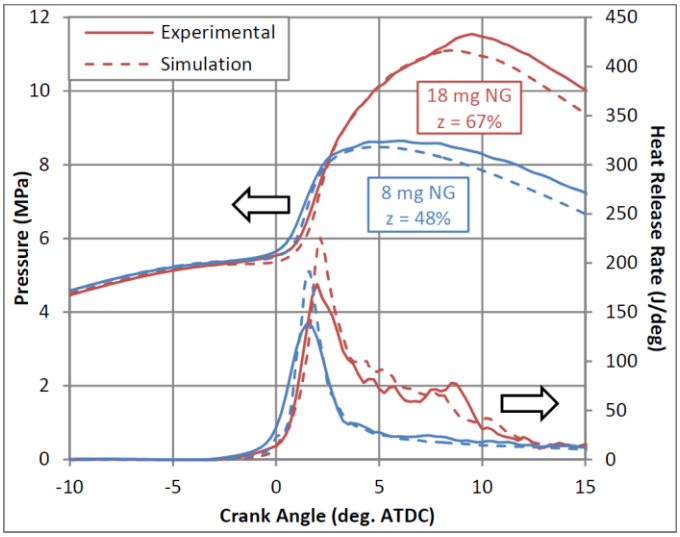

Figure 5.9. Comparisons of experimental and computational pressure and apparent heat release rates for the dual fuel load sweep using a constant diesel injection of 11 mg.

Comparisons between 100 cycle averaged experimental engine data and volume averaged simulation results for the case with additional propane, D12G22P2, are shown in Figure 5.10(a). The experimental AHRR curve shows a sudden acceleration in combustion rate occurring just before peak pressure, which indicates end gas auto-ignition of natural gas. The simulation also

captures the timing of this spike in AHRR, but the magnitude is somewhat higher leading to higher peak pressure. Figure 5.10(b) compares experimental pressure from a single cycle and simulated pressure from a single cell at the same location as the pressure transducer tip. The single cycle experimental pressure shows fluctuations that can be classified as engine knock. The single cell simulation pressure shows pressure fluctuations with similar frequency and amplitude and therefore the simulation has also predicted engine knock. While the expansion pressure predicted by the simulation is higher than the experimental, the results show that the CSU141 mechanism can be useful in predicting the chemical kinetic processes that cause natural gas auto-ignition and knocking in dual fuel engines.

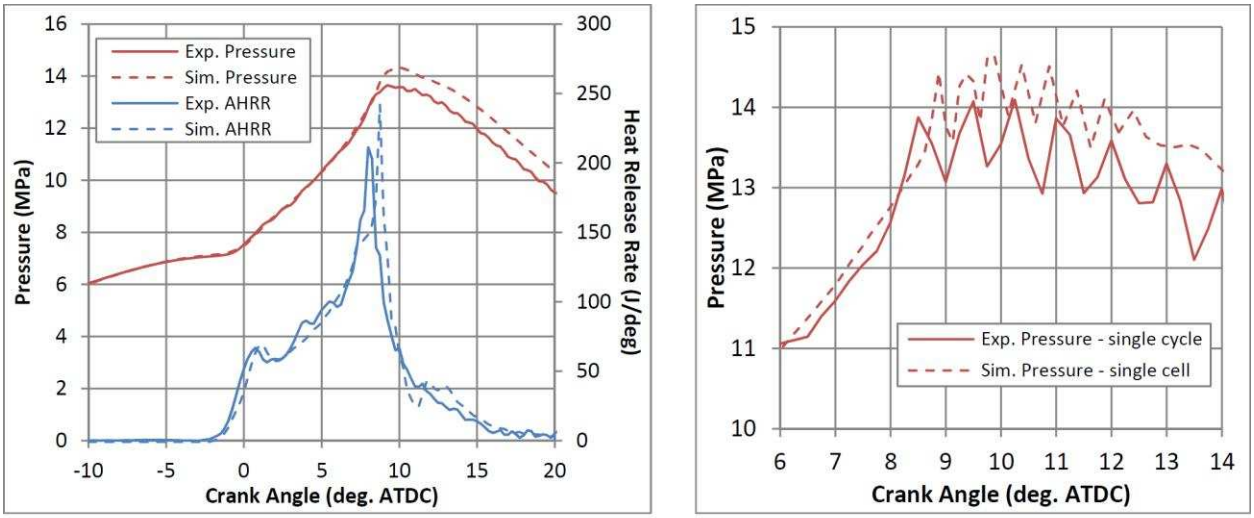

Figure 5.10. (a) 100 cycle averaged experimental pressure and volume averaged simulation pressure along with AHRR for the propane addition case. (b) Experimental pressure from a single cycle and simulation pressure at a single cell with same location as the pressure transducer tip.

5.5. Conclusions

A reduced chemical kinetic mechanism consisting of 141 species and 709 reactions has been formulated for natural gas/diesel dual fuel combustion whereby n-heptane is used to represent

diesel fuel and a mixture of methane, ethane, and propane represents natural gas. The final reduced mechanism is a combination of reduced versions of the detailed n-heptane mechanism from Curran et al. [38] [39] and the detailed methane through n-pentane mechanism from Healy et al. [37]. Ignition delay plots for n-heptane showed excellent agreement between the reduced CSU141 mechanism and the detailed LLNL mechanism across pressures from 10 to 80 bar, temperatures from 700 to 1400 K, and equivalence ratios from very lean ($\varphi = 0.2$) to rich ($\varphi = 2.0$). The natural gas chemistry was validated using ignition delay plots for two different natural gas compositions with varying ethane and propane contents and excellent agreement with the detailed NUIGIII mechanism was achieved at lean to stoichiometric conditions and pressures between 10 and 80 bar. However, the detailed mechanisms have only been validated with experimental data up to 30 bar, and therefore the agreement at 80 bar assumes the rate constants in the detailed mechanisms are accurate at higher pressure. Additionally, the reduced mechanism achieved excellent agreement with detailed mechanisms for initial temperature sweeps of adiabatic HCCI simulations for both n-heptane and two natural gas mixtures. Furthermore, the CSU141 mechanism was able to replicate experimental laminar flame speeds for lean CH4/He/O2 mixtures at 40 and 60 atm to within 16% relative error. Finally, the n-heptane chemistry in the CSU141 mechanism was able to predict the experimental ignition delay and lift-off length from a reacting diesel spray in a constant volume chamber at engine TDC conditions to within 14% and 20% error respectively.

Comparisons between natural gas/diesel dual fuel engine experiments and multi-dimensional CFD simulations showed excellent pressure and AHRR agreement for two start of injection timing sweeps with different substitution percentages, a natural gas load sweep at fixed diesel injection, and an engine knocking case using additional propane to increase mixture reactivity.

The simulations accurately captured the start of combustion timing, the pressure rise rate, the shape and magnitude of the heat release rate profile, and the combustion duration. In the engine knocking case, the simulation was able to predict the timing and magnitude of a sudden acceleration in combustion rate as well as the high frequency pressure oscillations. Some of the simulations showed a small discrepancy in peak pressure, but this could be due to error sources other than the chemical kinetics such as uncertainty in air and fuel mass flow rates, the RANS based turbulence model, assuming homogenous composition and temperature at IVC, and the assumption of spray symmetry from using sector geometry.

The level of agreement between the engine experiments and simulations validates that the reduced mechanism can model the important chemical kinetics in natural gas/diesel dual fuel engines. Agreement in start of combustion phasing and magnitude of the peak in AHRR at ignition validates the coupling of the diesel ignition chemistry and the spray models. In addition, the reduced mechanism is able to model diesel non-premixed jet flames as evidenced by the agreement for two different diesel injection masses between the two SOI sweeps. Furthermore, the simulations ability to match AHRR during the period of flame propagation for the two injection timing sweeps and also in the load sweep validates that the natural gas chemistry coupled with the RANS turbulence model has sufficiently captured flame speed at varying natural gas equivalence ratio and mixture reactivity. It particular, the reduced mechanism was able to model varying natural gas reactivity without relying on rate constant tuning. Finally, the agreement in the propane addition case where engine knock occurred validates that the reduced mechanism is able to model the important chemical kinetics in natural gas auto-ignition.

Future validation work with natural gas/diesel RCCI engine experiments is necessary to confirm if the CSU141 mechanism is capable of modeling premixed auto-ignition of large

reactivity gradients where the diesel/natural gas mixtures can vary from slightly rich to very lean. In addition, it should be reiterated that the CSU141 mechanism makes the assumption that heavier than propane hydrocarbons in the natural gas mixture are low enough in concentration that their effect on ignition delay and flame speed is negligible. Future work is necessary to develop a reduced dual fuel mechanism that includes the chemical kinetics of heavier hydrocarbons, such as butane, for dual fuel applications that require operation with a low methane number natural gas.

CHAPTER 6: CHARACTERIZING UNCONTROLLED FAST COMBUSTION IN A LIGHT DUTY NATURAL GAS/DIESEL DUAL FUEL ENGINE

6.1. Introduction

Dual fuel engine manufacturers are in need of a multi-dimensional modeling tool that can predict combustion behavior over a wide range of substitution rates, loads, and natural gas compositions. Accordingly, the first objective of this study is to use engine experiments to validate a multidimensional CFD model coupled with statistical spray models and detailed chemical kinetics for natural gas/diesel dual fuel combustion across a wide range of substitution percentages, wherein a non-premixed diesel flame can be present. As previously discussed, the presence of a non-premixed diesel flame is unlike previous dual fuel CFD models that used detailed chemistry, as those models were only validated for high substitution percentages where early pilot injections were used. The second objective is to demonstrate that the CFD model can predict the pressure and heat release rate under conditions where uncontrolled fast combustion rates occur and use the modeling results to elucidate the physical phenomena that lead to such fast combustion rates. This work begins by comparing experimental and computational engine pressure and heat release rate curves are made for injection timing sweeps at various substitution percentages. In addition, computations and experiments with increased natural gas reactivity (via propane addition) are presented. In-cylinder images from the simulations are used to yield new insight into dual fuel knock behavior.

This work concludes with a purely computational study on dual fuel combustion in a constant volume chamber for the purpose of understanding interactions between the non-premixed diesel spray flame and the premixed propagating natural gas flame without the interference of

combustion chamber walls. Comparisons are made between simulations of a diesel spray into air and the same spray into two different natural gas air mixtures. Also a comparison is made between NO_X formation rates in diesel and dual fuel combustion.

Dual fuel combustion behavior has unique features that can be discerned from apparent heat release rate (AHRR) profiles, which need to be defined for subsequent discussion. Ishiyama et al. [43] presented an experimental dual fuel load sweep using addition of natural gas while keeping the diesel injection constant and observed that the characteristics of the AHRR profile change as more natural gas is added. A generalized illustration of this behavior is depicted in Figure 6.1. The difference between the pure diesel curve and the dual fuel curves represents the energy contribution from natural gas. The natural gas delays the start of combustion slightly, increases the energy released at ignition significantly, and creates a large hump like shape after ignition. As the natural gas is increased, the gradual rise and decline of the AHRR curve developes into a constant slope followed by a sudden dramatic drop. Figure 6.1 shows that two distinct phases of combustion are common to all three curves, which are separated by the dashed line and will be referred to as the first and second combustion phases throughout this study. The first phase is characterized by the fast rise and local peak in AHRR due to igniton of the spray head. The shape of the AHRR curve during the remaining portion of the combustion duration can have different characteristics depending on the amount of natural gas present, but is always associated with the combination of the non-premixed diesel spray and the premixed propagating natural gas flame. In traditional diesel combustion this phase is often referred to as the mixing controlled combustion phase, but this description is not appropriate for dual fuel combustion since a premixed propagating flame is also present. Therefore this period of the combustion will be referred to as the second combustion phase in subsequent discussion.

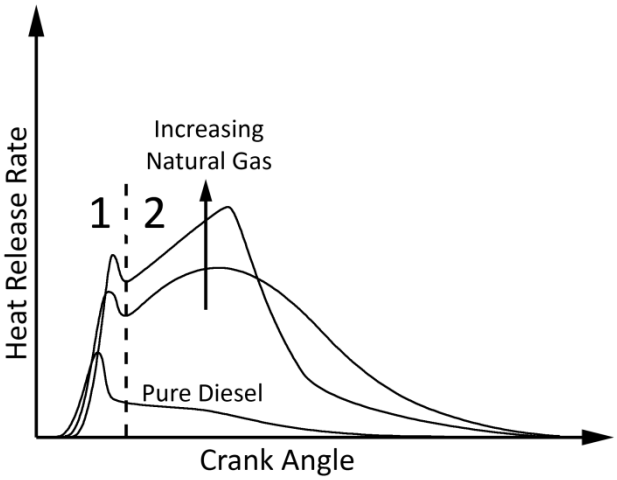

Figure 6.1. As natural gas is added to a constant diesel injection the AHRR shape changes. The two phases of dual fuel combustion are defined for subsequent discussion.

6.2. Engine Experiments

The experimental operating conditions are listed in Table 6.1. The nomenclature for referring to the different operating conditions in Table 6.1 is as follows. Each case name begins with a 'D' to designate diesel followed by the mass of diesel injected per cylinder per cycle in units of milligrams rounded to the nearest whole number. This is followed by the letter 'G' to signify natural gas followed by the mass of port injected natural gas per cylinder per cycle in milligrams rounded to the nearest whole number. For the case with propane addition, a 'P' is added followed by mass of propane added per cylinder per cycle. For example, the case with 25.4 mg of diesel and 16.5 mg of natural gas is designated as D25G17. Also the substitution rate was calculated with lower heating values of 42,500 kJ/kg for diesel fuel [44] and 49,993 kJ/kg for natural gas, where the latter is calculated based on the heating values of the major species in the measured natural gas composition.

Start of diesel injection timing was varied at 2200 rpm for two different loads and substitution rates. As indicated in Table 6.1, one sweep was performed at an IMEP of 15 bar with

Table 6.1. Experimental engine operating conditions.

Fuel case name	D25G17				D12G22				D12G22P2
Injected diesel per cylinder (mg)	25.4 ± 3				12.1 ± 3				11.7 ± 3
Natural gas per cylinder (mg)	16.5				21.8				22.1
Added propane per cylinder (mg)	0				0				2.3
Natural gas substitution, z (%)	43.3				67.9				71.9
Engine speed (RPM)	2200				2200				2200
Diesel injection pressure (bar)	700				700				700
Start of injection (°ATDC)	-8.8	-10	-12	-13	-8	-10	-12	-14	-10
Boost pressure (kPa abs)	169.3	167.9	166.6	167.2	168.2	168.5	164.9	163.6	163.0
Manifold temperature (°C)	43.6	43.5	43.5	43.5	44.6	44.6	44.4	44.4	48.2
Air mass per cylinder (mg)	750.4	742.8	740.2	740.2	739.8	731.3	699.3	692.2	685.3
Net IMEP (bar)	15.0	15.1	15.6	15.6	10.9	10.7	10.6	10.7	11.7
Natural gas equivalence ratio	0.357	0.361	0.362	0.362	0.479	0.485	0.507	0.512	0.600
Total equivalence ratio	0.845	0.853	0.856	0.856	0.712	0.724	0.757	0.765	0.824

a moderate substitution rate of 43% and the other timing sweep was performed at an IMEP of 11 bar with a high substitution rate of 68%. Timing was advanced until the maximum cylinder pressure of 140 bar was reached. Start of diesel injection timing was varied at 2200 rpm for two different loads and substitution rates. As indicated in Table 6.1, one sweep was performed at an IMEP of 15 bar with a moderate substitution rate of 43% and the other timing sweep was performed at an IMEP of 11 bar with a high substitution rate of 68%. Timing was advanced until the maximum cylinder pressure of 140 bar was reached. The D12G22 case had the lowest injected diesel mass that could give consistent combustion phasing. The mass of port injected natural gas in the D12G22 case was the maximum amount that could be achieved using the experimental setup presented herein and is due to restricting the injection of natural gas to the intake valve open period and the maximum natural gas injection pressure. Additionally, a high reactivity case was explored by adding 2.3 mg of propane to the D12G22 case with an SOI of -10° ATDC.

6.3. Computational Method

The computational method in this work follows the methods and models discussed in Chapter 2. However, there are some key differences that need to be mentioned. Firstly, this work used a preliminary dual fuel reduced mechanism rather than the CSU141 mechanism discussed in CHAPTER 5:. This mechanism was specifically reduced for the natural gas composition used in these experiments and for rich ignition of sprays. Secondly, at the time of this work, the injector rate shapes and durations had not been experimentally measured. However, Perini et al. [45] used the same seven hole Bosch CRIP 2 injector and published rate of injection profiles and injection durations over a range of injection pressures. However, the rate shapes from Perini et al. were for a constant injected mass of 8.8 mg, which is different than the mass used in the experiments herein. Accordingly, the rate shapes used for this study were taken from Perini et al. and scaled to different injection durations to account for different amounts of injected fuel. With the injected mass known from mass flow meters and a rate shape determined from literature, the injection duration was varied until the peak injection pressure calculated by CONVERGE™ was close to the experimentally measured rail pressure. Finally, tuning of the injected fuel mass within experimental uncertainty was used to provide the best match of pressure rise during ignition.

6.3.1. CSU86 Reduced Mechanism

A reduced chemical kinetic mechanism was constructed for simulating diesel/natural gas dual fuel combustion to allow for reasonable compute times with a multi-dimensional CFD code. As discussed previously, this reduced mechanism uses n-heptane as a fuel surrogate for diesel fuel and methane, ethane, and propane mixtures for natural gas. The present mechanism

combines reduced versions of the detailed methane through n-pentane mechanism (293 species, 1588 reactions) from Healy et al. [37], hereafter referred to as the NUIG III mechanism, and the 88 species skeletal n-heptane mechanism from Yoo et al. [46], hereafter referred to as the UCONN88 mechanism. The UCONN88 mechanism was previously reduced from the fully detailed n-heptane mechanism from Curran et al. [38] [39] at Lawrence Livermore National Laboratories (LLNL) with 561 species and 2539 reactions.

To develop the reduced mechanism, the direct relation graph with error propagation and sensitivity analysis (DRGEPSA) method [21] was first used to reduce the NUIG III mechanism based on ignition delay of a simulated natural gas mixture with air as described in Table 6.2. The reduced version resulted in a 47 species skeletal mechanism for methane, ethane, and propane mixtures. Next, DRGEPSA at the same conditions was used to reduce the UCONN88 n-heptane mechanism to a 68 species mechanism, which was then combined with the previous 47 species natural gas mechanism. Any duplicate reactions between the two DRGEPSA reduced mechanisms were given the rate constant values from the NUIG III mechanism in order to ensure that natural gas auto-ignition was well represented. The final combined mechanism (known hereafter as the CSU86 mechanism) resulted in an 86 species, 393 reactions reduced chemical kinetic mechanism for mixtures of methane, ethane, propane, and n-heptane, which can be used in simulations of diesel and natural gas dual fuel applications. Co-oxidation reactions between the n-heptane and the natural gas constituents were not included in the final mechanism, because the assumption was made that n-heptane will first break down into smaller lower carbon species within the interior of the spray for which co-oxidation reactions are included.

For validation, the n-heptane chemistry in the CSU86 mechanism was compared against ignition delay sweeps of the detailed LLNL n-heptane mechanism, while the natural gas

Table 6.2. Conditions used for reducing the base mechanisms using DRGEPSA.

	UCONN88	NUIG III
Target species	n-C7H16	CH4, C2H6, C3H8
Fuel composition (mole frac.)	$X_{nC7H16} = 1.0$	$X_{CH4} = 0.85$, $X_{C2H6} = 0.1$, $X_{C3H8} = 0.05$
Temperature (K)	800, 900, 1000, 1100, 1200	800, 900, 1000, 1100, 1200
Pressure (bar)	20, 40, 60, 80	20, 30, 40, 50, 60, 70, 80
Equivalence ratio, φ	0.5, 1.0, 1.5	0.2, 0.4, 0.6, 0.8, 1.0, 1.2, 1.4
Ignition delay error tolerance	0.3	0.1
Sensitivity analysis fraction	0.5	0.5

chemistry was compared against the detailed NUIG III mechanism. The ignition delays comparisons were performed using adiabatic constant volume simulations using CHEMKIN® as the solver. The natural gas composition was chosen to be the same as that shown in Table 2. The ignition delay period was defined by a 400 K increase in temperature, because this is the definition built into the DRGEPSA algorithm employed in CONVERGE™. The 400 K increase was compared with maximum temperature derivative for some of the cases and good agreement between the two definitions was observed.

Natural gas mixtures in dual fuel engines are kept lean and Figure 6.2(a) shows that the natural gas ignition delay periods predicted by the CSU86 mechanism agrees well with that predicted by the detailed NUIG III mechanism for lean mixtures at engine TDC pressures (40 to 80 bar) and temperatures (900 to 1100 K). At stoichiometric conditions the ignition delay periods predicted by the CSU86 mechanism also compare well with the detailed mechanism, but the CSU86 yields somewhat shorter ignition delay periods for the highest pressures as seen in Figure 6.2(b). The difference in predicted ignition delay period between CSU86 and the detailed NUIG III mechanism for $\varphi = 1.0$ at 1000 K and 80 bar is less than 0.5 ms or less than 6 crank angle degrees at 2000 rpm. For lean premixed natural gas/air mixtures, the CSU86 mechanism is sufficiently accurate to reproduce the onset of auto-ignition to within a few crank angle degrees.

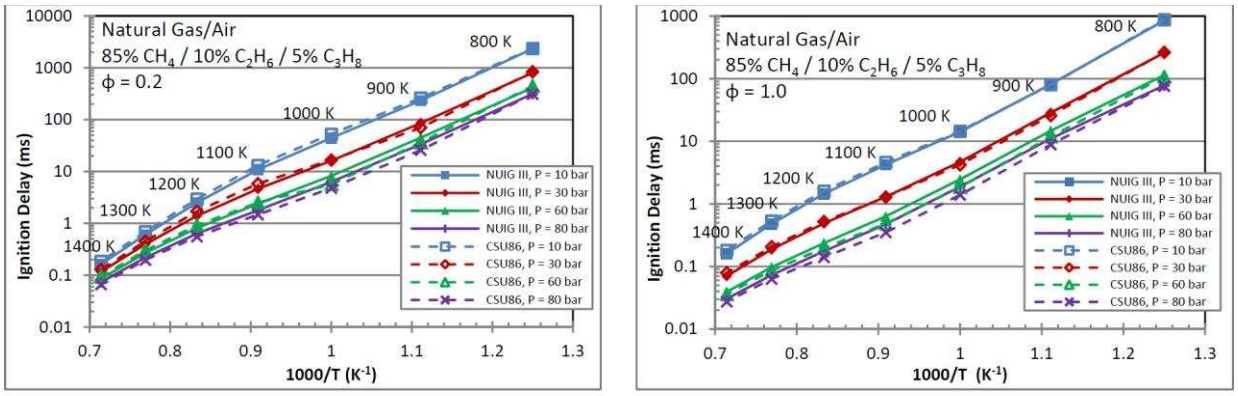

Figure 6.2. Natural gas/air ignition delay comparisons between the reduced CSU86 mechanism and the detailed NUIG III mechanism (Healy et al. 2010) for (a) lean φ = 0.2 mixtures and (b) stoichiometric mixtures.

The plots in Figure 6.3 show that the n-heptane chemistry in the CSU86 mechanism agrees well with the detailed LLNL mechanism at stoichiometric to rich conditions and at pressures and temperatures expected at TDC in a diesel CI engine. However, the CSU86 mechanism does predict longer ignition delay periods at temperatures lower than 900 K. Also, for very lean mixtures (φ = 0.2) at all pressures the CSU86 mechanism significantly over predicts the ignition delay periods. Because diesel ignition has been shown by Dec [47] to begin as rich premixed combustion (φ = 2 to 4) and because the compressed gas temperatures at TDC are typically greater than 900 K, the CSU86 mechanism should be sufficiently accurate to reproduce the ignition delay observed for a reacting spray. At very lean mixtures, the CSU86 significantly over predicts the ignition delay period. Therefore, this reduced mechanism should not be used for lean premixed diesel combustion such as in homogeneous charge compression ignition (HCCI) engines.

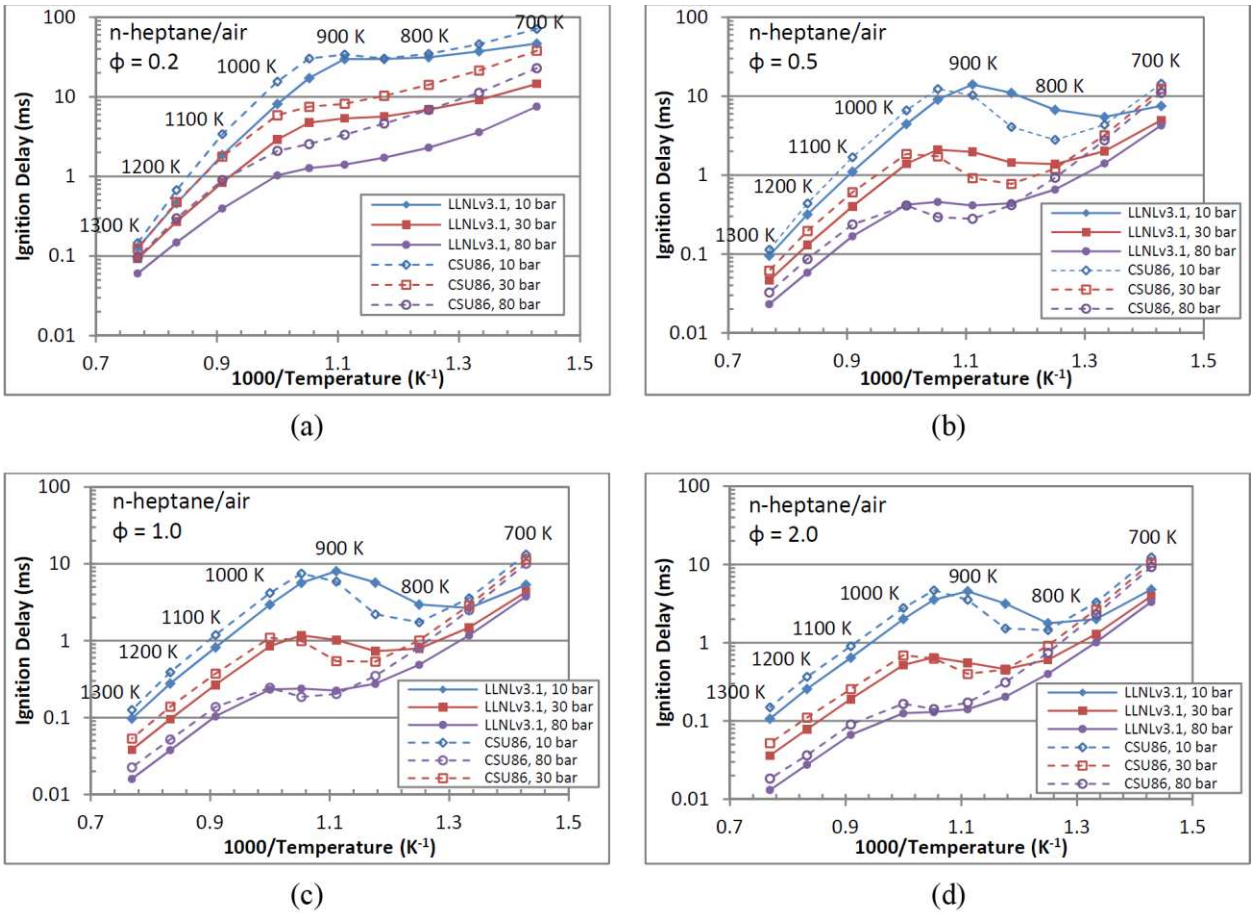

Figure 6.3. n-heptane/air ignition delay plots comparing the CSU86 reduced mechanism with the detailed LLNL mechanism (Curran et al. 1998, 2002) for (a) very lean φ = 0.2, (b) lean φ = 0.5, (c) stoichiometric, and (d) rich mixtures.

6.4. Results

6.4.1. D25G17 SOI Timing Sweep

The experimental in-cylinder pressure and apparent heat release rates for the D25G17 SOI sweep are shown in Figure 6.4(a). As injection timing is advanced the pressure curves become more triangular in shape, the pressure rise rate increases, the combustion duration gets shorter, and the peak pressure increases. The maximum AHRR during the spray ignition phase increases in magnitude as the timing is advanced, which is likely due to a longer ignition delay period associated with a lower charge temperature at earlier injection timings. A longer ignition delay will allow for more mass to be injected prior to ignition and a consequential more massive

premixed spray head undergoing ignition reactions. The initial rising slope in AHRR during the second combustion phase is nearly constant for all injection timings. However, for the earlier injection timing cases, the initial rising slope in AHRR is maintained for a longer duration until a maximum is reached and then a sharp drop in AHRR is observed. In contrast, the later injection timings have a AHRR profile that rises, decelerates, and falls off gradually.

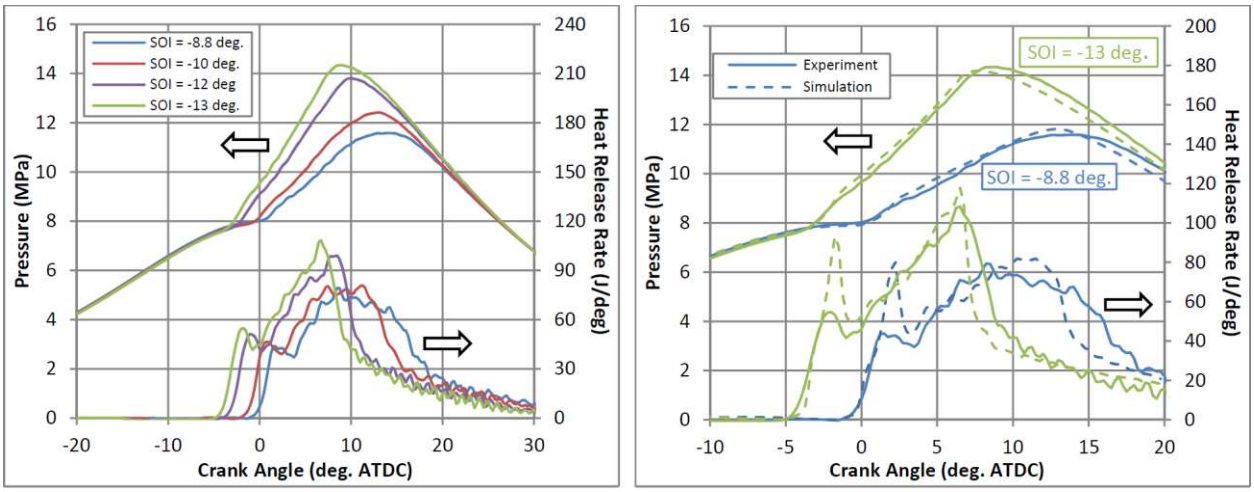

(a) (b)

Figure 6.4. (a) Experimental results for the D25G17 injection timing sweep. (b) Comparisons between experiment and simulation for the earliest and latest injection timings in the D25G17 SOI sweep.

Comparisons between the model and the experimental data for the earliest and latest injection timings are shown in Figure 6.4(b). The simulations took approximately 15 hours each using 8 cores. The model was able to predict the start of combustion timing to within one crank angle degree, the peak pressure to within 3 bar, the location of peak pressure to within one crank angle degree, and the initial pressure rise rate to within 2 bar/deg. The model also captures the qualitative changes in the shape of the heat release rate profile as injection timing is changed. However, the model over predicts the peak heat release rate during the spray ignition phase. The inability of the model to reproduce the peak AHRR during the spray ignition is likely to be a

result of the following sources of error: 1) not having measured the rate shape, 2) not having measured the injection duration, and 3) using a single species diesel surrogate. In the -8.8° SOI case, the model predicts a much steeper drop in AHRR than the more gradual decrease observed experimentally. This discrepancy could be a consequence of the reduced chemical kinetic mechanism's inability to reproduce turbulent flame speeds in comparison with the detailed mechanism. Overall, the model has captured the general trends in pressure and AHRR behavior for various injection timings. The model predictions are particularly noteworthy given the fact that no tuning of model constants was needed between different injection timing cases. The only changes made between these cases besides injection timing included small variations in manifold pressure and temperature, and the air mass flow rate as these parameters varied slightly in the experiments as injection timing was advanced.

In-cylinder temperature plots of the -13° SOI simulation in the plane of the spray axis are shown in Figure 6.5. From the temperature plots it can be seen that the ignition of the spray in dual fuel combustion is similar to traditional diesel spray ignition, where a premixed ignition reaction zone is observed around the periphery of the spray plume. The total equivalence ratio, φ_T, in this region was found to be approximately 2, which agrees with the experiments of Dec (1997) that reported equivalence ratios between 2 and 4 within the premixed spray ignition region. The premixed ignition grows around the spray and transitions into a non-premixed flame by approximately -1° ATDC as shown in Figure 6.5(c). The non-premixed spray flame then initiates a premixed propagating natural gas flame as seen by the growth of the green area, which indicates a flame temperature of approximately 2000 K. The images between 0° and 7° ATDC also show that the natural gas flame propagates into the center of the combustion bowl much

faster than it travels into the squish region, which is due to the higher rate of heat loss in the squish region from the walls being in close proximity to the flame.

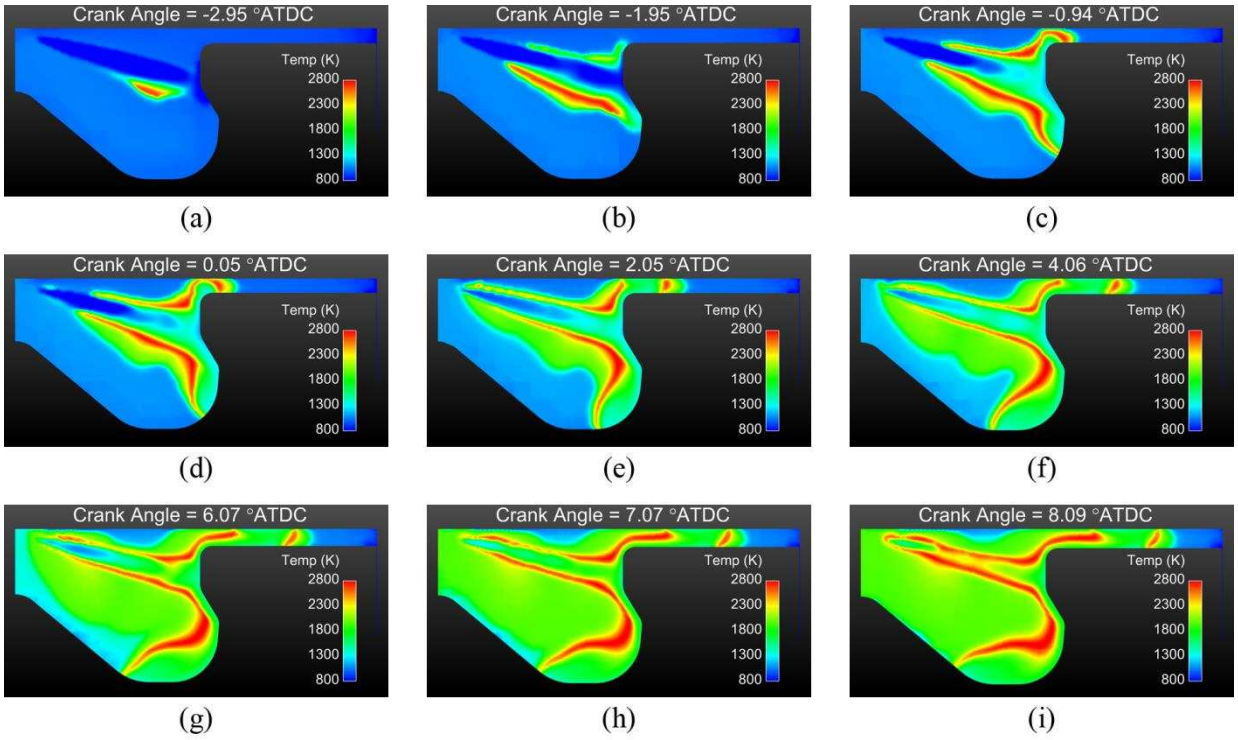

Figure 6.5. Time development of temperature in the plane of the spray axis for the D25G17, -13° ATDC SOI case. Time proceeds sequentially from (a) to (i).

A complete representation of the combustion phenomena occurring in the cylinder during the pressure rise period can be found when the natural gas flame has traveled far from the diesel jet flame, but has not reached the walls, which occurs at approximately 4° ATDC in Figure 6.5(f). Accordingly, this crank angle was chosen to investigate species mass fractions and local heat release rates, as shown in Figure 6.6. The local HRR image in Figure 6.6(a) clearly shows the location of both the non-premixed diesel spray flame and propagating premixed natural gas flame as thin HRR surfaces. Figure 6.6(b) shows the vapor boundary of the injected n-heptane fuel, in which the red region indicates a mass fraction greater than 1%. It is evident from this figure that the fuel vapor has penetrated to the bowl rim at this crank angle.

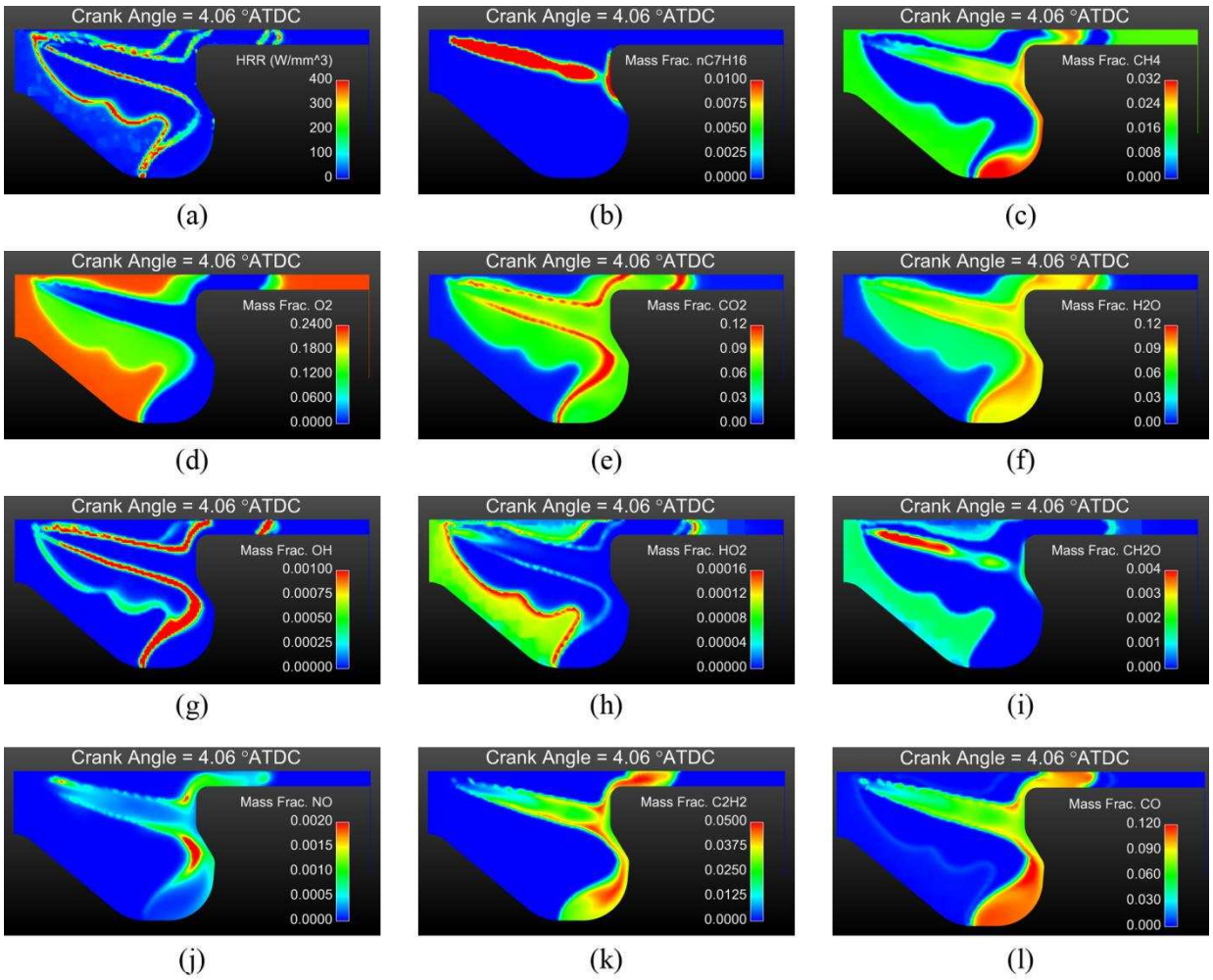

Figure 6.6. In-cylinder HRR and species mass fraction in the plane of the spray axis at 4° ATDC for the D25G17, -13° ATDC SOI case. (a) Local HRR, (b) n-heptane, (c) methane, (d) oxygen, (e) carbon dioxide, (f) water, (g) hydroxyl radical, (h) hydroperoxyl radical, (i) formaldehyde, (j) nitric oxide, (k) acetylene, and (l) carbon monoxide.

The methane plot in Figure 6.6(c) shows the edge of the premixed flame and the depletion of methane behind the flame as indicated by the blue region. The figure also shows that methane exists in the interior of the spray as indicated by the green and yellow regions in the interior of the spray. The model suggests that the presence of methane inside the spray is due to both thermal decomposition of n-heptane, which produces methane, and entrainment of natural gas from the viscous action of the spray near the nozzle.

The oxygen mass fraction plot in Figure 6.6(d) shows that oxygen is consumed by the propagating natural gas flame as indicated by the green region, but the oxygen is not completely consumed because the natural gas/air mixture is lean. Therefore, the diesel non-premixed flame in a dual fuel combustion engine reacts with a lower oxygen content mixture compared to a conventional diesel jet flame in air. In the near nozzle region the presence of oxygen flowing in the spray direction is visible, which indicates that the viscous action of the spray is entraining oxygen. This oxygen must then react with fuel to form intermediates, because further down the spray axis there is no discernable oxygen. This would support the formation of formaldehyde (CH_2O) downstream of the nozzle in Figure 6.6(i).

Figure 6.6(e) and Figure 6.6(f) show that the spray flame produces greater mass fractions of CO_2 and H_2O in comparison to the natural gas flame, which is to be expected because the non-premixed n-heptane flame burns at a stoichiometric ratio and will therefore produce a greater mass of products. It is for this same reason that the OH radical mass fractions are higher in the non-premixed flame compared to the premixed natural gas flame as shown in Figure 6.6(g). However, the HO_2 radical mass fraction is much higher in the preheat zone upstream of the natural gas flame in comparison to the non-premixed n-heptane flame as shown in Figure 6.6(h). Another interesting point is that significant amounts of HO_2 and CH_2O are being produced in the unburned gas in the bowl region far upstream of the natural gas flame. This result is indicative of auto-ignition reactions beginning in the end gas.

The mass fraction of NO is shown in Figure 6.6(j), where it can be seen to be greatest at the non-premixed flame surface of the n-heptane spray. Comparing with Figure 6.5(f), the locations of high NO production are also the locations of highest temperature, which is to be expected since the extended Zeldovich mechanism only accounts for thermal NO production. Very little

NO is formed by the premixed natural gas flame as lean premixed combustion generates lower temperatures. Additional work that includes other NO_X formation pathways, such as prompt NO and the N_2O route [48], is needed to construct a more complete picture of NO_X formation in dual fuel engines.

While this work did not include detailed soot formation and oxidation mechanisms, acetylene (C_2H_2) is a known soot precursor species [48] that can be used to qualitatively indicate possible soot formation locations in dual fuel combustion. From Figure 6.6(k), C_2H_2 formation begins in the interior of the spray and becomes most highly concentrated after impacting the bowl rim and traveling into the bottom of the bowl region or up into the squish region. The rich gas mixtures in these regions have slower velocities compared to the interior of the jet and they are nearer to the high temperature non-premixed flame surfaces. As such, these rich mixtures have a longer residence time at high temperature, which typically promote soot formation. There is no observable C_2H_2 where the premixed natural gas flame is propagating due to lean combustion.

The mass fraction of CO is shown in Figure 6.6(l), where it can be seen that CO is formed in the same rich hot regions where C_2H_2 is formed. This CO can be oxidized later in the expansion stroke, but the model was not carried out to these timings. There is a small amount of CO formed by the lean premixed natural gas flame, but this CO is quickly oxidized to CO_2 by the left over oxygen.

6.4.2. D12G22 SOI Sweep

The experimental pressure and AHRR data for the D12G22 timing sweep are shown in Figure 6.7(a). The simulations took approximately 8 hours each using 16 cores. Similar to the D25G17 cases, as the injection timing is advanced the pressure curve becomes more triangular,

the pressure rise rate increases, the peak pressure increases, the peak heat release rates increase during both the premixed spray ignition and the second combustion phase, and the combustion duration decreases. For the advanced injection timing cases (-12° and -14° ATDC), the AHRR during the second combustion phase increased at a constant rate and then experienced a rapid drop in AHRR. The later SOI cases had a more gradual decrease in AHRR.

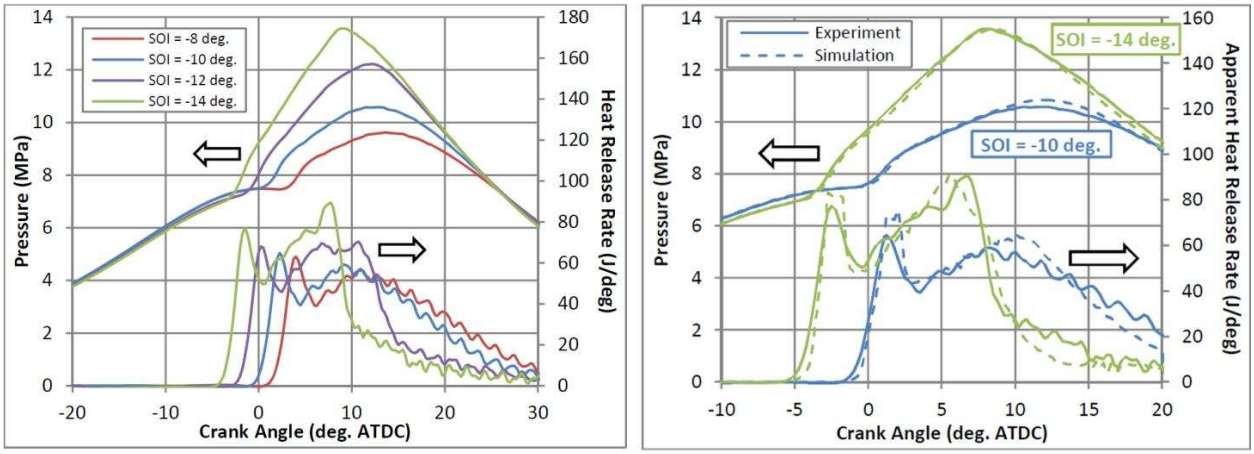

Figure 6.7. (a) Experimental pressure and AHRR data for the D12G22 SOI timing sweep. (b) Comparison of simulations with experiments for the -10° and -14° ATDC SOI timings.

The earliest and latest injection timing cases were selected for modeling and the simulation results are compared with experimental results in Figure 6.7(b). The simulations were able to capture the start of combustion timing to within 1 crank angle degree, the peak pressure to within 3 bar, the location of peak pressure to within 1 crank angle, the initial pressure rise rate to within 1 bar/deg, and the shape of the heat release rate curve as the injection timing was changed. Unlike the D25G17 cases, the peak AHRR during the ignition phase of combustion is well captured for these cases. One possible reason for the better agreement with the ignition phase could be that the rate shape used from Perini et al. [45] might be a more accurate representation of the true rate shape in the D12G22 case than in the D25G17 case. This is supported by the fact

that both the D12G22 and D25G17 cases used the same rate shape, but the D12G22 case had an injected mass of 12 mg, which is closer to the 8.8 mg used for the rate shape measurements from Perini et al. compared to the much larger 25 mg in the D25G17 cases. Additionally, the phasing for the rapid decrease in AHRR during the second combustion phase in the D12G22 cases exhibits better agreement with experiments than in the D25G17 cases from Figure 6.4(b). The rapid drop in AHRR during the second phase of combustion develops as the injection timing is advanced and since this trend was well captured by the D12G22 simulations, in-cylinder plots can be used to elucidate the differences in combustion behavior as injection timing is advanced.

To compare the differences in combustion behavior between the -10° and -14° SOI cases, it is useful to shift the crank angle data from degrees ATDC to degrees after start of combustion (ASOC), as this allows differences in the flame propagation speed to be more readily compared. This crank angle shift of the data from Figure 6.7(b) is shown in Figure 6.8, where it can be seen that the AHRR profiles begin at the same crank angle ASOC. Also shown in Figure 6.8 are the respective cylinder volumes, which have also been shifted to degrees ASOC. The vertical dashed lines denote respectively the beginning of the second combustion phase and the crank angle at which the AHRR peaks. For these two cases, the crank angle where the AHRR begins to fall was approximately equal at 11.5° ASOC. During the period where AHRR is increasing, the change in volume for the more advanced injection timing is less than half the volume change for the later injection timing. Therefore, the flame propagation in the advanced injection timing case occurs during a smaller increase in cylinder volume and therefore experiences less expansion cooling.

Comparisons of in-cylinder temperature in the plane of the spray axis for the two injection timings are shown in Figure 6.9 on a crank angle ASOC basis starting from the beginning of the second combustion phase, where it can be seen that the combustion zones are nearly identical in

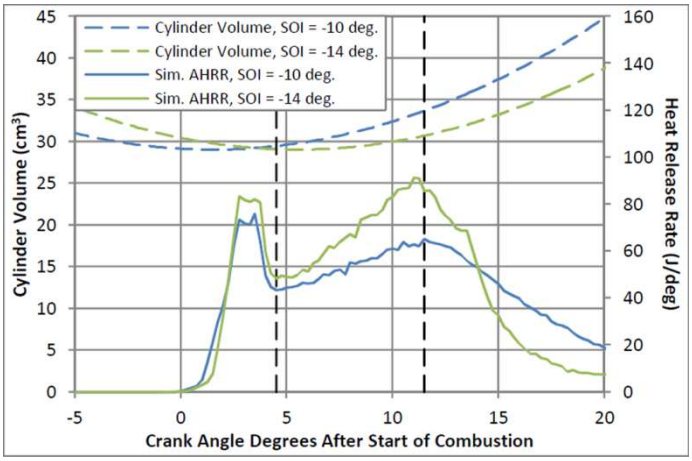

Figure 6.8. Simulation results the D12G22 SOI sweep, which have been shifted in crank angle so that their start of combustion timings are in phase. The corresponding cylinder volumes are also shown.

shape and size. Similar to the D25G17 cases a non-premixed diesel flame initiates a propagating natural gas flame. However, the injection duration is much shorter in the D12G22 cases and as a result the non-premixed diesel flame is not maintained for as long. By 11.5° ASOC in Figure 6.9(b), the premixed natural gas flame in the advanced injection timing case has propagated a further distance in the same amount of time after start of combustion, which means the flame speed is faster for the advanced injection timing. One explanation for the faster flame speed is that the unburned gas temperature is higher due to the advanced injection timing having a smaller increase in volume and less expansion cooling. The faster flame speed for the advanced injection timing is also responsible for the steeper positive slope in the AHRR profile seen in Figure 6.8.

Additionally, the fall in AHRR begins at approximately 11.5° ASOC and Figure 6.9(b) shows that the flame surface has nearly reached the bowl walls for the -14° SOI case, meaning most of the natural gas in the bowl region has been consumed at this point. Figure 6.9(c) shows the burned and unburned zones at 15° ASOC, which is after the rapid fall in AHRR for the advanced -14° SOI case. All of the natural gas in the bowl region has been consumed by 15°

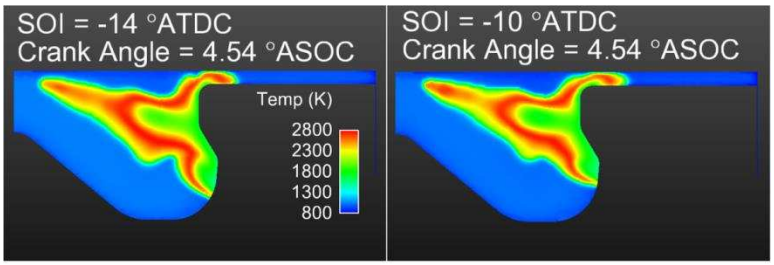

(a)

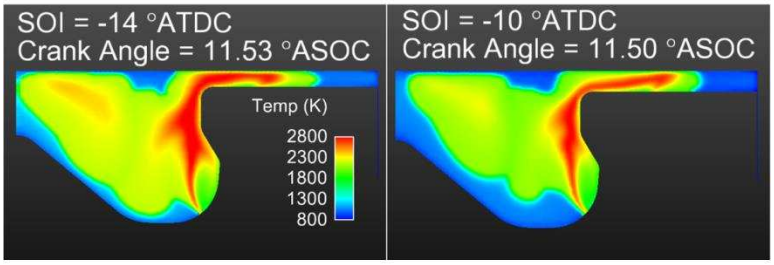

(b)

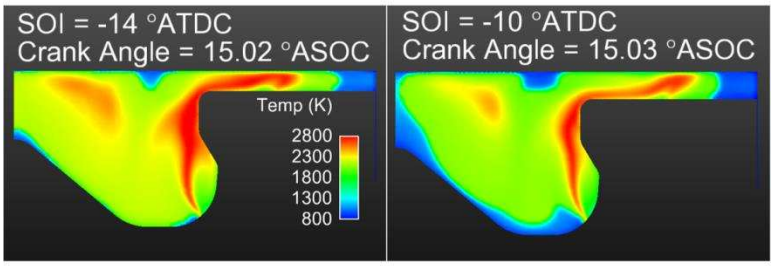

(c)

Figure 6.9. Comparison of temperature development in the plane of the spray axis for two different injection timings for the D12G22 SOI sweep, in which the comparisons are made at degrees ASOC rather than degrees ATDC.

ASOC in the advanced injection case, while in the retarded injection case the flame has not reached the bowl walls. The images from Figure 6.9(b) and Figure 6.9(c) suggest that the sharp decrease in AHRR for the early injection timing case coincides with a sudden change in available natural gas due to consumption of all the natural gas in the bowl. In contrast, the later injection timing case has a natural gas flame that decelerates due to greater expansion cooling and therefore does not experience a sudden drop in AHRR.

The decelerating flame speed for the late injection timing can ultimately result in flame quenching, which can leave a portion of the natural gas mass unburned. Increases in methane

emissions with retarded injection timing have been observed experimentally by Abd Alla et al. [49] and Ishiyama et al. [43]. A comparison of methane mass fraction between the two injection timings at 19° ASOC is shown in Figure 6.10, which clearly indicates that the later injection case has greater amounts of unburned methane late in the combustion duration because the flame speed has slowed considerably. If the SOI is overly retarded, then expansion cooling will eventually extinguish the natural gas flame before it can reach the bowl walls resulting in increased unburned natural gas emissions along with BSFC penalties. The model also shows that even with early injection timing the heat transfer cooling in the squish region reduces the flame propagation rate and could lead to flame quenching.

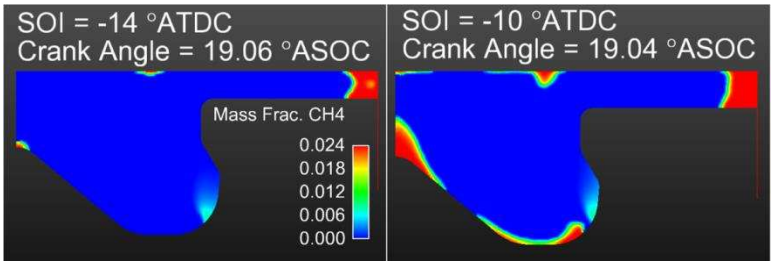

Figure 6.10. Comparison of methane mass fraction at the end of the combustion duration for two different injection timings in the D12G22 SOI sweep. Note that the crank angle refers to degrees ASOC rather than ATDC.

6.4.3. Heat Release Rate Contribution from Fuel Components

As discussed above, the AHRR profile has contributions from both fuels during both the first and second combustion phases. The relative contribution of the premixed natural gas combustion can be quantified by comparing a dual fuel simulation to one where the natural gas has been made non-reactive, while keeping the diesel spray constant. Such a simulation was performed for the D12G22, -14° SOI case by replacing the natural gas mass with a non-reactive pseudo species with the same thermodynamic properties as methane, but which is not present in any of the reactions. This procedure ensured that the trapped mass, temperature, and pressure at start of

injection were exactly the same as that in the dual fuel simulation. By comparing the difference in AHRR profiles between the dual fuel case and the diesel-only case, the energy contribution from natural gas can be deduced.

The predicted pressure and AHRR for both cases are presented in Figure 6.11 along with the experimental data. The most apparent difference is that the natural gas contributes a substantial portion of the heat release during both the first and the second combustion phases. The diesel-only case does not exhibit a sudden drop in AHRR during the second phase of combustion as seen in the dual fuel case, which provides further evidence that the rise and sudden fall in AHRR for the dual fuel case is due to the consumption of natural gas in the bowl region as discussed previously. Additionally, Figure 6.11 shows that the maximum AHRR during the spray ignition phase is substantially lower when the natural gas is made inert. This difference is due to the rapid burning of natural gas that has mixed with the diesel vapor during spray breakup and vaporization, which increases the pressure rise rate at ignition. Furthermore, the start of combustion timing for the diesel-only case is slightly earlier compared to the dual fuel case, which demonstrates that the presence of natural gas within the diesel spray slows down the ignition reactions. Karim et al. [6] has reported that dual fuel engine experiments have shown longer ignition delay in comparison to conventional diesel combustion. Since the oxygen concentration is the same in both cases, the results of Figure 6.11 suggest that the longer ignition delay is due to the chemical kinetic effects of methane rather than the displacement of oxygen.

6.4.4. Propane Addition and Uncontrolled Combustion Rates

Figure 6.12(a) shows 100-cycle averaged experimental pressure and AHRR for the D12G22P2 case with a -10° ATDC SOI timing as well as the volume averaged simulation

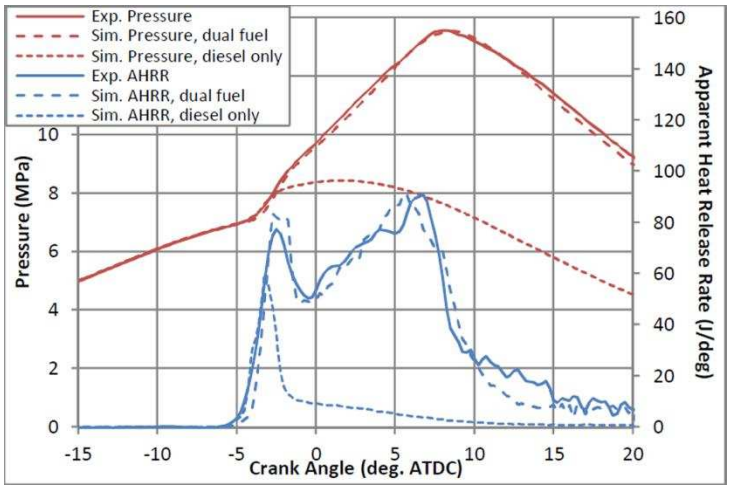

Figure 6.11. Comparison between the D12G22, -14° ATDC SOI simulation and the same simulation when the initial natural gas mass has been replaced with an inert with the same thermodynamic properties as methane.

results. Experimental pressure data from a single cycle is shown in Figure 6.12(b), which has been zoomed in near the peak pressure where high frequency pressure oscillations were observed. Also shown in Figure 6.12(b) is the simulated pressure from a single cell at the same location as the transducer tip in the engine. Unlike the volume averaged pressure, this single point recorder is capable of indicating the presence of pressure waves in the simulation.

To reduce damping of waves in the simulation, between 5° and 15° ATDC the multi-grid pressure solver was turned off and the CFL Mach number was reduced to 2. Figure 6.12(c) shows a comparison of the experimental and simulated instantaneous slope of the pressure or pressure rise rate. The frequencies of the pressure oscillations are compared in Figure 6.12(d), which were calculated using the time difference between successive peaks in the pressure data.

From the 100-cycle averaged experimental curves in Figure 6.12(a), the second combustion phase in the propane addition case begins with a steady increasing slope, but then experiences a sudden acceleration and large spike followed by a dramatic drop. The rapid spike in AHRR is accompanied by a sudden increase in pressure rise rate as demonstrated in the pressure rise rate

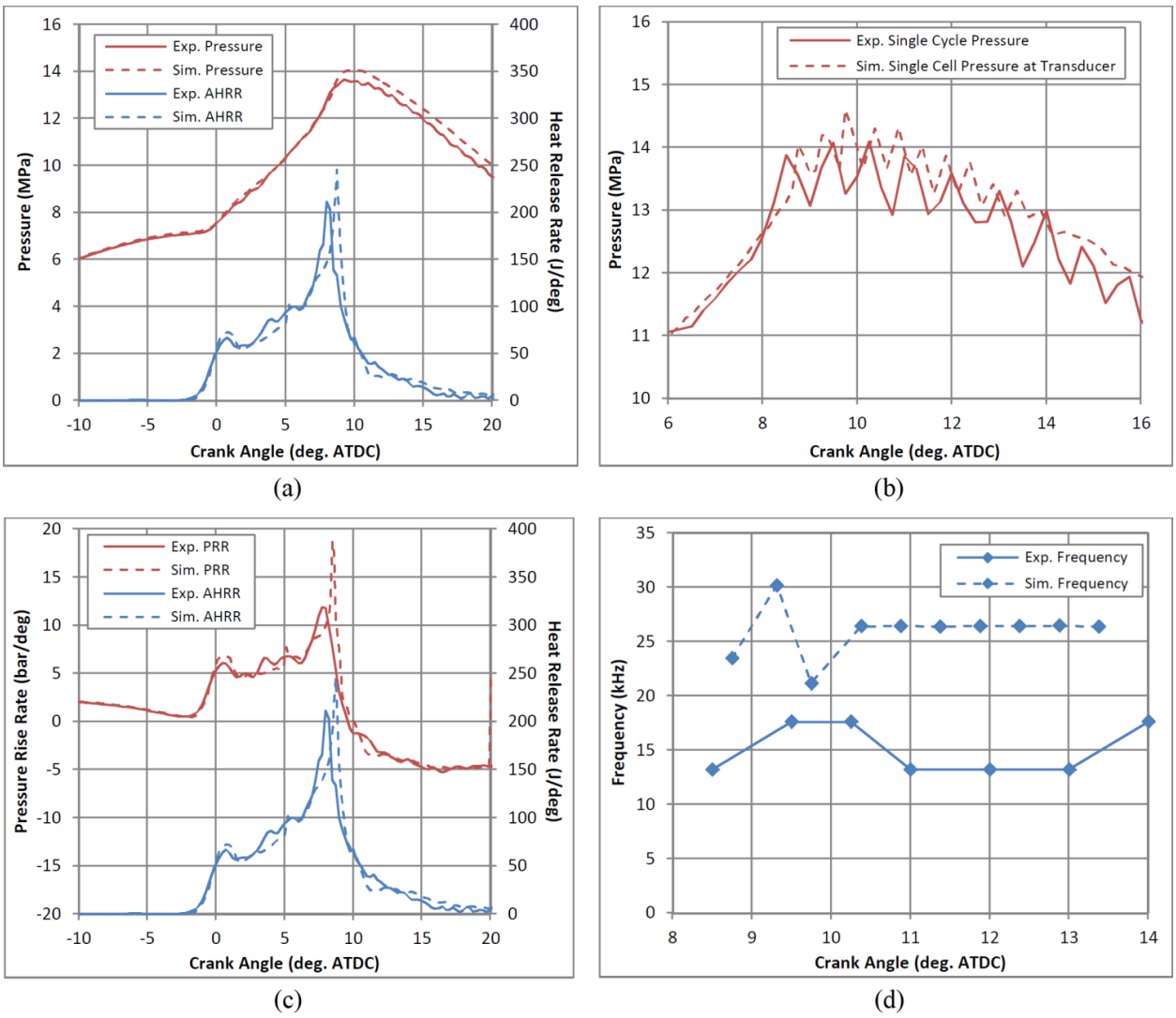

Figure 6.12. (a) Experimental and simulation results for the propane addition, D12G22P2 -10° ATDC SOI case. (b) A zoomed in plot comparing the single cycle experimental and single cell simulated pressure oscillations caused by the uncontrolled fast combustion. (c) Comparison of pressure rise rate. (d) Frequencies of the pressure oscillations.

plot of Figure 6.12(c). The sudden increase in pressure rise rate is then followed by high frequency, high magnitude pressure oscillations as seen in Figure 6.12(b). These pressure oscillations can be classified as engine knock.

As shown in Figure 6.12(a), the volume averaged pressure and AHRR for the simulation exhibit good agreement in terms of start of combustion, pressure rise rate, peak pressure, location

of peak pressure, and the timing and magnitude of the AHRR spike during the uncontrolled fast combustion event. Figure 6.12(c) shows that the pressure rise rate is especially well captured throughout the combustion event. The single cell simulation pressure in Figure 6.12(b) shows fluctuations with a slightly higher frequency and lower amplitude than observed in the experimental single cycle pressure. The simulated pressure waves also damp out at a faster rate. A more direct comparison of the frequencies is shown in Figure 6.12(d) where the simulated frequency is somewhat higher than the experimental. The average experimental frequency and peak to peak amplitude was found to be 15 ± 4 kHz and 10 ± 2 bar respectively, while the average simulated frequency and amplitude was found to be 26 ± 6 kHz and 6 ± 2 bar respectively. This agreement could be improved with a higher resolution crank encoder, because the 0.25 crank angle degree sampling rate is only able to capture 3 to 4 points per period of oscillation. Additionally, error in the simulations arises from not being able to use AMR based on pressure gradients and so there was no way to refine the grid as pressure waves moved into coarser grid regions.

Because the sudden acceleration in AHRR was well captured by the simulation, in-cylinder plots of temperature, species mass fraction, and local heat release rate can elucidate the cause of this uncontrolled combustion rate. Figure 6.13(a) through (f) are three dimensional images of the engine sector showing the development of a 2000 K iso-surface, which is indicative of the boundary between unburned and burned regions. Figure 6.13(a) shows the region where ignition of the diesel spray occurs. Due to the swirl motion this ignition region is not symmetric around the spray axis. At 1º ATDC in Figure 6.13(b) the combustion zone has enveloped the spray axis and the non-premixed diesel spray flame has been established. A portion of the temperature iso-surface has crossed the periodic boundary and therefore represents the combustion zone from the

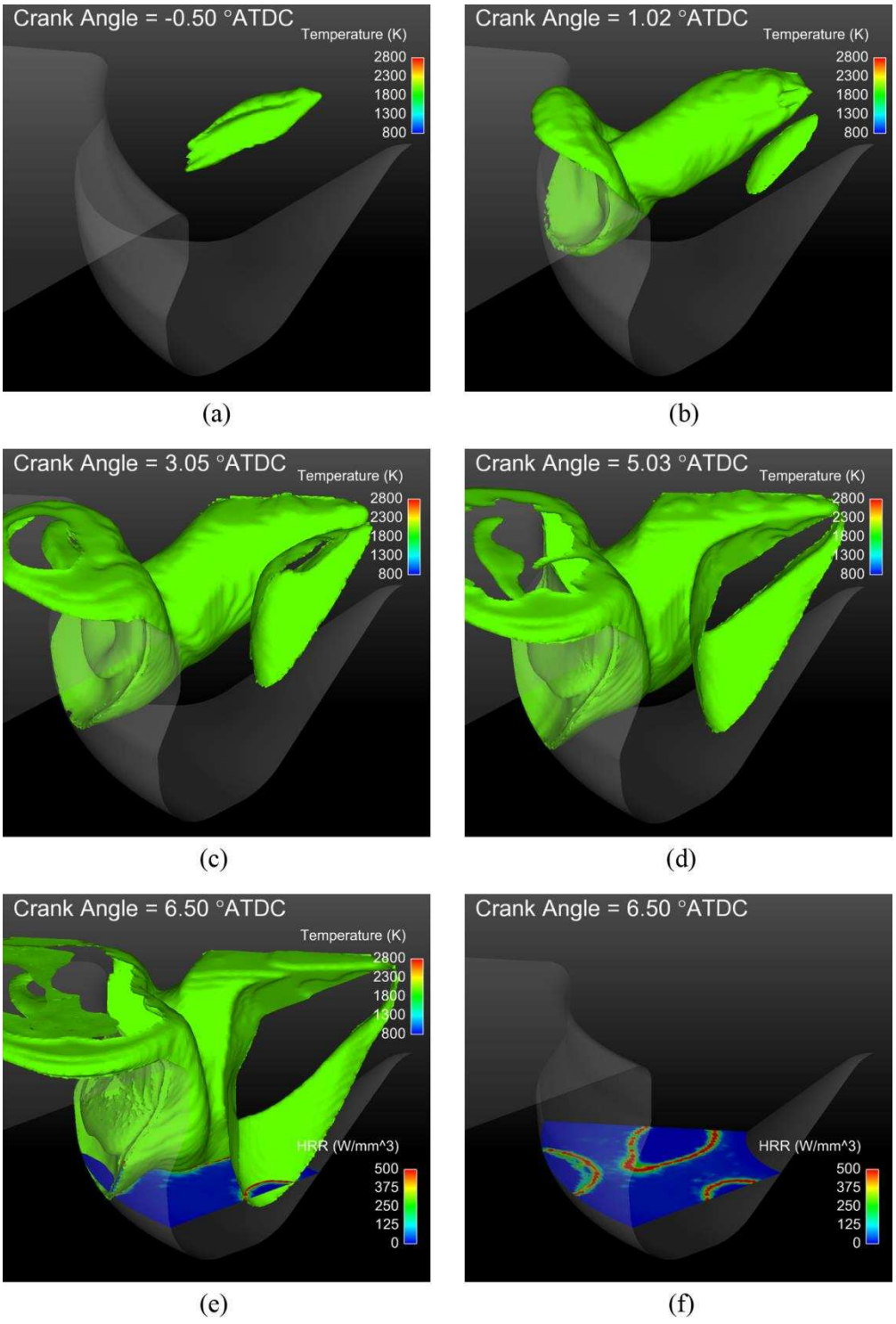

Figure 6.13. Development of a 2000 K temperature iso-surface with a local HRR clip plane showing three flames in the bottom of the bowl region for the D12G22P2 -10° ATDC SOI propane addition case.

adjacent diesel spray moving into the sector. By 3° ATDC in Figure 6.13(c), the combustion zone has grown outward from the spray axis and also into the squish region, which is a consequence of the propagating natural gas flame. The premixed flame from the adjacent spray has merged with the flame from this sector, creating a single premixed propagating flame surface with a cusp like crease between them. The natural gas flame continues to grow in Figure 6.13(d) and Figure 6.13(e) with the merged natural gas flame moving into the bottom of the bowl. After impacting the bowl rim, the non-premixed diesel flame moves downward along the far wall of the bowl. In the 6.5° ATDC images of Figure 6.13(e) and Figure 6.13(f), a planar cross section plot of local heat release rate has been added showing the location of the reaction zones in the bottom of the bowl in relation to the temperature iso-surface. The 2000 K iso-surface has been removed in Figure 6.13(f) for clarity, which depicts three flames moving towards each other. The flame along the bowl wall is the non-premixed diesel flame and the other two are the premixed natural gas flames originating from adjacent spray axes. All three are expanding in size as they travel into the bottom of the bowl.

The growth of these three flame zones during the uncontrolled fast combustion event are shown in terms of local heat release rate in Figure 6.14. As the flames move toward each other in Figure 6.14(a) and (b), volumetric heat release begins to occur throughout the volume of gas in front of and between the natural gas flames, which are about to merge. It should be noted volumetric heat release does not occur near the walls of the bowl due to heat transfer. A quarter of a degree later in Figure 6.14(c) the rate of heat release throughout the volume in front of the merging natural gas flames has increased considerably. This sudden enlargement of the reaction zone indicates the presence of volumetric auto-ignition reactions. This volumetric heat release occurs at 8.50° ATDC, which is the same timing as the peak in AHRR from the simulation. In

less than a quarter of a crank angle later in Figure 6.14(d), this volume is no longer producing heat and the flames have traveled to the walls where they are slowed down by heat transfer.

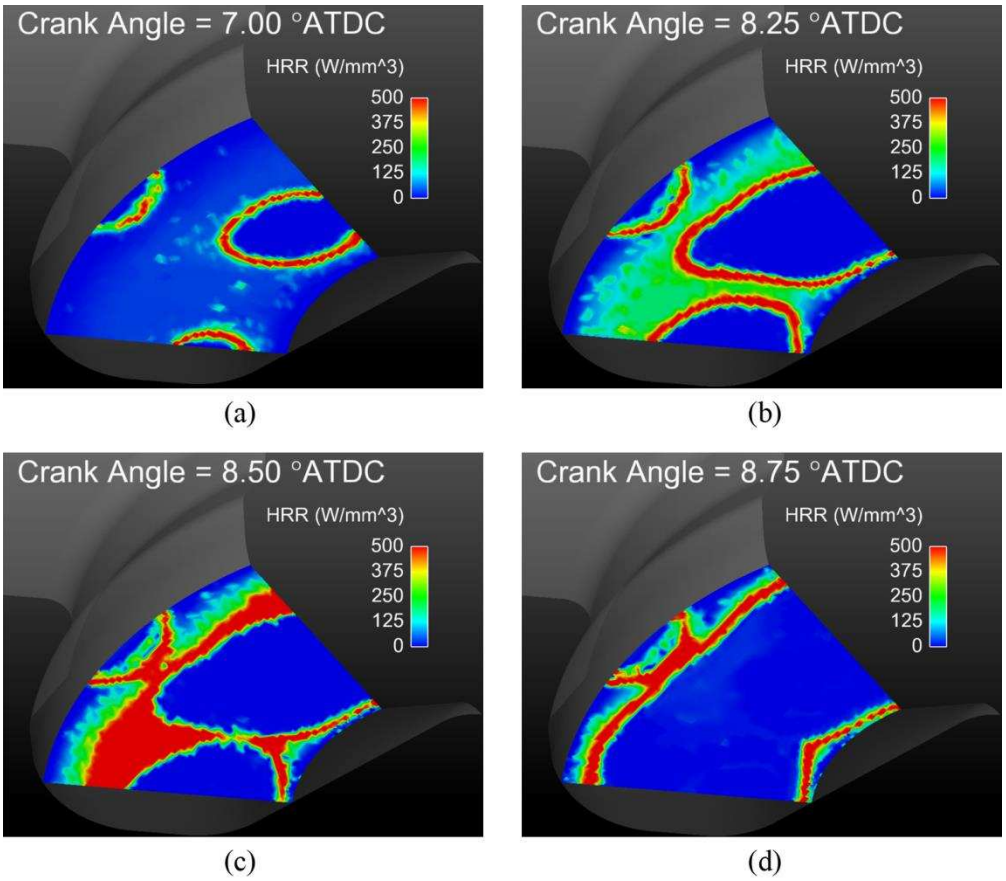

Figure 6.14. Plots of local heat release rate in the bowl region during the uncontrolled fast combustion event for the D12G22P2 propane addition case.

Figure 6.15 shows in-cylinder pressure during the peak in AHRR, where high pressure can be seen originating from the same location where auto-ignition occurred. This source of higher pressure leads to pressure waves traveling throughout the cylinder. Therefore, the simulation has shown that the uncontrolled combustion rate is due to auto-ignition of natural gas in front of the merging natural gas flames originating from adjacent diesel sprays, which consequently creates pressure waves that travel across the chamber.

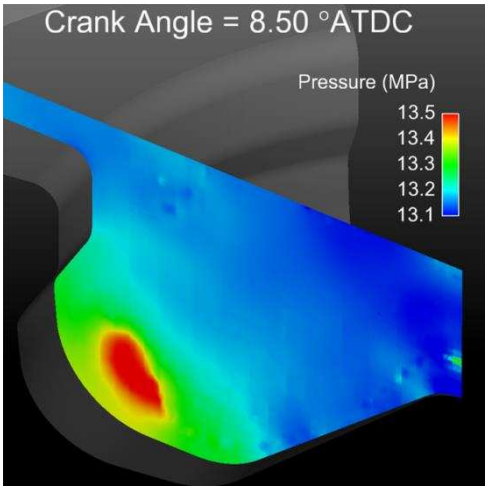

Figure 6.15. Pressure clip plane during the peak of the uncontrolled fast combustion event in the propane addition case showing a high pressure wave propagating outward from the location of auto-ignition.

The resulting dual fuel knock phenomena predicted by this simulation is qualitatively similar to the end gas auto-ignition type knocking that occurs in an SI engine. However, the mechanism and location for the onset of knock in the dual fuel conditions investigated herein are different from that of the SI engine. In an SI engine, compression heating of a volume of unburned gas between a single spherically expanding flame and the chamber walls leads. In contrast, a dual fuel engine has two natural gas flames from adjacent diesel sprays that are merging together and forming a pocket of unburned natural gas along the crease between them that is located far from the walls. Consequently, this pocket of unburned gas experiences less heat transfer than gas nearer to the walls and will undergo auto-ignition first. Additionally, the location of auto-ignition in an SI engine can vary from cycle to cycle due to the symmetry of a single spherically expanding flame, while the auto-ignition location in a dual fuel engine as identified in this simulation is confined between spray axes. Therefore, this simulation suggests that the auto-ignition locations for a dual fuel engine should not vary from cycle to cycle.

The AHRR diagram in Figure 6.16 presents a generalized explanation for dual fuel combustion undergoing uncontrolled fast combustion by separating the combustion duration into four characteristic parts as indicated by the dashed lines. The first phase of dual fuel combustion is identical to the first phase from Figure 6.1 and consists of premixed auto-ignition of the diesel spray head as well as any natural gas entrained within or in the immediate vicinity of the diesel spray head. The second phase of dual fuel combustion in Figure 6.16 is characterized by the increasing ramp in the AHRR curve, where the diesel fuel burns as a non-premixed spray flame and the natural gas burns as a thin premixed propagating flame. The third phase is characterized by a sudden uncontrolled spike in AHRR, which creates high frequency pressure waves that can be identified as engine knocking. After the fast combustion event, all the natural gas in the bowl region has been consumed and consequently there is a sudden reduction in available unburned natural gas as well as global heat release rate. This sudden drop in combustion rate marks the separation between the third and fourth phases in Figure 6.16 and is a consequence of the piston geometry. The fourth and final combustion phase in Figure 6.16 is characterized by a slow tailing off of the combustion rate and is due to the premixed natural gas flame slowly propagating into the squish region as well as any remaining diesel fuel burning. It should be noted that the observations described herein are for a specific engine at a single engine speed and a relatively high boost pressure. Further work is needed to investigate how the behaviors responsible for uncontrolled fast combustion or engine knock in dual fuel engines can change with engine speed, swirl ratio, boost pressure, bore size, piston geometry, and compression ratio.

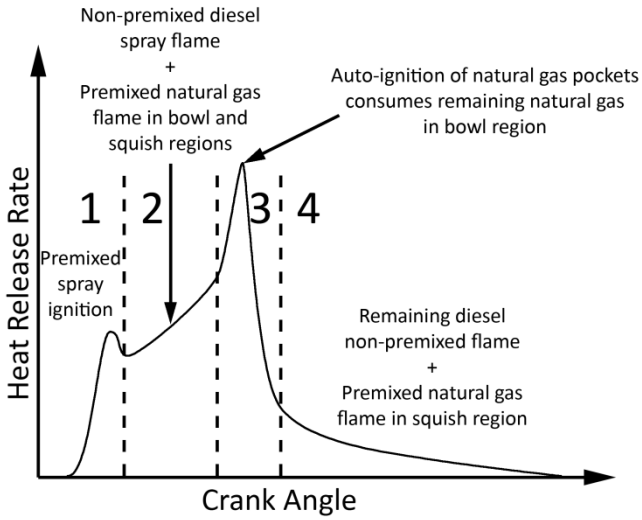

Figure 6.16. Diagram of the AHRR curve for dual fuel combustion when an uncontrolled fast combustion event occurs showing the different combustion phases.

6.5. Constant Volume Chamber Simulations

To better understand the interactions between the non-premixed spray flame and the premixed natural gas flame occurring in dual fuel combustion without the interference from engine geometry and volume expansion, simulations were performed for a single n-heptane spray in a large constant volume chamber containing a mixture of natural gas and air. These simulations inform the development of a simplified conceptual model for dual fuel combustion. For these constant volume simulations, the spray remained constant while the natural gas equivalence ratio was varied from 0 to 0.5 to 0.8. Spray parameters such as nozzle geometry, rate of injection, injection duration, and injected mass were chosen to be the same as the 500 bar injection pressure Spray A case from the ECN, except that the evaporated species n-dodecane was replaced by n-heptane so that the CSU86 combustion chemistry could be used. The 500 bar injection pressure case was chosen because the engine experiments used a relatively low injection pressure of 700 bar. The velocity and turbulence fields were initialized as zero at all

locations in the chamber. A complete list of the simulation inputs is provided in Table 6.3. The simulations were run for 2 ms.

Table 6.3. Spray parameters and ambient conditions for constant volume chamber simulations.

Liquid fuel properties	"DIESEL2"
Vaporized fuel species	n-heptane
Injected mass (mg)	7.8
Injection duration (ms)	5.65
Injection pressure (bar)	500
Orifice diameter (μm)	0.84
Discharge coefficient	0.86
Ambient temperature (K)	1000
Ambient pressure (bar)	76
Ambient density (kg/m^3)	25.8, 25.3, 24.8
Natural gas equivalence ratio	0, 0.5, 1.0

Figure 6.17 shows the time evolution of the temperature for the three natural gas equivalence ratio cases. The boundary of the non-premixed flame can be identified by where the highest temperatures (red) meet the lower temperature interior of the spray (green). The reaction zone for the premixed natural gas flame is located outside of the non-premixed flame where moderate temperatures (green for φ = 0.5 and orange for φ = 0.8) meet the low ambient temperatures (blue). The pure air case (φ = 0.0) has the shortest ignition delay while the case with the greatest amount of natural gas (φ = 0.8) has the longest ignition delay. Even though the φ = 0.8 case has a longer ignition delay it is able to quickly surpass the φ = 0.5 case in terms of flame propagation, which is evident in the much larger burned zone at 1.74 milliseconds. The φ = 0.5 case shows that the premixed natural gas flame propagation is much slower than the φ = 0.8 case and it is only able to propagate from the back end of the spray plume. In the φ = 0.8 case, the premixed natural gas flame speed is high enough that it propagates ahead of the spray plume head as seen in the images for 1 millisecond and later.

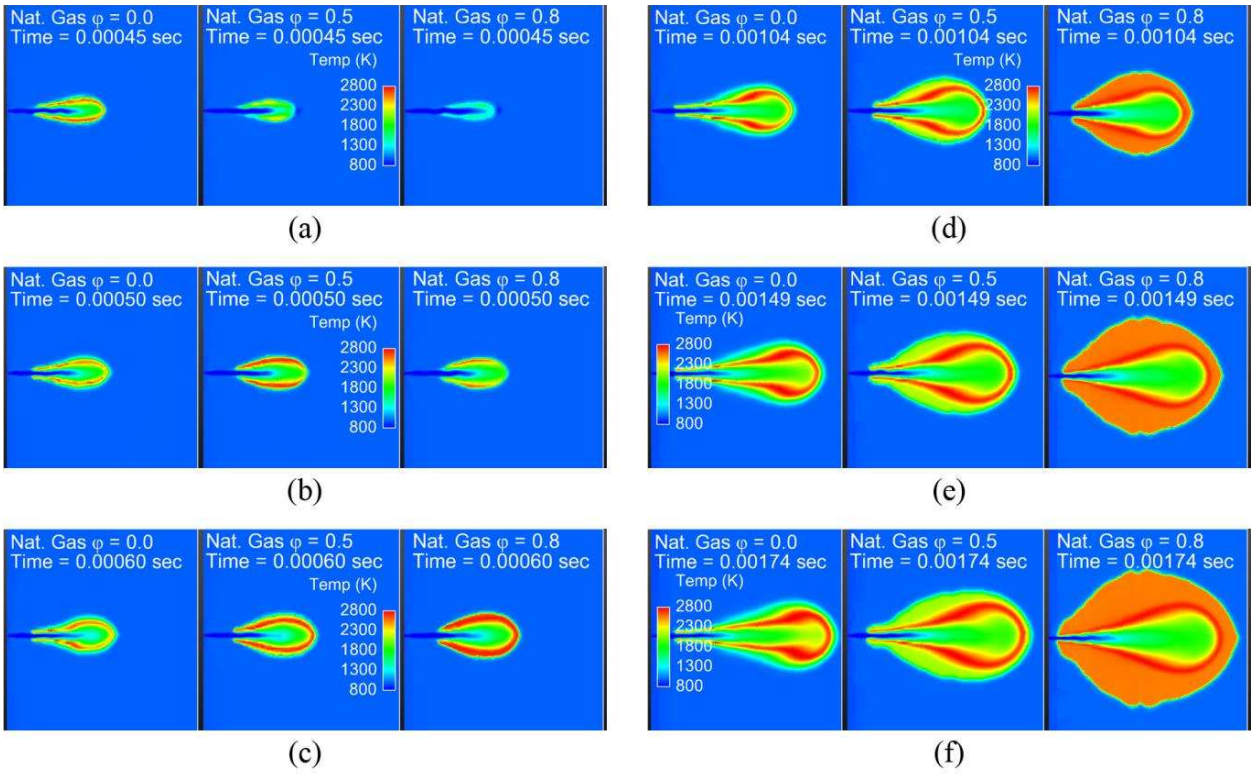

Figure 6.17. Time evolution of temperature for three different natural gas equivalence ratios for an n-heptane spray into a constant volume chamber at typical TDC temperature and pressure. Time proceeds sequentially from (a) to (f).

Figure 6.18 shows the local heat release rate and various species mass fractions at 1.49 milliseconds when the non-premixed has been fully established and the premixed natural gas flame has traveled a noticeable distance from the spray. The local heat release rate plot in Figure 6.18(a) shows the location of the reaction zones, which clearly indicate the location of both the premixed natural gas flame and non-premixed n-heptane flame. Figure 6.18(a) also shows there is a narrow reaction zone in the upstream region of the jet near the nozzle for all three cases. Comparison with the temperature plot in Figure 6.18(e) shows that the local temperature is much lower for this reaction zone, which implies that this heat release is caused by the low temperature chemistry of n-heptane. This near nozzle low temperature heat release is in agreement with the experimental observations made by Dec [47] for diesel spray combustion.

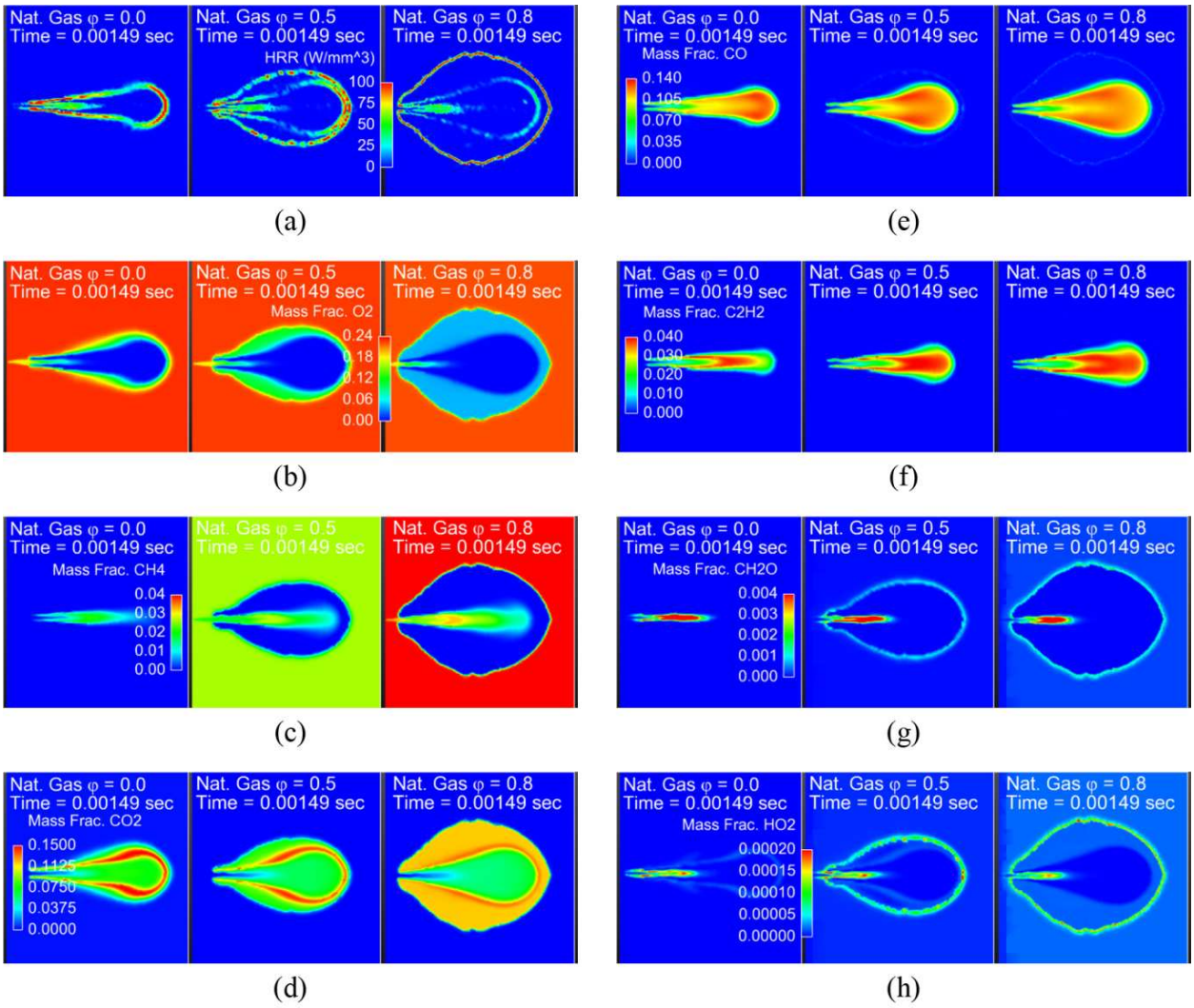

Figure 6.18. Heat release rate and mass fraction plots of various species at 1.49 ms. (a) Local HRR. (b) Oxygen. (c) Methane. (d) Carbon dioxide. (e) Carbon monoxide. (f) Acetylene. (g) Formaldehyde. (h) Hydroperoxyl radical.

For the dual fuel cases, the non-premixed reaction zone is weaker in local heat release rate and the non-premixed flame surface area is larger. This can be explained using the oxygen mass fraction in Figure 6.18(c) where there is a greater reduction in oxygen mass fraction behind the natural gas flame as the natural gas equivalence ratio is increased. The reaction zone for a non-premixed diffusion flame exists where the equivalence ratio is nearly stoichiometric and therefore the spray head must diffuse outward a greater distance in order to reach stoichiometric

proportions with a mixture of lower oxygen content. This larger and more diffused spray head also has a lower density of hydrocarbons on the fuel side of the non-premixed flame, resulting in lower local heat release rate. The reduced oxygen content for the n-heptane spray also implies that using a stoichiometric natural gas equivalence ratio will lead to insufficient oxygen for CO and soot oxidation. Furthermore, Figure 6.18(b) shows the presence of oxygen at the nozzle and within the upstream portion of the sprays, which indicates oxygen entrainment and subsequent rich oxidation reactions with the n-heptane spray.

Figure 6.18(c) shows that methane is produced in the interior of the spray for all three cases. In the pure air case methane is not present until after a noticeable distance downstream of the nozzle, while the dual fuel cases show methane at the nozzle orifice and throughout the entire spray interior. Also the methane mass fraction is highest in the dual fuel cases at a similar location to where the methane is produced in the pure air case. This implies that the viscous action of the spray is entraining methane near the nozzle in the dual fuel cases and later downstream the breakdown of n-heptane is producing methane as an intermediate. The entrained and produced methane is then completely oxidized at the non-premixed flame surface as there is no methane observed between the non-premixed flame and the natural gas flame.

The carbon dioxide mass fraction in Figure 6.18(d) shows that more CO_2 is produced by the non-premixed flame than the premixed natural gas flame, which is understandable as the non-premixed flame occurs at a nearly stoichiometric ratio and the natural gas flame is lean. In Figure 6.18(e) the mass fraction of CO is produced in the spray head and oxidized at the non-premixed flame, while no CO is left behind the lean natural gas flame. This implies that CO emissions in dual fuel engines are the result of incomplete combustion of the diesel spray. Because C_2H_2 is a known precursor to soot formation, Figure 6.18(f) suggests that soot is formed most strongly in

the head of the n-heptane spray for all three cases, which is a well-known behavior for diesel sprays [47], and very little to no soot is formed by the lean natural gas flame. The larger spray head in the dual fuel cases indicates that a greater mass of soot is likely to form in the spray heads of dual fuel combustion as the natural gas equivalence ratio is increased.

Combustion intermediate species CH_2O and the hydroperoxyl radical (HO_2) are shown in Figure 6.18(g) and Figure 6.18(h) respectively. CH_2O is an important species in one of the major chain branching pathways for methane combustion and Figure 6.18(g) shows the formation of CH_2O at the location of the lean natural gas flame. Figure 6.18(g) also shows CH_2O is produced at a high rate in the near nozzle region of the spray where low temperature heat release is observed, but not at the non-premixed diffusion flame surface where high temperature reactions are present. Therefore, CH_2O would be an effective species to use in an AMR scheme that refines the grid where the natural gas flame is located but not where the diffusion flame is located. HO_2 is initially formed in the H-atom abstraction reactions that initiate hydrocarbon combustion and is produced at high rates in lean combustion. Figure 6.18(h) confirms this as the HO_2 is present in the upstream region of the spray interior and at the natural gas flame surface. For the pure air and $\varphi = 0.5$ cases, HO_2 is produced in low quantities at the surface of the non-premixed diffusion flame. For the $\varphi = 0.8$ case, low levels of HO_2 remain in the products behind the natural gas flame, which is likely a result of less oxygen in the natural gas combustion products as the equivalence ratio is increased. Furthermore, the $\varphi = 0.8$ case shows HO_2 being produced homogeneously throughout the unburned natural gas/air mixture, which indicates homogenous auto-ignition reactions beginning in the unburned gases that can lead to knocking in dual fuel engines. Because the behavior of HO_2 is unique between all three cases, HO_2 would be a useful species to use in a multi-zone chemistry strategy.

6.5.1. NOx Comparison

The preceding section demonstrated the ability to compare diesel and dual fuel combustion in a fundamental sense using simulations. This method can also be applied to study NO_X formation. NO_X formation occurs at lean to stoichiometric conditions and at temperatures above roughly 2200 K [50]. NOx formation is well known to peak at slightly lean mixtures because the flame temperature is high and because there is excess oxygen available to react with nitrogen. Therefore, if a slightly lean natural gas mixture is added to a constant diesel spray then it is a trivial result that the NO_X formed is higher after a certain combustion duration. This would be analogous to comparing engine out NO_X emissions between diesel and dual fuel operation with the dual fuel case having a much high load than the diesel case. Therefore including a plot of NO_X in Figure 6.18 would have not have indicated the fundamental difference in NO_X formation between dual fuel and diesel. In order to make a fair comparison the diesel spray must be stopped part way through and natural gas allowed to release the remainder of the energy such that the total energy released is equal between the dual fuel and diesel cases. This is similar to how a dual fuel engine is operated at high load and high substitution rate.

In this section the diesel spray in the dual fuel case with $\varphi = 0.8$ is stopped just after ignition at 0.5 ms and the natural gas flame continues to propagate. The results are then compared to the pure diesel case when the dual fuel case has released the same amount of energy as the diesel case has at 2 ms. Then the mass of NO_X are compared and clip plane images are used to explain the differences.

Figure 6.19 compares the integrated heat release between both cases. Energy is released at a much greater rate in the dual fuel case for two reasons. Firstly, the diesel vapors in the head of the spray mix with natural gas and therefore more fuel mass combusts during ignition. Also, the

natural gas flame surface area quickly becomes much larger than the flame surface for the diesel jet. After 2 ms, the pure diesel simulation has released about 87 J of energy. This same about of energy is released by the dual fuel case at approximately 0.85 ms. By comparing the NO_X formed at these two times, it can be inferred as to which combustion mode is likely to generate greater NO_X for the same engine load.

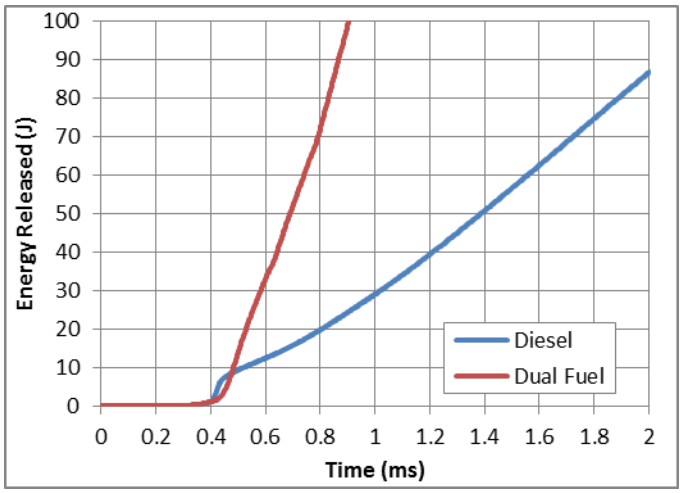

Figure 6.19. Comparison of energy released over time between the diesel and dual fuel cases. The diesel injection ends at 0.5 ms.

Figure 6.20 shows the mass of NO_X in the simulations over time. The NO_X in the diesel simulation at 2 ms is 0.08 mg, while that in the dual fuel case at 0.85 ms is 0.04 mg. Therefore, in order to release the same amount of energy the pure diesel case has formed about twice as much NO_X than the dual fuel case. The time that combustion occurs over is somewhat irrelevant for this comparison, because in an engine application the combustion duration will take as long as needed to meet the load requirements. The duration of the natural gas flame continue until all there is no longer any volume to burn and the mass of natural gas burned will already have been adjusted to meet the load required. The diesel flame will continue to inject until the load is met. An easier way to visualize this trend is to compare the NO_X formed with the energy released,

which is plotted in Figure 6.21. It is clear that pure diesel combustion produces more NO_X than dual fuel for any given amount of energy released or load demanded. Also this trend will continue for greater loads because the curves are diverging.

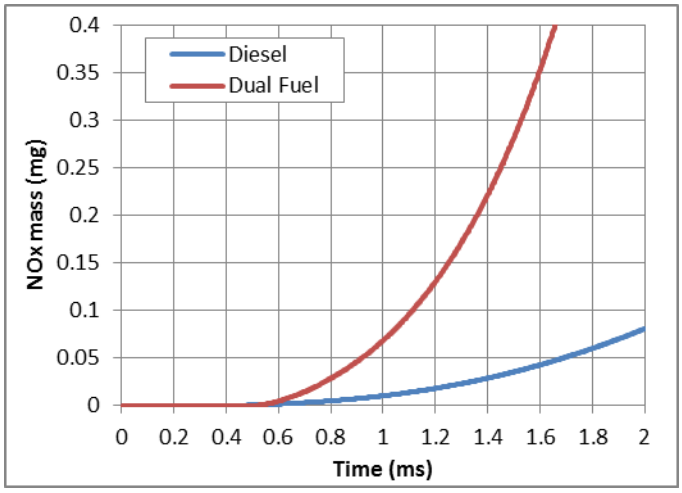

Figure 6.20. The NOx mass accumulated in the domain over time.

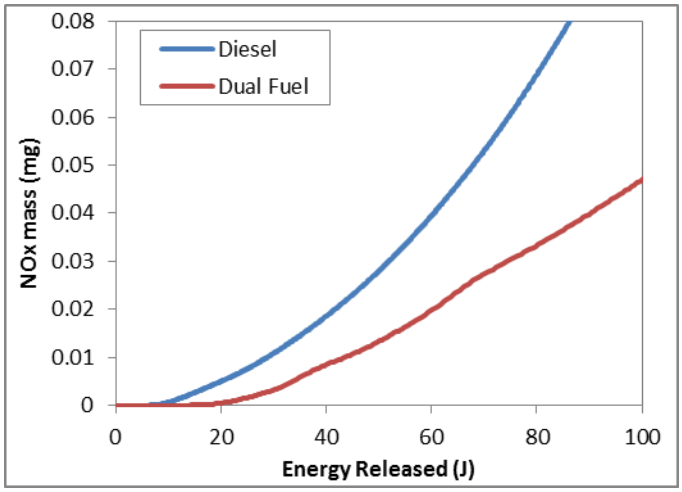

Figure 6.21. Accumulated NOx mass as a function of the energy released for the diesel spray and a dual fuel case where the injection ends just after ignition. The natural gas mixture in the dual fuel case has $\varphi = 0.8$.

Figure 6.22(a) shows a comparison of the NO_X field between the diesel and dual fuel cases at the two times compared previously when the energy released is equal. The dual fuel image is different than the images shown previously in Figure 6.18, because the diesel injection is turned

off at 0.5 ms. After the diesel injection ends, the natural gas flame is able to travel upstream towards the nozzle along the sides of the jet. This is more clearly seen in the temperature images in

Figure 6.22(b) and the local HRR plot in

Figure 6.22(c).

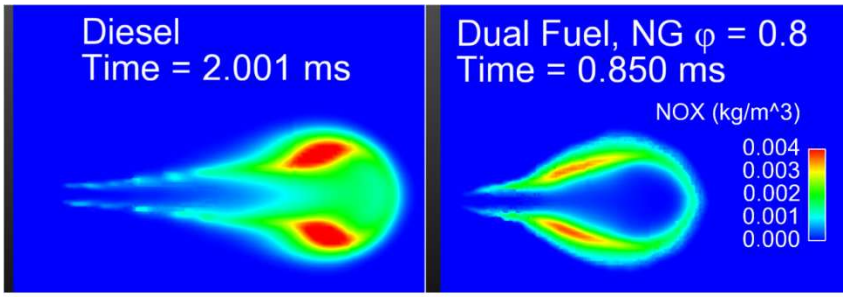

(a)

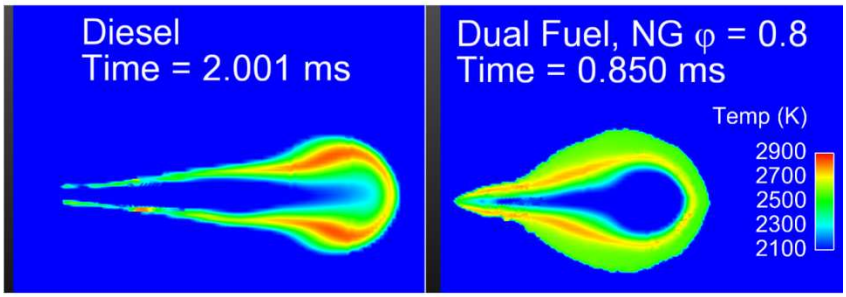

(b)

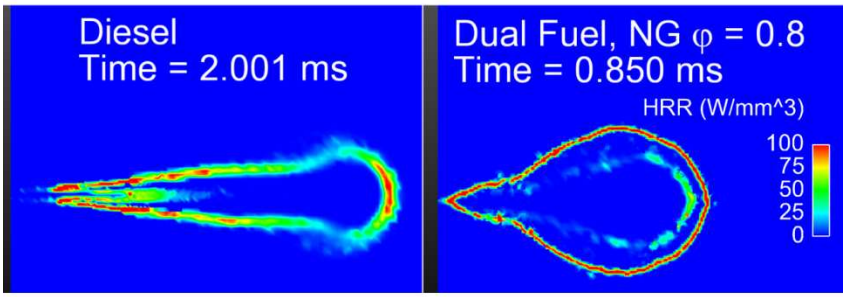

(c)

Figure 6.22. Comparison between pure diesel combustion and dual fuel combustion in which the diesel injection is turned off at 0.5 ms. (a) NO_X. (b) Temperature. (c) Local heat release rate.

The NO_X image in

Figure 6.22(a) shows that the diesel flame has a much larger volume of higher NO_X production. The natural gas flame in the dual fuel case has a large energy release rate over a large surface area but has a lower flame temperature as indicated by the green volume. The highest NO_X formation occurs in the exhaust products left behind the natural gas flame and since the temperature is lower than the diesel flame, the NO_X concentration is lower.

6.6. Conclusion

A multi-dimensional CFD model with an 86 species reduced chemical kinetic mechanism, a RANS turbulence model, and advanced spray models has been constructed and validated against in-cylinder pressure and heat release rates from natural gas/diesel conventional dual fuel engine experiments across varying substitution percentages including a case where engine knock occurred. The reduced chemical mechanism was developed for mixtures of n-heptane, methane, ethane, and propane using the DRGEPSA method from highly detailed base mechanisms. Engine experiments and simulations were performed by varying injection timing for two different loads with different natural gas substitution percentages. Dual fuel combustion with a more reactive natural gas mixture was explored by adding a small amount of propane to the natural gas in one of the high substitution cases. This propane addition experiment exhibited an uncontrolled fast combustion rate during the second combustion phase, which created high frequency pressure oscillations characteristic of engine knock.

For both injection timing sweeps and the propane addition experiment, the CFD simulations predicted start of combustion timing to within one crank angle degree, the initial pressure rise rate to within 2 bar/deg, the peak pressure to within 4 bar, and the phasing of peak pressure to within 1 crank angle degrees. For the propane addition case where knocking was observed, the

timing and magnitude of the uncontrolled fast combustion was well captured. Also, the simulation predicted pressure oscillations that were close in frequency to the experimentally observed oscillations. Qualitatively, the model achieved excellent agreement with the shape of the heat release rate profile for all experimental cases. In-cylinder images from these simulations provided information about the physics of dual fuel combustion and the following conclusions were drawn.

1. Under the operating conditions investigated, dual fuel combustion begins with rich premixed auto-ignition of the diesel spray and entrained natural gas. Then a non-premixed diesel spray flame is established that initiates a premixed propagating natural gas flame. The natural gas flame propagates normal to the spray axis and down into the bowl region. A natural gas flame also travels into the squish region, but at a slower rate due to greater heat transfer. The increasing surface area of the natural gas flame causes the AHRR to increase at a steady rate.
2. At advanced injection timings, the increasing slope in the AHRR profile during the second combustion phase continues until all of the natural gas in the bowl region has been consumed, after which there is a sudden decrease in available natural gas/air mixture and a corresponding drop in the AHRR profile. This results in a triangular shaped pressure curve. The tail end of the AHRR profile is due to the natural gas flame traveling through the squish region as well as combustion of any remaining diesel fuel.
3. At retarded injection timings, expansion cooling slows down the natural gas flame as it approaches the bowl walls and as a result there is not a sudden change in available natural gas/air mixture. This creates an AHRR profile that rises and falls gradually with a hump

like shape. As the SOI timing becomes increasingly retarded, the flame can become quenched in both the bowl and squish regions during expansion.

4. A comparison between dual fuel and a diesel-only simulation showed that the presence of entrained natural gas within the spray results in a higher magnitude spike in AHRR at ignition. It also showed that during the second combustion phase, the diesel fuel contributes a relatively constant contribution to the total AHRR.
5. Premixed flames from adjacent sprays merge together creating a single flame surface with a cusp like crease where they meet. These flames first merge near the center of the cylinder and this crease in the flame surface travels outwards towards the bowl rim. Merging natural gas flames form a pocket of unburned natural gas along the crease between them that are located far from piston walls.
6. Uncontrolled fast combustion rates that lead to dual fuel engine knocking can be caused by the pockets of unburned gas between merging natural gas flames undergoing auto-ignition. These gas pockets experience auto-ignition before the gas near the walls due to lower heat transfer. Therefore the auto-ignition locations in a dual fuel engine under these operating conditions are confined between spray axes.
7. The lean natural gas flame leaves behind excess oxygen and exhaust products for the oxidizer side of the non-premixed diesel flame.
8. The dual fuel constant volume chamber spray simulations showed that when the natural gas equivalence ratio is high enough, the natural gas flame speed becomes faster than the diesel flame surface's speed at the front of the spray head and as a result the natural gas flame can propagate downstream of the spray head.

9. For lean natural gas mixtures, the natural gas flame leaves oxygen behind for the oxidizer side of the non-premixed diesel jet flame. This concentration of left over oxygen decreases as the natural gas equivalence ratio is increased and as a result the non-premixed flame in dual fuel combustion grows to a larger surface area with lower local heat release rate.
10. Diesel sprays into a natural gas/air mixture result in the entrainment of natural gas within the interior of the spray, which is then oxidized at the surface of the non-premixed flame.

While the simulations had overall good agreement with experiments, there are still some aspects that need improvement. For example, the model over predicted the magnitude of the AHRR during ignition for the larger injected masses. This error can be attributed to not having measured the rate shape or the injection duration and instead relying on literature. These injector characteristics need to be experimentally measured for the operating conditions investigated and incorporated into the model in order to more rigorously determine the model's accuracy. In addition, while the use of a RANS turbulence model does account for sub-grid TCI effects of increased diffusion rates, it does not account for commutation error between the cell averaged temperature and cell averaged reaction rate. Therefore, the model presented herein does include some degree of TCI error. However, the agreement with experimental pressure and AHRR suggests that the error from TCI effects must be small and the behaviors observed in the simulations are still valid. Finally, further work is needed to determine if the model can accurately predict engine exhaust measurements for NO_X, soot, CO, and unburned hydrocarbons.

CHAPTER 7: SENSITIVITY STUDY ON RCCI MODELING

7.1. Introduction

Engine manufacturers face increasingly stringent emissions regulations due to concerns over human health and the environment, specifically with regards to emissions of carbon monoxide, unburned hydrocarbons (UHC), particulate matter (PM), and nitric oxides (NO_X). Additionally, the U.S. Environmental Protection Agency (EPA) recently initiated regulations on greenhouse gases (GHG), such as carbon dioxide, and raised fuel efficiency standards for light duty vehicles by 2018 and heavy duty vehicles by 2025 [2] [3]. Therefore, engine designers are facing difficult challenges to meet emissions regulations and increase engine efficiency. One promising strategy that has received considerable attention over the years is low temperature combustion, wherein fuel premixed with excess air generates lower combustion temperatures and less nitric oxide compared to combustion of diesel sprays and stoichiometric spark ignited (SI) mixtures. Additionally, lean premixed combustion avoids the rich regions within diesel sprays where soot is formed.

Homogeneous charge compression ignition (HCCI) is a low temperature combustion method whereby compression heating of a lean premixed fuel air mixture in a high compression ratio engine initiates ignition reactions throughout the chamber nearly simultaneously. This method generates very fast combustion rates over a short duration yielding high efficiencies, but also limits the operating range and introduces difficulties in combustion phasing control. In recent years some of the obstacles of HCCI have been overcome by stratifying the charge mixture with two fuels of different reactivity, known as reactivity controlled compression ignition (RCCI). This strategy uses a homogenous premixed low reactivity fuel and stratification of a high

reactivity fuel via early direct injection. By stratifying the high reactivity fuel, ignition proceeds from areas of high mixture reactivity to areas of low reactivity, which lengthens the combustion duration, lowers the pressure rise rate and peak pressure, and allows for high loads to be achieved. Additionally, the load range can be extended by using a higher percentage of high reactivity fuel at low load and more low reactivity fuel at high load. Splitter et al. [19] were able to achieve high efficiency RCCI operation using gasoline and diesel in a heavy duty single cylinder engine between 4 and 14.5 bar IMEP while meeting EPA emission standards for NO_X without aftertreatment.

The use of natural gas for RCCI operation is advantageous for three reasons. Firstly, as shown by Nieman et al. [15], the difference in reactivity between natural gas and diesel is wider in comparison to that between gasoline and diesel. This allows for further lengthening of the combustion duration, which consequently allows for lower pressure rise rate, lower peak pressures, and extension to higher engine loads. Secondly, natural gas can produce less carbon dioxide than gasoline or diesel on an energy equivalent basis, because it is composed primarily of methane, which has a higher hydrogen to carbon ratio and a higher heating value. Thirdly, natural gas is expected to remain less expensive than gasoline or diesel on an energy equivalent basis for many decades to come [1]. Therefore, utilizing natural gas in RCCI combustion allows for a significant range of the operating map in a diesel engine to achieve higher efficiency with significantly reduced emissions and lower fuel cost.

Greater understanding of RCCI from multi-dimensional modeling is necessary to explore emissions formation and find optimal control strategies that can overcome the difficulties of combustion phasing and large pressure rise rate. Previous modeling work with gasoline/diesel RCCI has been used for optimization of injection strategies, fuel ratios, and exploring the effects

of EGR [19] [50] [51] [52]. Many of these simulations have used n-heptane as a single component surrogate for diesel fuel, which is based on the similar cetane number and heating value. However, previous modeling studies on natural gas/diesel RCCI are limited and have demonstrated additional modeling challenges due to the wider reactivity difference between diesel and natural gas. Nieman et al. [15] used reduced chemical kinetics in a multi-dimensional CFD simulation coupled with a genetic sorting algorithm to optimize natural gas/diesel RCCI operation over a wide range of speeds and loads, including 23 bar IMEP. The diesel fuel was modeled using single component fuel surrogates where n-heptane represented diesel fuel and the natural gas was modeled as pure methane. However, this study did not compare simulated pressure and heat release rates with experiments and so it is not possible to ascertain the accuracy of the model when using single component chemistry. Some of their modeling results showed two periods of increasing combustion rate separated by a period of constant combustion rate, while Doosje et al. [53] showed experimentally that the increase in combustion rate should be gradual and continuous. Dahodwala et al. [16] used multi-dimensional CFD to model natural gas diesel RCCI at 6 bar BMEP and investigate how the mixture changes as the percentage of natural gas is increased and understand the causes of high methane and CO emissions. This study also used n-heptane to model diesel fuel and methane to model natural gas. Their comparison between simulation and experiment showed that the CFD model predicted a noticeably steeper increase in heat release rate at the start of combustion than seen in experiment. The issue of overly fast combustion rate increase and pauses in combustion rate increase seem to be common issues for CFD simulations of natural gas/diesel RCCI. Puduppakkam et al. [52] showed that for gasoline/diesel RCCI using multi-component gasoline chemistry was able to achieve better agreement with the AHRR profile than using a single component. It is of interest to explore

whether a multi-component chemistry and vaporization model for diesel fuel and multi-component chemistry model for natural gas can reduce the sudden increase in AHRR at start of combustion as well as periods of near constant AHRR that separating two combustion events.

This study seeks to explore the difficulties and sensitivities associated with multi-dimensional CFD modeling of natural gas/diesel RCCI. Simulations are compared with experimental engine data acquired from a light duty diesel engine modified with port injection of natural gas. Comparisons are made between using single component and multi-component diesel surrogates for vaporization and chemistry. To this end an existing multi-component diesel reaction mechanism has been combined with a newly reduced mechanism for methane, ethane, and propane, resulting in a new reduced natural gas/diesel dual fuel mechanism. Then a parameter sensitivity study was performed to investigate which inputs have a significant effect on reducing the fast combustion rate at ignition in order to better match experiments. Parameters investigated include ratio of diesel components, injected mass, injected fuel temperature, time step controls, wall temperatures, initial turbulence, and a multi-zone chemistry model. Recommendations are given for many of these inputs.

7.2. Multi-component dual fuel mechanism

Natural gas and diesel combustion chemistry was modeled using reduced chemical kinetic mechanisms. In chapter 6 a reduced natural gas/diesel chemical mechanism was presented for dual fuel engines, which used n-heptane for diesel fuel and methane, ethane, and propane for natural gas. This mechanism, referred to as CSU141, is initially used to model RCCI combustion. The natural gas chemistry in CSU141 was reduced from the detailed methane through n-pentane mechanism from Healy et al. [37] at the National University of Ireland

Galway and is referred to as NUIGIII. The n-heptane chemistry in CSU141 was reduced from the detailed n-heptane mechanism from Curran et al. [38] [39]. Comparisons were then made between the single component n-heptane chemistry and a two component diesel surrogate. Recently Pei et al. [54] presented a reduced chemical kinetic mechanism for a two component diesel surrogate consisting of n-dodecane and m-xylene, which consisted of 163 species and 887 reactions, and will be referred to as LLNL163. In order to use the LLNL163 diesel mechanism in a dual fuel engine, the natural gas chemistry from CSU141 was added. This is shown schematically in Figure 7.1.

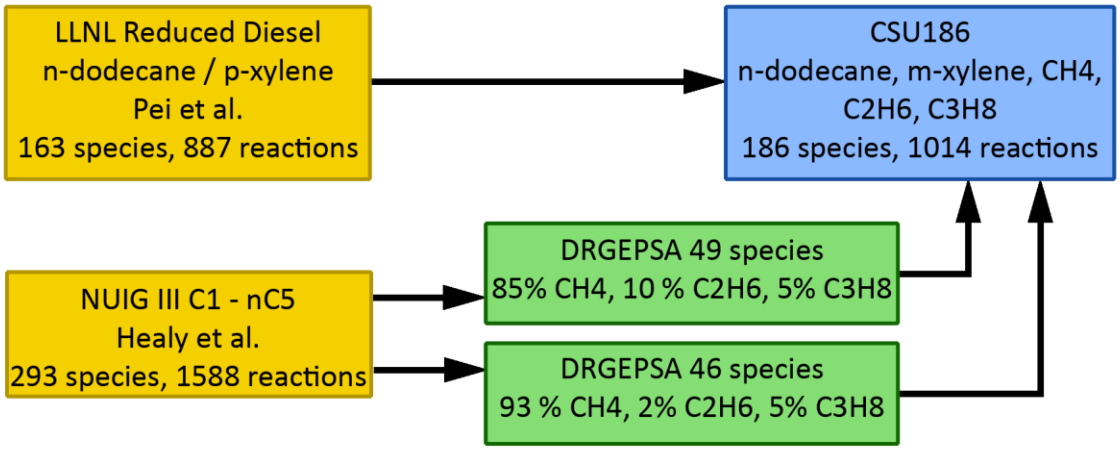

Figure 7.1. Schematic showing how the CSU186 multi-component dual fuel diesel and natural gas mechanism was formulated.

The natural gas chemistry consisted of two reductions of NUIGIII using the direct relation graph with error propagation and sensitivity analysis (DRGEPSA). The details of each reduction are listed in Table 7.1, where it can be seen that two different natural gas compositions were used in the reductions. These two reduced natural gas mechanisms were then appended to the LLNL163 diesel mechanism by adding any species not already in LLNL163. Reactions involving any of these additional species were then added. The result was a multi-component

mechanism for natural gas/diesel combustion consisting of 186 species and 1014 reactions, known as CSU186. This is a moderately large mechanism, but can still yield run times less than 24 hours.

Table 7.1. Conditions used for reducing the detailed natural gas mechanism using DRGEPSA.

Base Mechanism	NUIG III Natural Gas	NUIG III Natural Gas
Target species	CH4, C2H6, C3H8	CH4, C2H6, C3H8
Fuel composition (mole frac.)	X_{CH4} = 0.85, X_{C2H6} = 0.1, X_{C3H8} = 0.05	X_{CH4} = 0.93, X_{C2H6} = 0.02, X_{C3H8} = 0.05
Temperature (K)	800, 900, 1000, 1100, 1200	800, 900, 1000, 1100, 1200
Pressure (bar)	20, 30, 40, 50, 60, 70, 80	20, 30, 40, 50, 60, 70, 80
Equivalence ratio, φ	0.2, 0.4, 0.6, 0.8, 1.0, 1.2, 1.4	0.2, 0.4, 0.6, 0.8, 1.0, 1.2, 1.4
Ignition delay error tolerance	0.1	0.1
Sensitivity analysis fraction	0.5	0.5

Figure 7.2 shows comparisons of computed ignition delay period between the CSU186 mechanism and the LLNL163 base mechanism for a diesel surrogate mixture of 70% n-dodecane and 30% m-xylene at lean and stoichiometric equivalence ratios. The excellent agreement across the range of temperatures and pressures demonstrates that the behavior of the n-dodecane and m-xylene chemistry from LLNL163 has been retained after addition of the natural gas chemistry.

A similar ignition delay comparison between the reduced CSU186 mechanism and the detailed NUIGIII natural gas mechanism is shown in Figure 7.3 for an equivalence ratio of 0.5 at two different natural gas compositions. One is a mixture of 90% methane, 6.7% ethane, and 3.3% propane and the other is a mixture of 70% methane, 20% ethane, and 10% propane. A similar ignition delay comparison between the reduced CSU186 mechanism and the detailed NUIGIII natural gas mechanism is shown in Figure 7.3 for an equivalence ratio of 0.5 at two different natural gas compositions. One is a mixture of 90% methane, 6.7% ethane, and 3.3%

propane and the other is a mixture of 70% methane, 20% ethane, and 10% propane. Close agreement between

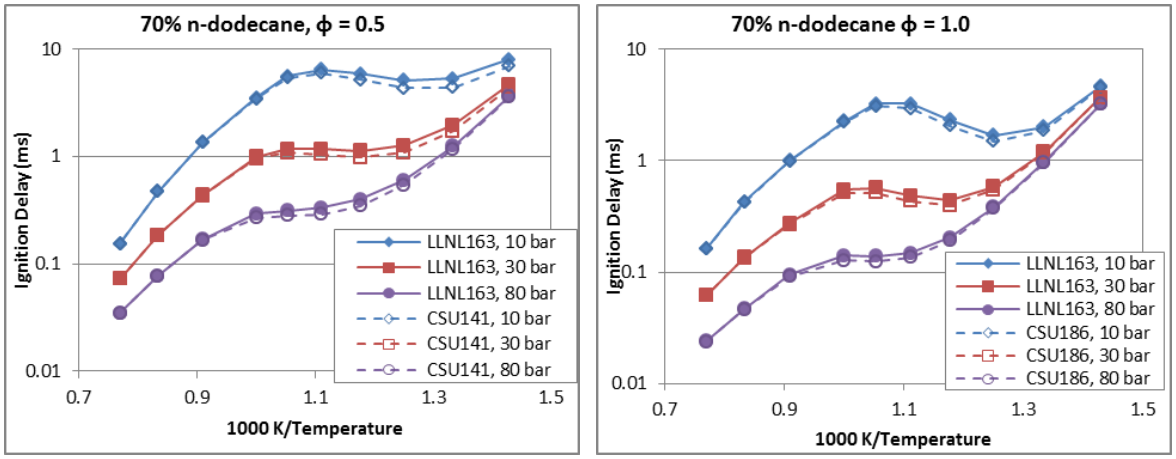

(a) (b)

Figure 7.2. Zero-dimensional adiabatic ignition delay calculations comparing the dual fuel reduced CSU186 to the base LLNL163 mechanism for a diesel surrogate of 70% n-dodecane / 30% m-xylene at (a) φ = 0.5 and (b) φ = 1.0.

the two mechanisms across a range of pressures and temperatures shows that the reduced mechanism can replicate the behavior of the detailed mechanism at engine top dead center (TDC) conditions for different natural gas compositions.

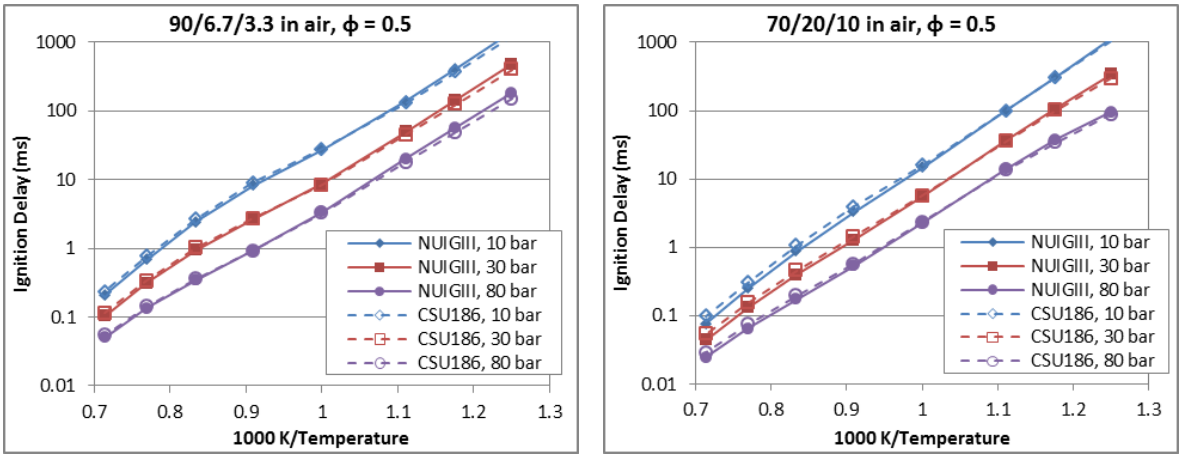

(a) (b)

Figure 7.3. Zero-dimensional adiabatic ignition delay calculations comparing the reduced dual fuel CSU186 mechanism to the detailed NUIG base mechanism for (a) the 90/6.7/3.3 natural gas mixture and (b) the 70/20/10 mixture.

7.3. Computational Details

For the multi-component diesel surrogate, the liquid properties were represented by a mass averaged mixture of n-dodecane and m-xylene and each liquid component vaporized into its respective gas phase species. The CSU186 mechanism was then used for the chemistry calculations. For the single component n-heptane model, the liquid phase was modeled using the physical and thermodynamic properties of diesel fuel obtained from the CONVERGE™ liquids property library and the CSU141 mechanism was used to model the chemistry. For both diesel models, the natural gas was represented by a mixture of methane, ethane, and propane that matched the composition from a gas sample.

7.4. Engine Experiments

The experimental operating conditions are listed in Table 7.2. A simple injection timing sweep at 8.8 bar net IMEP and 2000 rpm using a single diesel injection was performed while keeping the fuel masses constant. Two methods for determining the injected diesel fuel mass are presented. The total fuel consumption of the engine as measured by the Coriolis mass flow meters could be split evenly among the four cylinders to get an average diesel mass per cylinder per cycle. Additionally, during the process of measuring the rate shapes for each injector on the rate tube apparatus, the volume flow rate was measured using an AVL PLU131. This allowed for an injector specific characterization table to determine the injected mass. The difference between the two measurements is thought to be due to differences in mass flow between injectors when averaging the total fuel consumption and uncertainty in fuel density from uncertainty in fuel temperature.

Table 7.2. Experimental operating conditions.

Fuel case name	D4G14		
Diesel per cylinder from on engine flow meters (mg)	5 ± 2		
Diesel per cylinder from injector characterization (mg)	3.5 ± 1		
Natural gas per cylinder (mg)	13.5		
Natural gas energy share (%)	78.7		
Engine speed (RPM)	2000		
Diesel injection pressure (bar)	700		
Injection duration (ms)	0.4		
Commanded start of injection (°ATDC)	-46	-48	-52
Boost pressure (kPa abs)	141.1	141.8	141.0
Manifold temperature (°C)	37.5	38.8	38.7
Air mass per cylinder (mg)	617.8	623.2	623.2
Net IMEP (bar)	8.77	8.81	8.72
BMEP (bar)	4.5	4.5	4.5
NOx (ppm)	220	131	75

7.5. Experimental Results

The experimental pressure and AHRR plots for the injection timing sweep are shown in Figure 7.4. As injection timing is advanced the combustion phasing retards, there is less low temperature heat release, and the combustion duration increases. Computational modeling was then applied to the -46° ATDC injection timing case which had the most advanced combustion phasing. Initially, the amount of injected diesel fuel used in the model was chosen to be between the two measurements with a value of 4.2 mg per injection or 0.6 mg per injector nozzle.

7.6. Single Component Diesel Model

The simulation results using n-heptane chemistry from CSU141 to represent diesel fuel is compared against experimental pressure and AHRR in Figure 7.5. The phasing of low temperature heat release (LTHR) is slightly later in comparison to experiment, but the start of the high temperature heat release is in close agreement. However, there is a significant difference in

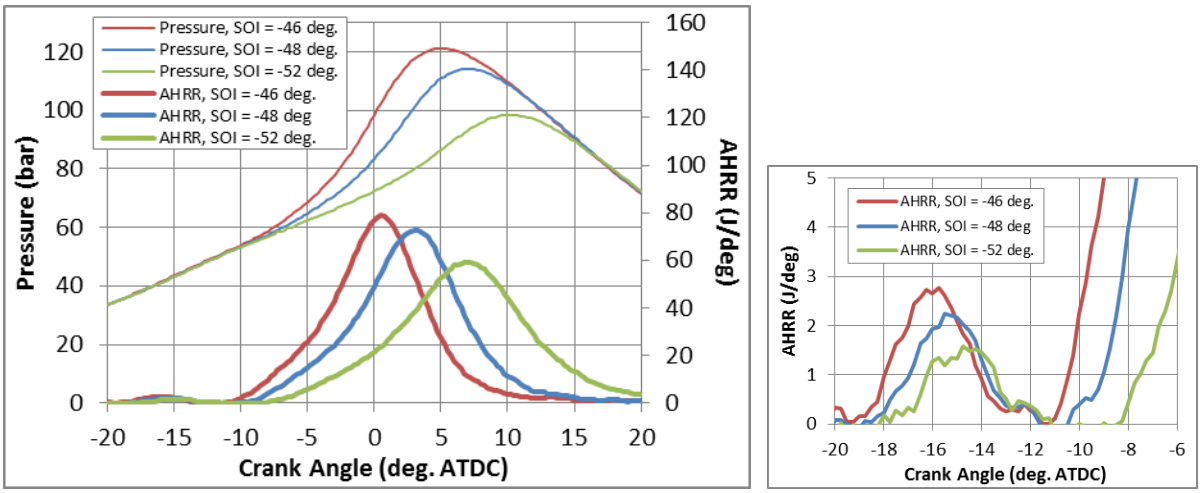

Figure 7.4. Experimental pressure and heat release rates for the SOI timing sweep.

the rate of change in the AHRR profile at the start of combustion with the simulation predicting a large and fast rise in AHRR while the experiment rises much more gradually. After the initial fast combustion rate, the heat release peaks, decreases slightly and remains constant, and then continues to rise to a peak that is close the experimental peak AHRR. After the maximum peak AHRR, the gradual decrease in AHRR during the second half of the combustion duration is well captured by the simulation. The simulated AHRR profile therefore shows two distinct combustion events separated by a local minimum, while the experimental shows a single smooth combustion event. The fast initial rise in AHRR and two peak behavior could not be eliminated with further tuning of such parameters as injected mass, exhaust residual mass, wall temperatures, turbulent kinetic energy, or swirl ratio. The initial fast rise is due to a large simultaneous ignition of a high reactivity region where n-heptane is concentrated. This indicates that the single component chemistry cannot produce a gradual gradient in reactivity. A multi-component vaporization and chemistry model for the diesel fuel may help to model a smoother transition in mixture reactivity.

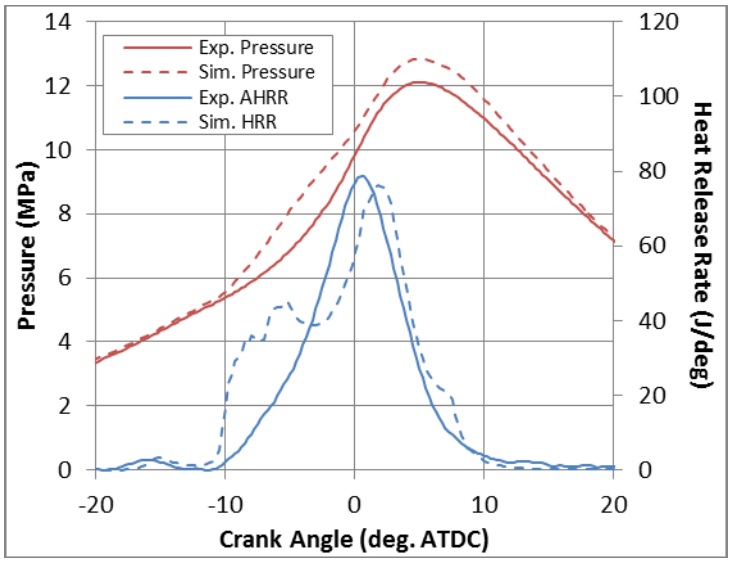

Figure 7.5. Comparison between experimental and simulated pressure and AHRR for the SOI = -46° ATDC case when the single component n-heptane chemistry is used to model diesel fuel.

7.7. Multi-component Vaporization and Chemistry Diesel Model

The comparison between the experiment and the simulation using the multi-component vaporization and chemistry model using the newly combined CSU186 mechanism is shown in Figure 7.6 along with the single component diesel simulation from Figure 7.5. Other than the chemical mechanism and diesel fuel surrogate, all other models inputs are identical. Comparing the two simulations with experiment shows that the multi-component diesel model was able to significantly reduce the delay time during the local minimum and eliminate the widely separated two peak behavior, resulting in an AHRR profile with a more continuous rise. Additionally, the rate of increase in AHRR at start of combustion is reduced with the multi-component surrogate, but still much faster than seen in experiment. Also, the maximum AHRR is greater than in experiment, which yields a higher peak pressure. Thus, the multi-component model was able to more closely predict the single peak shape of the experimental AHRR than the single component model, but could not eliminate the fast rise at ignition.

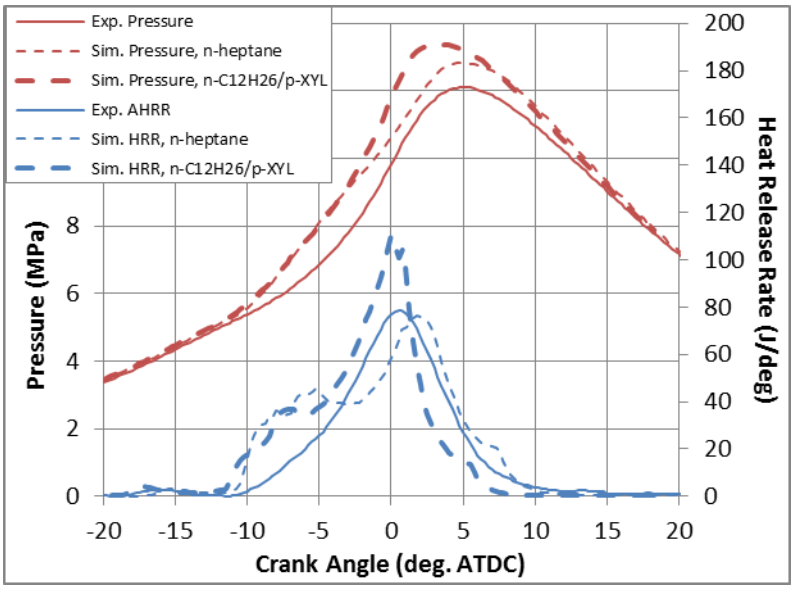

Figure 7.6. Comparisons between the SOI = -46° ATDC experimental pressure and AHRR with both the single component n-heptane diesel model and the n-dodecane/p-xylene diesel model.

A comparison between the two diesel models using in-cylinder imaging of the equivalence ratio in a clip plane along the squish surface of the piston just prior to combustion is shown in Figure 7.7. It can be seen that the direct injected diesel fuel is more spread out in the case with the multi-component vaporization model, which creates a more gradual reactivity gradient. Also the single component model has a larger rich region located near the liner wall. This larger volume of high reactivity mixture releases more energy upon ignition, thereby causing the larger rise in AHRR.

The difference in location of the rich regions in Figure 7.7 leads to different locations for the onset of high temperature heat release (HTHR) reactions. This is demonstrated in Figure 7.8, which shows the time evolution of a 30 W/mm^3 HRR iso-surface. The first image shows that the HTHR reactions begin near the liner wall in the single component diesel model, but begin in the center of the squish region in the multi-component model. As a result, the iso-surface in the multi-component diesel simulation reaches the fuel in the bowl region first, which causes a more

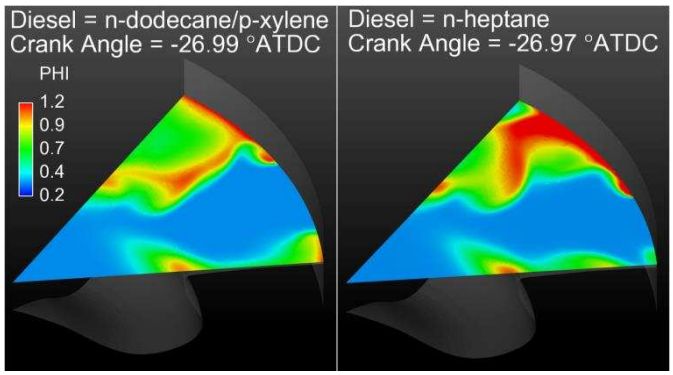

Figure 7.7. Clip plane showing equivalence ratio at -27° ATDC and comparing the multi-component diesel model with the single component model.

gradual change in global AHRR. Also the reaction zone travels faster in the bowl region in the multi-component model as evidenced by the larger change in the iso-surface between -6° and -2° ATDC. Therefore, the long pause in combustion rate near the local minimum in the AHRR profile for the single component case is due to the longer time it takes for the combustion zone to consume the fuel in the bowl region.

7.1. Sensitivity Study of Input Parameters

7.1.1. Ratio of n-dodecane to m-xylene

A parameter study was then carried out to assess which inputs the model is highly sensitive to and would alter the magnitude of the AHRR profile to more closely match experiment. For these parameter studies the base case used for comparison is the multi-component diesel simulation presented in Figure 7.6. The first parameter investigated was the effect of changing the ratio of n-dodecane to m-xylene in the diesel surrogate. Figure 7.9 presents a comparison between the base case simulation, which had a 70% n-dodecane / 30% m-xylene split, with a 65% / 35% split and a 60% / 30% split. For the 65% n-dodecane simulation, Figure 7.9 shows little differences at the start of combustion, but later demonstrates a more retarded phasing of the

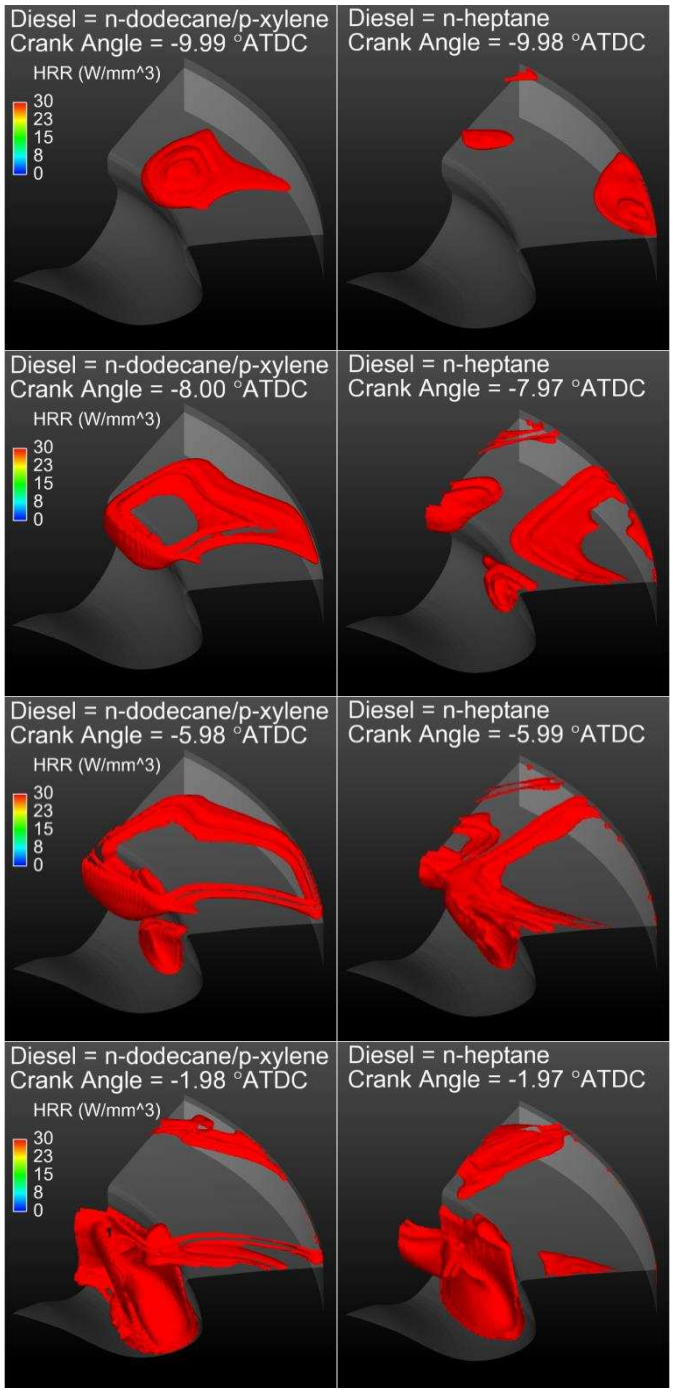

Figure 7.8. Comparisons of HRR iso-surfaces of 30 W/mm3 between the multi-component and single component models.

maximum AHRR. The 60% n-dodecane case shows a more dramatic retarding of combustion phasing, but the two peak behavior is less pronounced. Also the 60% n-dodecane case more closely matches the AHRR profile during the low temperature reactions. Therefore, 5% changes

to the diesel component ratio can shift combustion phasing slightly, but changes of 10% can change phasing significantly.

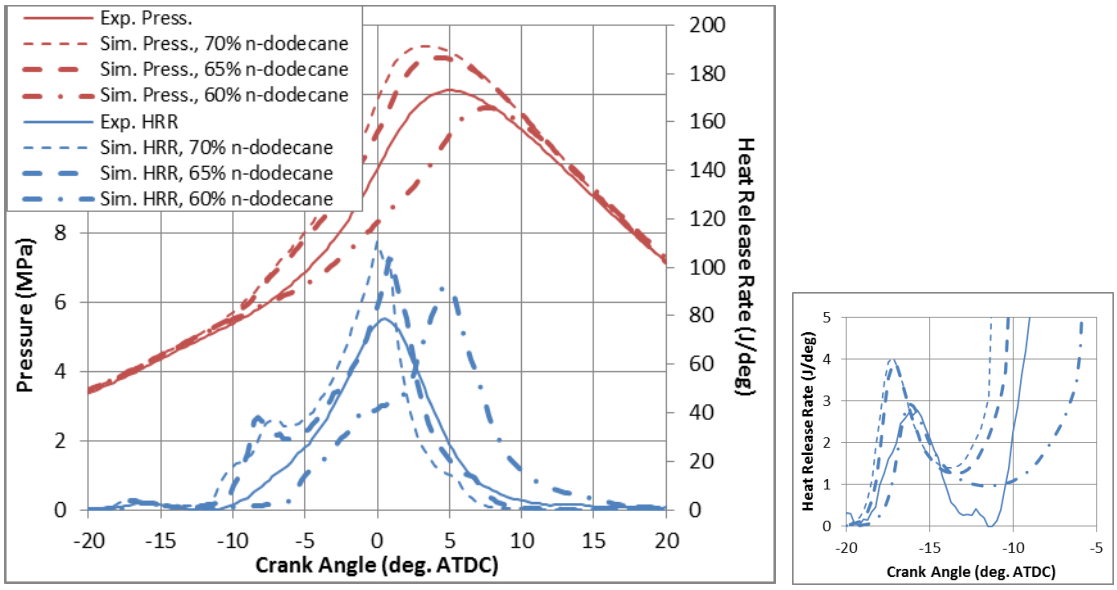

Figure 7.9. Comparison between experimental and simulated pressure and HRR as the ratio of n-dodecane to m-xylene is varied from 70% to 60% n-dodecane. Experimental data is from the SOI = -46° ATDC case.

In order to investigate how the combustion phasing changed with the split in diesel components, in-cylinder images from the three simulations in Figure 7.9 are compared in Figure 7.10, which shows a clip plane colored by equivalence ratio just prior to start of combustion at -12° ATDC. From these images it can be seen that as the percentage of n-dodecane is reduced, the region of near stoichiometric mixture becomes smaller, indicating greater dispersion of the injected fuel. Greater fuel dispersion with increasing m-xylene should be expected, because m-xylene is more volatile than n-dodecane. The more dispersed fuel distribution in the 60% n-dodecane case results in a more gradual reactivity gradient and explains the slower rising AHRR profile.

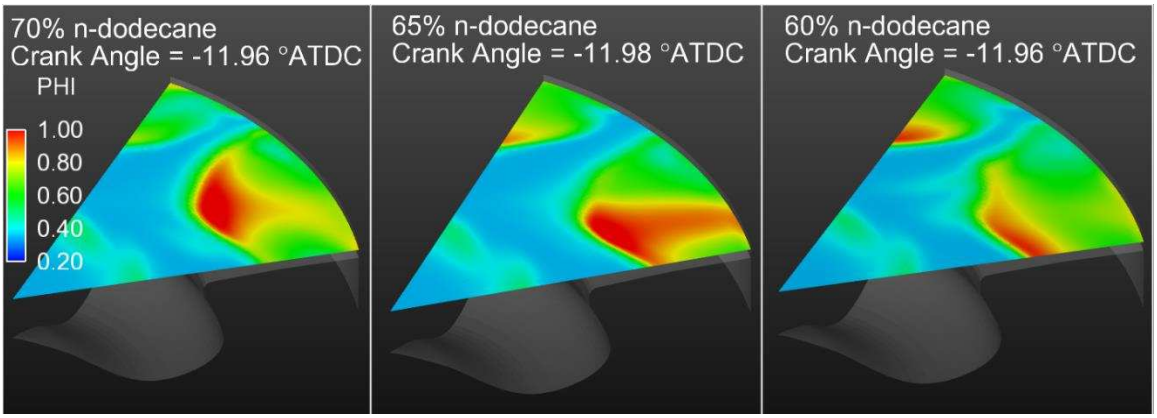

Figure 7.10. Comparison of equivalence ratio distribution just before ignition between the different diesel fuel ratios.

7.1.2. Injected mass

Figure 7.11 shows a comparison between the base case where 0.6 mg of diesel per nozzle was injected and a case where 0.5 mg per nozzle is injected. The 0.5 mg is equal to the amount measured during the injector characterization, while the 0.6 mg is closer to that measured by averaging the fuel consumption across all injectors. The peak pressure agreement is a closer match with experiment. Also, the phasing of the maximum AHRR is a closer match to experiment. The start of combustion timing is equivalent to the base case simulation, but the slope in AHRR is nearly vertical with a larger increase. In-cylinder images from the simulations can be used to investigate the cause for the large increase in AHRR at ignition. Figure 7.12 compares the two cases using a stoichiometric equivalence ratio iso-surface just prior to ignition. The 0.5 mg case has a larger volume of gas with an equivalence ratio greater than stoichiometric in comparison to the 0.6 mg case. This larger volume of stoichiometric mixture will release more energy upon ignition and explains the behavior seen in the AHRR profiles. Therefore, the 0.5 mg case has a fuel distribution that is not as well mixed.

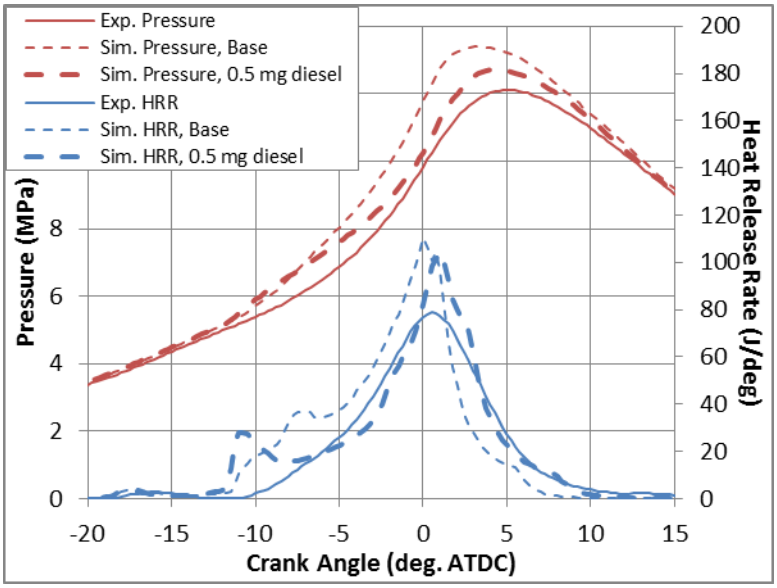

Figure 7.11. Comparison between experimental data and simulations showing the effect of decreasing the injected diesel mass. The base case has an injected mass of 0.6 mg per nozzle, while the other case has 0.5 mg per nozzle.

Figure 7.12. Iso-surface of φ = 1.0 comparing simulations of different injected mass.

7.1.3. Injection Velocity

The injection velocity can be raised by lowering the discharge coefficient. Figure 7.13(a) and (b) compare the injection velocity and injection pressure profiles between the base simulation with one that has had the discharge coefficient lowered from 0.86 to 0.8. The peak injection velocity increases from 373 m/s to 400 m/s, an increase of about 7%. The peak injection pressure has increased by about 16% from 500 bar to 580 bar.

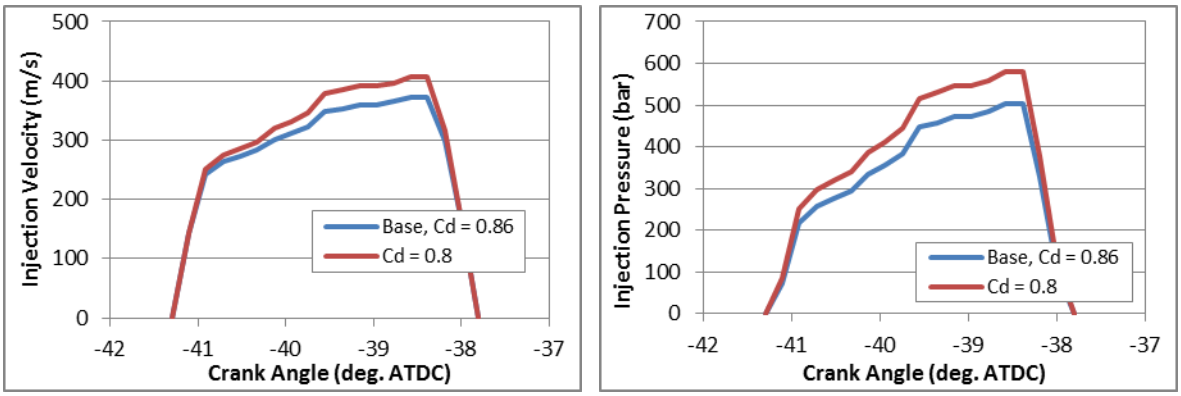

(a) (b)

Figure 7.13. (a) Calculated injection velocity profiles between different discharge coefficients and injector nozzle diameters. (b) Calculated injection pressure profiles between different discharge coefficients and injector nozzle diameters.

Figure 7.14(a) compares the base simulation with the simulation using the lower C_D value. The lower discharge coefficient is able to retard start of combustion and leads to a slower increase in combustion rate at ignition. There is still a fast combustion at the beginning of the combustion duration, but it is smaller in magnitude. While the maximum AHRR is still over predicted, the value of the AHRR profile during the rising and falling portions more closely matches the experimental AHRR profile in comparison to the base simulation. Consequently, the pressure curves are more closely matched, with better agreement in pressure rise rate and peak pressure. Therefore, a small increase in injection velocity has resulted in a significant improvement in matching experimental AHRR. The injection velocity profile is therefore an important boundary condition to have accurately defined.

While the results in Figure 7.14(a) appear to more accurately represent the in-cylinder physics, inspection of the spray in the simulation demonstrated non-physical behavior. The left side image in Figure 7.15 shows the parcels from the simulation in Figure 7.14(a) during the middle of the injection duration colored by droplet diameter. The lower C_D case is predicting a non-physical result where injected parcels equal to the orifice diameter are completely broken up

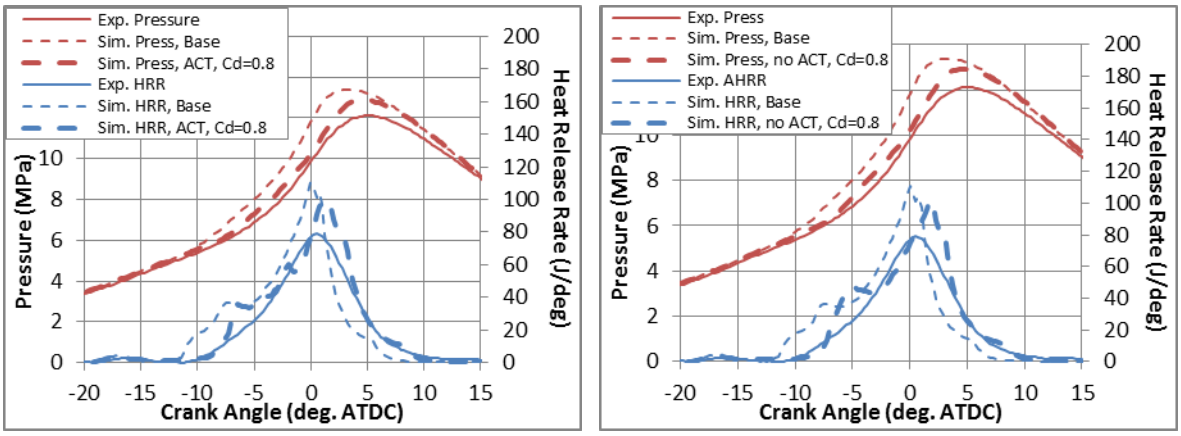

(a) (b)

Figure 7.14 (a) Comparison between the base simulation and one with a lower injector C_D of 0.8 while using the KH-ACT model. (b) Comparison between the base simulation and one with C_D = 0.8 and not using the KH-ACT model. The base simulation uses the KH-ACT model and has C_D = 0.86.

into very small droplets within the first two computational cells. This causes a very long and thin liquid phase, which does not agree with experimental images of diesel sprays [47]. Further simulation work revealed that the KH-ACT model of Som and Aggarwal [27], which includes initial disturbances in the KH model due to cavitation and turbulence, was responsible for this non-physical behavior. Therefore, the simulation was repeated using the standard KH model instead of the KH-ACT model and the results are shown in Figure 7.14(b). Removing the KH-ACT model resulted in nearly the same pressure and AHRR curves as in Figure 7.14(a). However, the spray parcels in this simulation, as shown on the right side of Figure 7.15, exhibit a much wider liquid phase with a smoother distribution of droplet diameter, which is in agreement with experimentally observed sprays. Inspection of the base case showed a similar parcel distribution the one shown in the right side of Figure 7.15. Therefore, when lowering the discharge coefficient to raise injection velocity it is also necessary to remove the KH-ACT model.

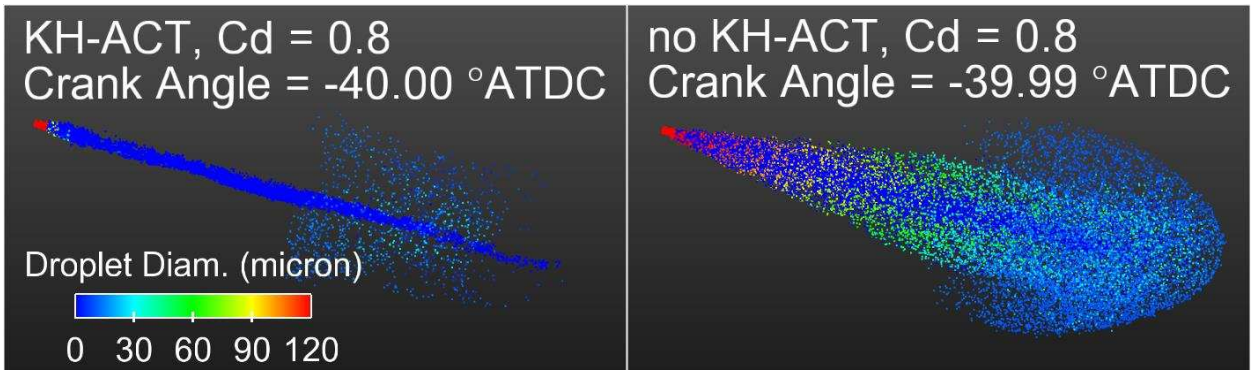

Figure 7.15. Comparison of spray parcel behavior colored by droplet diameter between using and not using the KH-ACT model with C_D = 0.8.

By comparing the fuel distributions prior to ignition between the base simulation and the lower discharge coefficient case without the KH-ACT model, the causes for the different combustion behavior can be deduced. This is shown in Figure 7.16 where a clip plane through squish region is colored by equivalence ratio. The case with higher injection velocity has a more spread out fuel distribution and covers more of the volume in the squish region. This can be attributed to the spray impacting the piston squish surface early and therefore having more time to spread out and mix. It also does not have a large region with $\varphi > 1$, which helps explain why ignition occurs later than the base case.

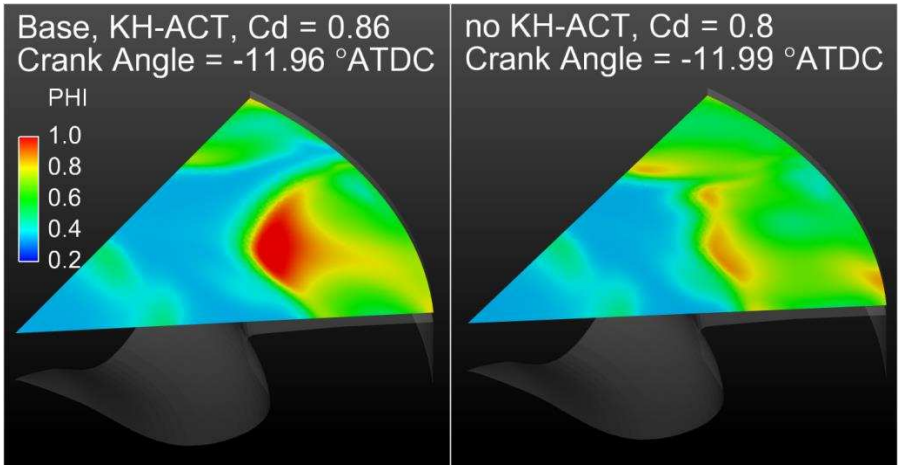

Figure 7.16. Comparison of equivalence ratio distribution just before ignition between the different injection velocity methods.

7.1.4. Multi-zone Chemistry

The sudden combustion rates at ignition seen in the simulations thus far can be affected by such numerical methods as the multi-zone chemistry strategy, the species convergence tolerance for the chemistry solver, and the time step size. The effects of the multi-zone chemistry method will be investigated first. Figure 7.17(a) shows a comparison between the base simulation and another simulation where the multi-zone chemistry has been turned off. By comparing these two simulations the accuracy of the multi-zone method can be analyzed. The absence of the multi-zone chemistry solver causes the start of combustion to retard about 2 crank angle degrees and the maximum in AHRR to retard about one crank angle. The in-cylinder images in Figure 7.18 shows an equivalence ratio iso-surface of $\varphi = 0.9$, which indicates that the mixture distribution of injected fuel is spread out to a greater extent when the multi-zone chemistry has been removed. The greater extent of mixing causes a reduction in maximum equivalence ratio and therefore explains the slightly retarded combustion phasing. It is uncertain how removing the multi-zone chemistry method could affect the distribution of fuel, but one possible explanation could be different species gradients from the multi-zone chemistry causes the species based AMR to refine the grid differently. Variations in the grid refinement near the fuel vapor boundary can cause different exchange rates in the transport equations. While the differences in the pressure and AHRR curves are not dramatic, this result demonstrates how sensitive the fuel distribution can be to model inputs, which makes RCCI modeling challenging.

An attempt was made to develop a multi-zone strategy that had close agreement with the simulation without multi-zone. Figure 7.17(b) presents a comparison between the simulation without multi-zone to a simulation using a revised multi-zone strategy, which is described in Table 7.3. Comparing the two multi-zone methods in Tables 1 and 6 shows that the intermediate

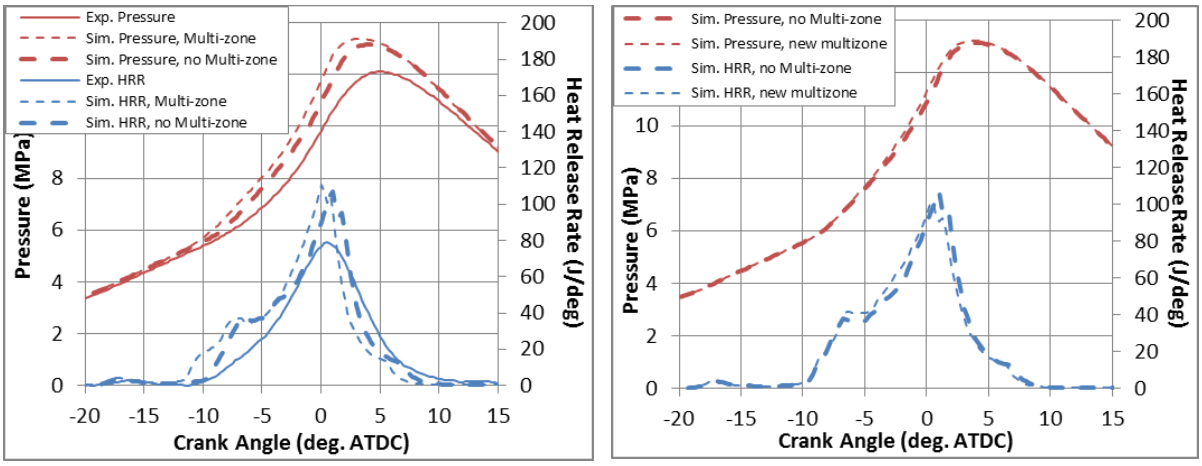

(a) (b)

Figure 7.17 (a) Comparing the base simulation with one where the multi-zone chemistry solver is turned off. (b) Comparing the simulation without multi-zone with a simulation with a revised multi-zone strategy.

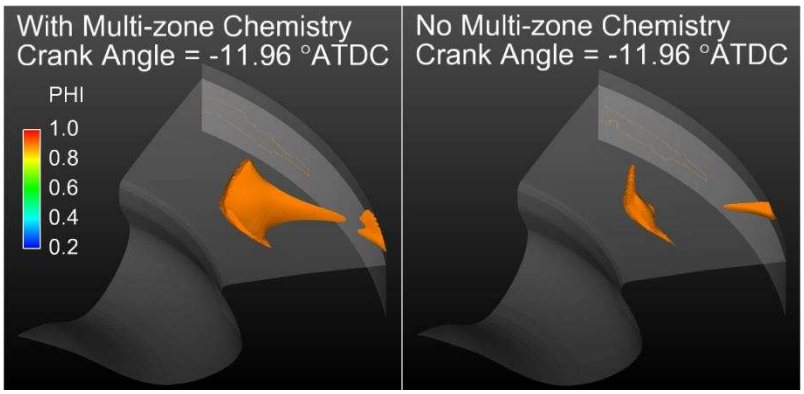

Figure 7.18. Equivalence ratio iso-surface of φ = 0.9 comparing the base simulation with one without multi-zone chemistry.

species C12H25O2-2, which is important in low temperature chemistry, has been replaced by OH and the species bin sizes have been reduced. The updated multi-zone method provides a nearly identical match to the simulation without multi-zone. Therefore, the multi-zone strategy in Table 6 should be used in future RCCI simulations.

Table 7.3. A revised multi-zone chemistry strategy.

Multi-zone bin: temperature (K)	5
Multi-zone bin: progress φ	0.001
Multi-zone bin: n-C12H26 mass fraction	0.0001
Multi-zone bin: m-xylene mass fraction	0.0001
Multi-zone bin: HO2 mass fraction	0.0001
Multi-zone bin: OH mass fraction	0.0001

7.1.5. Chemical Time Step Limit and Species Convergence Tolerance

There is a chemistry time step control parameter in CONVERGE™ that allows for the time step to be limited by a maximum change in temperature of a cell, called *mult_dt_chem* and defined as,

$$dt_{chem} = dt_{prev} \min\left[\frac{T}{\Delta T}\right] mult\_dt\_chem \tag{7.1}$$

where dt_{prev} is the previous time step, dt_{chem} is the new time step, T is the cell temperature, and ΔT is the change in temperature during the time step. In the base case, *mult_dt_chem* was set to 0.5 meaning the cell temperature could not change by more than 50% in a single time step. This maximum change in temperature was decreased to 10% to see how it affects the ignition, which is presented in Figure 7.19(a). The use of a smaller time step based on temperature change did not significantly affect the AHRR profile. Therefore, setting *mult_dt_chem* to 0.5 is appropriate for RCCI combustion.

The chemistry solver uses an absolute and relative species concentration tolerance to determine convergence. Some species during combustion are present in low concentrations but the accuracy of their concentration can have a significant impact on the overall combustion rate. Therefore, if the absolute convergence tolerance is too large then certain small concentrations could be in error and cause error in the global combustion rate. To investigate this effect, the base simulation was compared to a simulation where the absolute species convergence tolerance,

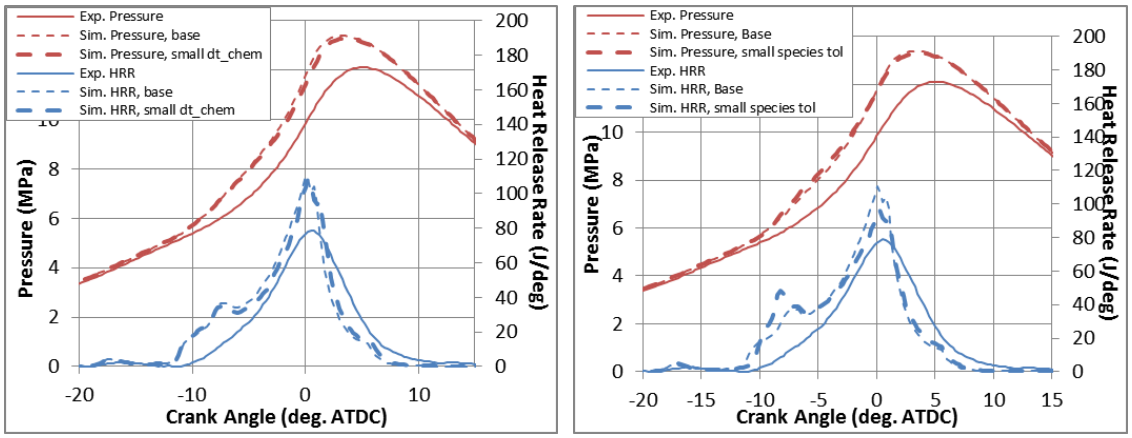

(a) (b)

Figure 7.19. (a) Comparison between the base simulation and one where the time step size only allows a 10% increase in temperature. (b) Comparison between the base simulation and one where the absolute species convergence tolerance has been decreased from 1E-15 to 1E-18.

known as *sage_abs_tol* in CONVERGE™, was reduced from 1E-15 to 1E-18. This comparison is shown in Figure 7.19(b), which shows that the majority of the AHRR profile is largely unaffected and the pressure curves are nearly indistinguishable. Therefore, using a smaller absolute species convergence tolerance can eliminate a small degree of error, but is not necessary.

7.1.6. Summary of chemistry solver parameters

A summary of the findings from the sections investigating errors related to the chemistry solver are presented in Table 7.4. Each of the parameter changes reduced error that already existed in the base simulation. The use of a smaller time step limit based on change in cell temperature did not reduce the error and added a significant amount of computational cost. Therefore the *mult_dt_chem* parameter should remain at 0.5. The absence of the multi-zone chemistry solver had the largest compute time, but also had the largest reduction in start of combustion error. However, the error reduction was only 2 crank angle degrees and the overall

combustion behavior was not different. Therefore, removing the multi-zone chemistry method does not justify doubling the compute time, especially because other parameters can be used to offset this error, such as wall temperatures. Increasing the absolute species convergence tolerance does not remove very much error, but also does not add a significant amount of compute time. Therefore, an intermediate value of 1E-16 should reduce some error and not add a large computational cost.

Table 7.4. Compute times and SOC phasing errors relative to the base simulation for chemistry solver parameters.

Chemistry Solver Parameter Change	Compute Time (hours)	Reduction in SOC error (crank deg.)
Base: mult_dt_chem=0.5, sage_abs_tol=1E-15, multi-zone	19.6	NA
mult_dt_chem = 0.1	31.1	0
No multi-zone chemistry	39.0	2
sage_abs_tol = 1E-18	21.5	1

7.1.7. Wall Temperatures

Measurements do not exist for the piston and head temperatures. Furthermore, the wall temperatures are not constant throughout the compression and combustion and nor are they uniform in value. Therefore, the constant and uniform cylinder wall temperatures are often tuned to get better agreement. This is especially true for RCCI, because the injected fuel is primarily located in the squish region where the walls are in close proximity to where combustion reactions begin. To investigate the sensitivity of the model to wall temperatures, the base simulation was compared to one where the piston and head temperatures were lowered by 30 K. This comparison is made in Figure 7.20, which shows the start of combustion and the location of maximum AHRR has retarded one crank angle degree, while the shape of the HRR remains relatively unchanged. Therefore, piston and head temperatures can be used to tune for small

changes in combustion phasing without sacrificing the general behavior seen in the AHRR profile and should be able to offset small errors from other sources.

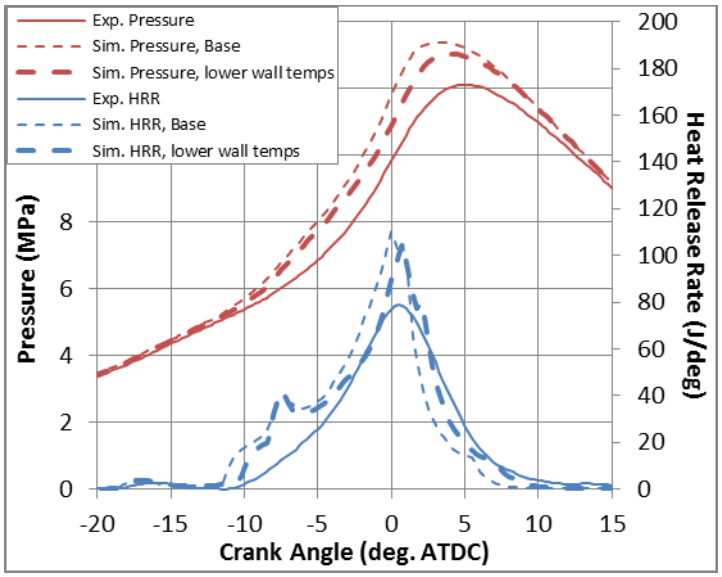

Figure 7.20. Comparison between the base simulation and one where the piston and head temperatures have been decreased by 30 K.

7.1.8. Interpretations from Sensitivity Study

The sensitivity study performed thus far has shown that the results are highly sensitive to the ratio of diesel surrogate components, the multi-zone strategy, the injection velocity, and the injected mass. The sensitivity of the results on the injection velocity brings into question the method that should be used to determine the injection velocity profile. The injector discharge coefficient is measured with the needle fully open and at steady state injection rate. A comparison of measured rate shapes between the one used in this experiment and one for a longer injection duration at the same rail pressure is made in Figure 7.21, which have been normalized by the maximum value for the long duration. The short duration rate shape used in this experiment does not reach the steady state value where the discharge coefficient was measured to be 0.86. In addition, since the measured rail pressure was 700 bar, then the peak

calculated steady state injection pressure for the longer duration case in Figure 7.21 should be equal to the pressure difference between the rail and the cylinder pressure or about 650 bar. Since the peak normalized injection rate for the short duration is about 82% of the steady state rate, then the peak calculated injection pressure should be about 82% of 650 bar or 530 bar. Therefore the discharge coefficient should be adjusted until the injection pressure is 530 bar and the resulting injection velocity should be used.

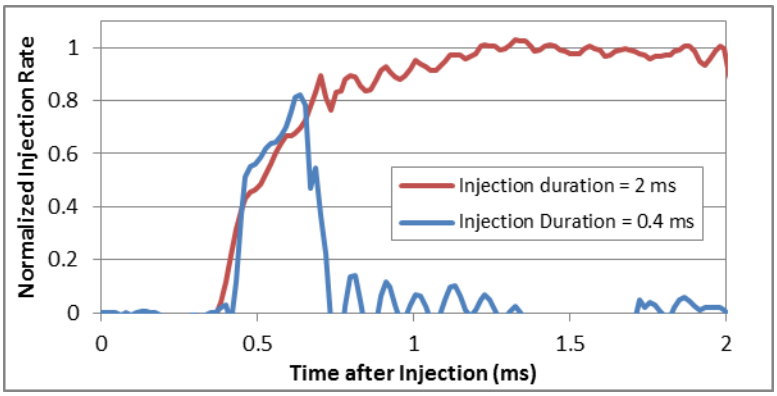

Figure 7.21. Comparison of the experimental rate shape with another one where the injection duration is much longer. The rate shapes have been normalized by the steady state injection rate.

Reducing the injected mass within experimental uncertainty also showed closer agreement with the experimental data, but had a larger amount of energy released at the start of combustion as shown by the vertical line in the simulated heat release in Figure 7.11. Figure 7.12 showed that this was due to a larger volume of rich mixture. One explanation for the reduced mixing when using reduced injection mass is the resulting reduction in injection velocity when all other injection parameters are held constant. This is supported by the results from the injection velocity comparisons, which demonstrated a larger rich mixture volume in the base case where the injection velocity was lower. Therefore, the injection velocity should be increased whenever using reduced injection mass in order to avoid a large volume of rich mixture. More specifically

for this experiment, the injection velocity should be raised by lowering the discharge coefficient until the peak injection pressure is 530 bar as previously discussed. The method is explored in the next section.

The major sources of error not accounted for in this model are the turbulence-chemistry interactions that are absent in a RANS type turbulence model and the reactivity of real diesel fuel, due to using only two species as a surrogate. TCI effects slow down combustion rates from inhomogeneity in the turbulent structure. Using reduced injection mass can reduce the energy released during auto-ignition at each location and therefore can compensate for TCI error. Having more species to represent diesel fuel would promote a slower release of energy at each location as the most reactive species will oxidize and release energy first, which agrees with the experiments of Splitter et al. [55]. Also, the different diffusion rates of the various species in real diesel fuel can spread out the reactivity gradient and lead to a more gradual transition in auto-ignition location. This would result in a more gradual rise in heat release as seen in experiment. The injection velocity comparison showed a smoother distribution of equivalence ratio with higher injection velocity. However, if the injection velocity is too high it may create excessive mixing leading to a large volume that is leaner, but more homogeneous. A more homogeneous mixture will release energy simultaneously rather than in the sequential fashion characteristic of RCCI. Therefore, using reduced injection mass to reduce the energy released at each location and an optimal injection velocity to create smoother changes in mixture reactivity might be a viable way to compensate for TCI errors and diesel surrogate errors.

7.2. Improved Simulation Result for SOI = -46° ATDC

An improved model for the SOI = -46° ATDC case was performed using the information gained from the sensitivity analysis and is compared with experimental data in Figure 7.22. The injected mass was set to 0.5 mg per injector, which is the mass measured during the injector characterization using the rate tube measurements and represents the low end of the uncertainty range. A target peak injection pressure of 530 bar was used due to the reasons given in the discussion of Figure 7.21. This required a reduced discharge coefficient of 0.7. A 70% n-dodecane / 30% m-xylene diesel surrogate is used here because this mixture seemed to have good agreement with start of combustion phasing in the base simulation. Also, the sub-grid scale tolerance for temperature and velocity AMR was reduced to 0.5 K and 0.1 m/s respectively. The improved multi-zone strategy is utilized. This simulation took approximately 20 hours to compute using 48 cores. There is still a larger increase in combustion rate at ignition than seen in experiment, but the magnitude has been significantly reduced in comparison to the single component model from Figure 7.5 and the rate of increase is more gradual compared to the base case multi-component model used for the sensitivity study in Figure 7.6. The maximum AHRR is in much closer agreement with experiment than the base case. The phasing of start of combustion is well predicted and the phasing of maximum AHRR occurs only 1.75 crank angle degrees later. The peak pressure is predicted to within 2 bar. Even though the pause in combustion rate during increasing AHRR has not been eliminated, the simulation prediction in Figure 7.22 is much closer to experiment than using a single component diesel model and shows that proper knowledge of the more sensitive model inputs can produce useful results.

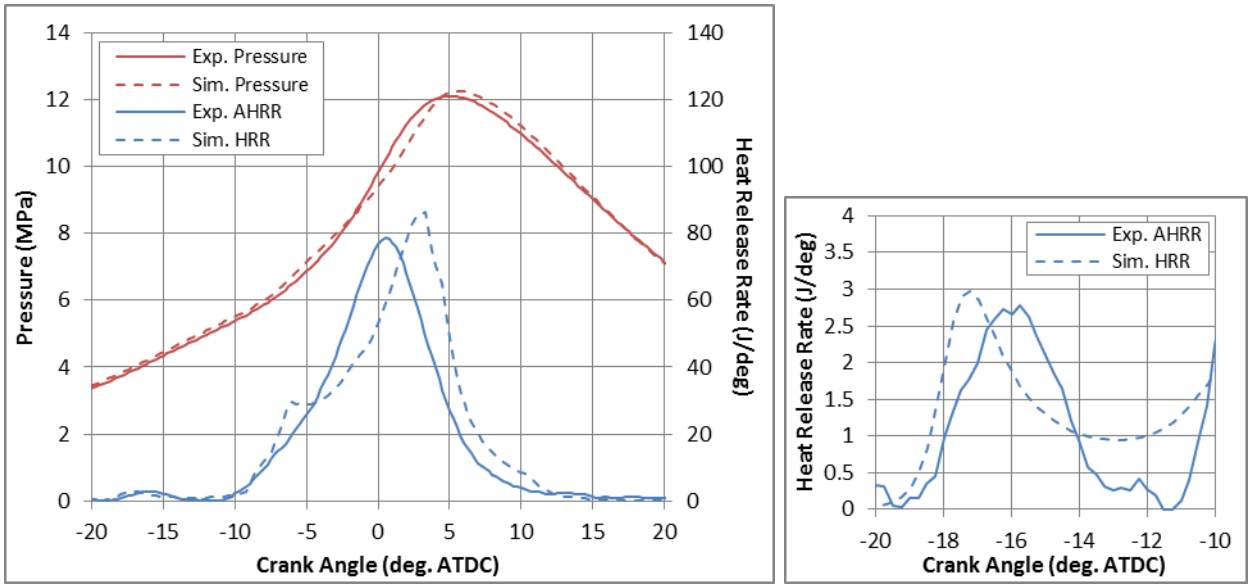

Figure 7.22. Comparison between experimental data and the improved simulation prediction for the SOI = -46° ATDC case.

7.3. Simulation Results for SOI = -52° ATDC

The more advanced injection timing case of SOI = -52° ATDC was modeled using the same method as was described for the improved model in Figure 7.22 and is compared with experimental data in Figure 7.23. The only difference between the models in Figure 7.22 and Figure 7.23 are the injection timings and a slight variation in initial temperature and pressure to reflect the slight change in trapped air mass as described in Table 7.2. Also a slight reduction of the piston temperature was necessary as this more retarded combustion phasing causes lower wall temperature. The start of low temperature heat release and high temperature heat release are well captured by the model. The climb in combustion rate is gradual and similar in value to experiment. The peak pressure, the pressure rise rate, and the combustion duration agree well with experiment. The peak heat release is slightly lower than experiment leading to a slightly lower peak pressure and lower pressure during expansion. Overall, the agreement with experimental pressure and AHRR shows that the model is able to capture the changes in pressure and AHRR due to injection timing change without relying on model tuning.

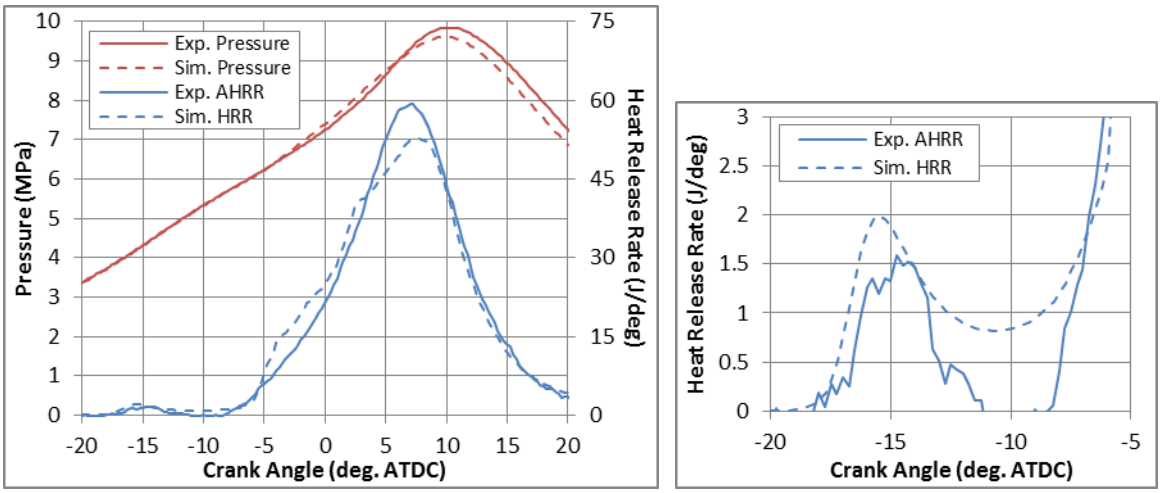

Figure 7.23. Comparison between experimental data and simulation prediction for the SOI = -52° ATDC case using the improved method.

7.4. Conclusions

This study investigated multi-dimensional CFD modeling of natural gas/diesel RCCI by incorporating a multi-component fuel surrogate for both diesel and natural gas. This necessitated the formulation of a new chemical kinetic mechanism for natural gas and diesel dual fuel combustion, which represents diesel fuel as a blend of n-dodecane and m-xylene and natural gas as a mixture of methane, ethane, and propane. Experimental data from a start of injection timing sweep on a light duty diesel engine was modeled using the multi-component mechanism and a single component n-heptane mechanism. A sensitivity study was then performed on the multi-component model to assess which input parameters are most important and develop a modeling strategy that could be applied to the other injection timing cases. It was found that an RCCI model can be very sensitive and therefore it is important to have highly accurate measurements of the boundary and initial conditions. Comparisons of simulations from the parameter study with experimental pressure and AHRR resulted in the following conclusions.

1. Large sudden increases in combustion rate at ignition and during the period of rising AHRR could be minimized, but not be removed. These sudden combustion rates are likely due to TCI error, because the sub-grid turbulent eddy structure is not resolved and therefore clusters of neighboring cells have nearly identical compositions and temperatures leading to simultaneous energy release.
2. The multi-component diesel vaporization and chemistry model was able to substantially reduce the magnitude of the increase in combustion rate at ignition in comparison to using the single component n-heptane model. In-cylinder images from the simulations show this reduction was due to a more spread out fuel distribution.
3. The model was most sensitive to the ratio of diesel surrogate components, the multi-zone method, the injected mass, and the injection velocity.
4. Better agreement was realized when using the lower injected mass measurement. This amount of diesel fuel was predicted by individual injector characterization during the rate of injection measurements. The cylinder averaged injected mass from total fuel consumption measurements can introduce error because each injector has differences in delivered mass.
5. When using a lower injected mass, it is necessary to maintain a peak injection velocity such that the peak injection pressure is correct. This can be accomplished by using a lower discharge coefficient. The correct injection pressure should be based on a long steady state injection rate shape having a steady injection pressure that is close the measured rail pressure. Short duration sprays should then follow the same increase in pressure until the rate shape falls off (see Figure 7.21).

6. Using a lower discharge coefficient with the KH-ACT breakup model resulted in non-physical spray behavior. This can be corrected by using the standard KH model.
7. The initial multi-zone chemistry strategy introduced error in the combustion phasing, but the general shape of the AHRR profile was intact. A revised multi-zone strategy was developed, which had nearly zero error compared to not using multi-zone and is recommend for future natural gas/diesel RCCI simulations. The large additional compute time from not using a multi-zone method is not worth the small reduction in combustion phasing error.
8. A chemical time step limit based on temperature increase does not need to be less than 50%.
9. A value of 1E-15 for the species absolute convergence tolerance provided satisfactory results.
10. Tuning of piston and head wall temperatures can be used to make small shifts in combustion phasing without affecting the general characteristics of the AHRR profile.

Future work should investigate the validity of the spray model to predict short duration pulse injections with long mixing time prior to ignition. This will require experimental spray data from high speed imaging and laser diagnostics of short pilot injections.

CHAPTER 8: LIMITS TO NATURAL GAS SUBSTITUTION IN DUAL FUEL ENGINES

8.1. Introduction

Spark ignited engines have lower compression ratio than diesel engines because premixed propagating flames can result in end gas knocking if the unburned gas temperatures become too high. Also premixed combustion can lead to problems with pre-ignition as the compression ratio is increased. Therefore, it comes as no surprise that fumigating a high compression ratio diesel engine with natural gas will eventually result in the onset of knock and/or pre-ignitions. This typically occurs at high load when using a high natural gas percentage and becomes a limit to the substitution percentage and the maximum load of the engine. Understanding the limitations to maximum load as substitution rate is increased allows for a comparison of performance capability between dual fuel and conventional diesel operation. This comparison can then be used to assess whether or not dual fuel can meet the demands of a particular application.

In order to explore the limits to maximum load and natural gas substitution percentage, sweeps of maximum load with engine speed were performed. This was done for pure diesel operation and for dual fuel operation using varying natural gas percentages.

8.2. Engine Experiments

Engine experiments were conducted using the GM 1.9 L light duty diesel engine as discussed previously in Chapter 3. These experiments were conducted at Facility 2 which has a natural gas composition as described in **Error! Reference source not found.**. Maximum load was recorded for pure diesel operation, dual fuel while maintaining a constant substitution percentage of 65%, and dual fuel using the minimum diesel injection possible. The minimum diesel injection was

based on reducing the electronic pulse width until the COV of IMEP began to increase significantly from inconsistent diesel mass. The maximum load was defined in terms of performance and emissions constraints, which are listed in Table 8.1. The knock intensity is the maximum peak to peak amplitude from pressure oscillations. These maximum loads were recorded at 1400, 1600, 1800, and 2200 RPM. It was not possible to record data at higher engine speeds, because the Woodward ECU was not fast enough to read and interpret the pressure cylinder data, which is used in a CA50 control algorithm. At each operating point the main injection timing was adjusted by the ECU to maintain a commanded CA50 phasing. Other than fuel mass, the variable space used to obtain the maximum load included the number of injections, the injection pressure, the boost pressure, and the CA50 target.

Table 8.1. Defined limits for maximum load testing.

Peak pressure (bar)	140
Pressure rise rate (bar/deg)	10
Methane slip (% mass)	2
Total hydrocarbon slip (% mass)	3
NOx (g/kWh)	0.4
Knock Intensity (bar)	2

Methane and total hydrocarbons were measured using a flame ionization detector (FID) from California Analytical Instruments (model 600 MHFID). This FID had a non-methane cutter that allowed for simultaneous measurement of methane and THC. The methane signal fluctuated from the THC measurement to the methane measurement every 30 seconds, because the cutter could not be run continuously. Therefore, careful attention to the methane signal was made to ensure the correct measurement. The methane and THC emissions were measured in parts per million and it was necessary to convert this to a mass measurement for methane and THC slip calculation. The methane slip was calculated as,

$$CH_4\ slip = \frac{\left(\frac{PPM_{CH4}}{10^6}\right)\left(\frac{M_{CH4}}{M_{exh}}\right)(\dot{m}_{air} + \dot{m}_{diesel} + \dot{m}_{NG})}{X_{CH4,NG}\left(\frac{M_{CH4}}{M_{NG}}\right)\dot{m}_{NG}}, \quad (8.1)$$

where $X_{CH4,NG}$ is the mole fraction of methane in the natural gas. The molecular weight of the exhaust was assumed to be equal to that of air. The THC slip was calculated from,

$$THC\ slip = \frac{\left(\frac{PPM_{THC}}{10^6}\right)\left(\frac{M_{C3H8}}{M_{exh}}\right)(\dot{m}_{air} + \dot{m}_{diesel} + \dot{m}_{NG})}{\dot{m}_{diesel} + \dot{m}_{NG}}. \quad (8.2)$$

Notice that the molecular weight of propane is used to represent the molecular weight of all hydrocarbons in the THC measurement.

8.3. Results

8.3.1. Max Load Curves

Figure 8.1 shows the maximum torque obtained for pure diesel with multiple injections, dual fuel with a 65% substitution rate, and dual fuel using the minimum injection duration. Each data point is labeled by the load limiting factor that was encountered at that condition. The variable space used to find the maximum load at each speed and fueling constraint included the number of injections, the boost pressure, the injection pressure, and the injection timing. At most conditions, the dual fuel cases only used one diesel injection. The percentage of the maximum load using pure diesel operation for the dual fuel sweeps is illustrated in Figure 8.2. The *z* = 65% dual fuel sweep can achieve nearly 90% of the diesel maximum load, while the minimum diesel injection sweep achieves between 80 and 87%. Also the percentage of diesel maximum load increases with engine speed, except at 1400 RPM.

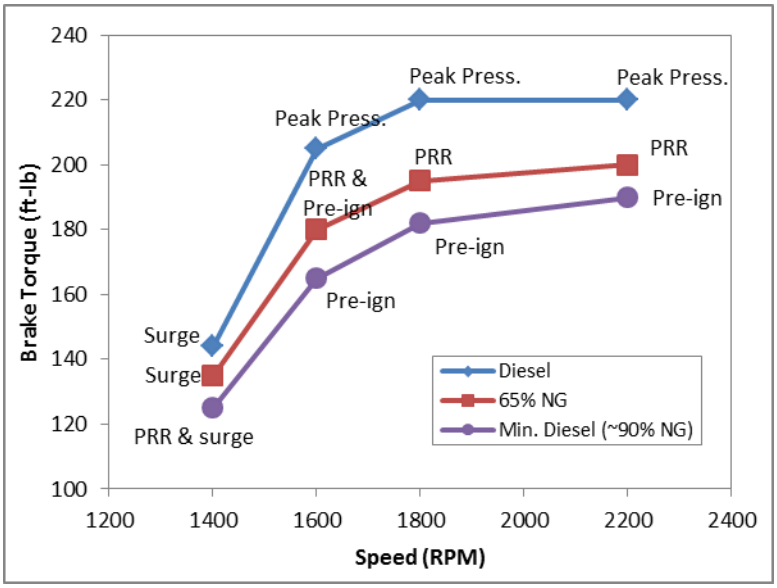

Figure 8.1. Maximum torque curves for pure diesel using multiple injections, dual fuel with a constant z = 65%, and dual fuel using the minimum injection electronic pulse width.

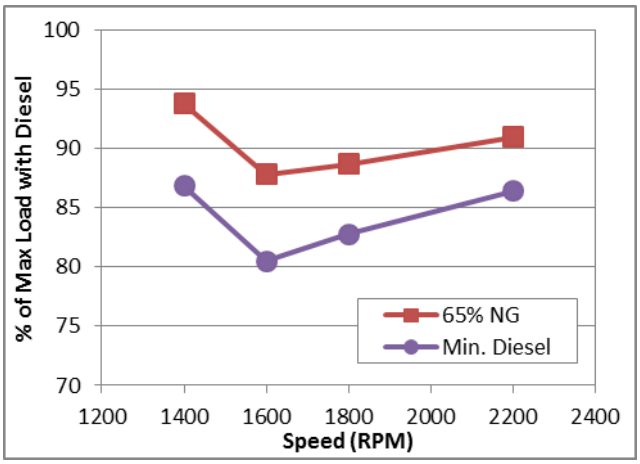

Figure 8.2. Maximum load of the dual fuel sweeps expressed as a percentage of the maximum load achieved using pure diesel operation.

The ability to maintain a constant substitution rate of z = 65% is illustrated in Figure 8.3(a). The substitution rate at 2200 RPM was slightly higher than desired with z = 68%. For the minimum diesel injection sweep, Figure 8.3(a) shows that the substitution rate increased from z = 85% at 1400 RPM to z = 90% at 2200 RPM. The minimum diesel injection refers to the minimum electronic current pulse that could be applied to the injector and ensure the needle

opened reliably. Using shorter pulse widths resulted in some misfires, because the needle opening dynamics are not perfectly consistent. The amount of diesel fuel injected per cylinder per cycle is shown in Figure 8.3(b). In the pure diesel case, the amount of diesel fuel used at 2200 RPM is slightly lower than the amount used at 1800 RPM even though the load was the same. This indicates better combustion efficiency for the 2200 RPM case. During the minimum injection sweep the diesel mass varied between 6.7 and 5.5 mg per cycle per cylinder, which is acceptable to consider constant. The reason the diesel mass is not perfectly constant even though the pulse width and rail pressure are the same is due to differences in the boost pressure used at different engine speeds, which affects the pressure difference across the injector orifice. The boost pressure for each operating point is shown in Figure 8.4, which shows that the boost pressure is lower at low engine speed and that the diesel sweep was capable of higher boost pressure. The rail pressure for all operating points is shown in Figure 8.5, which shows the dual fuel cases used a low injection pressure to limit the pressure rise rate.

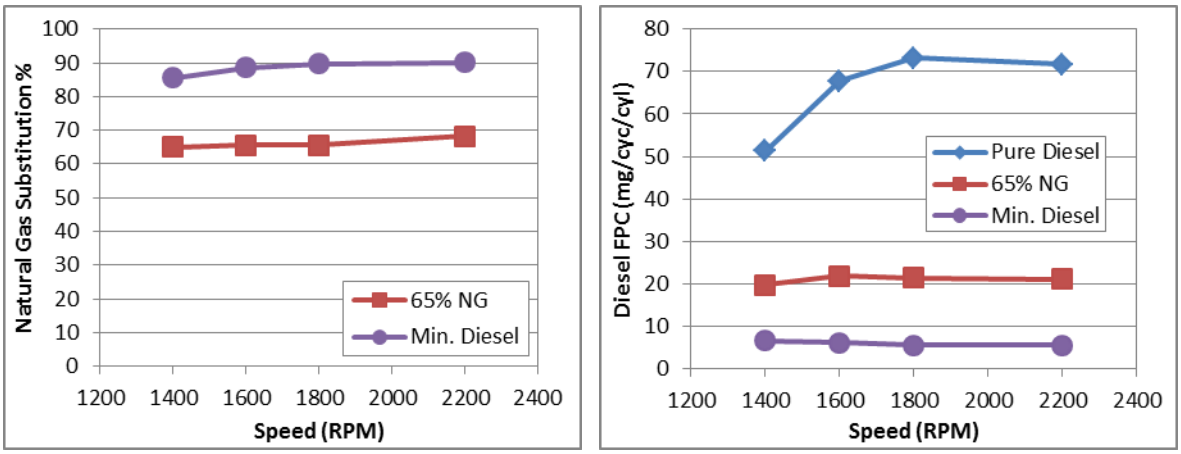

(a) (b)

Figure 8.3. (a) natural gas substitution rate used for the dual fuel sweeps. (b) Amount of diesel fuel injected per cycle per cylinder during the max load sweeps.

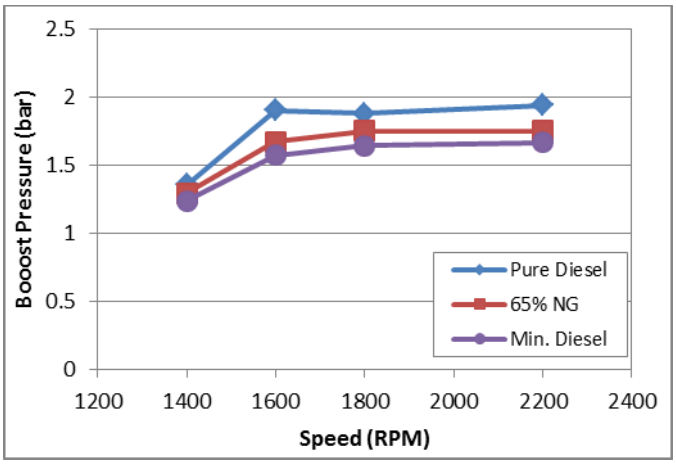

Figure 8.4. Boost pressure used in each of the max load sweeps.

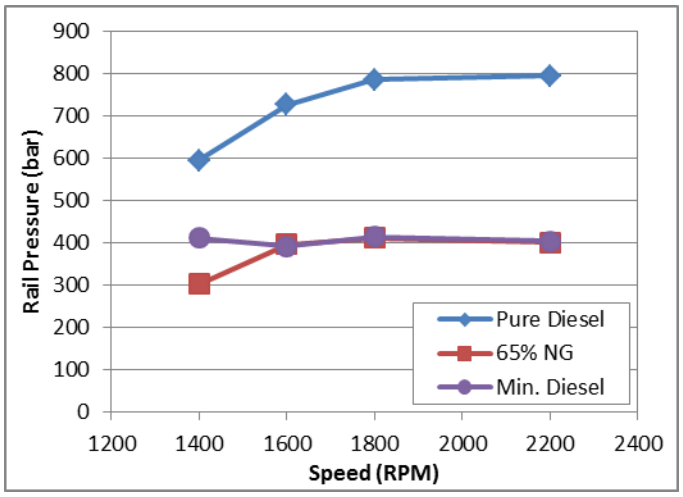

Figure 8.5. Diesel rail pressure for the three max load sweeps.

The load limits at 1800 and 2200 RPM provide an example of how different fuel combinations can have different load limits. Throughout all the cases tested the knock intensity limit was never exceeded. However, this is a small bore engine and therefore the end gas has less time to undergo auto-ignition reactions. Knock limits should be expected in large bore heavy duty diesel engines. In the pure diesel case the maximum boost of the engine (2 bar) was used and fuel was added until the 140 bar peak pressure was nearly reached, as shown in Figure 8.6. At high boost pressure, controlling a constant boost pressure became difficult as the boost pressure fluctuated between 1.5 and 2 bar. This caused the peak pressure to fluctuate as well.

Care was taken to record cylinder data when the boost was near its maximum and the peak pressure limit was reached. Three different injections were used to obtain the maximum load in this case. The first small pilot injection acts to increase the cylinder pressure for the other injections so they don't have to achieve as large of a pressure increase. This injection results in a fast increase in combustion rate occurring after the end of injection, which indicates auto-ignition of the pilot fuel. The second pilot injection helps to reduce the ignition delay of the main injection, which also reduces the pressure rise rate from the main injection. The energy addition from the second injection raises the pressure to nearly the peak pressure limit. During combustion of the main injection, the cylinder pressure is nearly constant along the peak pressure limit. The AHRR after the main injection shows a gradual increase in combustion rate followed by a long steady decline which creates a long combustion duration. This case achieved 220 ft-lbs, which is nearly the rated torque of 235 ft-lbs at 2000 RPM.

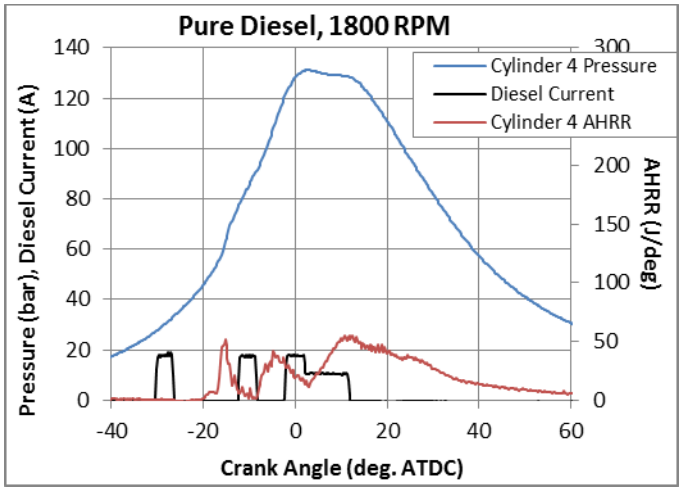

Figure 8.6. Cylinder data for the pure diesel case at 1800 RPM.

For the z = 65% dual fuel case the load was limited by the 10 bar/deg pressure rise rate, which occurred before the peak pressure was reached. There was not enough exhaust pressure to increase the boost pressure past 1.6 bar. A single injection is used and the start of combustion is

retarded to help reduce pressure rise rate, which was the limit in this case. Also, a low injection pressure of 400 bar was used to keep the pressure rise rate as low as possible. The AHRR profile shows a very large increase in combustion rate at ignition. Figure 8.8 shows the natural gas equivalence ratio for the dual fuel cases, where the z = 65% sweep had a φ_{NG} close to 0.7. Because the natural gas equivalence ratio is high and the load is high, a large amount of natural gas mixes with the diesel spray vapors where ignition reactions occur and this leads to a very large increase in combustion rate. The large rise in AHRR is followed by a gradual decline and then sharp drop, which is due to flame propagation.

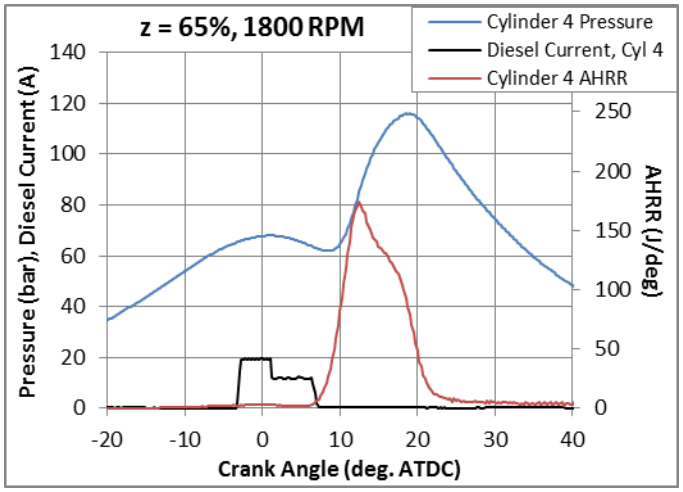

Figure 8.7. Cylinder data for the z = 65% case at 1800 RPM.

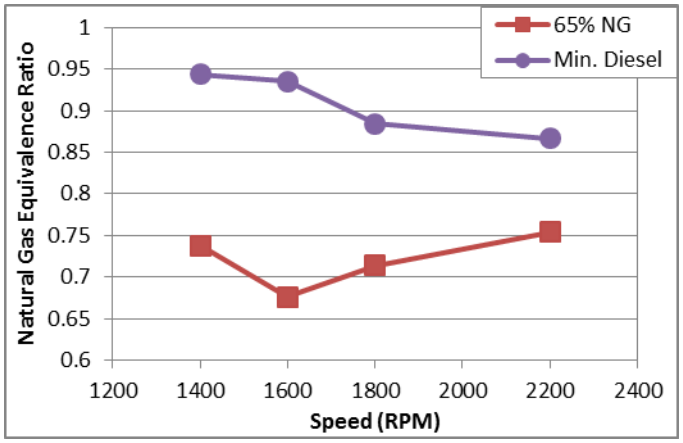

Figure 8.8. Natural gas equivalence ratio for the dual fuel sweeps.

Figure 8.9 shows the 100 cycle averaged cylinder data for the dual fuel case using the minimum diesel injection. In this case the load was limited by the onset of pre-ignitions or early ignition, which cannot be seen in 100 cycle averaged data. Early ignition is when a few cycles out of 100 ignite much earlier than the rest, which leads to much higher peak pressure and pressure rise rate for that cycle. Pre-ignitions are very early ignition cycles which ignite before the start of injection. Pre-ignitions and early ignitions are dangerous because the maximum cylinder pressure is often exceeded. Pre-ignition cycles also usually have high frequency, large amplitude pressure oscillations indicating strong engine knock. Figure 8.10 presents single cycle pressure data for two consecutive cycles where a pre-ignition event is demonstrated. Cycle 32 is similar to the 100 cycle average, but cycle 33 begins combustion around the same time that the injector current is applied. The start of injection occurs after the current is applied to the injector and therefore the start of combustion for cycle 33 is before the start of injection. The peak pressure in cycle 33 is close the 140 bar peak pressure limit. These pre-ignitions only occurred about once or twice every 100 cycles. Attempts to increase the boost pressure or add more natural gas resulted in earlier pre-ignition events which exceeded the peak pressure limit. Pre-ignitions were only a limiting factor for the minimum injection dual fuel cases, because the equivalence ratio was the highest at 0.85 as indicated in Figure 8.8. As a result a higher boost pressure was achievable in the z = 65% case, which is the reason slightly higher loads were recorded compared to the minimum diesel sweep.

The reason that pure diesel is able to achieve much higher loads than the dual fuel cases is because it can utilize multiple combustion events. In the pure diesel case a very early pilot injection helped raise the cylinder pressure so that the pressure increase from the main injection

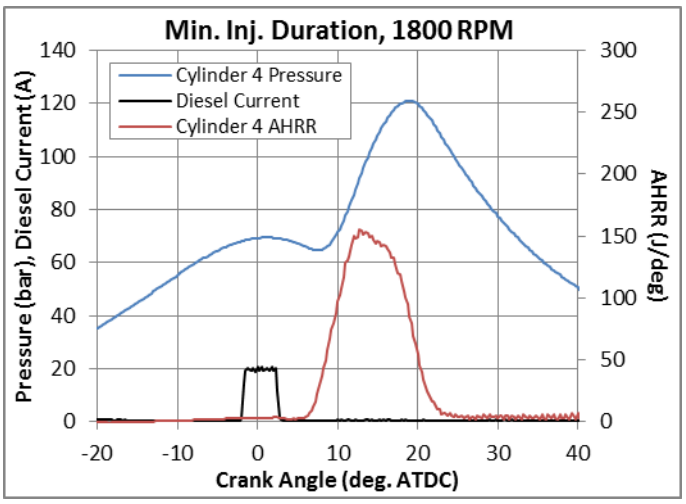

Figure 8.9. Cylinder data for the minimum diesel injection at 1800 RPM.

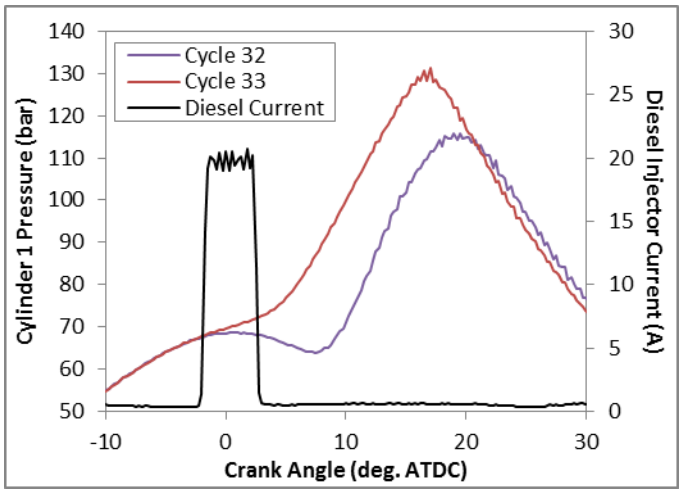

Figure 8.10. Single cycle pressure data from two consecutive cycles showing a pre-ignition.

didn't have to be as large. Also the second pilot injection is able to significantly reduce the pressure rise rate of the main injection. In the dual fuel cases, as soon as any injection is used the natural gas begins to burn and the pressure rise gets very large. Therefore dual fuel cases can't use a pre-injection to reduce the pressure rise rate. The only way to reduce the pressure rise rate in dual fuel engines is to use a smaller injection pressure, smaller injected mass, or retard the injection, but the extent to which the PRR can be reduced is not enough to allow the pressure to reach the 140 bar limit. The natural gas flame propagation in the dual fuel cases also makes the

combustion duration much shorter than was capable in the pure diesel case. Because the peak pressure cannot be achieved and because the combustion duration cannot be made longer, the dual fuel cases where not able to achieve the maximum load using pure diesel.

In-cylinder data for 1400 RPM are shown in Figure 8.11 through Figure 8.13. The important difference in these cases was that the boost pressure was limited by the low engine speed. Also the amount of fuel that could be added was not limited by such things as pressure rise rate or pre-ignitions, but by turbo charger surge. When turbo surge occurs the boost pressure fluctuates dramatically from cycle to cycle and the load drops significantly. In the pure diesel case, Figure 8.11 shows that unlike at 1800 RPM only two injections were used, because adding an early pilot injection to raise the pressure for the main injection resulted in turbo surge. The diesel fuel in the main injection was increased until surge occurred.

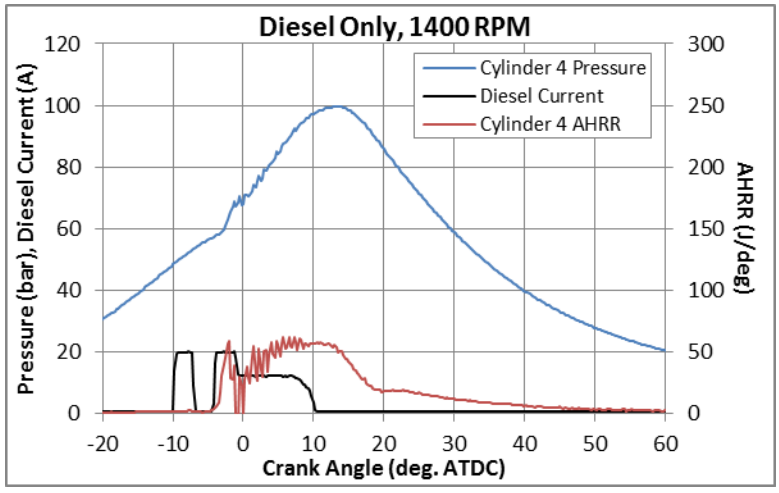

Figure 8.11. Cylinder pressure and AHRR for pure diesel at 1400 RPM.

Figure 8.12 shows the z = 65% case. Initially a single injection was used and as more fuel was added the pressure rise rate limit was reached before turbo surge was observed. Therefore, a two injection strategy was used at this condition. The first injection was a small pilot injection used to initiate combustion of the natural gas. This small injection resulted in a lower pressure

rise rate because less diesel fuel mass mixes with the natural gas and air during the ignition delay. The rest of the fuel was then put into a second post injection to maintain the z = 65% ratio. It was found that having the post injection close to TDC resulted in the greatest load. A back and forth iterative process between increasing the boost pressure and increasing the total fuel was used to maximize the load until turbo surge occurred. Also, the rail pressure used at this condition is 300 bar as opposed to the 400 bar pressure used at the other engine speeds, because it reduced the PRR.

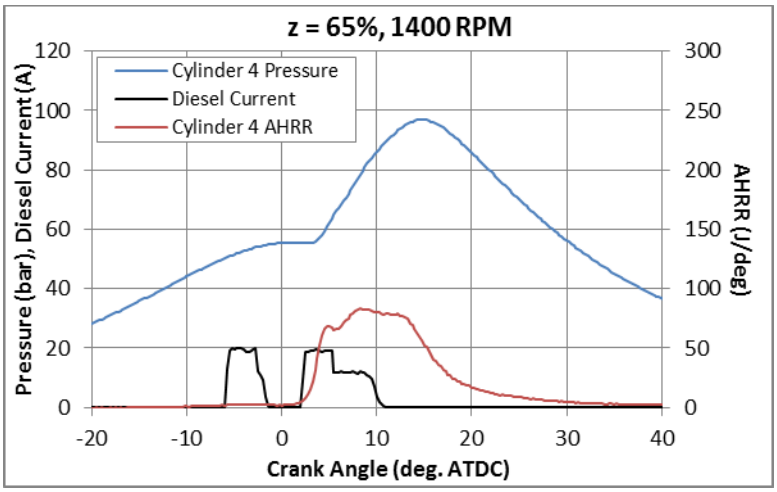

Figure 8.12. Cylinder 4 pressure and AHRR for the z = 65% sweep at 1400 RPM.

For the minimum diesel injection shown in Figure 8.13, natural gas was added until the pressure rise rate was at a maximum. Then the injection timing was retarded to lower the PRR and more natural gas was added until the PRR limit was reached again. This was repeated until the combustion became overly retarded such that the load began to drop. Finally the boost pressure was increased until turbo surge occurred. It was found that the maximum load was limited simultaneously by both the 10 bar/deg PRR limit and turbo surge.

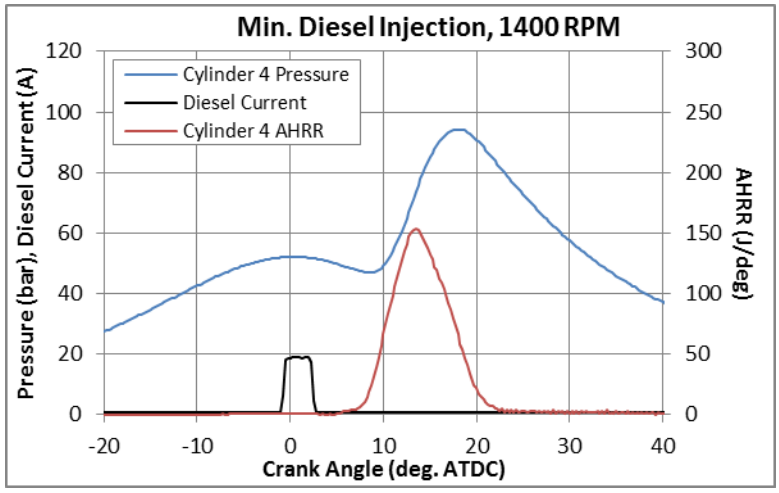

Figure 8.13. Cylinder 4 pressure and AHRR from the minimum diesel sweep at 1400 RPM.

8.3.2. Emissions

The methane slip and total hydrocarbon (THC) slip are plotted in Figure 8.14. At no point were methane emissions or THC emissions greater than the 3% limit. For the z = 65% sweep the methane emissions were constant at just under 1% slip and the THC emissions were relatively constant near 2% slip. For most of the minimum diesel injection sweep, the methane emissions increased with engine speed and were lower than the values in the z = 65% sweep. However, at 1400 RPM the methane slip was higher than at other speeds in the minimum diesel sweep. It is uncertain what is responsible for the higher methane emission at this operating point, especially considering the methane emissions did not increase at 1400 RPM in the z = 65% sweep. The THC emissions for the minimum diesel injection sweep are higher than in the z = 65% sweep. It is interesting that lower methane was observed for most of the minimum injection sweep than for the z = 65% sweep considering that the mass of natural gas is higher and the load is lower, which usually means lower temperatures during expansion. This trend can be attributed to the fact that the natural gas equivalence ratio is closer to stoichiometric for the minimum injection sweep and this leads to more complete combustion near the walls.

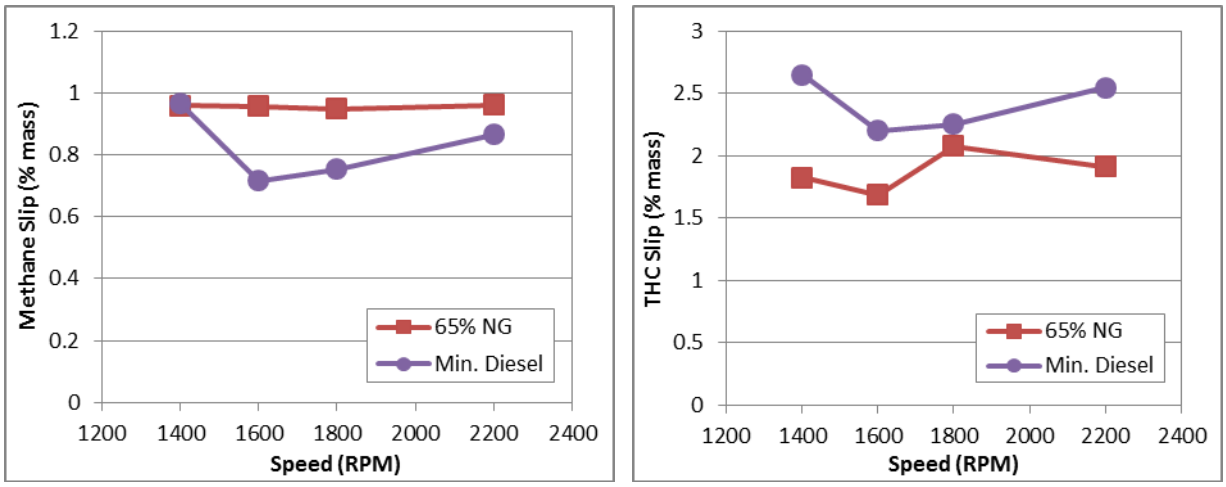

(a) (b)

Figure 8.14. (a) Methane slip for the dual fuel cases. (b) Total hydrocarbon slip.

The NO_X emissions results are plotted in Figure 8.15. The pure diesel case had the lowest NO_X levels even though it had higher load and therefore higher bulk cylinder temperatures, which tends to increase NO_X formation. This suggests that the flame temperatures are lower for the diesel combustion than the natural gas combustion. At a particular engine speed, as the substitution ratio is increased the NO_X levels increase. This can be attributed to higher flame temperature as the natural gas equivalence ratio is increased. Furthermore, in the case of minimum diesel injection, there is a large increase in NO_X emissions between 1600 and 1800 RPM. It is uncertain why this sudden increase occurred for the minimum diesel injection and not in either of the dual fuel cases. At all operating points the brake specific NO_X emissions were below the Tier 4 emissions regulation of 0.4 g/kWh.

The NO_X results from Figure 8.15 conflict with the behavior observed by previous authors who compared emissions between diesel and dual fuel operation. Papagiannakis and Hountalas [56] compared NO emissions in diesel and dual fuel mode at the same load and speed using a sweep of substitution percentages. They found that the NO emissions dropped as the substitution percentage increased and the drop was most dramatic at high load. However, they were also

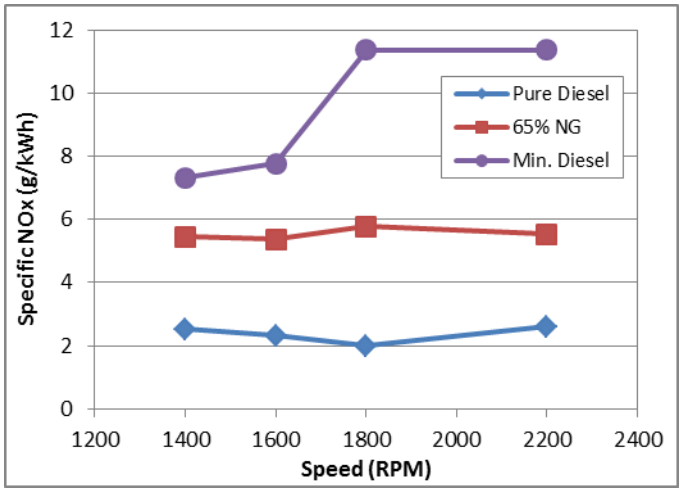

Figure 8.15. NO_X emissions for the three maximum load sweeps.

using a single injection with constant timing. Additionally, the NOx comparisons made using the constant volume chamber simulations in Section 5.5.1 showed that diesel combustion should have higher NO_X than dual fuel for the same energy released (see Figure 6.21). While the data was not taken at a constant load, reducing the load in the pure diesel case should only make its NO_X emissions lower as the combustion duration would be shorter.

Inspection of the AHRR in the pure diesel plot for 1800 RPM in Figure 8.6 shows that the main diesel injection is combusting during the expansion stroke until 60 degrees ATDC. The dual fuel cases in Figure 8.7 and Figure 8.9 show that the combustion duration ends by 20 degrees ATDC. Prehaps more retarded combustion in the diesel case resulted in lower flame temperature than the natural gas flames in the dual fuel cases. Also the dual fuel cases were not able to achieve as high of boost pressure as the pure diesel cases and therefore this requires a higher natural gas equivalence ratio to produce the maximum load, which translates to higher flame temperature and higher NO_X. Simulations of the three fuel combinations at 1800 RPM

should be performed to see if the included thermal NO mechanism can predict the observed trend and provide insight as to why it is different than expected.

There is a possibility that the NO_X measurements are not accurate. The pure diesel sweep was performed first and these conditions resulted in a noticeably high level of smoke. It is possible that a large amount of soot entered the NOx analyzers and interferred with the results during the dual fuel sweeps. The NOx analyzers should be recalibrated and some of the data points should be verified.

8.3.3. Efficiency Results

The brake specific fuel consumption is shown in Figure 8.16. The pure diesel case had the worst fuel consumption and as the natural gas substitution rate was increased the fuel efficiency improved. As is typically seen the fuel consumption improved as the engine speed increased, which is due to the higher boost pressures attainable and therefore greater load per gram of fuel.

The brake fuel conversion efficiency is shown in Figure 8.17, which is the ratio of brake work per cycle to the fuel energy used per cycle. Because the combustion efficiency is unknown, the true thermal efficiency cannot be determined. At low engine speed the efficiencies are nearly identical between the three cases, while at high engine speed the dual fuel case with minimum diesel injection has the greatest efficiency of 53%. Therefore, dual fuel combustion has resulted in a small efficiency increase.

8.4. Conclusions

Maximum load curves have been recorded on a GM 1.9 L turbo-charged diesel engine between 1400 and 2200 RPM for pure diesel operation, dual fuel with a substitution percentage of 65% natural gas, and dual fuel using the minimum amount of diesel fuel. Load limits were

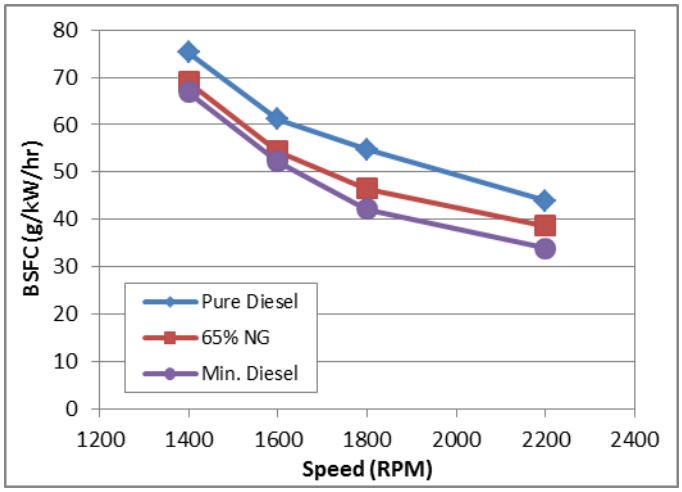

Figure 8.16. Brake specific fuel consumption for the three maximum load sweeps.

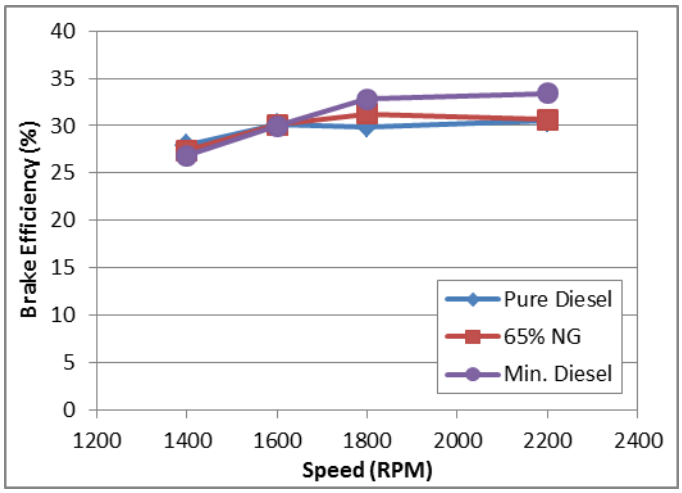

Figure 8.17. Fuel conversion efficiency for the three maximum load sweeps.

applied based on peak pressure, pressure rise rate, knock intensity, methane slip, THC slip, and the Tier 4 NO_X regulation. Other load limiting factors that had to be avoided during the sweeps included pre-ignitions and turbocharger surge. The knock limit was not encountered at any of the operating points investigated. Pure diesel operation was able to achieve the highest maximum load and the maximum load decreased as the natural gas substitution percentage increased. The following conclusions were made from the load sweeps.

1. Pure diesel operation is able to achieve higher loads than the dual fuel cases because multiple injections can be used to significantly reduce PRR and because higher boost pressure is possible. The reduced PRR from using pre-injections allows for a nearly constant pressure to be maintained near TDC, which allows for much greater expansion pressure. In dual fuel operation, the first injection will always initiate the natural gas combustion and cause a large increase in pressure and a large pressure rise rate. If a pre-ignition occurs the increase in pressure is much larger and often exceeded the 140 bar peak pressure limit. Consequently, retarding of the combustion phasing was necessary to reduce the PRR and peak pressure, which allowed for more fuel and higher load. It was not possible to maintain a constant pressure near TDC with dual fuel operation as the n
2. As boost pressure was increased the pre-ignitions began to occur earlier and eventually exceeded the 140 bar peak pressure limit. Because pure diesel operation did not suffer from pre-ignitions, a higher boost pressure could be used than was possible with dual fuel.
3. At very high substitution percentages, pre-ignitions became the dominant load limiting factor for this engine. At a substitution percentage of 65% the load limiting factor was PRR. At the lowest engine speed the load limiting factor for all three sweeps was turbocharger surge.
4. Methane slip remained less than 1% at all dual fuel conditions investigated.
5. The NOx emissions were higher for dual fuel operation and increased as the substitution percentage increased.
6. Dual fuel operation had better brake specific fuel consumption compared to diesel operation.

7. At the highest engine speed of 2200 RPM, the minimum diesel injection case had a substitution percentage of nearly 90%, the maximum load was within 85% of the load achieved with pure diesel operation, the PRR was less than 10 bar/deg, the methane slip was less than 1%, the fuel conversion efficiency was over 50%, the NOx emissions were within Tier 4 regulations, and the brake specific CO_2 emissions were reduced by nearly 45%. This condition demonstrates the potential of dual fuel operation to achieve emissions regulations with a reduced fuel cost in a light duty diesel engine.
8. At low engine speed where boost pressure is limited, adding a post injection can help increase the load provided that the natural gas equivalence ratio remains lean.

Future work should focus on trying to understand if the trend of increasing NOx with substitution rate is valid. In doing so all three fuel combinations should be tested at the same brake torque so that differences in total fuel energy are not a factor. For instance at 2200 RPM the diesel case and z = 65% case should be run at 190 ft-lbs and the NOx emissions compared. Also the NO_X analyzers should be recalibrated to ensure that heavy soot emissions from the diesel case did not interfere with any measurements that followed. In addition, the computational model presented in the previous chapters should be applied to the three fuel combinations at 2200 RPM to explain the differences in NO_X formation and determine if the model can quantitatively predict the methane slip seen in these experiments. These simulations could also be used to test different strategies to reduce the pressure rise rate when operating in dual fuel mode, such as different injector designs and different swirl ratios. Furthermore, there is need for a model that can predict the occurrence of pre-ignition so that methods to mitigate it can be explored.

CHAPTER 9: CONCLUSIONS AND FUTURE WORK

9.1. Conclusion

A multi-dimensional CFD model using reduced chemical kinetics has been developed for use in simulating natural gas/diesel dual fuel engines. This model was validated against experimental pressure and heat release rate data from light duty turbocharged diesel engine across a wide range of loads, natural gas substitution percentages, injection timings, and natural gas compositions. The process of constructing this model necessitated the development and validation of a new reduced chemical kinetic mechanism for dual fuel combustion whereby natural gas is represented by a mixture of methane, ethane, and propane and diesel is represented with as a single component of n-heptane. Applying this model to RCCI combustion found that a single component diesel surrogate was not able to capture the reactivity gradient from real diesel fuel and so a two component diesel surrogate model was incorporated into another reduced chemical mechanism. Using the multi-component mechanism and after performing a sensitivity study on various model parameters, agreement with pressure from RCCI experiments was greatly improved. Finally, an experimental comparison between diesel and dual fuel operation at maximum load provided a quantitative and qualitative understanding of the performance limitations for light duty dual fuel engines

Simulations of dual fuel engine experiments demonstrated excellent agreement in terms of start of combustion phasing, pressure rise rate, peak pressure, location of peak pressure, shape and magnitude of the AHRR profile, and combustion duration. This was done at loads ranging from 7 to 15 IMEP, substitution percentages ranging from 43% to 70%, advanced and retarded combustion phasing, and two different natural gas compositions with methane percentages of

95% and 88%. Also a knocking experiment using additional propane was simulated and the phasing and magnitude of uncontrolled fast combustion was well captured. Inspection of combustion physics using clip planes and iso-surfaces from the simulations helped formulate an explanation for the processes in dual fuel combustion. Entrainment of natural gas with the spray leads to a larger release of energy during ignition. Establishment of a non-premixed diesel jet flame initiates a premixed propagating natural gas flame that propagates normal to the spray axis and down into the bowl region. A natural gas flame also travels into the squish region, but at a slower rate due to greater heat transfer. The AHRR will increase as the natural gas flame surface area increases. When the natural gas flame reaches the walls of the bowl region there is a sudden decrease in available natural gas/air mixture and a corresponding drop in the AHRR profile. However, at retarded injection timings, expansion cooling slows down the natural gas flame as it approaches the bowl walls and as a result there is not a sudden change in available natural gas/air mixture. The tail end of the AHRR profile is due to the natural gas flame traveling through the squish region as well as combustion of any remaining diesel fuel. As the SOI timing becomes increasingly retarded, the flame can become quenched in both the bowl and squish regions during expansion. A comparison between dual fuel and a diesel-only simulation showed that during the period of natural gas flame propagation, the diesel fuel contributes a relatively constant contribution to the total heat release rate.

Simulation of the propane addition experiment where engine knock was observed revealed unique characteristics of end gas auto-ignition in dual fuel engines. Premixed flames from adjacent sprays merge together creating a single flame surface with a cusp like crease where they meet. These flames first merge near the center of the cylinder and this crease in the flame surface travels outwards towards the bowl rim. Merging natural gas flames form a pocket of unburned

natural gas along the crease between them that are located far from piston walls where heat transfer is low. Under the right conditions, these pockets of unburned gas between merging natural gas flames can undergo auto-ignition and create pressure waves characteristic of engine knock. Therefore the auto-ignition locations in a dual fuel engine under these operating conditions are consistently located between spray axes. This is unlike end gas auto-ignition in SI engines which can initiate from different locations from cycle to cycle.

Additional information was obtained from simulations of a diesel spray into a constant volume chamber. Comparisons were made between a diesel spray into air, an ambient natural gas/air mixture with $\varphi = 0.5$, and one with $\varphi = 0.8$. It was found that the natural gas flame leaves excess oxygen behind for the oxidizer side of the non-premixed diesel jet flame. This concentration of left over oxygen decreases as the natural gas equivalence ratio is increased and as a result the non-premixed flame in dual fuel combustion grows to a larger surface area with lower local heat release rate. Natural gas entrained within the interior of the spray is oxidized at the non-premixed diesel flame. A comparison between a simulation of a diesel spray in air and a dual fuel simulation in which the diesel injection ends just after ignition showed that the pure diesel case generates higher NOx for the same amount of energy released, because the flame temperature is higher. This comparison also showed that the rate of energy release in the dual fuel case was much greater even long after the diesel injection ended because the flame surface area quickly becomes much larger than the diesel flame.

The 141 species reduced chemical kinetic mechanism for dual fuel engine simulations was well validated across a range of conditions using comparisons with ignition delay with detailed mechanisms, adiabatic HCCI simulations of detailed mechanisms, laminar flame speed experiments of methane at 40 and 60 atm, a diesel spray experiment in a constant volume

chamber, and simulations of dual fuel engine experiments. The engine experiments included a range of loads, natural gas percentages, and two different natural gas compositions. These computations were completed in roughly 12 hours using 48 cores. Based on the validation, this reduced mechanism should be capable of simulating diesel spray ignition, natural gas flames, and natural gas auto-ignition in high compression ratio diesel engines. Unlike previous modeling work on dual fuel combustion where natural gas was represented with pure methane, this mechanism allows for the reactivity of the natural gas source to be more accurately represented through the addition of ethane and propane chemistry. While the CSU141 mechanism retains agreement with the detailed n-heptane mechanism at very lean conditions, this mechanism may not be suitable for RCCI modeling because the reactivity of real diesel fuel is not well captured using a single component surrogate.

The study on RCCI modeling showed that using a two component diesel surrogate consisting of n-dodecane and p-xylene gave a more accurate representation of the gradual increase in heat release rate observed experimentally compared to using a single component of n-heptane. This is due to the smoother transition in reactivity created as the diesel mixes with natural gas as the aromatic p-xylene as a reactivity between n-dodecane and methane. In addition, the sensitivity study on parameters for the RCCI engine simulations helped formulate a modeling strategy that resulted in closer agreement with experimental pressure and AHRR obtained from an RCCI start of injection timing sweep. This modeling strategy utilized a reduced injection mass while maintaining the original injection velocity. The reduced diesel mass helps compensate for the TCI commutation error between mean cell temperature and mean cell reaction rate induced from using a RANS turbulence model. The injection velocity must be similar the value obtained before reducing the injected mass so as to create the proper spreading of the injected fuel and

was accomplished using either a reduced discharge coefficient or reduced nozzle diameter. Furthermore, the sensitivity study revealed a multi-zone chemistry strategy that had close agreement when not using multi-zone chemistry.

The final portion of the work was an experimental study comparing conventional diesel and dual fuel operation at maximum load on a light duty diesel engine between 1400 and 2200 RPM. The dual fuel operation included a moderate substitution percentage of 65% and the maximum substitution percentage, which utilized the smallest diesel injection possible. Load limits included peak pressure, pressure rise rate, knock intensity, pre-ignitions, methane slip, THC slip, Tier 4 NOx regulation, and turbocharger surge. It was found that dual fuel operation had a reduced maximum load at all engine speeds with the load reduction being largest for the maximum substitution percentage. At low engine speed all three cases were load limited by turbocharger surge. At higher engine speed conventional diesel operation was limited by peak pressure, the 65% substitution rate case was limited by pressure rise rate, and the minimum diesel injection case was limited by the onset of pre-ignitions. The observed pre-ignitions caused very high peak pressures that exceeded the maximum allowable design pressure and created knocking. Diesel operation was able to achieve higher loads because it could utilize multiple injection strategies to reduce the pressure rise rate and therefore allow for higher boost pressure. Dual fuel operation is not able to utilize similar multiple injection strategies because natural gas flame propagation will always begin with the first injection and create a large pressure rise. To avoid high pressure rise rate and pre-ignitions, a lower boost pressure had to be used and the fuel had to be limited. Dual fuel also had lower maximum load because it could not create a long combustion duration that would allow for near constant pressure near TDC as could be done with diesel operation.

The emissions measurements during the maximum load sweeps showed that the methane slip was less than 1% during dual fuel operation. Total hydrocarbon slip remained under 3% for all dual fuel conditions. The NOx emissions increased as the substitution percentage increased, which is counter to the observations made by previous authors and is in conflict with the constant volume chamber simulations conducted earlier in this work. At all operating points the NOx emission remained under the EPA Tier 4 regulation. Dual fuel operation had better brake specific fuel consumption compared to diesel operation and the fuel consumption improved as substitution rate increased. At 2200 RPM and a substitution percentage of 90% the fuel conversion efficiency was over 50%, the load was within 85% of the load achieved with pure diesel operation, and the calculated brake specific CO_2 emissions were reduced by nearly 45% in comparison to diesel operation. This performance with dual fuel is specific to this engine.

9.2. Future Work

The engine model presented in this work has been validated against experimental pressure and heat release rate curves, but has not been extensively validated against emissions measurements. One of the reasons this was not completed was because most of the engine experiments used for model simulation only included NOx measurements. While the simulations did include the extended Zeldovich thermal NOx mechanism, previous work has shown that prompt NOx can be an important source of NOx formation. Prompt NOx modeling necessitates the use of a much larger chemical mechanism which can significantly increase the computational cost. Additional modeling should be performed for some of the dual fuel cases explored in the maximum load testing, because these experiments included methane and total hydrocarbon

measurements. This would determine the ability of the model to predict unburned natural gas and demonstrate its usefulness as tool for exploring strategies to reduce methane slip.

The ability of the dual fuel model to predict engine knock has been demonstrated. Next steps should be taken to use the model to extrapolate which strategies would be more effective at mitigating knock. For instance increasing the swirl ratio could allow for greater heat transfer rates that would cool down the end gases. Also, increasing the number of injector nozzles would create a shorter distance for the flame to travel and therefore less time for auto-ignition reactions.

The spray model used in this work was validated against optical experiments of a diesel spray into a constant volume chamber at two different injection pressures. Those experiments used long injection durations where the steady state injection rate was reached for most of the duration. However, dual fuel operation at high substitution rate utilizes short injection durations where the needle is likely to never reach the fully reacted position and the steady state injection rate is not reached. Therefore the transient injector dynamics could present error in the model, because the model uses a discharge coefficient measured at the steady state rate over a long duration. Using the measured discharge coefficient for short injection duration resulted in the peak injection pressure being much lower than the measured rail pressure. This can result in a low peak injection velocity. The RCCI simulation explored in this work had a short injection duration and showed better agreement when applying a lower discharge coefficient to increase the injection velocity. Further experiments with vaporizing non-reacting diesel sprays in a constant volume chamber should be conducted using short injection durations where the steady state injection rate is not reached. This data should then be used to assess the accuracy of the model in predicting the injection velocity and if a lower discharge coefficient is appropriate.

In the dual fuel maximum load experiments, the NOx emissions were seen to increase as the substitution rate was increased and the load became lower. This trend seems to be in conflict with observations made by previous authors, in which the NOx emissions went down as the natural gas percentage increased or the load decreased. The NOx analyzers should be recalibrated and the three fuel combinations should be tested at the same brake torque, which should be the 190 ft-lbs achieved at 2200 RPM in the minimum diesel injection case. If the same trend is observed, then the model should be applied to these cases to see if the extended Zeldovich mechanism for thermal NOx formation predicts the same trend.

BIBLIOGRAPHY

[1] U.S. Energy Information Administration, "Annual Energy Outlook 2014 with Projections to 2040," DOE/EIA-0383(2014), 2014.

[2] U.S. Environmental Protection Agency, "EPA and NHTSA Adopt First-Ever Program to Reduce Greenhouse Gas Emissions and Improve Fuel Efficiency of Medium- and Heavy-Duty Vehicles," EPA-420-F-11-031, 2011.

[3] U.S. Environmental Protection Agency, "EPA and NHTSA Set Standards to Reduce Greenhouse Gases and Improve Fuel Economy for Model Years 2017-2025 Cars and Light Trucks," EPA-420-F-12-051, 2012.

[4] D. Serrano and L. Bertrand, "Exploring the Potential of Dual Fuel Diesel-CNG Combustion for Passenger Car Engine," in *Proc. FISITA 2012 World Automotive Congress*, 2012.

[5] Intergovernmental Panel on Climate Change, "IPCC Forth Assessment Report: Climate Change 2007: Working Group I: The Physical Science Basis, section 2.10.2 Direct Global Warming Potentials, Table 2.14," 2007.

[6] G. Karim, "Combustion in Gas Fueled Compression: Ignition Engines of the Dual Fuel Type," *ASME J. Eng. Gas Turbines and Power*, vol. 125, pp. 827-836, 2003.

[7] T. Kuboyama, Y. Moriyoshi and K. Morikawa, "Visualization and Analysis of LSPI Mechanism Caused by Oil Droplet, Particle and Deposit in Highly Boosted SI Combustion in Low Speed Range," *SAE Int. J. Engines*, vol. 8, no. 2, pp. 529-537, 2015.

[8] C. Dahnz, K. Han and U. Spicher, "Investigations on Pre-Ignition in Highly Supercharged SI Engines," *SAE Int. J. Engines*, vol. 3, no. 1, pp. 214-224, 2010.

[9] S. Singh, S. Kong, R. D. Reitz, S. Krishnan and K. Midkiff, "Modeling and Experiments of Dual-Fuel Engine Combustion and Emissions," *SAE Technical Paper 2004-01-0092,* 2004.

[10] M. Mittel, R. Donahue, P. Winnie and A. Gillette, "Combustion and Gaseous Emissions Characteristics of a Six-Cylinder Diesel Engine Operating within Wide Range of Natural Gas Substitutions at Different Operating Conditions for Generator Application," *SAE Technical Paper 2014-01-1312,* 2014.

[11] M. Selim, "Sensitivity of dual fuel engine combustion and knocking limits to gaseous fuel composition," *Energy Conversion and Management,* vol. 45, pp. 411-425, 2004.

[12] C. Mansour, A. Bounif, A. Aris and F. Gailllard, "Gas–Diesel (dual-fuel) modeling in diesel engine environment," *International Journal of Thermal Sciences,* vol. 40, pp. 409-424, 2001.

[13] D. Hountalas and R. Papagiannakis, "Development of a Simulation Model for Direct Injection Dual Fuel Diesel-Natural Gas Engines," *SAE Technical Paper 2000-01-0286,* 2000.

[14] Y. Zhang, S. Kong and R. D. Reitz, "Modeling and Simulation of a Dual Fuel (Diesel/Natural Gas) Engine with Multidimensional CFD," *SAE Technical Paper 2003-01-0755,* 2003.

[15] D. Niemann, A. Dempsey and R. D. Reitz, "Heavy-Duty RCCI Operation Using Natural Gas and Diesel," *SAE Technical Paper 2012-01-0379,* 2012.

[16] M. Dahodwala, S. Joshni, E. Koehler, M. Franke and D. Tomazic, "Experimental and Computational Analysis of Diesel-Natural Gas RCCI Combustion in Heavy-Duty

Engines," *SAE Technical Paper 2015-01-0849,* 2015.

[17] G. Borque, D. Healy, H. Curran, C. Zinner, D. Kalitan, J. de Vries, C. Aul and E. Petersen, "Ignition and Flame Speed Kinetics of Two Natural Gas Blends with High Levels of Heavier Hydrocarbons," *Proc. ASME Turbo Expo,* vol. 3, p. 1051, 2008.

[18] F. Zhao, T. Asmus, D. Assanis, J. Dec, J. Eng and P. Najt, Homogenous Charge Compression Ignition (HCCI) Engines: Key Research and Development, Warrendale, PA: Society of Automotive Engineers, 2003.

[19] D. Splitter, R. Hanson, S. Kokjohn and R. Reitz, "Reactivity Controlled Compression Ignition (RCCI) Heavy-Duty Engine Operation at Mid- and High-Loads with Conventional and Alternative Fuels," *SAE Technical Paper 2011-01-0363,* 2011.

[20] R. Issa, "Solution of the Implicitly Discretised Fluid Flow Equations by Operator-Splitting," *Journal of Computational Physics,* vol. 62, pp. 40-65, 1986.

[21] Convergent Science Inc., CONVERGE 2.2.0 Theory Manual, 2013.

[22] P. Senecal, E. Pomraning, K. Richards and S. Som, "Grid-convergent spray models for internal combustion engine CFD simulations," in *Proc. ASME ICEF, ICEF2012-92043,* 2012.

[23] Z. Han and R. D. Reitz, "Turbulence Modeling of Internal Combustion Engines Using RNG k-e models," *Combustion Science and Technology,* vol. 106, pp. 267-295, 1995.

[24] E. Pomraning, K. Richards and P. Senecal, "Modeling Turbulent Combustion Using a RANS Model, Detailed Chemistry, and Adaptive Mesh Refinement," *SAE Technical Paper 2014-01-1116,* 2014.

[25] B. Launder and D. Spalding, "The Numerical Computation of Turbulent Flows," *Computer*

Methods in Applied Mechanics and Engineering, 1974.

[26] A. Amsden, "KIVA 3-V: A Block Structured KIVA Program for Engines with Vertical or Canted Valves," Los Alamos National Laboratory Report No. LA-13313-MS, 1997.

[27] S. Som and S. Aggarwal, "Effect of primary breakup modeling on spray and combustion characteristics of compression ignition engines," *Combustion and Flame*, vol. 157, pp. 1179-1193, 2010.

[28] D. Schmidt and C. Rutland, "A New Droplet Collision Algorithm," *Journal of Computational Physics*, vol. 164, pp. 62-80, 2000.

[29] S. Post and J. Abraham, "Modeling the Outcome of Drop-Drop Collisions in Diesel Sprays," *International Journal of Multiphase Flow*, vol. 28, pp. 997-1019, 2002.

[30] A. Babajimopoulos, D. Assanis, D. Flowers, S. Aceves and R. Hessel, "A fully coupled computational fluid dynamics and multi-zone model with detailed chemical kinetics for the simulation of premixed charge compression ignition engines," *Int. J. Engine Research*, vol. 6, p. 497, 2005.

[31] Engine Combustion Network, "Diesel Spray Combustion," Sandia National Laboratories, 2012. [Online]. Available: http://www.sandia.gov/ecn/dieselSprayCombustion.php.

[32] L. Pickett, J. Manin, C. Genzale, D. Siebers, M. Musculus and C. Idicheria, "Relationship Between Diesel Fuel Spray Vapor Penetration/Dispersion and Local Fuel Mixture Fraction," *SAE Int. J. Engines*, vol. 4, pp. 764-799, 2011.

[33] M. Musculus, T. Lauchaux, L. Pickett and C. Idicheria, "End-of-Injection Over-Mixing and Unburned Hydrocarbon Emissions in Low-Temperature Combustion Diesel Engines," *SAE Technical Paper 2007-01-0907*, 2007.

[34] A. Rahimi, E. Fatehifar and R. Saray, "Development of an optimized chemical kinetic mechanism for homogeneous charge compression ignition combustion of a fuel blend of n-heptane and natural gas using a genetic algorithm," *Proc. Inst. Mech. Engineers,* vol. 224, pp. 1141-1159, 2010.

[35] P. Dagaut, "On the kinetics of hydrocarbons oxidation from natural gas to kerosene and diesel fuel," *Phys. Chem. Chem. Phys.,* p. 2079–2094, 2002.

[36] A. Turbiez, A. El Bakali, J. Pauwels, A. Rida and P. Meunier, "Experimental study of a low pressure stoichiometric premixed methane, methane/ethane, methane/ethane/propane and synthetic natural gas flames," *Fuel,* vol. 83, p. 933–941, 2004.

[37] D. Healy, D. Kalitan, C. Aul, E. Petersen, G. Bourque and H. Curran, "Oxidation of C1-C5 Alkane Quinternary Natural Gas Mixtures at High Pressures," *Energy and Fuels,* vol. 24, pp. 1521-1528, 2010.

[38] H. Curran, P. Gaffuri, W. Pitz and C. Westbrook, "A Comprehensive Modeling Study of n-Heptane Oxidation," *Combustion and Flame,* vol. 114, pp. 149-177, 1998.

[39] H. Curran, P. Gaffuri, W. Pitz and C. Westbrook, "A Comprehensive Modeling Study of iso-Octane Oxidation," *Combustion and Flame,* vol. 129, pp. 253-280, 2002.

[40] K. E. Niemeyer, C.-J. Sung and M. P. Raju, "Skeletal mechanism generation for surrogate fuels using directed relation graph with error propagation and sensitivity analysis," *Combustion and Flame,* vol. 157, pp. 1760-1770, 2010.

[41] G. Rozenchan, D. Zhu, C. K. Law and S. Tse, "Outward Propagation, Burning Velocities, and Chemical Effects of Methane Flames up to 60 atm," *Proc. Comb. Inst.,* vol. 29, pp. 1461-1469, 2002.

[42] D. Martinez, L. Tozzi and A. J. Marchese, "A Reduced Chemical Kinetic Mechanism for CFD Simulations of High BMEP, Lean-Burn Natural Gas Engines," in *Proc. ASME ICES, ICES2012-81109*, 2012.

[43] T. Ishiyama, M. Shioji, S. Mitani and H. Shibata, "Improvement of Performance and Exhaust Emissions in a Converted Dual-Fuel Natural Gas Engine," *SAE Technical Paper 2000-01-1866,* 2000.

[44] W. Pulkrabek, Engineering Fundamentals of the Internal Combustion Engine, New Jersey: Prentice Hall Inc., 1997.

[45] F. Perini, A. Dempsey, R. D. Reitz, D. Sahoo, B. Petersen and P. Miles, "A Computational Investigation of the Effects of Swirl Ratio and Injection Pressure on Mixture Preparation and Wall Heat Transfer in a Light-Duty Diesel Engine," *SAE Technical Paper 2013-01-1105,* 2013.

[46] C. Yoo, T. Lu, J. Chen and C. Law, "Direct numerical simulations of ignition of a lean n-heptane/air mixture with temperature inhomogeneities at constant volume: Parametric study," *Combustion and Flame,* vol. 158, pp. 1727-1741, 2011.

[47] J. Dec, "A Conceptual Model of DI Diesel Combustion Based on Laser-Sheet Imaging," *SAE Technical Paper 970873,* 1997.

[48] C. K. Law, Combustion Physics, New York: Cambridge University Press, 2006.

[49] G. Abd Alla, H. Soliman, O. Badr and M. Abd Rabbo, "Effect of injection timing on the performance of a dual fuel engine," *Energy Conversion and Management,* vol. 43, pp. 269-277, 2002.

[50] S. Kokjohn, R. Hanson, D. Splitter and R. Reitz, "Experiments and Modeling of Dual-Fuel

HCCI and PCCI Combustion Using In-Cylinder Fuel Blending," *SAE Technical Paper 2009-01-2647,* 2009.

[51] R. Hanson, S. Kokjohn, D. Splitter and R. Reitz, "An Experimental Investigation of Fuel Reactivity Controlled PCCI Combustion in a Heavy-Duty Engine," *SAE Technical Paper 2010-01-0864,* 2010.

[52] K. Puduppakkam, L. Liang, C. Naik, E. Meeks, S. Kokjohn and R. D. Reitz, "Use of Detailed Kinetics and Advanced Chemistry-Solution Techniques in CFD to Investigate Dual-Fuel Engine Concepts," *SAE Technical Paper 2011-01-0895,* 2011.

[53] E. Doosje, F. Willems and R. Baert, "Experimental Demonstration of RCCI in Heavy-Duty Engines using Diesel and Natural Gas," *SAE Technical Paper 2014-01-1318,* 2014.

[54] Y. Pei, M. Mehl, W. Liu, T. Lu, W. Pitz and S. Som, " Multicomponent Blend asa Diesel Fuel Surrogate for Compression Ignition Engine Applications," *ASME J. Eng. Gas Turbines and Power,* vol. 137, no. 11, pp. GTP-15-1057, 2015.

[55] D. Splitter, S. Kokjohn, K. Rein, R. Hanson, S. Sanders and R. D. Reitz, "An Optical Investigation of Ignition Processes in Fuel Reactivity Controlled PCCI Combustion," *SAE Int. J. Engines,* vol. 3, no. 1, pp. 142-162, 2010.

[56] R. Papagiannakis and D. Hountalas, "Experimental investigation concerning the effect of natural gas percentage on performance and emissions of a DI dual fuel diesel engine," *Applied Thermal Engineering,* vol. 23, pp. 353-365, 2003.

[57] R. G. Gilbert, K. Luther and J. Troe, "Theory of Thermal Unimolecular Reactions in the Fall-off Range. II. Weak Collision Rate Constants," *Ber. Bunsenges. Phys. Chem.,* vol. 87, no. 2, p. 169, 1983.

[58] Reaction Design, "CHEMKIN 10131: CHEMKIN Theory Manual," Reaction Design, San Diego, 2013.

[59] O. Badr, G. Karim and B. Liu, "An examination of the flame spread limits in a dual fuel engine," *Applied Thermal Engineering,* vol. 19, pp. 1071-1080, 2002.

[60] J. Beale and R. D. Reitz, "Modeling Spray Atomization with the Kelvin-Helmholtz/Rayleigh-Taylor Hybrid Model," *Atomization and Sprays,* vol. 9, pp. 623-650, 1999.

[61] J. Dec, "A Conceptual Model of DI Diesel Combustion Based on Laser-Sheet Imaging," *SAE Technical Paper 970873,* 1997.

[62] S. Cordiner, V. Rocco, R. Scarelli, M. Gambino and S. Iannacone, "Experiments and Multi-dimensional Simulation of Dual-Fuel Diesel/Natural Gas Engines," *SAE Technical Paper2007-24-0124,* 2007.

[63] M. Galal, M. Abdel All and M. El Kady, "A Comparative Study between Diesel and Dual-Fuel Engines," *Combustion Science and Technology,* vol. 174, pp. 241-256, 2002.

[64] C. Gunea, M. Razavi and G. Karim, "The Effects of Pilot Fuel Quality on Dual Fuel Engine Ignition Delay," *SAE Technical Paper 982453,* 1998.

[65] Z. Han and R. D. Reitz, "A Temperature Wall Function Formulation for Variable Density Turbulence Flow with Application to Engine Convective Heat Transfer Modeling," *International Journal of Heat and Mass Transfer,* vol. 40, pp. 613-625, 1997.

[66] S. Krishnan, K. Srinivasan, S. Singh, S. Bell and K. Midkiff, "Strategies for Reduced NOx Emissions in Pilot-Ignited Natural Gas Engines," *ASME J. Eng. Gas Tubines and Power,* vol. 126, pp. 665-671, 2004.

[67] R. Papagiannakis, D. Hountalas, C. Rakopoulos and D. Rakopoulos, "Combustion and Performance Characteristics of a DI Diesel Engine Operating from Low to High Natural Gas Supplement Ratios at Various Operating Conditions," *SAE Technical Paper 2008-01-1392,* 2008.

[68] R. Papagiannakis and D. Hountalas, "Combustion and exhaust emission characteristics of a dual fuel compression ignition engine operated with pilot Diesel fuel and natural gas," *Energy Conversion and Management,* vol. 45, pp. 2971-2987, 2004.

[69] S. Singh, L. Liang, S. Kong and R. D. Reitz, "Development of a Flame Propagation Model for Dual-Fuel Partially Premixed Compression Ignition Engines," *Int. J. Engine Research,* vol. 7, no. 1, pp. 65-75, 2006.

[70] S. Singh, R. D. Reitz, M. Musculus and T. Lachaux, "Validation of engine combustion models against detailed in-cylinder optical diagnostics data for a heavy-duty compression-ignition engine," *Int. J. Engine Research,* vol. 8, no. 1, pp. 97-126, 2007.

[71] K. Srinivasan, S. Krishnan, Y. Qi, K. Midkiff and H. Yang, "Analysis of Diesel Pilot-Ignited Natural Gas Low-Temperature Combustion with Hot Exhaust Gas Recirculation," *Combustion Science and Technology,* vol. 179, pp. 1737-1776, 2007.

[72] F. Konigsson, "Advancing the Limits of Dual Fuel Combustion," Department of Machine Design, Royal Institute of Technology, Stockholm, Sweden, 2012.

APPENDIX A: CSU141 NATURAL GAS/DIESEL DUAL FUEL MECHANISM

The following is a list of the chemical species and reactions that form the CSU141 reduced dual fuel mechanism for natural gas/diesel combustion, which was discussed in Chapter CHAPTER 6:. The list of reactions contains rate constant information in the Arrhenius form. Some of the reactions include third body efficiencies and Troe [57] pressure dependent reaction rates. More information about the format of the mechanism and expressions for rate constants can be found in the CHEMKIN® theory manual [58]. This reduced mechanism uses n-heptane to represent diesel fuel kinetics and a surrogate mixture of methane, ethane, and propane to represent the kinetics of natural gas. This mechanism is a combination of reduced forms of the methane through n-pentane mechanism of Healy et al. [37] and the n-heptane mechanism of Curran et al. [38] [39]. The detailed mechanisms were reduced using the direct relation graph with error propagation and sensitivity analysis (DRGEPSA), which is described in detail in the CONVERGE™ theory manual [21].

ELEMENTS CONSIDERED	ATOMIC WEIGHT
1. C	12.0112
2. H	1.00797
3. N	14.0067
4. O	15.9994
5. AR	39.9480
6. HE	4.00260

UNITS for the following reactions (unless otherwise noted):
A units mole-cm-sec-K, E units cal/mole

SPECIES CONSIDERED	PHASE	CHARGE	MOLECULAR WEIGHT	TEMPERATURE LOW	TEMPERATURE HIGH	ELEMENT COUNT C	H	N	O	AR	HE
1. H	G	0	1.0080E+00	300	5000	0	1	0	0	0	0
2. H2	G	0	2.0159E+00	300	5000	0	2	0	0	0	0
3. O	G	0	1.5999E+01	300	5000	0	0	0	1	0	0
4. O2	G	0	3.1999E+01	300	5000	0	0	0	2	0	0
5. OH	G	0	1.7007E+01	300	5000	0	1	0	1	0	0
6. H2O	G	0	1.8015E+01	300	5000	0	2	0	1	0	0
7. N2	G	0	2.8013E+01	300	5000	0	0	2	0	0	0
8. HO2	G	0	3.3007E+01	200	3500	0	1	0	2	0	0
9. H2O2	G	0	3.4015E+01	300	5000	0	2	0	2	0	0
10. AR	G	0	3.9948E+01	300	5000	0	0	0	0	1	0
11. CO	G	0	2.8011E+01	300	5000	1	0	0	1	0	0
12. CO2	G	0	4.4010E+01	300	5000	1	0	0	2	0	0
13. CH2O	G	0	3.0026E+01	300	5000	1	2	0	1	0	0
14. HCO	G	0	2.9019E+01	300	5000	1	1	0	1	0	0
15. HOCH2O	G	0	4.7034E+01	300	5000	1	3	0	2	0	0
16. CH3OH	G	0	3.2042E+01	300	5000	1	4	0	1	0	0
17. CH2OH	G	0	3.1034E+01	300	5000	1	3	0	1	0	0
18. CH3O	G	0	3.1034E+01	300	5000	1	3	0	1	0	0
19. CH3O2H	G	0	4.8042E+01	300	5000	1	4	0	2	0	0
20. CH3O2	G	0	4.7034E+01	300	5000	1	3	0	2	0	0
21. CH4	G	0	1.6043E+01	300	5000	1	4	0	0	0	0
22. CH3	G	0	1.5035E+01	300	5000	1	3	0	0	0	0
23. C2H6	G	0	3.0070E+01	300	5000	2	6	0	0	0	0
24. C2H5	G	0	2.9062E+01	300	5000	2	5	0	0	0	0
25. C2H4	G	0	2.8054E+01	300	5000	2	4	0	0	0	0
26. C2H3	G	0	2.7046E+01	300	5000	2	3	0	0	0	0
27. C2H2	G	0	2.6038E+01	300	5000	2	2	0	0	0	0
28. CH3CHO	G	0	4.4054E+01	300	5000	2	4	0	1	0	0
29. CH3CO	G	0	4.3046E+01	300	5000	2	3	0	1	0	0
30. CH2CHO	G	0	4.3046E+01	300	5000	2	3	0	1	0	0
31. CH2CO	G	0	4.2038E+01	300	5000	2	2	0	1	0	0
32. HCCO	G	0	4.1030E+01	300	4000	2	1	0	1	0	0
33. CH3CO3H	G	0	7.6052E+01	300	5000	2	4	0	3	0	0
34. CH3CO3	G	0	7.5044E+01	300	5000	2	3	0	3	0	0
35. CH3CO2	G	0	5.9045E+01	300	5000	2	3	0	2	0	0
36. C2H5O	G	0	4.5062E+01	300	5000	2	5	0	1	0	0
37. SC2H4OH	G	0	4.5062E+01	300	5000	2	5	0	1	0	0
38. C2H5O2H	G	0	6.2069E+01	300	5000	2	6	0	2	0	0
39. C2H5O2	G	0	6.1061E+01	300	5000	2	5	0	2	0	0
40. C2H3O1-2	G	0	4.3046E+01	300	5000	2	3	0	1	0	0
41. CH3COCH2	G	0	5.7073E+01	300	5000	3	5	0	1	0	0
42. CH3COCH2O2	G	0	8.9072E+01	300	5000	3	5	0	3	0	0
43. CH3COCH2O2H	G	0	9.0079E+01	300	5000	3	6	0	3	0	0
44. CH3COCH2O	G	0	7.3072E+01	300	5000	3	5	0	2	0	0
45. C2H3CHO	G	0	5.6065E+01	300	5000	3	4	0	1	0	0
46. C2H3CO	G	0	5.5057E+01	300	5000	3	3	0	1	0	0
47. C2H5CHO	G	0	5.8081E+01	300	5000	3	6	0	1	0	0
48. C2H5CO	G	0	5.7073E+01	300	5000	3	5	0	1	0	0
49. HE	G	0	4.0026E+00	300	5000	0	0	0	0	0	1
50. C3H8	G	0	4.4097E+01	300	5000	3	8	0	0	0	0
51. NC3H7	G	0	4.3089E+01	300	5000	3	7	0	0	0	0
52. C3H6	G	0	4.2081E+01	300	5000	3	6	0	0	0	0
53. C3H5-A	G	0	4.1073E+01	300	5000	3	5	0	0	0	0
54. C3H5-S	G	0	4.1073E+01	300	5000	3	5	0	0	0	0
55. C3H5O	G	0	5.7073E+01	300	5000	3	5	0	1	0	0
56. C3H6OOH1-2	G	0	7.5088E+01	300	5000	3	7	0	2	0	0
57. C3H6OOH2-1	G	0	7.5088E+01	300	5000	3	7	0	2	0	0
58. NC3H7O2H	G	0	7.6096E+01	300	5000	3	8	0	2	0	0
59. NC3H7O2	G	0	7.5088E+01	300	5000	3	7	0	2	0	0
60. NC3H7O	G	0	5.9089E+01	300	5000	3	7	0	1	0	0
61. C4H8-1	G	0	5.6108E+01	300	5000	4	8	0	0	0	0
62. PC4H9	G	0	5.7116E+01	300	5000	4	9	0	0	0	0
63. C4H71-3	G	0	5.5100E+01	300	5000	4	7	0	0	0	0
64. C4H6	G	0	5.4092E+01	300	5000	4	6	0	0	0	0
65. PC4H9O2	G	0	8.9115E+01	300	5000	4	9	0	2	0	0
66. PC4H9O	G	0	7.3116E+01	300	5000	4	9	0	1	0	0
67. C4H7O	G	0	7.1100E+01	300	5000	4	7	0	1	0	0
68. C4H8OOH1-3	G	0	8.9115E+01	300	5000	4	9	0	2	0	0
69. C4H8OOH1-3O2	G	0	1.2111E+02	300	5000	4	9	0	4	0	0
70. NC4KET13	G	0	1.0411E+02	300	5000	4	8	0	3	0	0
71. C2H5COCH2	G	0	7.1100E+01	300	5000	4	7	0	1	0	0
72. CH2CH2COCH3	G	0	7.1100E+01	300	5000	4	7	0	1	0	0

73. C2H3COCH3	G	0	7.0092E+01	300	5000	4	6	0	1	0	0
74. NC3H7CHO	G	0	7.2108E+01	300	5000	4	8	0	1	0	0
75. NC3H7CO	G	0	7.1100E+01	300	5000	4	7	0	1	0	0
76. C5H11-1	G	0	7.1143E+01	300	5000	5	11	0	0	0	0
77. C5H10-1	G	0	7.0135E+01	300	5000	5	10	0	0	0	0
78. C5H91-3	G	0	6.9127E+01	300	5000	5	9	0	0	0	0
79. C5H11O2-1	G	0	1.0314E+02	300	5000	5	11	0	2	0	0
80. C5H11O-1	G	0	8.7143E+01	300	5000	5	11	0	1	0	0
81. C5H10OOH1-3	G	0	1.0314E+02	300	5000	5	11	0	2	0	0
82. C5H10OOH1-3O2	G	0	1.3514E+02	300	5000	5	11	0	4	0	0
83. NC5KET13	G	0	1.1813E+02	300	5000	5	10	0	3	0	0
84. C6H13-1	G	0	8.5171E+01	300	5000	6	13	0	0	0	0
85. C6H12-1	G	0	8.4163E+01	300	5000	6	12	0	0	0	0
86. C6H13O2-1	G	0	1.1717E+02	300	5000	6	13	0	2	0	0
87. C6H12OOH1-3	G	0	1.1717E+02	300	5000	6	13	0	2	0	0
88. C6H12OOH1-3O2	G	0	1.4917E+02	300	5000	6	13	0	4	0	0
89. NC6KET13	G	0	1.3216E+02	300	5000	6	12	0	3	0	0
90. C6H13O-1	G	0	1.0117E+02	300	5000	6	13	0	1	0	0
91. NC4H9CHO	G	0	8.6135E+01	300	5000	5	10	0	1	0	0
92. NC4H9CO	G	0	8.5127E+01	300	5000	5	9	0	1	0	0
93. NC3H7COCH2	G	0	8.5127E+01	300	5000	5	9	0	1	0	0
94. C2H5COC2H4P	G	0	8.5127E+01	300	5000	5	9	0	1	0	0
95. NC7H16	G	0	1.0021E+02	300	5000	7	16	0	0	0	0
96. C7H15-1	G	0	9.9198E+01	300	5000	7	15	0	0	0	0
97. C7H15-2	G	0	9.9198E+01	300	5000	7	15	0	0	0	0
98. C7H15-3	G	0	9.9198E+01	300	5000	7	15	0	0	0	0
99. C7H15-4	G	0	9.9198E+01	300	5000	7	15	0	0	0	0
100. C7H14-1	G	0	9.8190E+01	300	5000	7	14	0	0	0	0
101. C7H14-2	G	0	9.8190E+01	300	5000	7	14	0	0	0	0
102. C7H14-3	G	0	9.8190E+01	300	5000	7	14	0	0	0	0
103. C7H131-3	G	0	9.7182E+01	300	5000	7	13	0	0	0	0
104. C7H133-1	G	0	9.7182E+01	300	5000	7	13	0	0	0	0
105. C7H133-5	G	0	9.7182E+01	300	5000	7	13	0	0	0	0
106. C7H13O1-3	G	0	1.1318E+02	300	5000	7	13	0	1	0	0
107. C7H15O2-1	G	0	1.3120E+02	300	5000	7	15	0	2	0	0
108. C7H15O2-2	G	0	1.3120E+02	300	5000	7	15	0	2	0	0
109. C7H15O2-3	G	0	1.3120E+02	300	5000	7	15	0	2	0	0
110. C7H15O2-4	G	0	1.3120E+02	300	5000	7	15	0	2	0	0
111. C7H15O2H-3	G	0	1.3220E+02	300	5000	7	16	0	2	0	0
112. C7H15O-1	G	0	1.1520E+02	300	5000	7	15	0	1	0	0
113. C7H15O-2	G	0	1.1520E+02	300	5000	7	15	0	1	0	0
114. C7H15O-3	G	0	1.1520E+02	300	5000	7	15	0	1	0	0
115. C7H15O-4	G	0	1.1520E+02	300	5000	7	15	0	1	0	0
116. C7H14OOH1-3	G	0	1.3120E+02	300	5000	7	15	0	2	0	0
117. C7H14OOH2-4	G	0	1.3120E+02	300	5000	7	15	0	2	0	0
118. C7H14OOH3-5	G	0	1.3120E+02	300	5000	7	15	0	2	0	0
119. C7H14OOH4-2	G	0	1.3120E+02	300	5000	7	15	0	2	0	0
120. C7H14OOH1-3O2	G	0	1.6320E+02	300	5000	7	15	0	4	0	0
121. C7H14OOH2-4O2	G	0	1.6320E+02	300	5000	7	15	0	4	0	0
122. C7H14OOH3-5O2	G	0	1.6320E+02	300	5000	7	15	0	4	0	0
123. C7H14OOH4-2O2	G	0	1.6320E+02	300	5000	7	15	0	4	0	0
124. C7H14O1-3	G	0	1.1419E+02	300	5000	7	14	0	1	0	0
125. C7H14O2-4	G	0	1.1419E+02	300	5000	7	14	0	1	0	0
126. NC7KET13	G	0	1.4619E+02	300	5000	7	14	0	3	0	0
127. NC7KET24	G	0	1.4619E+02	300	5000	7	14	0	3	0	0
128. NC7KET35	G	0	1.4619E+02	300	5000	7	14	0	3	0	0
129. NC7KET42	G	0	1.4619E+02	300	5000	7	14	0	3	0	0
130. C5H91-1	G	0	6.9127E+01	300	5000	5	9	0	0	0	0
131. CHCHCHO	G	0	5.5057E+01	300	5000	3	3	0	1	0	0
132. IC3H7	G	0	4.3089E+01	300	5000	3	7	0	0	0	0
133. C3H6OOH1-2O2	G	0	1.0709E+02	300	5000	3	7	0	4	0	0
134. C3H6OOH2-1O2	G	0	1.0709E+02	300	5000	3	7	0	4	0	0
135. IC3H7O	G	0	5.9089E+01	300	5000	3	7	0	1	0	0
136. C3KET12	G	0	9.0079E+01	300	5000	3	6	0	3	0	0
137. C3KET21	G	0	9.0079E+01	300	5000	3	6	0	3	0	0
138. C3H6OOH1-3	G	0	7.5088E+01	300	5000	3	7	0	2	0	0
139. C3H6OOH1-3O2	G	0	1.0709E+02	300	5000	3	7	0	4	0	0
140. IC3H7O2	G	0	7.5088E+01	300	5000	3	7	0	2	0	0
141. C3KET13	G	0	9.0079E+01	300	5000	3	6	0	3	0	0

REACTIONS CONSIDERED			(k = A T**b exp(-E/RT)) A	b	E
1. H+O2=O+OH			3.55E+15	-0.4	16600.0
Reverse Arrhenius coefficients:			1.03E+13	0.0	-133.0
2. O+H2=H+OH			5.08E+04	2.7	6292.0
Reverse Arrhenius coefficients:			2.64E+04	2.7	4880.0
3. OH+H2=H+H2O			2.16E+08	1.5	3430.0
Reverse Arrhenius coefficients:			2.29E+09	1.4	18320.0
4. O+H2O=OH+OH			2.97E+06	2.0	13400.0
Reverse Arrhenius coefficients:			1.45E+05	2.1	-2904.0
5. H2+M=H+H+M			4.58E+19	-1.4	104400.0
H2	Enhanced by	2.500E+00			
H2O	Enhanced by	1.200E+01			
CO	Enhanced by	1.900E+00			
CO2	Enhanced by	3.800E+00			
Reverse Arrhenius coefficients:			1.14E+20	-1.7	820.0
6. O2+M=O+O+M			4.42E+17	-0.6	118900.0
H2	Enhanced by	2.500E+00			
H2O	Enhanced by	1.200E+01			
AR	Enhanced by	8.300E-01			
CO	Enhanced by	1.900E+00			

```
    CO2             Enhanced by    3.800E+00
    CH4             Enhanced by    2.000E+00
    C2H6            Enhanced by    3.000E+00
    HE              Enhanced by    8.300E-01
    Reverse Arrhenius coefficients:              6.16E+15   -0.5        0.0
 7. OH+M=O+H+M                                    9.78E+17   -0.7   102100.0
    H2              Enhanced by    2.500E+00
    H2O             Enhanced by    1.200E+01
    AR              Enhanced by    7.500E-01
    CO              Enhanced by    1.500E+00
    CO2             Enhanced by    2.000E+00
    CH4             Enhanced by    2.000E+00
    C2H6            Enhanced by    3.000E+00
    HE              Enhanced by    7.500E-01
    Reverse Arrhenius coefficients:              4.71E+18   -1.0        0.0
 8. H2O+M=H+OH+M                                  1.91E+23   -1.8   118500.0
    H2              Enhanced by    7.300E-01
    H2O             Enhanced by    1.200E+01
    AR              Enhanced by    3.800E-01
    CH4             Enhanced by    2.000E+00
    C2H6            Enhanced by    3.000E+00
    HE              Enhanced by    3.800E-01
    Reverse Arrhenius coefficients:              4.50E+22   -2.0        0.0
 9. H+O2(+M)=HO2(+M)                              1.48E+12    0.6        0.0
    Low pressure limit:  0.34820E+17 -0.41100E+00 -0.11150E+04
    TROE centering:      0.50000E+00  0.10000E-29  0.10000E+31  0.10000E+11
    H2              Enhanced by    1.300E+00
    H2O             Enhanced by    1.400E+01
    AR              Enhanced by    6.700E-01
    CO              Enhanced by    1.900E+00
    CO2             Enhanced by    3.800E+00
    CH4             Enhanced by    2.000E+00
    C2H6            Enhanced by    3.000E+00
    HE              Enhanced by    6.700E-01
10. HO2+H=H2+O2                                   1.66E+13    0.0      823.0
    Reverse Arrhenius coefficients:              3.17E+12    0.3    55510.0
11. HO2+H=OH+OH                                   7.08E+13    0.0      295.0
    Reverse Arrhenius coefficients:              2.03E+10    0.7    36840.0
12. HO2+O=OH+O2                                   3.25E+13    0.0        0.0
    Reverse Arrhenius coefficients:              3.22E+12    0.3    53280.0
13. HO2+OH=H2O+O2                                 2.89E+13    0.0     -497.0
    Reverse Arrhenius coefficients:              5.84E+13    0.2    69080.0
14. H2O2+O2=HO2+HO2                               1.14E+16   -0.3    49730.0
    Reverse Arrhenius coefficients:              1.03E+14    0.0    11040.0
    Declared duplicate reaction...
15. H2O2+O2=HO2+HO2                               2.14E+13   -0.3    37280.0
    Reverse Arrhenius coefficients:              1.94E+11    0.0    -1409.0
    Declared duplicate reaction...
16. H2O2(+M)=OH+OH(+M)                            2.95E+14    0.0    48430.0
    Low pressure limit:  0.12020E+18  0.00000E+00  0.45500E+05
    TROE centering:      0.50000E+00  0.10000E-29  0.10000E+31  0.10000E+11
    H2              Enhanced by    2.500E+00
    H2O             Enhanced by    1.200E+01
    AR              Enhanced by    6.400E-01
    CO              Enhanced by    1.900E+00
    CO2             Enhanced by    3.800E+00
    CH4             Enhanced by    2.000E+00
    C2H6            Enhanced by    3.000E+00
    HE              Enhanced by    6.400E-01
17. H2O2+H=H2O+OH                                 2.41E+13    0.0     3970.0
    Reverse Arrhenius coefficients:              1.26E+08    1.3    71410.0
18. H2O2+H=H2+HO2                                 2.15E+10    1.0     6000.0
    Reverse Arrhenius coefficients:              3.72E+07    1.7    22000.0
19. H2O2+O=OH+HO2                                 9.55E+06    2.0     3970.0
    Reverse Arrhenius coefficients:              8.57E+03    2.7    18560.0
20. H2O2+OH=H2O+HO2                               2.00E+12    0.0      427.2
    Reverse Arrhenius coefficients:              3.66E+10    0.6    31320.0
    Declared duplicate reaction...
21. H2O2+OH=H2O+HO2                               1.70E+18    0.0    29410.0
    Reverse Arrhenius coefficients:              3.12E+16    0.6    60300.0
    Declared duplicate reaction...
22. CO+O(+M)=CO2(+M)                              1.80E+10    0.0     2384.0
    Low pressure limit:  0.13500E+25 -0.27880E+01  0.41910E+04
    H2              Enhanced by    2.000E+00
    O2              Enhanced by    6.000E+00
    H2O             Enhanced by    6.000E+00
    AR              Enhanced by    5.000E-01
    CO              Enhanced by    1.500E+00
    CO2             Enhanced by    3.500E+00
    CH4             Enhanced by    2.000E+00
    C2H6            Enhanced by    3.000E+00
    HE              Enhanced by    5.000E-01
23. CO+O2=CO2+O                                   1.05E+12    0.0    42540.0
    Reverse Arrhenius coefficients:              8.04E+15   -0.8    51230.0
24. CO+OH=CO2+H                                   1.78E+05    1.9    -1158.0
    Reverse Arrhenius coefficients:              4.72E+11    0.7    24260.0
25. CO+HO2=CO2+OH                                 1.57E+05    2.2    17940.0
    Reverse Arrhenius coefficients:              1.19E+08    1.7    79910.0
26. HCO+M=H+CO+M                                  4.75E+11    0.7    14870.0
    H2              Enhanced by    2.000E+00
    H2O             Enhanced by    1.200E+01
    CO              Enhanced by    1.500E+00
    CO2             Enhanced by    2.000E+00
    CH4             Enhanced by    2.000E+00
    C2H6            Enhanced by    3.000E+00
```

```
    Reverse Arrhenius coefficients:              3.58E+10    1.0     -457.3
27. HCO+O2=CO+HO2                                 7.58E+12    0.0      410.0
    Reverse Arrhenius coefficients:              1.20E+12    0.3    33950.0
28. HCO+H=CO+H2                                   7.34E+13    0.0        0.0
    Reverse Arrhenius coefficients:              2.21E+12    0.7    88230.0
29. HCO+O=CO+OH                                   3.02E+13    0.0        0.0
    Reverse Arrhenius coefficients:              4.72E+11    0.6    86820.0
30. HCO+O=CO2+H                                   3.00E+13    0.0        0.0
    Reverse Arrhenius coefficients:              1.24E+18   -0.6   112200.0
31. HCO+OH=CO+H2O                                 1.02E+14    0.0        0.0
    Reverse Arrhenius coefficients:              3.26E+13    0.6   103100.0
32. HCO+CH3=CH4+CO                                2.65E+13    0.0        0.0
    Reverse Arrhenius coefficients:              7.29E+14    0.2    89770.0
33. HCO+HO2=CH2O+O2                               2.50E+14   -0.1    13920.0
    Reverse Arrhenius coefficients:              8.07E+15    0.0    53420.0
34. HCO+HO2=CO2+H+OH                              3.00E+13    0.0        0.0
    Warning...all REV parameters are zero...          0.00000E+00 0.00000E+00 0.00000E+00
            this reaction will be treated as irreversible
35. CH2O+CO=HCO+HCO                               9.19E+13    0.4    73040.0
    Reverse Arrhenius coefficients:              1.80E+13    0.0        0.0
36. HCO+HCO=H2+CO+CO                              3.00E+12    0.0        0.0
    Warning...all REV parameters are zero...          0.00000E+00 0.00000E+00 0.00000E+00
            this reaction will be treated as irreversible
37. HCO+H(+M)=CH2O(+M)                            1.09E+12    0.5     -260.0
    Low pressure limit:  0.13500E+25 -0.25700E+01  0.14250E+04
    TROE centering:      0.78240E+00  0.27100E+03  0.27550E+04  0.65700E+04
    H2              Enhanced by    2.000E+00
    H2O             Enhanced by    6.000E+00
    AR              Enhanced by    7.000E-01
    CO              Enhanced by    1.500E+00
    CO2             Enhanced by    2.000E+00
    CH4             Enhanced by    2.000E+00
    C2H6            Enhanced by    3.000E+00
    HE              Enhanced by    7.000E-01
38. CO+H2(+M)=CH2O(+M)                            4.30E+07    1.5    79600.0
    Low pressure limit:  0.50700E+28 -0.34200E+01  0.84348E+05
    TROE centering:      0.93200E+00  0.19700E+03  0.15400E+04  0.10300E+05
    H2              Enhanced by    2.000E+00
    H2O             Enhanced by    6.000E+00
    AR              Enhanced by    7.000E-01
    CO              Enhanced by    1.500E+00
    CO2             Enhanced by    2.000E+00
    CH4             Enhanced by    2.000E+00
    C2H6            Enhanced by    3.000E+00
    HE              Enhanced by    7.000E-01
39. CH2O+OH=HCO+H2O                               7.82E+07    1.6    -1055.0
    Reverse Arrhenius coefficients:              4.90E+06    1.8    29030.0
40. CH2O+H=HCO+H2                                 5.74E+07    1.9     2740.0
    Reverse Arrhenius coefficients:              3.39E+05    2.2    17930.0
41. CH2O+O=HCO+OH                                 6.26E+09    1.1     2260.0
    Reverse Arrhenius coefficients:              1.92E+07    1.4    16040.0
42. CH2O+CH3=HCO+CH4                              3.83E+01    3.4     4312.0
    Reverse Arrhenius coefficients:              2.06E+02    3.2    21040.0
43. CH2O+HO2=HCO+H2O2                             7.10E-03    4.5     6580.0
    Reverse Arrhenius coefficients:              2.43E-02    4.1     5769.0
44. HOCH2O=CH2O+OH                                2.06E+21   -2.3    25730.0
    Reverse Arrhenius coefficients:              4.50E+15   -1.1        0.0
45. CH3O(+M)=CH2O+H(+M)                           6.80E+13    0.0    26170.0
    Low pressure limit:  0.18670E+26 -0.30000E+01  0.24307E+05
    TROE centering:      0.90000E+00  0.25000E+04  0.13000E+04  0.10000+100
    H2              Enhanced by    2.000E+00
    H2O             Enhanced by    6.000E+00
    CO              Enhanced by    1.500E+00
    CO2             Enhanced by    2.000E+00
    CH4             Enhanced by    2.000E+00
    C2H6            Enhanced by    3.000E+00
46. CH3O+O2=CH2O+HO2                              4.38E-19    9.5    -5501.0
    Reverse Arrhenius coefficients:              1.42E-20    9.8    21080.0
47. CH2O+CH3O=CH3OH+HCO                           6.62E+11    0.0     2294.0
    Reverse Arrhenius coefficients:              8.39E+10    0.1    17710.0
48. CH4+CH3O=CH3+CH3OH                            6.12E+02    2.9     8248.0
    Reverse Arrhenius coefficients:              1.44E+01    3.1     6935.0
49. CH3O+CH3=CH2O+CH4                             1.20E+13    0.0        0.0
    Reverse Arrhenius coefficients:              6.75E+13    0.2    82810.0
50. CH3O+H=CH2O+H2                                2.00E+13    0.0        0.0
    Reverse Arrhenius coefficients:              1.23E+11    0.7    81270.0
51. CH3O+HO2=CH2O+H2O2                            3.01E+11    0.0        0.0
    Reverse Arrhenius coefficients:              1.07E+12    0.0    65270.0
52. CH2O+H(+M)=CH2OH(+M)                          5.40E+11    0.5     3600.0
    Low pressure limit:  0.12700E+33 -0.48200E+01  0.65300E+04
    TROE centering:      0.71870E+00  0.10300E+03  0.12910E+04  0.41600E+04
    H2              Enhanced by    2.000E+00
    H2O             Enhanced by    6.000E+00
    CO              Enhanced by    1.500E+00
    CO2             Enhanced by    2.000E+00
    CH4             Enhanced by    2.000E+00
    C2H6            Enhanced by    3.000E+00
53. CH2OH+O2=CH2O+HO2                             1.51E+15   -1.0        0.0
    Reverse Arrhenius coefficients:              1.98E+14   -0.6    20060.0
    Declared duplicate reaction...
54. CH2OH+O2=CH2O+HO2                             2.41E+14    0.0     5017.0
    Reverse Arrhenius coefficients:              3.15E+13    0.4    25080.0
    Declared duplicate reaction...
55. CH2OH+H=CH2O+H2                               6.00E+12    0.0        0.0
    Reverse Arrhenius coefficients:              1.50E+11    0.8    74750.0
```

```
56. CH2OH+HO2=CH2O+H2O2                           1.20E+13    0.0        0.0
    Reverse Arrhenius coefficients:               1.73E+14    0.1    58750.0
57. CH2OH+HCO=CH2O+CH2O                           1.80E+14    0.0        0.0
    Reverse Arrhenius coefficients:               7.60E+14    0.5    59560.0
58. CH2OH+CH3O=CH2O+CH3OH                         2.40E+13    0.0        0.0
    Reverse Arrhenius coefficients:               1.28E+13    0.6    74980.0
59. CH2OH+CH2O=CH3OH+HCO                          1.88E+04    2.7     4208.0
    Reverse Arrhenius coefficients:               9.63E+03    2.9    13110.0
60. OH+CH2OH=H2O+CH2O                             2.40E+13    0.0        0.0
    Reverse Arrhenius coefficients:               6.35E+12    0.7    89640.0
61. O+CH2OH=OH+CH2O                               4.20E+13    0.0        0.0
    Reverse Arrhenius coefficients:               5.44E+11    0.7    73340.0
62. CH2O+CH3OH=CH2OH+CH2OH                        6.50E+12    0.7    68460.0
    Reverse Arrhenius coefficients:               3.00E+12    0.0        0.0
63. CH2OH+HO2=HOCH2O+OH                           1.00E+13    0.0        0.0
    Reverse Arrhenius coefficients:               8.17E+13    0.0    33470.0
64. CH3OH(+M)=CH3+OH(+M)                          1.90E+16    0.0    91730.0
    Low pressure limit:  0.29500E+45 -0.73500E+01  0.95460E+05
    TROE centering:      0.41400E+00  0.27900E+03  0.54590E+04  0.10000E+11
65. CH3OH(+M)=CH2OH+H(+M)                         2.69E+16   -0.1    98940.0
    Low pressure limit:  0.23400E+41 -0.63300E+01  0.10310E+06
    TROE centering:      0.77300E+00  0.69300E+03  0.53330E+04  0.10000E+11
66. CH3OH+H=CH3O+H2                               3.60E+12    0.0     6095.0
    Reverse Arrhenius coefficients:               1.68E+11    0.2     5868.0
67. CH3OH+H=CH2OH+H2                              1.20E+06    2.4     2583.0
    Reverse Arrhenius coefficients:               1.39E+04    2.5     8871.0
68. CH3OH+O=CH2OH+OH                              3.88E+05    2.5     3080.0
    Reverse Arrhenius coefficients:               2.32E+03    2.6     7956.0
69. CH3OH+OH=CH3O+H2O                             5.13E+05    2.1     2450.0
    Reverse Arrhenius coefficients:               2.53E+05    2.2    17120.0
70. CH3OH+OH=CH2OH+H2O                            1.44E+06    2.0     -839.0
    Reverse Arrhenius coefficients:               1.76E+05    2.0    20340.0
71. CH3OH+O2=CH2OH+HO2                            2.05E+13    0.0    44900.0
    Reverse Arrhenius coefficients:               1.24E+12   -0.2    -3501.0
72. CH3OH+HO2=CH2OH+H2O2                          1.08E+04    2.5    10530.0
    Reverse Arrhenius coefficients:               7.20E+04    2.0      819.0
73. CH3OH+CH3=CH2OH+CH4                           3.19E+01    3.2     7172.0
    Reverse Arrhenius coefficients:               3.35E+02    2.8    15000.0
74. CH3O+CH3OH=CH2OH+CH3OH                        3.00E+11    0.0     4074.0
    Reverse Arrhenius coefficients:               7.42E+10   -0.1    10590.0
75. CH3OH+CH2O=CH3O+CH3O                          7.98E+12    0.5    81490.0
    Reverse Arrhenius coefficients:               6.03E+13    0.0        0.0
76. CH3+H(+M)=CH4(+M)                             1.27E+16   -0.6      383.0
    Low pressure limit:  0.19816E+34 -0.47600E+01  0.24440E+04
    TROE centering:      0.78300E+00  0.74000E+02  0.29400E+04  0.69600E+04
    H2              Enhanced by    2.000E+00
    H2O             Enhanced by    6.000E+00
    AR              Enhanced by    7.000E-01
    CO              Enhanced by    1.500E+00
    CO2             Enhanced by    2.000E+00
    CH4             Enhanced by    2.000E+00
    C2H6            Enhanced by    3.000E+00
    HE              Enhanced by    7.000E-01
77. CH4+H=CH3+H2                                  6.14E+05    2.5     9587.0
    Reverse Arrhenius coefficients:               6.73E+02    2.9     8047.0
78. CH4+OH=CH3+H2O                                5.83E+04    2.6     2190.0
    Reverse Arrhenius coefficients:               6.78E+02    2.9    15540.0
79. CH4+O=CH3+OH                                  1.02E+09    1.5     8600.0
    Reverse Arrhenius coefficients:               5.80E+05    1.9     5648.0
80. CH4+HO2=CH3+H2O2                              1.13E+01    3.7    21010.0
    Reverse Arrhenius coefficients:               7.17E+00    3.5     3468.0
81. CH3+OH=CH2O+H2                                8.00E+09    0.5    -1755.0
    Reverse Arrhenius coefficients:               1.07E+12    0.3    68210.0
82. CH3+OH=CH3O+H                                 6.94E+07    1.3    11200.0
    Reverse Arrhenius coefficients:               1.50E+12    0.5     -110.0
83. CH3+OH=CH2OH+H                                3.09E+07    1.6     4506.0
    Reverse Arrhenius coefficients:               1.65E+11    0.7     -284.0
84. CH3+HO2=CH3O+OH                               1.00E+12    0.3     -687.5
    Reverse Arrhenius coefficients:               6.19E+12    0.1    24550.0
85. CH3+HO2=CH4+O2                                1.16E+05    2.2    -3022.0
    Reverse Arrhenius coefficients:               2.02E+07    2.1    53210.0
86. CH3+O=CH2O+H                                  5.54E+13    0.1     -136.0
    Reverse Arrhenius coefficients:               3.83E+15   -0.1    68410.0
87. CH3+O2=CH3O+O                                 7.55E+12    0.0    28320.0
    Reverse Arrhenius coefficients:               4.72E+14   -0.5      288.0
88. CH3+O2=CH2O+OH                                2.64E+00    3.3     8105.0
    Reverse Arrhenius coefficients:               5.28E-01    3.5    59920.0
89. CH3+O2(+M)=CH3O2(+M)                          7.81E+09    0.9        0.0
    Low pressure limit:  0.68500E+25 -0.30000E+01  0.00000E+00
    TROE centering:      0.60000E+00  0.10000E+04  0.70000E+02  0.17000E+04
90. CH3O2+CH2O=CH3O2H+HCO                         1.99E+12    0.0    11660.0
    Reverse Arrhenius coefficients:               1.32E+14   -0.9     9259.0
91. CH4+CH3O2=CH3+CH3O2H                          1.81E+11    0.0    18480.0
    Reverse Arrhenius coefficients:               2.23E+12   -0.7     -655.0
92. CH3OH+CH3O2=CH2OH+CH3O2H                      1.81E+12    0.0    13710.0
    Reverse Arrhenius coefficients:               2.35E+14   -1.0     2404.0
93. CH3O2+CH3=CH3O+CH3O                           5.08E+12    0.0    -1411.0
    Reverse Arrhenius coefficients:               1.97E+12    0.2    28070.0
94. CH3O2+HO2=CH3O2H+O2                           2.47E+11    0.0    -1570.0
    Reverse Arrhenius coefficients:               5.30E+14   -0.8    35520.0
95. CH3O2+CH3O2=CH2O+CH3OH+O2                     3.11E+14   -1.6    -1051.0
    Warning...all REV parameters are zero...          0.00000E+00 0.00000E+00 0.00000E+00
              this reaction will be treated as irreversible
96. CH3O2+CH3O2=O2+CH3O+CH3O                      1.40E+16   -1.6     1860.0
    Warning...all REV parameters are zero...          0.00000E+00 0.00000E+00 0.00000E+00
```

```
              this reaction will be treated as irreversible
 97. CH3O2+H=CH3O+OH                                   9.60E+13    0.0        0.0
     Reverse Arrhenius coefficients:                  1.72E+09    1.0    40780.0
 98. CH3O2+O=CH3O+O2                                   3.60E+13    0.0        0.0
     Reverse Arrhenius coefficients:                  2.23E+11    0.6    57520.0
 99. CH3O2+OH=CH3OH+O2                                 6.00E+13    0.0        0.0
     Reverse Arrhenius coefficients:                  1.54E+13    0.4    59160.0
100. CH3O2H=CH3O+OH                                    6.31E+14    0.0    42300.0
     Reverse Arrhenius coefficients:                  2.51E+06    1.9    -2875.0
101. CH3+CH3(+M)=C2H6(+M)                              9.21E+16   -1.2      635.8
     Low pressure limit:  0.11350E+37 -0.52460E+01  0.17050E+04
     TROE centering:      0.40500E+00  0.11200E+04  0.69600E+02  0.10000E+11
     H2              Enhanced by    2.000E+00
     H2O             Enhanced by    6.000E+00
     AR              Enhanced by    7.000E-01
     CO              Enhanced by    1.500E+00
     CO2             Enhanced by    2.000E+00
     CH4             Enhanced by    2.000E+00
     C2H6            Enhanced by    3.000E+00
     HE              Enhanced by    7.000E-01
102. C2H5+H(+M)=C2H6(+M)                               5.21E+17   -1.0     1580.0
     Low pressure limit:  0.19900E+42 -0.70800E+01  0.66850E+04
     TROE centering:      0.84200E+00  0.12500E+03  0.22190E+04  0.68820E+04
     H2              Enhanced by    2.000E+00
     H2O             Enhanced by    6.000E+00
     AR              Enhanced by    7.000E-01
     CO              Enhanced by    1.500E+00
     CO2             Enhanced by    2.000E+00
     CH4             Enhanced by    2.000E+00
     C2H6            Enhanced by    3.000E+00
     HE              Enhanced by    7.000E-01
103. C2H6+H=C2H5+H2                                    1.15E+08    1.9     7530.0
     Reverse Arrhenius coefficients:                  1.06E+04    2.6     9760.0
104. C2H6+O=C2H5+OH                                    3.55E+06    2.4     5830.0
     Reverse Arrhenius coefficients:                  1.70E+02    3.1     6648.0
105. C2H6+OH=C2H5+H2O                                  1.48E+07    1.9      950.0
     Reverse Arrhenius coefficients:                  1.45E+04    2.5    18070.0
106. C2H6+O2=C2H5+HO2                                  6.03E+13    0.0    51870.0
     Reverse Arrhenius coefficients:                  2.92E+10    0.3     -593.0
107. C2H6+CH3=C2H5+CH4                                 5.48E-01    4.0     8280.0
     Reverse Arrhenius coefficients:                  4.62E-02    4.2    12050.0
108. C2H6+HO2=C2H5+H2O2                                6.92E+01    3.6    16920.0
     Reverse Arrhenius coefficients:                  3.70E+00    3.6     3151.0
109. C2H6+CH3O2=C2H5+CH3O2H                            1.94E+01    3.6    17100.0
     Reverse Arrhenius coefficients:                  2.02E+01    3.2     1734.0
110. C2H6+CH3O=C2H5+CH3OH                              2.41E+11    0.0     7090.0
     Reverse Arrhenius coefficients:                  4.78E+08    0.5     9547.0
111. C2H4+H(+M)=C2H5(+M)                               1.08E+12    0.5     1822.0
     Low pressure limit:  0.12000E+43 -0.76200E+01  0.69700E+04
     TROE centering:      0.97500E+00  0.21000E+03  0.98400E+03  0.43740E+04
     H2              Enhanced by    2.000E+00
     H2O             Enhanced by    6.000E+00
     AR              Enhanced by    7.000E-01
     CO              Enhanced by    1.500E+00
     CO2             Enhanced by    2.000E+00
     CH4             Enhanced by    2.000E+00
     C2H6            Enhanced by    3.000E+00
     HE              Enhanced by    7.000E-01
112. H2+CH3O2=H+CH3O2H                                 1.50E+14    0.0    26030.0
     Reverse Arrhenius coefficients:                  1.69E+18   -1.1     8434.0
113. H2+C2H5O2=H+C2H5O2H                               1.50E+14    0.0    26030.0
     Reverse Arrhenius coefficients:                  1.69E+18   -1.1     8438.0
114. C2H5+C2H3=C2H4+C2H4                               6.86E+11    0.1    -4300.0
     Reverse Arrhenius coefficients:                  4.82E+14    0.0    71530.0
115. CH3+C2H5=CH4+C2H4                                 1.18E+04    2.5    -2921.0
     Reverse Arrhenius coefficients:                  2.39E+06    2.4    66690.0
116. C2H5+H=CH3+CH3                                    9.69E+13    0.0      220.0
     Reverse Arrhenius coefficients:                  2.03E+09    1.0    10510.0
117. C2H5+H=C2H4+H2                                    2.00E+12    0.0        0.0
     Reverse Arrhenius coefficients:                  4.44E+11    0.4    68070.0
118. C2H5+O=CH3CHO+H                                   1.10E+14    0.0        0.0
     Reverse Arrhenius coefficients:                  1.03E+17   -0.5    77420.0
119. C2H5+HO2=C2H5O+OH                                 1.10E+13    0.0        0.0
     Reverse Arrhenius coefficients:                  9.68E+15   -0.7    27650.0
120. CH3O2+C2H5=CH3O+C2H5O                             8.00E+12    0.0    -1000.0
     Reverse Arrhenius coefficients:                  4.40E+14   -0.4    30890.0
121. C2H5O+O2=CH3CHO+HO2                               4.28E+10    0.0     1097.0
     Reverse Arrhenius coefficients:                  1.32E+08    0.6    34130.0
122. C2H5O=CH3+CH2O                                    1.32E+20   -2.0    20750.0
     Reverse Arrhenius coefficients:                  3.00E+11    0.0     6336.0
123. C2H5O=CH3CHO+H                                    5.43E+15   -0.7    22230.0
     Reverse Arrhenius coefficients:                  8.00E+12    0.0     6400.0
124. C2H5O2=C2H5+O2                                    1.31E+62  -14.8    49180.0
     Reverse Arrhenius coefficients:                  2.88E+56  -13.8    14620.0
125. C2H5O2+CH2O=C2H5O2H+HCO                           1.99E+12    0.0    11660.0
     Reverse Arrhenius coefficients:                  1.32E+14   -0.9     9263.0
126. CH4+C2H5O2=CH3+C2H5O2H                            1.81E+11    0.0    18480.0
     Reverse Arrhenius coefficients:                  2.24E+12   -0.7     -651.0
127. CH3OH+C2H5O2=CH2OH+C2H5O2H                        1.81E+12    0.0    13710.0
     Reverse Arrhenius coefficients:                  2.35E+14   -1.0     2408.0
128. C2H5O2+HO2=C2H5O2H+O2                             1.75E+10    0.0    -3275.0
     Reverse Arrhenius coefficients:                  3.76E+13   -0.8    33820.0
129. C2H6+C2H5O2=C2H5+C2H5O2H                          8.60E+00    3.8    17200.0
     Reverse Arrhenius coefficients:                  8.96E+00    3.3     1838.0
130. C2H5O2H=C2H5O+OH                                  6.31E+14    0.0    42300.0
```

```
     Reverse Arrhenius coefficients:              5.66E+08    1.0    -1705.0
131. C2H5+O2=C2H4+HO2                              3.78E+14   -1.0     4749.0
     Reverse Arrhenius coefficients:              4.40E+14   -1.0    18130.0
     Declared duplicate reaction...
132. C2H5+O2=C2H4+HO2                              4.00E-01    3.9    13620.0
     Reverse Arrhenius coefficients:              4.66E-01    3.9    27000.0
     Declared duplicate reaction...
133. C2H5+O2=CH3CHO+OH                             8.26E+02    2.4     5285.0
     Reverse Arrhenius coefficients:              2.25E+03    2.3    65970.0
134. C2H5O2=CH3CHO+OH                              2.52E+41  -10.2    43710.0
     Reverse Arrhenius coefficients:              1.50E+36   -9.3    69840.0
135. C2H5O2=C2H4+HO2                               1.82E+38   -8.4    37890.0
     Reverse Arrhenius coefficients:              4.63E+32   -7.4    16700.0
136. C2H3O1-2=CH3CO                                8.50E+14    0.0    14000.0
     Reverse Arrhenius coefficients:              1.00E+14    0.0    48710.0
137. C2H3O1-2=CH2CHO                               1.00E+14    0.0    14000.0
     Reverse Arrhenius coefficients:              1.24E+15   -0.4    44010.0
138. CH3CHO=CH3+HCO                                7.69E+20   -1.3    86950.0
     Reverse Arrhenius coefficients:              1.75E+13    0.0        0.0
139. CH3CHO+H=CH3CO+H2                             2.37E+13    0.0     3642.0
     Reverse Arrhenius coefficients:              1.64E+10    0.6    17600.0
140. CH3CHO+O=CH3CO+OH                             5.94E+12    0.0     1868.0
     Reverse Arrhenius coefficients:              2.13E+09    0.6    14410.0
141. CH3CHO+OH=CH3CO+H2O                           3.37E+12    0.0     -619.0
     Reverse Arrhenius coefficients:              2.47E+10    0.5    28230.0
142. CH3CHO+O2=CH3CO+HO2                           3.01E+13    0.0    39150.0
     Reverse Arrhenius coefficients:              1.09E+11    0.3    -1588.0
143. CH3CHO+CH3=CH3CO+CH4                          7.08E-04    4.6     1966.0
     Reverse Arrhenius coefficients:              4.47E-04    4.8    17460.0
144. CH3CHO+HO2=CH3CO+H2O2                         3.01E+12    0.0    11920.0
     Reverse Arrhenius coefficients:              1.20E+12   -0.1     9877.0
145. CH3O2+CH3CHO=CH3O2H+CH3CO                     3.01E+12    0.0    11920.0
     Reverse Arrhenius coefficients:              2.34E+13   -0.5     8282.0
146. CH3CHO+CH3CO3=CH3CO+CH3CO3H                   3.01E+12    0.0    11920.0
     Reverse Arrhenius coefficients:              1.92E+12    0.0    12650.0
147. CH3CHO+OH=CH2CHO+H2O                          1.72E+05    2.4      815.0
     Reverse Arrhenius coefficients:              1.33E+05    2.5    24950.0
148. CH3CO(+M)=CH3+CO(+M)                          3.00E+12    0.0    16720.0
     Low pressure limit:  0.12000E+16  0.00000E+00  0.12518E+05
149. CH3CO+H=CH2CO+H2                              2.00E+13    0.0        0.0
     Reverse Arrhenius coefficients:              1.04E+13    0.2    60560.0
150. CH3CO+O=CH2CO+OH                              2.00E+13    0.0        0.0
     Reverse Arrhenius coefficients:              5.38E+12    0.2    59140.0
151. CH3CO+CH3=CH2CO+CH4                           5.00E+13    0.0        0.0
     Reverse Arrhenius coefficients:              2.36E+16   -0.2    62100.0
152. CH3CO3=CH3CO+O2                               6.86E+19   -1.9    38530.0
     Reverse Arrhenius coefficients:              1.20E+11    0.0    -1100.0
153. CH3CO3+HO2=CH3CO3H+O2                         1.75E+10    0.0    -3275.0
     Reverse Arrhenius coefficients:              3.08E+12   -0.3    38180.0
154. H2O2+CH3CO3=HO2+CH3CO3H                       2.41E+12    0.0     9936.0
     Reverse Arrhenius coefficients:              3.84E+12    0.1    12710.0
155. CH4+CH3CO3=CH3+CH3CO3H                        1.81E+11    0.0    18480.0
     Reverse Arrhenius coefficients:              1.83E+11   -0.2     3711.0
156. CH2O+CH3CO3=HCO+CH3CO3H                       1.99E+12    0.0    11660.0
     Reverse Arrhenius coefficients:              1.08E+13   -0.4    13620.0
157. C2H6+CH3CO3=C2H5+CH3CO3H                      1.70E+13    0.0    20460.0
     Reverse Arrhenius coefficients:              1.45E+12    0.0     9460.0
158. CH3CO3H=CH3CO2+OH                             5.01E+14    0.0    40150.0
     Reverse Arrhenius coefficients:              3.62E+07    1.8     1338.0
159. CH3CO2+M=CH3+CO2+M                            4.40E+15    0.0    10500.0
     Reverse Arrhenius coefficients:              4.55E+08    1.4    17520.0
160. CH2CHO=CH2CO+H                                4.07E+15   -0.3    50600.0
     Reverse Arrhenius coefficients:              5.00E+13    0.0    12300.0
161. CH2CHO+O2=CH2O+CO+OH                          8.95E+13   -0.6    10120.0
     Warning...all REV parameters are zero...          0.00000E+00 0.00000E+00 0.00000E+00
               this reaction will be treated as irreversible
162. CH2CO+H=CH3+CO                                1.10E+13    0.0     3400.0
     Reverse Arrhenius coefficients:              2.40E+12    0.0    40200.0
163. CH2CO+H=HCCO+H2                               2.00E+14    0.0     8000.0
     Reverse Arrhenius coefficients:              1.43E+11    0.5     4520.0
164. CH2CO+O=HCCO+OH                               1.00E+13    0.0     8000.0
     Reverse Arrhenius coefficients:              3.72E+09    0.5     3108.0
165. CH2CO+OH=HCCO+H2O                             1.00E+13    0.0     2000.0
     Reverse Arrhenius coefficients:              7.60E+10    0.4    13410.0
166. CH2CO+OH=CH2OH+CO                             2.00E+12    0.0    -1010.0
     Reverse Arrhenius coefficients:              8.17E+09    0.5    24530.0
167. HCCO+OH=H2+CO+CO                              1.00E+14    0.0        0.0
     Warning...all REV parameters are zero...          0.00000E+00 0.00000E+00 0.00000E+00
               this reaction will be treated as irreversible
168. HCCO+O=H+CO+CO                                8.00E+13    0.0        0.0
     Warning...all REV parameters are zero...          0.00000E+00 0.00000E+00 0.00000E+00
               this reaction will be treated as irreversible
169. HCCO+O2=OH+CO+CO                              4.20E+10    0.0      850.0
     Warning...all REV parameters are zero...          0.00000E+00 0.00000E+00 0.00000E+00
               this reaction will be treated as irreversible
170. C2H3+H(+M)=C2H4(+M)                           6.08E+12    0.3      280.0
     Low pressure limit:  0.14000E+31 -0.38600E+01  0.33200E+04
     TROE centering:      0.78200E+00  0.20750E+03  0.26630E+04  0.60950E+04
     H2              Enhanced by    2.000E+00
     H2O             Enhanced by    6.000E+00
     AR              Enhanced by    7.000E-01
     CO              Enhanced by    1.500E+00
     CO2             Enhanced by    2.000E+00
     CH4             Enhanced by    2.000E+00
     C2H6            Enhanced by    3.000E+00
```

```
     HE              Enhanced by    7.000E-01
171. C2H4(+M)=C2H2+H2(+M)                          8.00E+12    0.4    88770.0
     Low pressure limit:  0.70000E+51 -0.93100E+01  0.99860E+05
     TROE centering:      0.73450E+00  0.18000E+03  0.10350E+04  0.54170E+04
     H2              Enhanced by    2.000E+00
     H2O             Enhanced by    6.000E+00
     AR              Enhanced by    7.000E-01
     CO              Enhanced by    1.500E+00
     CO2             Enhanced by    2.000E+00
     CH4             Enhanced by    2.000E+00
     C2H6            Enhanced by    3.000E+00
     HE              Enhanced by    7.000E-01
172. C2H4+H=C2H3+H2                                5.07E+07    1.9    12950.0
     Reverse Arrhenius coefficients:               1.60E+04    2.4     5190.0
173. C2H4+O=CH3+HCO                                8.56E+06    1.9      183.0
     Reverse Arrhenius coefficients:               3.30E+02    2.6    26140.0
174. C2H4+O=CH2CHO+H                               4.99E+06    1.9      183.0
     Reverse Arrhenius coefficients:               1.54E+09    1.2    18780.0
175. C2H4+OH=C2H3+H2O                              1.80E+06    2.0     2500.0
     Reverse Arrhenius coefficients:               6.03E+03    2.4     9632.0
176. C2H4+CH3=C2H3+CH4                             6.62E+00    3.7     9500.0
     Reverse Arrhenius coefficients:               1.91E+00    3.8     3280.0
177. C2H4+O2=C2H3+HO2                              4.00E+13    0.0    58200.0
     Reverse Arrhenius coefficients:               6.63E+10    0.2    -4249.0
178. C2H4+CH3O=C2H3+CH3OH                          1.20E+11    0.0     6750.0
     Reverse Arrhenius coefficients:               8.14E+08    0.3     -783.0
179. C2H4+CH3O2=C2H3+CH3O2H                        2.23E+12    0.0    17190.0
     Reverse Arrhenius coefficients:               7.93E+12   -0.6    -8167.0
180. C2H4+C2H5O2=C2H3+C2H5O2H                      2.23E+12    0.0    17190.0
     Reverse Arrhenius coefficients:               7.94E+12   -0.6    -8163.0
181. C2H4+CH3CO3=C2H3+CH3CO3H                      1.13E+13    0.0    30430.0
     Reverse Arrhenius coefficients:               3.30E+12   -0.1     9440.0
182. C2H3(+M)=C2H2+H(+M)                           3.86E+08    1.6    37050.0
     Low pressure limit:  0.25650E+28 -0.34000E+01  0.35799E+05
     TROE centering:      0.19816E+01  0.53837E+04  0.42932E+01 -0.79500E-01
     H2              Enhanced by    2.000E+00
     H2O             Enhanced by    6.000E+00
     AR              Enhanced by    7.000E-01
     CO              Enhanced by    1.500E+00
     CO2             Enhanced by    2.000E+00
     CH4             Enhanced by    2.000E+00
     C2H6            Enhanced by    3.000E+00
     HE              Enhanced by    7.000E-01
183. C2H3+O2=C2H2+HO2                              5.19E+15   -1.2     3310.0
     Reverse Arrhenius coefficients:               2.66E+16   -1.3    17860.0
184. C2H3+O2=CH2O+HCO                              8.50E+28   -5.3     6500.0
     Reverse Arrhenius coefficients:               3.99E+27   -4.9    93450.0
185. C2H3+O2=CH2CHO+O                              5.50E+14   -0.6     5260.0
     Reverse Arrhenius coefficients:               3.00E+18   -1.4    16300.0
186. CH3+C2H3=CH4+C2H2                             3.92E+11    0.0        0.0
     Reverse Arrhenius coefficients:               3.50E+14   -0.2    70780.0
187. C2H3+H=C2H2+H2                                9.64E+13    0.0        0.0
     Reverse Arrhenius coefficients:               9.43E+13    0.3    69240.0
188. C2H3+OH=C2H2+H2O                              3.01E+13    0.0        0.0
     Reverse Arrhenius coefficients:               3.12E+14    0.1    84130.0
189. C2H2+O2=HCCO+OH                               2.00E+08    1.5    30100.0
     Reverse Arrhenius coefficients:               2.04E+06    1.5    32270.0
190. C2H2+O=HCCO+H                                 5.30E+04    2.7     2360.0
     Reverse Arrhenius coefficients:               1.87E+05    2.3    21260.0
191. C2H2+OH=CH2CO+H                               3.24E+13    0.0    12000.0
     Reverse Arrhenius coefficients:               3.06E+17   -0.8    35790.0
192. C2H2+OH=CH3+CO                                4.83E-04    4.0    -2000.0
     Reverse Arrhenius coefficients:               3.49E-06    4.6    52120.0
193. CH3COCH2=CH2CO+CH3                            1.00E+14    0.0    31000.0
     Reverse Arrhenius coefficients:               1.00E+11    0.0     6000.0
194. CH3COCH2O2=CH3COCH2+O2                        2.02E+15   -1.0    24460.0
     Reverse Arrhenius coefficients:               1.20E+11    0.0    -1100.0
195. CH2O+CH3COCH2O2=HCO+CH3COCH2O2H               1.29E+11    0.0     9000.0
     Reverse Arrhenius coefficients:               2.51E+10    0.0    10100.0
196. HO2+CH3COCH2O2=CH3COCH2O2H+O2                 1.00E+12    0.0        0.0
     Warning...all REV parameters are zero...          0.00000E+00 0.00000E+00 0.00000E+00
              this reaction will be treated as irreversible
197. CH3COCH2O2H=CH3COCH2O+OH                      1.00E+16    0.0    43000.0
     Reverse Arrhenius coefficients:               4.24E+08    1.7    -4342.0
198. CH3COCH2O=CH3CO+CH2O                          3.73E+20   -2.2    17260.0
     Reverse Arrhenius coefficients:               1.00E+11    0.0    11900.0
199. C2H3CHO=C2H3+HCO                              2.00E+24   -2.1   103400.0
     Reverse Arrhenius coefficients:               1.81E+13    0.0        0.0
200. C2H3CHO+H=C2H3CO+H2                           1.34E+13    0.0     3300.0
     Reverse Arrhenius coefficients:               3.31E+10    0.6    22680.0
201. C2H3CHO+O=C2H3CO+OH                           5.94E+12    0.0     1868.0
     Reverse Arrhenius coefficients:               7.62E+09    0.6    19840.0
202. C2H3CHO+OH=C2H3CO+H2O                         9.24E+06    1.5     -962.0
     Reverse Arrhenius coefficients:               2.42E+05    2.0    33310.0
203. C2H3CHO+O2=C2H3CO+HO2                         1.00E+13    0.0    40700.0
     Reverse Arrhenius coefficients:               1.30E+11    0.3     5391.0
204. C2H3CHO+HO2=C2H3CO+H2O2                       3.01E+12    0.0    11920.0
     Reverse Arrhenius coefficients:               4.30E+12   -0.1    15300.0
205. C2H3CHO+CH3=C2H3CO+CH4                        2.61E+06    1.8     5911.0
     Reverse Arrhenius coefficients:               5.88E+06    1.9    26830.0
206. C2H3CHO+C2H3=C2H3CO+C2H4                      1.74E+12    0.0     8440.0
     Reverse Arrhenius coefficients:               1.00E+13    0.0    28000.0
207. C2H3CHO+CH3O=C2H3CO+CH3OH                     1.00E+12    0.0     3300.0
     Reverse Arrhenius coefficients:               5.30E+10    0.4    22910.0
208. C2H3CHO+CH3O2=C2H3CO+CH3O2H                   3.01E+12    0.0    11920.0
```

```
     Reverse Arrhenius coefficients:              8.37E+13   -0.5    13710.0
209. C2H3CO=C2H3+CO                                1.37E+21   -2.2    39410.0
     Reverse Arrhenius coefficients:              1.51E+11    0.0     4810.0
210. C2H5CHO=C2H5+HCO                              1.50E+27   -3.2    87040.0
     Reverse Arrhenius coefficients:              1.81E+13    0.0        0.0
211. C2H5CHO+H=C2H5CO+H2                           4.00E+13    0.0     4200.0
     Reverse Arrhenius coefficients:              2.38E+10    0.7    18130.0
212. C2H5CHO+O=C2H5CO+OH                           5.00E+12    0.0     1790.0
     Reverse Arrhenius coefficients:              1.54E+09    0.6    14310.0
213. C2H5CHO+OH=C2H5CO+H2O                         2.69E+10    0.8     -340.0
     Reverse Arrhenius coefficients:              1.70E+08    1.3    28480.0
214. C2H5CHO+CH3=C2H5CO+CH4                        2.61E+06    1.8     5911.0
     Reverse Arrhenius coefficients:              1.41E+06    2.0    21380.0
215. C2H5CHO+HO2=C2H5CO+H2O2                       2.80E+12    0.0    13600.0
     Reverse Arrhenius coefficients:              9.63E+11    0.0    11530.0
216. C2H5CHO+CH3O=C2H5CO+CH3OH                     1.00E+12    0.0     3300.0
     Reverse Arrhenius coefficients:              1.28E+10    0.4    17460.0
217. C2H5CHO+CH3O2=C2H5CO+CH3O2H                   3.01E+12    0.0    11920.0
     Reverse Arrhenius coefficients:              2.01E+13   -0.5     8260.0
218. C2H5CHO+C2H5=C2H5CO+C2H6                      1.00E+12    0.0     8000.0
     Reverse Arrhenius coefficients:              6.43E+12    0.0    19700.0
219. C2H5CHO+C2H5O2=C2H5CO+C2H5O2H                 3.01E+12    0.0    11920.0
     Reverse Arrhenius coefficients:              2.02E+13   -0.5     8264.0
220. C2H5CHO+O2=C2H5CO+HO2                         1.00E+13    0.0    40700.0
     Reverse Arrhenius coefficients:              3.13E+10    0.3      -58.0
221. C2H5CHO+CH3CO3=C2H5CO+CH3CO3H                 3.01E+12    0.0    11920.0
     Reverse Arrhenius coefficients:              1.65E+12    0.0    12630.0
222. C2H5CHO+C2H3=C2H5CO+C2H4                      1.70E+12    0.0     8440.0
     Reverse Arrhenius coefficients:              3.20E+12    0.1    30130.0
223. C2H5CO=C2H5+CO                                2.46E+23   -3.2    17550.0
     Reverse Arrhenius coefficients:              1.51E+11    0.0     4810.0
224. C3H8(+M)=CH3+C2H5(+M)                         1.29E+37   -5.8    97380.0
     Low pressure limit:  0.56400E+75 -0.15740E+02  0.98714E+05
     TROE centering:      0.31000E+00  0.50000E+02  0.30000E+04  0.90000E+04
     H2              Enhanced by    2.000E+00
     H2O             Enhanced by    6.000E+00
     AR              Enhanced by    7.000E-01
     CO              Enhanced by    1.500E+00
     CO2             Enhanced by    2.000E+00
     CH4             Enhanced by    2.000E+00
     C2H6            Enhanced by    3.000E+00
     HE              Enhanced by    7.000E-01
225. C3H8=NC3H7+H                                  3.75E+17   -0.4   101200.0
     Reverse Arrhenius coefficients:              1.00E+14    0.0        0.0
226. C3H8=IC3H7+H                                  2.38E+18   -0.7    98680.0
     Reverse Arrhenius coefficients:              1.00E+14    0.0        0.0
227. C3H8+O2=IC3H7+HO2                             2.00E+13    0.0    49640.0
     Reverse Arrhenius coefficients:              1.76E+09    0.6     -169.0
228. C3H8+O2=NC3H7+HO2                             6.00E+13    0.0    52290.0
     Reverse Arrhenius coefficients:              3.35E+10    0.3      -59.0
229. H+C3H8=H2+IC3H7                               1.30E+06    2.4     4471.0
     Reverse Arrhenius coefficients:              2.19E+01    3.3     9351.0
230. H+C3H8=H2+NC3H7                               3.49E+05    2.7     6450.0
     Reverse Arrhenius coefficients:              3.72E+01    3.3     8790.0
231. C3H8+O=IC3H7+OH                               5.49E+05    2.5     3140.0
     Reverse Arrhenius coefficients:              4.79E+00    3.4     6608.0
232. C3H8+O=NC3H7+OH                               3.71E+06    2.4     5505.0
     Reverse Arrhenius coefficients:              2.05E+02    3.0     6433.0
233. C3H8+OH=NC3H7+H2O                             1.05E+10    1.0     1586.0
     Reverse Arrhenius coefficients:              1.19E+07    1.5    18820.0
234. C3H8+OH=IC3H7+H2O                             4.67E+07    1.6      -35.0
     Reverse Arrhenius coefficients:              8.33E+03    2.5    19740.0
235. C3H8+HO2=IC3H7+H2O2                           6.32E+01    3.4    13720.0
     Reverse Arrhenius coefficients:              6.15E-01    3.6     2598.0
236. C3H8+HO2=NC3H7+H2O2                           4.08E+01    3.6    17160.0
     Reverse Arrhenius coefficients:              2.52E+00    3.5     3500.0
237. CH3+C3H8=CH4+IC3H7                            6.40E+04    2.2     7520.0
     Reverse Arrhenius coefficients:              9.82E+02    2.7    13940.0
238. CH3+C3H8=CH4+NC3H7                            9.04E-01    3.6     7154.0
     Reverse Arrhenius coefficients:              8.79E-02    3.8    11030.0
239. IC3H7+C3H8=NC3H7+C3H8                         3.00E+10    0.0    12900.0
     Reverse Arrhenius coefficients:              3.00E+10    0.0    12900.0
240. C2H3+C3H8=C2H4+IC3H7                          1.00E+11    0.0    10400.0
     Reverse Arrhenius coefficients:              1.31E+11    0.0    17800.0
241. C2H3+C3H8=C2H4+NC3H7                          1.00E+11    0.0    10400.0
     Reverse Arrhenius coefficients:              1.31E+11    0.0    17800.0
242. C2H5+C3H8=C2H6+IC3H7                          1.00E+11    0.0    10400.0
     Reverse Arrhenius coefficients:              3.63E+10    0.0     9934.0
243. C2H5+C3H8=C2H6+NC3H7                          1.00E+11    0.0    10400.0
     Reverse Arrhenius coefficients:              3.63E+10    0.0     9934.0
244. C3H8+C3H5-A=NC3H7+C3H6                        7.94E+11    0.0    20500.0
     Reverse Arrhenius coefficients:              5.37E+16   -1.3    13400.0
245. C3H8+C3H5-A=IC3H7+C3H6                        7.94E+11    0.0    16200.0
     Reverse Arrhenius coefficients:              5.37E+16   -1.3     9095.0
246. C3H8+CH3O=NC3H7+CH3OH                         3.00E+11    0.0     7000.0
     Reverse Arrhenius coefficients:              1.22E+10    0.0     9182.0
247. C3H8+CH3O=IC3H7+CH3OH                         3.00E+11    0.0     7000.0
     Reverse Arrhenius coefficients:              1.22E+10    0.0     9182.0
248. CH3O2+C3H8=CH3O2H+NC3H7                       1.39E+00    4.0    18280.0
     Reverse Arrhenius coefficients:              1.66E+00    3.5     3024.0
249. CH3O2+C3H8=CH3O2H+IC3H7                       1.02E+01    3.6    14810.0
     Reverse Arrhenius coefficients:              1.93E+00    3.4     2090.0
250. C2H5O2+C3H8=C2H5O2H+NC3H7                     1.39E+00    4.0    18280.0
     Reverse Arrhenius coefficients:              1.67E+00    3.5     3028.0
251. C2H5O2+C3H8=C2H5O2H+IC3H7                     1.02E+01    3.6    14810.0
```

```
     Reverse Arrhenius coefficients:              1.93E+00    3.4     2094.0
252. C3H8+CH3CO3=IC3H7+CH3CO3H                     2.00E+12    0.0    17000.0
     Reverse Arrhenius coefficients:              3.10E+10    0.3     8650.0
253. C3H8+CH3CO3=NC3H7+CH3CO3H                     1.70E+13    0.0    20460.0
     Reverse Arrhenius coefficients:              1.67E+12    0.0     9570.0
254. IC3H7=H+C3H6                                  6.92E+13    0.0    37690.0
     Reverse Arrhenius coefficients:              2.64E+13    0.0     2160.0
255. IC3H7+H=C2H5+CH3                              2.00E+13    0.0        0.0
     Reverse Arrhenius coefficients:              4.34E+07    1.2     8620.0
256. IC3H7+O2=C3H6+HO2                             4.50E-19    0.0     5020.0
     Reverse Arrhenius coefficients:              2.00E-19    0.0    17500.0
257. IC3H7+OH=C3H6+H2O                             2.41E+13    0.0        0.0
     Reverse Arrhenius coefficients:              2.98E+12    0.6    83820.0
258. IC3H7+O=CH3CHO+CH3                            4.82E+13    0.0        0.0
     Reverse Arrhenius coefficients:              1.28E+11    0.8    86480.0
259. NC3H7=CH3+C2H4                                9.97E+40   -8.6    41430.0
     Reverse Arrhenius coefficients:              1.90E+34   -7.0    17100.0
260. NC3H7=H+C3H6                                  8.78E+39   -8.1    46580.0
     Reverse Arrhenius coefficients:              2.07E+37   -7.4    12020.0
261. NC3H7+O2=C3H6+HO2                             3.00E-19    0.0     3000.0
     Reverse Arrhenius coefficients:              2.00E-19    0.0    17500.0
262. C2H5CHO+NC3H7=C2H5CO+C3H8                     1.70E+12    0.0     8440.0
     Reverse Arrhenius coefficients:              1.90E+14    0.0    18790.0
263. C2H5CHO+IC3H7=C2H5CO+C3H8                     1.70E+12    0.0     8440.0
     Reverse Arrhenius coefficients:              1.90E+14    0.0    18790.0
264. C2H5CHO+C3H5-A=C2H5CO+C3H6                    1.70E+12    0.0     8440.0
     Reverse Arrhenius coefficients:              1.00E+13    0.0    28000.0
265. C2H3+CH3(+M)=C3H6(+M)                         2.50E+13    0.0        0.0
     Low pressure limit:  0.42700E+59 -0.11940E+02  0.97698E+04
     TROE centering:      0.17500E+00  0.13406E+04  0.60000E+05  0.10140E+05
266. C3H6=C3H5-A+H                                 2.01E+61  -13.3   118500.0
     Reverse Arrhenius coefficients:              2.04E+61  -13.5    30610.0
267. C3H6=C3H5-S+H                                 7.71E+69  -16.1   140000.0
     Reverse Arrhenius coefficients:              2.55E+67  -15.9    28690.0
268. C3H6+O=C2H5+HCO                               1.58E+07    1.8    -1216.0
     Reverse Arrhenius coefficients:              9.19E+01    2.7    23110.0
269. C3H6+O=CH2CO+CH3+H                            2.50E+07    1.8       76.0
     Warning...all REV parameters are zero...          0.00000E+00 0.00000E+00 0.00000E+00
               this reaction will be treated as irreversible
270. C3H6+O=C3H5-A+OH                              5.24E+11    0.7     5884.0
     Reverse Arrhenius coefficients:              1.10E+11    0.7    20150.0
271. C3H6+O=C3H5-S+OH                              1.20E+11    0.7     8959.0
     Reverse Arrhenius coefficients:              8.24E+07    1.2     -207.0
272. C3H6+OH=C3H5-A+H2O                            3.12E+06    2.0     -298.0
     Reverse Arrhenius coefficients:              1.34E+07    1.9    30270.0
273. C3H6+OH=C3H5-S+H2O                            2.11E+06    2.0     2778.0
     Reverse Arrhenius coefficients:              2.96E+04    2.4     9916.0
274. C3H6+HO2=C3H5-A+H2O2                          2.70E+04    2.5    12340.0
     Reverse Arrhenius coefficients:              6.34E+06    1.8    12010.0
275. C3H6+HO2=C3H5-S+H2O2                          1.80E+04    2.5    27620.0
     Reverse Arrhenius coefficients:              1.38E+04    2.3     3864.0
276. C3H6+H=C3H5-A+H2                              1.73E+05    2.5     2492.0
     Reverse Arrhenius coefficients:              7.02E+04    2.5    18170.0
277. C3H6+H=C3H5-S+H2                              8.04E+05    2.5    12280.0
     Reverse Arrhenius coefficients:              1.06E+03    3.0     4526.0
278. C3H6+H=C2H4+CH3                               2.30E+13    0.0     2547.0
     Reverse Arrhenius coefficients:              7.27E+07    1.3    11200.0
279. C3H6+O2=C3H5-A+HO2                            4.00E+12    0.0    39900.0
     Reverse Arrhenius coefficients:              8.51E+12   -0.3      887.0
280. C3H6+O2=C3H5-S+HO2                            2.00E+12    0.0    62900.0
     Reverse Arrhenius coefficients:              1.39E+10    0.2      459.0
281. C3H6+CH3=C3H5-A+CH4                           2.21E+00    3.5     5675.0
     Reverse Arrhenius coefficients:              8.18E+02    3.1    22890.0
282. C3H6+CH3=C3H5-S+CH4                           1.35E+00    3.5    12850.0
     Reverse Arrhenius coefficients:              1.63E+00    3.6     6635.0
283. C3H6+C2H5=C3H5-A+C2H6                         1.00E+11    0.0     9800.0
     Reverse Arrhenius coefficients:              5.37E+05    1.3    16440.0
284. C3H6+CH3CO3=C3H5-A+CH3CO3H                    3.24E+11    0.0    14900.0
     Reverse Arrhenius coefficients:              2.00E+10    0.0    15000.0
285. C3H6+CH3O2=C3H5-A+CH3O2H                      3.24E+11    0.0    14900.0
     Reverse Arrhenius coefficients:              2.00E+10    0.0    15000.0
286. C3H6+C2H5O2=C3H5-A+C2H5O2H                    3.24E+11    0.0    14900.0
     Reverse Arrhenius coefficients:              2.00E+10    0.0    15000.0
287. C3H5-A=C2H2+CH3                               2.40E+48   -9.9    82080.0
     Reverse Arrhenius coefficients:              2.61E+46   -9.8    36950.0
288. C3H5-A+HO2=C3H5O+OH                           7.00E+12    0.0    -1000.0
     Reverse Arrhenius coefficients:              1.60E+12    0.1    11660.0
289. C3H5-A+CH3O2=C3H5O+CH3O                       7.00E+12    0.0    -1000.0
     Reverse Arrhenius coefficients:              1.99E+15   -0.7    17020.0
290. C3H5-A+C2H5=C2H4+C3H6                         4.00E+11    0.0        0.0
     Reverse Arrhenius coefficients:              6.94E+16   -1.3    52800.0
291. C3H5-A+O2=CH2CHO+CH2O                         7.14E+15   -1.2    21050.0
     Reverse Arrhenius coefficients:              4.94E+16   -1.4    88620.0
292. C3H5-A+O2=C2H3CHO+OH                          2.47E+13   -0.4    23020.0
     Reverse Arrhenius coefficients:              1.99E+13   -0.6    75140.0
293. C3H5-A+O2=C2H2+CH2O+OH                        9.72E+29   -5.7    21450.0
     Warning...all REV parameters are zero...          0.00000E+00 0.00000E+00 0.00000E+00
               this reaction will be treated as irreversible
294. C3H5-S=C2H2+CH3                               9.60E+39   -8.2    42030.0
     Reverse Arrhenius coefficients:              1.61E+40   -8.6    20330.0
295. C3H5-S+O2=CH3CHO+HCO                          4.34E+12    0.0        0.0
     Reverse Arrhenius coefficients:              1.61E+17   -1.3    96530.0
296. NC3H7+HO2=NC3H7O+OH                           7.00E+12    0.0    -1000.0
     Reverse Arrhenius coefficients:              6.22E+15   -0.7    25310.0
297. IC3H7+HO2=IC3H7O+OH                           7.00E+12    0.0    -1000.0
```

```
     Reverse Arrhenius coefficients:              1.05E+16   -0.6    27320.0
298. CH3O2+NC3H7=CH3O+NC3H7O                       7.00E+12    0.0    -1000.0
     Reverse Arrhenius coefficients:              3.89E+14   -0.4    29550.0
299. CH3O2+IC3H7=CH3O+IC3H7O                       7.00E+12    0.0    -1000.0
     Reverse Arrhenius coefficients:              6.57E+14   -0.3    31560.0
300. NC3H7O2=NC3H7+O2                              2.40E+20   -1.6    35960.0
     Reverse Arrhenius coefficients:              4.52E+12    0.0        0.0
301. IC3H7O2=IC3H7+O2                              3.13E+22   -2.2    38160.0
     Reverse Arrhenius coefficients:              7.54E+12    0.0        0.0
302. NC3H7O2+CH3O2=NC3H7O+CH3O+O2                  1.40E+16   -1.6     1860.0
     Warning...all REV parameters are zero...          0.00000E+00 0.00000E+00 0.00000E+00
               this reaction will be treated as irreversible
303. IC3H7O2+CH3O2=IC3H7O+CH3O+O2                  1.40E+16   -1.6     1860.0
     Warning...all REV parameters are zero...          0.00000E+00 0.00000E+00 0.00000E+00
               this reaction will be treated as irreversible
304. IC3H7O2+CH3CO3=IC3H7O+CH3CO2+O2               1.40E+16   -1.6     1860.0
     Warning...all REV parameters are zero...          0.00000E+00 0.00000E+00 0.00000E+00
               this reaction will be treated as irreversible
305. NC3H7O2+CH3CO3=NC3H7O+CH3CO2+O2               1.40E+16   -1.6     1860.0
     Warning...all REV parameters are zero...          0.00000E+00 0.00000E+00 0.00000E+00
               this reaction will be treated as irreversible
306. IC3H7O2+C2H5O2=IC3H7O+C2H5O+O2                1.40E+16   -1.6     1860.0
     Warning...all REV parameters are zero...          0.00000E+00 0.00000E+00 0.00000E+00
               this reaction will be treated as irreversible
307. NC3H7O2+C2H5O2=NC3H7O+C2H5O+O2                1.40E+16   -1.6     1860.0
     Warning...all REV parameters are zero...          0.00000E+00 0.00000E+00 0.00000E+00
               this reaction will be treated as irreversible
308. IC3H7O2+IC3H7O2=O2+IC3H7O+IC3H7O              1.40E+16   -1.6     1860.0
     Warning...all REV parameters are zero...          0.00000E+00 0.00000E+00 0.00000E+00
               this reaction will be treated as irreversible
309. NC3H7O2+NC3H7O2=O2+NC3H7O+NC3H7O              1.40E+16   -1.6     1860.0
     Warning...all REV parameters are zero...          0.00000E+00 0.00000E+00 0.00000E+00
               this reaction will be treated as irreversible
310. IC3H7O2+NC3H7O2=IC3H7O+NC3H7O+O2              1.40E+16   -1.6     1860.0
     Warning...all REV parameters are zero...          0.00000E+00 0.00000E+00 0.00000E+00
               this reaction will be treated as irreversible
311. IC3H7O2+CH3=IC3H7O+CH3O                       7.00E+12    0.0    -1000.0
     Reverse Arrhenius coefficients:              1.14E+11    0.7    26720.0
312. IC3H7O2+C2H5=IC3H7O+C2H5O                     7.00E+12    0.0    -1000.0
     Reverse Arrhenius coefficients:              1.63E+13    0.1    29130.0
313. IC3H7O2+IC3H7=IC3H7O+IC3H7O                   7.00E+12    0.0    -1000.0
     Reverse Arrhenius coefficients:              2.78E+13    0.3    29800.0
314. IC3H7O2+NC3H7=IC3H7O+NC3H7O                   7.00E+12    0.0    -1000.0
     Reverse Arrhenius coefficients:              1.64E+13    0.1    27800.0
315. IC3H7O2+C3H5-A=IC3H7O+C3H5O                   7.00E+12    0.0    -1000.0
     Reverse Arrhenius coefficients:              4.24E+09    0.9    14140.0
316. NC3H7O2+CH3=NC3H7O+CH3O                       7.00E+12    0.0    -1000.0
     Reverse Arrhenius coefficients:              5.30E+12    0.0    26920.0
317. NC3H7O2+C2H5=NC3H7O+C2H5O                     7.00E+12    0.0    -1000.0
     Reverse Arrhenius coefficients:              7.54E+14   -0.6    29330.0
318. NC3H7O2+IC3H7=NC3H7O+IC3H7O                   7.00E+12    0.0    -1000.0
     Reverse Arrhenius coefficients:              1.29E+15   -0.4    30000.0
319. NC3H7O2+NC3H7=NC3H7O+NC3H7O                   7.00E+12    0.0    -1000.0
     Reverse Arrhenius coefficients:              7.61E+14   -0.6    28000.0
320. NC3H7O2+C3H5-A=NC3H7O+C3H5O                   7.00E+12    0.0    -1000.0
     Reverse Arrhenius coefficients:              1.96E+11    0.2    14340.0
321. NC3H7O=C2H5+CH2O                              2.72E+21   -2.4    15700.0
     Reverse Arrhenius coefficients:              1.00E+11    0.0     3496.0
322. NC3H7O=C2H5CHO+H                              8.90E+10    0.7    19800.0
     Reverse Arrhenius coefficients:              4.00E+12    0.0     6260.0
323. IC3H7O=CH3+CH3CHO                             5.33E+19   -1.7    17140.0
     Reverse Arrhenius coefficients:              1.00E+11    0.0     9256.0
324. NC3H7O2=C3H6OOH1-2                            6.00E+11    0.0    26850.0
     Reverse Arrhenius coefficients:              1.12E+08    0.6    11720.0
325. NC3H7O2=C3H6OOH1-3                            1.12E+11    0.0    24400.0
     Reverse Arrhenius coefficients:              2.72E+11   -0.5     8936.0
326. C3H6OOH1-2=C3H6+HO2                           7.83E+15   -1.3    15950.0
     Reverse Arrhenius coefficients:              1.00E+11    0.0    11000.0
327. C3H6OOH1-3=OH+CH2O+C2H4                       3.04E+15   -0.8    27400.0
     Warning...all REV parameters are zero...          0.00000E+00 0.00000E+00 0.00000E+00
               this reaction will be treated as irreversible
328. C3H6OOH1-2=C2H4+CH2O+OH                       1.31E+33   -7.0    48120.0
     Warning...all REV parameters are zero...          0.00000E+00 0.00000E+00 0.00000E+00
               this reaction will be treated as irreversible
329. C3H6OOH1-2O2=C3H6OOH1-2+O2                    2.39E+25   -2.9    40100.0
     Reverse Arrhenius coefficients:              5.00E+12    0.0        0.0
330. C3H6OOH1-3O2=C3H6OOH1-3+O2                    2.85E+20   -1.6    35690.0
     Reverse Arrhenius coefficients:              4.52E+12    0.0        0.0
331. C3H6OOH1-2O2=C3KET12+OH                       6.00E+11    0.0    26400.0
     Reverse Arrhenius coefficients:              9.25E+04    1.3    48920.0
332. C3H6OOH1-3O2=C3KET13+OH                       7.50E+10    0.0    21400.0
     Reverse Arrhenius coefficients:              4.10E+03    1.5    44740.0
333. C3H6OOH2-1O2=C3KET21+OH                       3.00E+11    0.0    23850.0
     Reverse Arrhenius coefficients:              1.40E+03    1.8    49750.0
334. C3KET12=CH3CHO+HCO+OH                         9.45E+15    0.0    43000.0
     Warning...all REV parameters are zero...          0.00000E+00 0.00000E+00 0.00000E+00
               this reaction will be treated as irreversible
335. C3KET13=CH2O+CH2CHO+OH                        1.00E+16    0.0    43000.0
     Warning...all REV parameters are zero...          0.00000E+00 0.00000E+00 0.00000E+00
               this reaction will be treated as irreversible
336. C3KET21=CH2O+CH3CO+OH                         1.00E+16    0.0    43000.0
     Warning...all REV parameters are zero...          0.00000E+00 0.00000E+00 0.00000E+00
               this reaction will be treated as irreversible
337. C3H5O=C2H3CHO+H                               1.00E+14    0.0    29100.0
     Reverse Arrhenius coefficients:              1.68E+14   -0.2    19690.0
```

```
338. C3H5O=C2H3+CH2O                          1.46E+20   -2.0    35090.0
     Reverse Arrhenius coefficients:         1.50E+11    0.0    10600.0
339. C3H5O+O2=C2H3CHO+HO2                     1.00E+12    0.0     6000.0
     Reverse Arrhenius coefficients:         1.29E+11    0.0    32000.0
340. IC3H7O2=C3H6+HO2                         1.20E+43   -9.4    41530.0
     Reverse Arrhenius coefficients:         2.30E+33   -7.3    16710.0
341. NC3H7O2=C3H6+HO2                         4.31E+36   -7.5    39510.0
     Reverse Arrhenius coefficients:         1.02E+28   -5.6    19440.0
342. PC4H9=C2H5+C2H4                          3.50E+12    0.5    29470.0
     Reverse Arrhenius coefficients:         1.32E+04    2.5     6130.0
343. PC4H9=C4H8-1+H                           2.62E+12    0.3    35700.0
     Reverse Arrhenius coefficients:         2.50E+11    0.5     2620.0
344. PC4H9+O2=C4H8-1+HO2                      8.37E-01    3.6    11960.0
     Reverse Arrhenius coefficients:         1.67E-01    3.8    27750.0
345. C4H8-1=C3H5-A+CH3                        5.08E+19   -1.3    76510.0
     Reverse Arrhenius coefficients:         1.35E+13    0.0        0.0
346. C4H8-1=C2H3+C2H5                         2.88E+23   -2.0   101600.0
     Reverse Arrhenius coefficients:         9.00E+12    0.0        0.0
347. C4H8-1=H+C4H71-3                         3.72E+14   -0.1    85200.0
     Reverse Arrhenius coefficients:         5.00E+13    0.0        0.0
348. C4H8-1+O2=C4H71-3+HO2                    2.00E+13    0.0    37190.0
     Reverse Arrhenius coefficients:         4.65E+12    0.1     -168.0
349. C4H8-1+O=C4H71-3+OH                      1.75E+11    0.7     5884.0
     Reverse Arrhenius coefficients:         4.88E+09    1.1    22840.0
350. C4H8-1+H=C4H71-3+H2                      1.73E+05    2.5     2492.0
     Reverse Arrhenius coefficients:         9.28E+03    2.9    20860.0
351. C4H8-1+OH=C4H71-3+H2O                    3.12E+06    2.0     -298.0
     Reverse Arrhenius coefficients:         1.78E+06    2.3    32960.0
352. C4H8-1+CH3=C4H71-3+CH4                   2.21E+00    3.5     5675.0
     Reverse Arrhenius coefficients:         1.08E+02    3.4    25580.0
353. C4H8-1+HO2=C4H71-3+H2O2                  2.70E+04    0.7     5884.0
     Reverse Arrhenius coefficients:         8.38E+05    0.4     8246.0
354. C4H8-1+CH3O2=C4H71-3+CH3O2H              2.70E+04    0.7     5884.0
     Reverse Arrhenius coefficients:         1.63E+07   -0.1     6651.0
355. C4H8-1+CH3O=C4H71-3+CH3OH                4.00E+01    2.9     8609.0
     Reverse Arrhenius coefficients:         2.47E+02    2.7    27000.0
356. C4H8-1+CH3CO3=C4H71-3+CH3CO3H            1.00E+11    0.0     8000.0
     Reverse Arrhenius coefficients:         2.00E+10    0.0    10000.0
357. C4H8-1+C3H5-A=C4H71-3+C3H6               7.90E+10    0.0    12400.0
     Reverse Arrhenius coefficients:         1.00E+11    0.0    17500.0
358. C4H8-1+C4H6=C4H71-3+C4H71-3              2.35E+12    0.0    46720.0
     Reverse Arrhenius coefficients:         1.60E+12    0.0        0.0
359. C4H8-1+C2H5O2=C4H71-3+C2H5O2H            1.40E+12    0.0    14900.0
     Reverse Arrhenius coefficients:         3.16E+11    0.0    13000.0
360. C4H71-3=C4H6+H                           1.20E+14    0.0    49300.0
     Reverse Arrhenius coefficients:         4.00E+13    0.0     1300.0
361. C4H71-3+C2H5=C4H8-1+C2H4                 2.59E+12    0.0     -131.0
     Reverse Arrhenius coefficients:         1.15E+13    0.1    49440.0
362. C4H71-3+CH3O=C4H8-1+CH2O                 2.41E+13    0.0        0.0
     Reverse Arrhenius coefficients:         2.48E+12    0.3    66330.0
363. C4H71-3+O=C2H3CHO+CH3                    6.03E+13    0.0        0.0
     Reverse Arrhenius coefficients:         3.38E+15   -0.8    81630.0
364. C4H71-3+HO2=C4H7O+OH                     9.64E+12    0.0        0.0
     Reverse Arrhenius coefficients:         7.29E+15   -1.1    15530.0
365. C4H71-3+CH3O2=C4H7O+CH3O                 9.64E+12    0.0        0.0
     Reverse Arrhenius coefficients:         7.12E+17   -1.7    20290.0
366. C3H5-A+C4H71-3=C3H6+C4H6                 6.31E+12    0.0        0.0
     Reverse Arrhenius coefficients:         1.00E+10    0.0    50000.0
367. C4H71-3+O2=C4H6+HO2                      1.00E+09    0.0        0.0
     Reverse Arrhenius coefficients:         1.00E+11    0.0    17000.0
368. H+C4H71-3=C4H6+H2                        3.16E+13    0.0        0.0
     Reverse Arrhenius coefficients:         1.07E+13    0.0    56810.0
369. C2H5+C4H71-3=C4H6+C2H6                   3.98E+12    0.0        0.0
     Reverse Arrhenius coefficients:         3.21E+12    0.0    49840.0
370. C2H3+C4H71-3=C2H4+C4H6                   3.98E+12    0.0        0.0
     Reverse Arrhenius coefficients:         1.16E+13    0.0    57710.0
371. C4H71-3+C2H5O2=C4H7O+C2H5O               3.80E+12    0.0    -1200.0
     Reverse Arrhenius coefficients:         2.00E+10    0.0        0.0
372. IC3H7O2+C4H71-3=IC3H7O+C4H7O             3.80E+12    0.0    -1200.0
     Reverse Arrhenius coefficients:         2.00E+10    0.0        0.0
373. NC3H7O2+C4H71-3=NC3H7O+C4H7O             3.80E+12    0.0    -1200.0
     Reverse Arrhenius coefficients:         2.00E+10    0.0        0.0
374. C4H7O=CH3CHO+C2H3                        7.94E+14    0.0    19000.0
     Reverse Arrhenius coefficients:         1.00E+10    0.0    20000.0
375. C4H7O=C2H3CHO+CH3                        7.94E+14    0.0    19000.0
     Reverse Arrhenius coefficients:         1.00E+10    0.0    20000.0
376. C4H6=C2H3+C2H3                           4.03E+19   -1.0    98150.0
     Reverse Arrhenius coefficients:         1.26E+13    0.0        0.0
377. C4H6+OH=C2H5+CH2CO                       1.00E+12    0.0        0.0
     Reverse Arrhenius coefficients:         3.73E+12    0.0    30020.0
378. C4H6+OH=CH2O+C3H5-A                      1.00E+12    0.0        0.0
     Reverse Arrhenius coefficients:         3.50E+06    0.0    71060.0
379. C4H6+OH=C2H3+CH3CHO                      1.00E+12    0.0        0.0
     Reverse Arrhenius coefficients:         5.44E+11    0.0    18550.0
380. C4H6+O=C2H4+CH2CO                        1.00E+12    0.0        0.0
     Reverse Arrhenius coefficients:         6.38E+11    0.0    94340.0
381. C2H3+C2H4=C4H6+H                         5.00E+11    0.0     7300.0
     Reverse Arrhenius coefficients:         1.00E+13    0.0     4700.0
382. PC4H9O2=PC4H9+O2                         2.85E+20   -1.6    35930.0
     Reverse Arrhenius coefficients:         4.52E+12    0.0        0.0
383. IC3H7O2+PC4H9=IC3H7O+PC4H9O              7.00E+12    0.0    -1000.0
     Reverse Arrhenius coefficients:         2.28E+13    0.1    27480.0
384. NC3H7O2+PC4H9=NC3H7O+PC4H9O              7.00E+12    0.0    -1000.0
     Reverse Arrhenius coefficients:         1.06E+15   -0.6    27680.0
385. PC4H9O2+HO2=PC4H9O+OH+O2                 1.40E-14   -1.6     1860.0
```

```
     Warning...all REV parameters are zero...          0.00000E+00 0.00000E+00 0.00000E+00
               this reaction will be treated as irreversible
386. C4H71-3+PC4H9O2=C4H7O+PC4H9O                      7.00E+12    0.0    -1000.0
     Reverse Arrhenius coefficients:                  1.19E+14   -0.8    16100.0
387. PC4H9O2+PC4H9O2=O2+PC4H9O+PC4H9O                  1.40E+16   -1.6     1860.0
     Warning...all REV parameters are zero...          0.00000E+00 0.00000E+00 0.00000E+00
               this reaction will be treated as irreversible
388. PC4H9O2+NC3H7O2=PC4H9O+NC3H7O+O2                  1.40E+16   -1.6     1860.0
     Warning...all REV parameters are zero...          0.00000E+00 0.00000E+00 0.00000E+00
               this reaction will be treated as irreversible
389. PC4H9O2+IC3H7O2=PC4H9O+IC3H7O+O2                  1.40E+16   -1.6     1860.0
     Warning...all REV parameters are zero...          0.00000E+00 0.00000E+00 0.00000E+00
               this reaction will be treated as irreversible
390. PC4H9O2+C2H5O2=PC4H9O+C2H5O+O2                    1.40E+16   -1.6     1860.0
     Warning...all REV parameters are zero...          0.00000E+00 0.00000E+00 0.00000E+00
               this reaction will be treated as irreversible
391. PC4H9O2+CH3O2=PC4H9O+CH3O+O2                      1.40E+16   -1.6     1860.0
     Warning...all REV parameters are zero...          0.00000E+00 0.00000E+00 0.00000E+00
               this reaction will be treated as irreversible
392. PC4H9O2+CH3CO3=PC4H9O+CH3CO2+O2                   1.40E+16   -1.6     1860.0
     Warning...all REV parameters are zero...          0.00000E+00 0.00000E+00 0.00000E+00
               this reaction will be treated as irreversible
393. PC4H9O2+CH3=PC4H9O+CH3O                           7.00E+12    0.0    -1000.0
     Reverse Arrhenius coefficients:                  6.20E+12    0.0    26630.0
394. PC4H9O2+C2H5=PC4H9O+C2H5O                         7.00E+12    0.0    -1000.0
     Reverse Arrhenius coefficients:                  8.81E+14   -0.6    29040.0
395. PC4H9O2+IC3H7=PC4H9O+IC3H7O                       7.00E+12    0.0    -1000.0
     Reverse Arrhenius coefficients:                  1.50E+15   -0.5    29710.0
396. PC4H9O2+NC3H7=PC4H9O+NC3H7O                       7.00E+12    0.0    -1000.0
     Reverse Arrhenius coefficients:                  8.90E+14   -0.6    27710.0
397. PC4H9O2+PC4H9=PC4H9O+PC4H9O                       7.00E+12    0.0    -1000.0
     Reverse Arrhenius coefficients:                  1.24E+15   -0.6    27390.0
398. PC4H9O2+C3H5-A=PC4H9O+C3H5O                       7.00E+12    0.0    -1000.0
     Reverse Arrhenius coefficients:                  2.30E+11    0.2    14050.0
399. PC4H9+HO2=PC4H9O+OH                               7.00E+12    0.0    -1000.0
     Reverse Arrhenius coefficients:                  8.63E+15   -0.7    25000.0
400. CH3O2+PC4H9=CH3O+PC4H9O                           7.00E+12    0.0    -1000.0
     Reverse Arrhenius coefficients:                  5.40E+14   -0.4    29240.0
401. PC4H9O=NC3H7+CH2O                                 1.56E+21   -2.4    15230.0
     Reverse Arrhenius coefficients:                  5.00E+10    0.0     3457.0
402. PC4H9O2=C4H8OOH1-3                                2.50E+10    0.0    20850.0
     Reverse Arrhenius coefficients:                  3.23E+09   -0.1     7871.0
403. PC4H9O2=C4H8-1+HO2                                4.31E+36   -7.5    39510.0
     Reverse Arrhenius coefficients:                  1.37E+28   -5.7    19370.0
404. C4H8OOH1-3=OH+CH2O+C3H6                           6.64E+13   -0.2    29900.0
     Warning...all REV parameters are zero...          0.00000E+00 0.00000E+00 0.00000E+00
               this reaction will be treated as irreversible
405. C4H8OOH1-3O2=C4H8OOH1-3+O2                        5.60E+22   -2.2    37960.0
     Reverse Arrhenius coefficients:                  7.54E+12    0.0        0.0
406. C4H8OOH1-3O2=NC4KET13+OH                          2.50E+10    0.0    21400.0
     Reverse Arrhenius coefficients:                  1.44E+03    1.5    44740.0
407. NC4KET13=CH3CHO+CH2CHO+OH                         1.05E+16    0.0    41600.0
     Warning...all REV parameters are zero...          0.00000E+00 0.00000E+00 0.00000E+00
               this reaction will be treated as irreversible
408. CH2CH2COCH3=C2H4+CH3CO                            1.00E+14    0.0    18000.0
     Reverse Arrhenius coefficients:                  1.00E+11    0.0        0.0
409. C2H5COCH2=CH2CO+C2H5                              1.00E+14    0.0    35000.0
     Reverse Arrhenius coefficients:                  1.00E+11    0.0        0.0
410. NC3H7CHO+O2=NC3H7CO+HO2                           1.20E+05    2.5    37560.0
     Reverse Arrhenius coefficients:                  1.00E+07    0.5     4000.0
411. NC3H7CHO+OH=NC3H7CO+H2O                           2.00E+06    1.8    -1300.0
     Reverse Arrhenius coefficients:                  1.55E+04    2.3    28050.0
412. NC3H7CHO+H=NC3H7CO+H2                             4.14E+09    1.1     2320.0
     Reverse Arrhenius coefficients:                  3.03E+06    1.7    16780.0
413. NC3H7CHO+O=NC3H7CO+OH                             5.94E+12    0.0     1868.0
     Reverse Arrhenius coefficients:                  2.26E+09    0.6    14920.0
414. NC3H7CHO+HO2=NC3H7CO+H2O2                         4.09E+04    2.5    10200.0
     Reverse Arrhenius coefficients:                  1.73E+04    2.4     8662.0
415. NC3H7CHO+CH3=NC3H7CO+CH4                          2.89E-03    4.6     3210.0
     Reverse Arrhenius coefficients:                  1.93E-03    4.8    19210.0
416. NC3H7CHO+CH3O=NC3H7CO+CH3OH                       1.00E+12    0.0     3300.0
     Reverse Arrhenius coefficients:                  1.57E+10    0.4    17990.0
417. NC3H7CHO+CH3O2=NC3H7CO+CH3O2H                     4.09E+04    2.5    10200.0
     Reverse Arrhenius coefficients:                  3.37E+05    2.0     7067.0
418. NC3H7CO=NC3H7+CO                                  1.00E+11    0.0     9600.0
     Reverse Arrhenius coefficients:                  2.19E+03    1.8    -1100.0
419. C2H3COCH3+OH=CH3CHO+CH3CO                         1.00E+11    0.0        0.0
     Warning...all REV parameters are zero...          0.00000E+00 0.00000E+00 0.00000E+00
               this reaction will be treated as irreversible
420. C2H3COCH3+OH=CH2CO+C2H3+H2O                       5.10E+11    0.0     1192.0
     Warning...all REV parameters are zero...          0.00000E+00 0.00000E+00 0.00000E+00
               this reaction will be treated as irreversible
421. C2H3COCH3+HO2=CH2CHO+CH3CO+OH                     6.03E+09    0.0     7949.0
     Warning...all REV parameters are zero...          0.00000E+00 0.00000E+00 0.00000E+00
               this reaction will be treated as irreversible
422. C2H3COCH3+HO2=CH2CO+C2H3+H2O2                     8.50E+12    0.0    20460.0
     Warning...all REV parameters are zero...          0.00000E+00 0.00000E+00 0.00000E+00
               this reaction will be treated as irreversible
423. C2H3COCH3+CH3O2=CH2CHO+CH3CO+CH3O                 3.97E+11    0.0    17050.0
     Warning...all REV parameters are zero...          0.00000E+00 0.00000E+00 0.00000E+00
               this reaction will be treated as irreversible
424. C2H3COCH3+CH3O2=CH2CO+C2H3+CH3O2H                 3.01E+12    0.0    17580.0
     Warning...all REV parameters are zero...          0.00000E+00 0.00000E+00 0.00000E+00
               this reaction will be treated as irreversible
425. C5H11-1=C2H4+NC3H7                                2.09E+12    0.5    29430.0
```

```
     Reverse Arrhenius coefficients:              5.75E+03    2.5     6130.0
426. C5H11-1=H+C5H10-1                             3.35E+11    0.6    35640.0
     Reverse Arrhenius coefficients:              2.50E+11    0.5     2620.0
427. C5H10-1=C2H5+C3H5-A                           9.86E+21   -2.1    75060.0
     Reverse Arrhenius coefficients:              4.00E+12    0.0     -596.0
428. C5H10-1+H=C5H91-3+H2                          3.38E+05    2.4      207.0
     Reverse Arrhenius coefficients:              3.10E+05    2.5    20320.0
429. C5H10-1+O=C5H91-3+OH                          6.60E+05    2.4     1210.0
     Reverse Arrhenius coefficients:              2.66E+05    2.6    19230.0
430. C5H10-1+OH=C5H91-3+H2O                        2.76E+04    2.6    -1919.0
     Reverse Arrhenius coefficients:              1.10E+05    2.8    33350.0
431. C5H10-1+CH3=C5H91-3+CH4                       3.69E+00    3.3     4002.0
     Reverse Arrhenius coefficients:              8.84E+01    3.5    24590.0
432. C5H10-1+O2=C5H91-3+HO2                        2.20E+12    0.0    37220.0
     Reverse Arrhenius coefficients:              3.66E+10    0.5     -152.0
433. C5H10-1+HO2=C5H91-3+H2O2                      4.82E+03    2.5    10530.0
     Reverse Arrhenius coefficients:              1.14E+05    2.4    14330.0
434. C5H10-1+CH3O2=C5H91-3+CH3O2H                  4.82E+03    2.5    10530.0
     Reverse Arrhenius coefficients:              2.37E+05    2.2    11310.0
435. C5H10-1+CH3O=C5H91-3+CH3OH                    4.00E+01    2.9     8609.0
     Reverse Arrhenius coefficients:              1.77E+01    3.1    26990.0
436. C5H91-3=C4H6+CH3                              7.55E+14   -0.5    38520.0
     Reverse Arrhenius coefficients:              1.00E+11    0.0     7800.0
437. C5H11-1+O2=C5H10-1+HO2                        8.37E-01    3.6    11960.0
     Reverse Arrhenius coefficients:              1.31E+00    3.4    27810.0
438. C5H11-1+HO2=C5H11O-1+OH                       9.00E+12    0.0    -1000.0
     Reverse Arrhenius coefficients:              1.94E+15   -0.5    26210.0
439. C5H11-1+CH3O2=C5H11O-1+CH3O                   9.00E+12    0.0    -1000.0
     Reverse Arrhenius coefficients:              1.22E+14   -0.2    30450.0
440. C5H11-1+C5H11O2-1=C5H11O-1+C5H11O-1           9.00E+12    0.0    -1000.0
     Reverse Arrhenius coefficients:              5.94E+13   -0.1    29910.0
441. C5H11O2-1+CH3O2=O2+C5H11O-1+CH3O              1.40E+16   -1.6     1860.0
     Warning...all REV parameters are zero...          0.00000E+00 0.00000E+00 0.00000E+00
               this reaction will be treated as irreversible
442. C5H11O2-1+C5H11O2-1=O2+C5H11O-1+C5H11O-1      1.40E+16   -1.6     1860.0
     Warning...all REV parameters are zero...          0.00000E+00 0.00000E+00 0.00000E+00
               this reaction will be treated as irreversible
443. C5H11O-1=CH2O+PC4H9                           5.66E+20   -2.2    24960.0
     Reverse Arrhenius coefficients:              6.25E+10    0.0    11900.0
444. C5H11O2-1=C5H11-1+O2                          2.34E+20   -1.6    35830.0
     Reverse Arrhenius coefficients:              4.52E+12    0.0        0.0
445. C5H11O2-1=C5H10OOH1-3                         2.50E+10    0.0    20450.0
     Reverse Arrhenius coefficients:              2.60E+09   -0.1     7450.0
446. C5H11O2-1=C5H10-1+HO2                         5.04E+38   -8.1    40490.0
     Reverse Arrhenius coefficients:              1.52E+31   -6.7    20510.0
447. C5H10OOH1-3=OH+CH2O+C4H8-1                    8.28E+13   -0.2    30090.0
     Warning...all REV parameters are zero...          0.00000E+00 0.00000E+00 0.00000E+00
               this reaction will be treated as irreversible
448. C5H10OOH1-3O2=C5H10OOH1-3+O2                  8.04E+22   -2.3    37970.0
     Reverse Arrhenius coefficients:              7.54E+12    0.0        0.0
449. C5H10OOH1-3O2=NC5KET13+OH                     2.50E+10    0.0    21000.0
     Reverse Arrhenius coefficients:              1.11E+03    1.5    44340.0
450. NC5KET13=C2H5CHO+CH2CHO+OH                    1.00E+16    0.0    39000.0
     Warning...all REV parameters are zero...          0.00000E+00 0.00000E+00 0.00000E+00
               this reaction will be treated as irreversible
451. C6H13-1+HO2=C6H13O-1+OH                       7.00E+12    0.0    -1000.0
     Reverse Arrhenius coefficients:              3.27E+15   -0.6    26150.0
452. C6H13-1+CH3O2=C6H13O-1+CH3O                   7.00E+12    0.0    -1000.0
     Reverse Arrhenius coefficients:              2.04E+14   -0.3    30390.0
453. C6H13-1+O2=C6H12-1+HO2                        3.00E-19    0.0     3000.0
     Reverse Arrhenius coefficients:              2.00E-19    0.0    17500.0
454. C6H13-1=C2H4+PC4H9                            6.39E+19   -2.0    30640.0
     Reverse Arrhenius coefficients:              3.30E+11    0.0     7200.0
455. C6H13-1=C6H12-1+H                             9.62E+13   -0.3    36000.0
     Reverse Arrhenius coefficients:              1.00E+13    0.0     2900.0
456. C6H12-1=NC3H7+C3H5-A                          1.00E+16    0.0    71000.0
     Reverse Arrhenius coefficients:              1.00E+13    0.0        0.0
457. C6H12-1+OH=C5H11-1+CH2O                       1.00E+11    0.0    -4000.0
     Warning...all REV parameters are zero...          0.00000E+00 0.00000E+00 0.00000E+00
               this reaction will be treated as irreversible
458. C6H12-1+O=C5H11-1+HCO                         1.00E+11    0.0    -1050.0
     Warning...all REV parameters are zero...          0.00000E+00 0.00000E+00 0.00000E+00
               this reaction will be treated as irreversible
459. C6H13O2-1=C6H13-1+O2                          5.15E+20   -1.7    35790.0
     Reverse Arrhenius coefficients:              4.52E+12    0.0        0.0
460. C6H13-1+C6H13O2-1=C6H13O-1+C6H13O-1           7.00E+12    0.0    -1000.0
     Reverse Arrhenius coefficients:              9.78E+13   -0.2    29840.0
461. C6H13O2-1=C6H12-1+HO2                         5.04E+38   -8.1    40490.0
     Reverse Arrhenius coefficients:              9.64E+29   -6.2    20470.0
462. C6H13O2-1=C6H12OOH1-3                         2.50E+10    0.0    20850.0
     Reverse Arrhenius coefficients:              3.00E+09   -0.1     7860.0
463. C6H13O2-1+CH3O2=C6H13O-1+CH3O+O2              1.40E+16   -1.6     1860.0
     Warning...all REV parameters are zero...          0.00000E+00 0.00000E+00 0.00000E+00
               this reaction will be treated as irreversible
464. C6H13O2-1+C6H13O2-1=O2+C6H13O-1+C6H13O-1      1.40E+16   -1.6     1860.0
     Warning...all REV parameters are zero...          0.00000E+00 0.00000E+00 0.00000E+00
               this reaction will be treated as irreversible
465. C6H13O-1=C5H11-1+CH2O                         5.23E+20   -2.1    24830.0
     Reverse Arrhenius coefficients:              1.00E+11    0.0    11900.0
466. C6H12OOH1-3=OH+CH2O+C5H10-1                   7.70E+13   -0.2    30090.0
     Warning...all REV parameters are zero...          0.00000E+00 0.00000E+00 0.00000E+00
               this reaction will be treated as irreversible
467. C6H12OOH1-3O2=C6H12OOH1-3+O2                  8.87E+22   -2.3    37980.0
     Reverse Arrhenius coefficients:              7.54E+12    0.0        0.0
468. C6H12OOH1-3O2=NC6KET13+OH                     2.50E+10    0.0    21400.0
```

```
     Reverse Arrhenius coefficients:              8.82E+02    1.6    44710.0
469. NC6KET13=NC3H7CHO+CH2CHO+OH                   1.00E+16    0.0    39000.0
     Warning...all REV parameters are zero...          0.00000E+00 0.00000E+00 0.00000E+00
              this reaction will be treated as irreversible
470. NC4H9CHO+O2=NC4H9CO+HO2                       2.00E+13    0.5    42200.0
     Reverse Arrhenius coefficients:              1.00E+07    0.0    40000.0
471. NC4H9CHO+OH=NC4H9CO+H2O                       2.69E+10    0.8     -340.0
     Reverse Arrhenius coefficients:              2.14E+10    0.7    31240.0
472. NC4H9CHO+H=NC4H9CO+H2                         4.00E+13    0.0     4200.0
     Reverse Arrhenius coefficients:              1.80E+13    0.0    24000.0
473. NC4H9CHO+O=NC4H9CO+OH                         5.00E+12    0.0     1790.0
     Reverse Arrhenius coefficients:              1.00E+12    0.0    19000.0
474. NC4H9CHO+HO2=NC4H9CO+H2O2                     2.80E+12    0.0    13600.0
     Reverse Arrhenius coefficients:              1.00E+12    0.0    10000.0
475. NC4H9CHO+CH3=NC4H9CO+CH4                      1.70E+12    0.0     8440.0
     Reverse Arrhenius coefficients:              1.50E+13    0.0    28000.0
476. NC4H9CHO+CH3O=NC4H9CO+CH3OH                   1.15E+11    0.0     1280.0
     Reverse Arrhenius coefficients:              3.00E+11    0.0    18000.0
477. NC4H9CHO+CH3O2=NC4H9CO+CH3O2H                 1.00E+12    0.0     9500.0
     Reverse Arrhenius coefficients:              2.50E+10    0.0    10000.0
478. NC4H9CO=PC4H9+CO                              1.00E+11    0.0     9600.0
     Reverse Arrhenius coefficients:              1.00E+11    0.0        0.0
479. NC3H7COCH2=NC3H7+CH2CO                        1.23E+18   -1.4    43450.0
     Reverse Arrhenius coefficients:              1.00E+11    0.0    11600.0
480. C2H5COC2H4P=C2H5CO+C2H4                       1.77E+17   -1.5    29540.0
     Reverse Arrhenius coefficients:              8.00E+10    0.0    11300.0
481. NC7H16=H+C7H15-1                              2.68E+88  -21.2   142800.0
     Reverse Arrhenius coefficients:              7.26E+84  -20.8    41560.0
482. NC7H16=H+C7H15-2                              1.30E+88  -21.0   139500.0
     Reverse Arrhenius coefficients:              2.26E+83  -20.3    40830.0
483. NC7H16=H+C7H15-3                              1.30E+88  -21.0   139500.0
     Reverse Arrhenius coefficients:              2.26E+83  -20.3    40830.0
484. NC7H16=H+C7H15-4                              6.50E+87  -21.0   139500.0
     Reverse Arrhenius coefficients:              2.25E+83  -20.3    40830.0
485. NC7H16(+M)=C6H13-1+CH3(+M)                    4.32E+24   -2.1    89900.0
     Low pressure limit:  0.49630E+43 -0.77800E+01  0.42800E+05
     TROE centering:      0.89200E+00  0.10000E+11  0.22280E+01  0.17980E+10
486. NC7H16(+M)=C5H11-1+C2H5(+M)                   6.82E+26   -2.7    88910.0
     Low pressure limit:  0.37530E+49 -0.94600E+01  0.41310E+05
     TROE centering:      0.90000E-01  0.36556E+01  0.10000E+11  0.93300E+10
487. NC7H16(+M)=PC4H9+NC3H7(+M)                    1.36E+26   -2.5    88760.0
     Low pressure limit:  0.65090E+49 -0.95700E+01  0.41290E+05
     TROE centering:      0.91100E+00  0.10000E+11  0.22382E+02  0.50000E+10
488. NC7H16+H=C7H15-1+H2                           1.88E+05    2.8     6280.0
     Reverse Arrhenius coefficients:              2.04E+01    3.4     8618.0
489. NC7H16+H=C7H15-2+H2                           2.60E+06    2.4     4471.0
     Reverse Arrhenius coefficients:              1.81E+01    3.4     9318.0
490. NC7H16+H=C7H15-3+H2                           2.60E+06    2.4     4471.0
     Reverse Arrhenius coefficients:              1.81E+01    3.4     9318.0
491. NC7H16+H=C7H15-4+H2                           1.30E+06    2.4     4471.0
     Reverse Arrhenius coefficients:              1.80E+01    3.4     9318.0
492. NC7H16+O=C7H15-1+OH                           1.93E+05    2.7     3716.0
     Reverse Arrhenius coefficients:              1.08E+01    3.3     4642.0
493. NC7H16+O=C7H15-2+OH                           9.54E+04    2.7     2106.0
     Reverse Arrhenius coefficients:              3.48E-01    3.7     5541.0
494. NC7H16+O=C7H15-3+OH                           9.54E+04    2.7     2106.0
     Reverse Arrhenius coefficients:              3.48E-01    3.7     5541.0
495. NC7H16+O=C7H15-4+OH                           4.77E+04    2.7     2106.0
     Reverse Arrhenius coefficients:              3.47E-01    3.7     5541.0
496. NC7H16+OH=C7H15-1+H2O                         2.57E+07    1.8      954.0
     Reverse Arrhenius coefficients:              2.95E+04    2.3    18180.0
497. NC7H16+OH=C7H15-2+H2O                         4.90E+06    2.0     -596.0
     Reverse Arrhenius coefficients:              3.62E+02    2.9    19140.0
498. NC7H16+OH=C7H15-3+H2O                         4.90E+06    2.0     -596.0
     Reverse Arrhenius coefficients:              3.62E+02    2.9    19140.0
499. NC7H16+OH=C7H15-4+H2O                         2.45E+06    2.0     -596.0
     Reverse Arrhenius coefficients:              3.61E+02    2.9    19140.0
500. NC7H16+HO2=C7H15-1+H2O2                       4.08E+01    3.6    17160.0
     Reverse Arrhenius coefficients:              2.56E+00    3.5     3498.0
501. NC7H16+HO2=C7H15-2+H2O2                       1.26E+02    3.4    13720.0
     Reverse Arrhenius coefficients:              4.98E-01    3.7     2562.0
502. NC7H16+HO2=C7H15-3+H2O2                       1.26E+02    3.4    13720.0
     Reverse Arrhenius coefficients:              4.98E-01    3.7     2562.0
503. NC7H16+HO2=C7H15-4+H2O2                       6.32E+01    3.4    13720.0
     Reverse Arrhenius coefficients:              4.95E-01    3.7     2562.0
504. NC7H16+CH3=C7H15-1+CH4                        9.04E-01    3.6     7154.0
     Reverse Arrhenius coefficients:              8.93E-02    3.8    11030.0
505. NC7H16+CH3=C7H15-2+CH4                        5.41E+04    2.3     7287.0
     Reverse Arrhenius coefficients:              3.43E+02    2.8    13670.0
506. NC7H16+CH3=C7H15-3+CH4                        5.41E+04    2.3     7287.0
     Reverse Arrhenius coefficients:              3.43E+02    2.8    13670.0
507. NC7H16+CH3=C7H15-4+CH4                        2.70E+04    2.3     7287.0
     Reverse Arrhenius coefficients:              3.42E+02    2.8    13670.0
508. NC7H16+O2=C7H15-1+HO2                         4.20E+13    0.0    52800.0
     Reverse Arrhenius coefficients:              2.39E+10    0.3      453.0
509. NC7H16+O2=C7H15-2+HO2                         2.80E+13    0.0    50150.0
     Reverse Arrhenius coefficients:              1.00E+09    0.6      309.0
510. NC7H16+O2=C7H15-3+HO2                         2.80E+13    0.0    50150.0
     Reverse Arrhenius coefficients:              1.00E+09    0.6      309.0
511. NC7H16+O2=C7H15-4+HO2                         1.40E+13    0.0    50150.0
     Reverse Arrhenius coefficients:              9.94E+08    0.6      309.0
512. NC7H16+C2H5=C7H15-1+C2H6                      1.00E+11    0.0    13400.0
     Reverse Arrhenius coefficients:              3.20E+11    0.0    12300.0
513. NC7H16+C2H5=C7H15-2+C2H6                      1.00E+11    0.0    10400.0
     Reverse Arrhenius coefficients:              1.00E+11    0.0    12900.0
```

```
514. NC7H16+C2H5=C7H15-3+C2H6                  1.00E+11    0.0    10400.0
     Reverse Arrhenius coefficients:          1.00E+11    0.0    12900.0
515. NC7H16+C2H5=C7H15-4+C2H6                  5.00E+10    0.0    10400.0
     Reverse Arrhenius coefficients:          1.00E+11    0.0    12900.0
516. NC7H16+CH3O=C7H15-1+CH3OH                 3.16E+11    0.0     7000.0
     Reverse Arrhenius coefficients:          1.20E+10    0.0     9200.0
517. NC7H16+CH3O=C7H15-2+CH3OH                 2.19E+11    0.0     5000.0
     Reverse Arrhenius coefficients:          8.90E+09    0.0     7200.0
518. NC7H16+CH3O=C7H15-3+CH3OH                 2.19E+11    0.0     5000.0
     Reverse Arrhenius coefficients:          8.90E+09    0.0     7200.0
519. NC7H16+CH3O=C7H15-4+CH3OH                 1.10E+11    0.0     5000.0
     Reverse Arrhenius coefficients:          8.90E+09    0.0     7200.0
520. NC7H16+C2H3=C7H15-1+C2H4                  1.00E+12    0.0    18000.0
     Reverse Arrhenius coefficients:          2.57E+12    0.0    25400.0
521. NC7H16+C2H3=C7H15-2+C2H4                  8.00E+11    0.0    16800.0
     Reverse Arrhenius coefficients:          2.00E+12    0.0    24200.0
522. NC7H16+C2H3=C7H15-3+C2H4                  8.00E+11    0.0    16800.0
     Reverse Arrhenius coefficients:          2.00E+12    0.0    24200.0
523. NC7H16+C2H3=C7H15-4+C2H4                  4.00E+11    0.0    16800.0
     Reverse Arrhenius coefficients:          2.00E+12    0.0    24200.0
524. NC7H16+CH3O2=C7H15-1+CH3O2H               1.39E+00    4.0    18280.0
     Reverse Arrhenius coefficients:          1.69E+00    3.5     3024.0
525. NC7H16+CH3O2=C7H15-2+CH3O2H               2.04E+01    3.6    14810.0
     Reverse Arrhenius coefficients:          1.56E+00    3.4     2054.0
526. NC7H16+CH3O2=C7H15-3+CH3O2H               2.04E+01    3.6    14810.0
     Reverse Arrhenius coefficients:          1.56E+00    3.4     2054.0
527. NC7H16+CH3O2=C7H15-4+CH3O2H               1.02E+01    3.6    14810.0
     Reverse Arrhenius coefficients:          1.55E+00    3.4     2054.0
528. NC7H16+C7H15O2-3=C7H15-1+C7H15O2H-3       1.21E+13    0.0    20430.0
     Reverse Arrhenius coefficients:          1.44E+10    0.0    15000.0
529. NC7H16+C7H15O2-3=C7H15-2+C7H15O2H-3       8.06E+12    0.0    17700.0
     Reverse Arrhenius coefficients:          1.44E+10    0.0    15000.0
530. NC7H16+C7H15O2-3=C7H15-3+C7H15O2H-3       8.06E+12    0.0    17700.0
     Reverse Arrhenius coefficients:          1.44E+10    0.0    15000.0
531. NC7H16+C7H15O2-3=C7H15-4+C7H15O2H-3       4.03E+12    0.0    17700.0
     Reverse Arrhenius coefficients:          1.44E+10    0.0    15000.0
532. NC7H16+C7H15-1=C7H15-2+NC7H16             1.00E+11    0.0    10400.0
     Reverse Arrhenius coefficients:          1.50E+11    0.0    12300.0
533. NC7H16+C7H15-1=C7H15-3+NC7H16             1.00E+11    0.0    10400.0
     Reverse Arrhenius coefficients:          1.50E+11    0.0    12300.0
534. NC7H16+C7H15-1=C7H15-4+NC7H16             5.00E+10    0.0    10400.0
     Reverse Arrhenius coefficients:          1.50E+11    0.0    12300.0
535. NC7H16+C7H15-2=C7H15-3+NC7H16             1.00E+11    0.0    10400.0
     Reverse Arrhenius coefficients:          1.00E+11    0.0    10400.0
536. NC7H16+C7H15-2=C7H15-4+NC7H16             5.00E+10    0.0    10400.0
     Reverse Arrhenius coefficients:          1.00E+11    0.0    10400.0
537. NC7H16+C7H15-3=C7H15-4+NC7H16             5.00E+10    0.0    10400.0
     Reverse Arrhenius coefficients:          1.00E+11    0.0    10400.0
538. C7H15-1=C5H11-1+C2H4                      1.23E+19   -1.9    31400.0
     Reverse Arrhenius coefficients:          1.00E+11    0.0     8200.0
539. C7H15-1=C7H14-1+H                         9.65E+13   -0.3    36010.0
     Reverse Arrhenius coefficients:          1.00E+13    0.0     2900.0
540. C7H15-2=PC4H9+C3H6                        9.76E+18   -1.8    31360.0
     Reverse Arrhenius coefficients:          1.00E+11    0.0     8200.0
541. C7H15-2=C7H14-1+H                         6.07E+12    0.1    36810.0
     Reverse Arrhenius coefficients:          1.00E+13    0.0     1200.0
542. C7H15-2=C7H14-2+H                         1.23E+13   -0.1    35640.0
     Reverse Arrhenius coefficients:          1.00E+13    0.0     2900.0
543. C7H15-3=C4H8-1+NC3H7                      6.16E+18   -1.7    30960.0
     Reverse Arrhenius coefficients:          1.00E+11    0.0     7700.0
544. C7H15-3=C6H12-1+CH3                       2.70E+17   -1.4    31480.0
     Reverse Arrhenius coefficients:          1.75E+11    0.0     7200.0
545. C7H15-3=C7H14-2+H                         1.23E+13   -0.1    35640.0
     Reverse Arrhenius coefficients:          1.00E+13    0.0     2900.0
546. C7H15-3=C7H14-3+H                         9.15E+12    0.0    35730.0
     Reverse Arrhenius coefficients:          1.00E+13    0.0     2900.0
547. C7H15-4=C2H5+C5H10-1                      1.14E+18   -1.3    31430.0
     Reverse Arrhenius coefficients:          1.00E+11    0.0     8200.0
548. C7H15-4=C7H14-3+H                         1.82E+13    0.0    35730.0
     Reverse Arrhenius coefficients:          1.00E+13    0.0     2900.0
549. C7H15-1+O2=C7H14-1+HO2                    3.00E-09    0.0     3000.0
     Reverse Arrhenius coefficients:          6.52E-10    0.2    18760.0
550. C7H15-2+O2=C7H14-1+HO2                    4.50E-09    0.0     5020.0
     Reverse Arrhenius coefficients:          1.53E-08   -0.2    18270.0
551. C7H15-2+O2=C7H14-2+HO2                    3.00E-09    0.0     3000.0
     Reverse Arrhenius coefficients:          5.04E-09    0.0    19120.0
552. C7H15-3+O2=C7H14-2+HO2                    3.00E-09    0.0     3000.0
     Reverse Arrhenius coefficients:          5.04E-09    0.0    19120.0
553. C7H15-3+O2=C7H14-3+HO2                    3.00E-09    0.0     3000.0
     Reverse Arrhenius coefficients:          6.77E-09   -0.1    19030.0
554. C7H15-4+O2=C7H14-3+HO2                    6.00E-09    0.0     3000.0
     Reverse Arrhenius coefficients:          6.79E-09   -0.1    19030.0
555. C7H15-1=C7H15-3                           1.39E+09    1.0    33760.0
     Reverse Arrhenius coefficients:          8.72E+07    1.3    36270.0
556. C7H15-1=C7H15-4                           2.54E+09    0.3    19760.0
     Reverse Arrhenius coefficients:          3.18E+08    0.7    22270.0
557. C7H15-2=C7H15-3                           9.59E+08    1.4    39700.0
     Reverse Arrhenius coefficients:          9.59E+08    1.4    39700.0
558. C7H15-1=C7H15-2                           5.48E+08    1.6    38760.0
     Reverse Arrhenius coefficients:          3.44E+07    2.0    41270.0
559. C7H14-1+H=C7H131-3+H2                     3.38E+05    2.4      207.0
     Reverse Arrhenius coefficients:          4.39E+06    2.1    20620.0
560. C7H14-1+OH=C7H131-3+H2O                   2.76E+04    2.6    -1919.0
     Reverse Arrhenius coefficients:          1.56E+06    2.4    33650.0
561. C7H14-1+CH3=C7H131-3+CH4                  3.69E+00    3.3     4002.0
```

```
     Reverse Arrhenius coefficients:              1.25E+03    3.0    24890.0
562. C7H14-1+HO2=C7H131-3+H2O2                     4.82E+03    2.5    10530.0
     Reverse Arrhenius coefficients:              1.61E+06    2.0    14630.0
563. C7H14-1+CH3O2=C7H131-3+CH3O2H                 4.82E+03    2.5    10530.0
     Reverse Arrhenius coefficients:              3.36E+06    1.8    11610.0
564. C7H14-1+CH3O=C7H131-3+CH3OH                   4.00E+01    2.9     8609.0
     Reverse Arrhenius coefficients:              2.51E+02    2.7    27290.0
565. C7H14-2+H=C7H131-3+H2                         1.73E+05    2.5     2492.0
     Reverse Arrhenius coefficients:              4.56E+06    2.1    20030.0
566. C7H14-2+OH=C7H131-3+H2O                       3.12E+06    2.0     -298.0
     Reverse Arrhenius coefficients:              3.56E+08    1.6    32400.0
567. C7H14-2+CH3=C7H131-3+CH4                      2.21E+00    3.5     5675.0
     Reverse Arrhenius coefficients:              1.52E+03    3.1    23700.0
568. C7H14-2+HO2=C7H131-3+H2O2                     9.64E+03    2.6    13910.0
     Reverse Arrhenius coefficients:              6.53E+06    1.8    15140.0
569. C7H14-2+CH3O2=C7H131-3+CH3O2H                 9.64E+03    2.6    13910.0
     Reverse Arrhenius coefficients:              1.36E+07    1.7    12120.0
570. C7H14-2+CH3O=C7H131-3+CH3OH                   9.00E+01    3.0    11990.0
     Reverse Arrhenius coefficients:              1.14E+03    2.5    27800.0
571. C7H14-3+H=C7H133-1+H2                         6.65E+05    2.5     6756.0
     Reverse Arrhenius coefficients:              3.10E+04    2.5    11260.0
572. C7H14-3+H=C7H133-5+H2                         3.38E+05    2.4      207.0
     Reverse Arrhenius coefficients:              4.38E+06    2.1    20560.0
573. C7H14-3+OH=C7H133-1+H2O                       1.05E+10    1.0     1586.0
     Reverse Arrhenius coefficients:              2.12E+09    1.0    21240.0
574. C7H14-3+OH=C7H133-5+H2O                       2.76E+04    2.6    -1919.0
     Reverse Arrhenius coefficients:              1.55E+06    2.4    33590.0
575. C7H14-3+CH3=C7H133-1+CH4                      9.04E-01    3.6     7154.0
     Reverse Arrhenius coefficients:              1.10E+00    3.6    12130.0
576. C7H14-3+CH3=C7H133-5+CH4                      3.69E+00    3.3     4002.0
     Reverse Arrhenius coefficients:              1.25E+03    3.0    24830.0
577. C7H14-3+HO2=C7H133-1+H2O2                     4.76E+04    2.5    16490.0
     Reverse Arrhenius coefficients:              5.70E+04    2.2     4686.0
578. C7H14-3+HO2=C7H133-5+H2O2                     4.82E+03    2.5    10530.0
     Reverse Arrhenius coefficients:              1.61E+06    2.0    14570.0
579. C7H14-3+CH3O2=C7H133-1+CH3O2H                 4.76E+04    2.5    16490.0
     Reverse Arrhenius coefficients:              1.19E+05    2.0     1666.0
580. C7H14-3+CH3O2=C7H133-5+CH3O2H                 4.82E+03    2.5    10530.0
     Reverse Arrhenius coefficients:              3.35E+06    1.8    11550.0
581. C7H14-3+CH3O=C7H133-1+CH3OH                   4.34E+11    0.0     6458.0
     Reverse Arrhenius coefficients:              9.74E+09    0.0     9228.0
582. C7H14-3+CH3O=C7H133-5+CH3OH                   4.00E+01    2.9     8609.0
     Reverse Arrhenius coefficients:              2.50E+02    2.7    27230.0
583. C7H131-3+HO2=C7H13O1-3+OH                     9.64E+12    0.0        0.0
     Reverse Arrhenius coefficients:              4.44E+15   -1.0    15400.0
584. C7H131-3+CH3O2=C7H13O1-3+CH3O                 9.64E+12    0.0        0.0
     Reverse Arrhenius coefficients:              4.33E+17   -1.6    20160.0
585. C7H131-3+C2H5O2=C7H13O1-3+C2H5O               9.64E+12    0.0        0.0
     Reverse Arrhenius coefficients:              2.84E+14   -0.7    18000.0
586. C7H131-3=C4H6+NC3H7                           1.10E+19   -1.5    40700.0
     Reverse Arrhenius coefficients:              8.50E+10    0.0     8300.0
587. C7H13O1-3=C2H3CHO+PC4H9                       9.62E+19   -2.0    10850.0
     Reverse Arrhenius coefficients:              1.00E+11    0.0     9600.0
588. C7H13O1-3=NC4H9CHO+C2H3                       1.03E+18   -1.5    23300.0
     Reverse Arrhenius coefficients:              1.00E+11    0.0     9600.0
589. C7H14-1+OH=CH2O+C6H13-1                       1.00E+11    0.0    -4000.0
     Warning...all REV parameters are zero...          0.00000E+00 0.00000E+00 0.00000E+00
               this reaction will be treated as irreversible
590. C7H14-1+OH=CH3CHO+C5H11-1                     1.00E+11    0.0    -4000.0
     Warning...all REV parameters are zero...          0.00000E+00 0.00000E+00 0.00000E+00
               this reaction will be treated as irreversible
591. C7H14-2+OH=CH3CHO+C5H11-1                     1.00E+11    0.0    -4000.0
     Warning...all REV parameters are zero...          0.00000E+00 0.00000E+00 0.00000E+00
               this reaction will be treated as irreversible
592. C7H14-2+OH=C2H5CHO+PC4H9                      1.00E+11    0.0    -4000.0
     Warning...all REV parameters are zero...          0.00000E+00 0.00000E+00 0.00000E+00
               this reaction will be treated as irreversible
593. C7H14-3+OH=C2H5CHO+PC4H9                      1.00E+11    0.0    -4000.0
     Warning...all REV parameters are zero...          0.00000E+00 0.00000E+00 0.00000E+00
               this reaction will be treated as irreversible
594. C7H14-1+O=CH2CHO+C5H11-1                      1.00E+11    0.0    -1050.0
     Warning...all REV parameters are zero...          0.00000E+00 0.00000E+00 0.00000E+00
               this reaction will be treated as irreversible
595. C7H14-2+O=CH3CHO+C5H10-1                      1.00E+11    0.0    -1050.0
     Warning...all REV parameters are zero...          0.00000E+00 0.00000E+00 0.00000E+00
               this reaction will be treated as irreversible
596. C7H14-3+O=CH3CHO+C5H10-1                      1.00E+11    0.0    -1050.0
     Warning...all REV parameters are zero...          0.00000E+00 0.00000E+00 0.00000E+00
               this reaction will be treated as irreversible
597. C7H14-1=PC4H9+C3H5-A                          3.17E+21   -1.6    75330.0
     Reverse Arrhenius coefficients:              1.00E+13    0.0        0.0
598. C7H14-2=C4H71-3+NC3H7                         3.74E+21   -1.7    75710.0
     Reverse Arrhenius coefficients:              1.00E+13    0.0        0.0
599. C7H14-3=C5H91-3+C2H5                          5.95E+21   -1.9    75790.0
     Reverse Arrhenius coefficients:              1.00E+13    0.0        0.0
600. C7H15O2-1=C7H15-1+O2                          2.66E+20   -1.7    35400.0
     Reverse Arrhenius coefficients:              4.52E+12    0.0        0.0
601. C7H15O2-2=C7H15-2+O2                          1.36E+23   -2.4    37670.0
     Reverse Arrhenius coefficients:              7.54E+12    0.0        0.0
602. C7H15O2-3=C7H15-3+O2                          1.36E+23   -2.4    37670.0
     Reverse Arrhenius coefficients:              7.54E+12    0.0        0.0
603. C7H15O2-4=C7H15-4+O2                          1.36E+23   -2.4    37670.0
     Reverse Arrhenius coefficients:              7.54E+12    0.0        0.0
604. C7H15-1+C7H15O2-1=C7H15O-1+C7H15O-1           7.00E+12    0.0    -1000.0
     Reverse Arrhenius coefficients:              1.12E+14   -0.2    30250.0
```

```
605. C7H15-1+C7H15O2-2=C7H15O-1+C7H15O-2           7.00E+12    0.0    -1000.0
     Reverse Arrhenius coefficients:             6.35E+13   -0.2    29880.0
606. C7H15-1+C7H15O2-3=C7H15O-1+C7H15O-3           7.00E+12    0.0    -1000.0
     Reverse Arrhenius coefficients:             6.35E+13   -0.2    29880.0
607. C7H15-1+C7H15O2-4=C7H15O-1+C7H15O-4           7.00E+12    0.0    -1000.0
     Reverse Arrhenius coefficients:             6.35E+13   -0.2    29880.0
608. C7H15-2+C7H15O2-1=C7H15O-2+C7H15O-1           7.00E+12    0.0    -1000.0
     Reverse Arrhenius coefficients:             9.69E+15   -0.8    32160.0
609. C7H15-2+C7H15O2-2=C7H15O-2+C7H15O-2           7.00E+12    0.0    -1000.0
     Reverse Arrhenius coefficients:             5.51E+15   -0.7    31790.0
610. C7H15-2+C7H15O2-3=C7H15O-2+C7H15O-3           7.00E+12    0.0    -1000.0
     Reverse Arrhenius coefficients:             5.51E+15   -0.7    31790.0
611. C7H15-2+C7H15O2-4=C7H15O-2+C7H15O-4           7.00E+12    0.0    -1000.0
     Reverse Arrhenius coefficients:             5.51E+15   -0.7    31790.0
612. C7H15-3+C7H15O2-1=C7H15O-3+C7H15O-1           7.00E+12    0.0    -1000.0
     Reverse Arrhenius coefficients:             9.69E+15   -0.8    32160.0
613. C7H15-3+C7H15O2-2=C7H15O-3+C7H15O-2           7.00E+12    0.0    -1000.0
     Reverse Arrhenius coefficients:             5.51E+15   -0.7    31790.0
614. C7H15-3+C7H15O2-3=C7H15O-3+C7H15O-3           7.00E+12    0.0    -1000.0
     Reverse Arrhenius coefficients:             5.51E+15   -0.7    31790.0
615. C7H15-3+C7H15O2-4=C7H15O-3+C7H15O-4           7.00E+12    0.0    -1000.0
     Reverse Arrhenius coefficients:             5.51E+15   -0.7    31790.0
616. C7H15-4+C7H15O2-1=C7H15O-4+C7H15O-1           7.00E+12    0.0    -1000.0
     Reverse Arrhenius coefficients:             9.69E+15   -0.8    32160.0
617. C7H15-4+C7H15O2-2=C7H15O-4+C7H15O-2           7.00E+12    0.0    -1000.0
     Reverse Arrhenius coefficients:             5.51E+15   -0.7    31790.0
618. C7H15-4+C7H15O2-3=C7H15O-4+C7H15O-3           7.00E+12    0.0    -1000.0
     Reverse Arrhenius coefficients:             5.51E+15   -0.7    31790.0
619. C7H15-4+C7H15O2-4=C7H15O-4+C7H15O-4           7.00E+12    0.0    -1000.0
     Reverse Arrhenius coefficients:             5.51E+15   -0.7    31790.0
620. C7H15-1+HO2=C7H15O-1+OH                       7.00E+12    0.0    -1000.0
     Reverse Arrhenius coefficients:             3.55E+15   -0.6    26160.0
621. C7H15-2+HO2=C7H15O-2+OH                       7.00E+12    0.0    -1000.0
     Reverse Arrhenius coefficients:             3.08E+17   -1.1    28070.0
622. C7H15-3+HO2=C7H15O-3+OH                       7.00E+12    0.0    -1000.0
     Reverse Arrhenius coefficients:             3.08E+17   -1.1    28070.0
623. C7H15-4+HO2=C7H15O-4+OH                       7.00E+12    0.0    -1000.0
     Reverse Arrhenius coefficients:             3.08E+17   -1.1    28070.0
624. C7H15-1+CH3O2=C7H15O-1+CH3O                   7.00E+12    0.0    -1000.0
     Reverse Arrhenius coefficients:             2.22E+14   -0.3    30400.0
625. C7H15-2+CH3O2=C7H15O-2+CH3O                   7.00E+12    0.0    -1000.0
     Reverse Arrhenius coefficients:             1.93E+16   -0.8    32310.0
626. C7H15-3+CH3O2=C7H15O-3+CH3O                   7.00E+12    0.0    -1000.0
     Reverse Arrhenius coefficients:             1.93E+16   -0.8    32310.0
627. C7H15-4+CH3O2=C7H15O-4+CH3O                   7.00E+12    0.0    -1000.0
     Reverse Arrhenius coefficients:             1.93E+16   -0.8    32310.0
628. C7H15O2-1=C7H14-1+HO2                         1.00E+39   -8.1    41490.0
629. C7H15O2-2=C7H14-1+HO2                         1.01E+43   -9.4    42490.0
630. C7H15O2-2=C7H14-2+HO2                         1.00E+39   -8.1    41490.0
631. C7H15O2-3=C7H14-2+HO2                         1.00E+39   -8.1    41490.0
632. C7H15O2-3=C7H14-3+HO2                         1.00E+39   -8.1    41490.0
633. C7H15O2-4=C7H14-3+HO2                         2.01E+39   -8.1    41490.0
634. C7H15O2-1=C7H14OOH1-3                         2.50E+10    0.0    20450.0
635. C7H15O2-2=C7H14OOH2-4                         2.50E+10    0.0    20450.0
636. C7H15O2-3=C7H14OOH3-5                         2.50E+10    0.0    20450.0
637. C7H15O2-4=C7H14OOH4-2                         5.00E+10    0.0    20450.0
638. C7H15O2-3+HO2=C7H15O2H-3+O2                   1.75E+10    0.0    -3275.0
     Reverse Arrhenius coefficients:             4.50E+13   -0.8    34040.0
639. H2O2+C7H15O2-3=HO2+C7H15O2H-3                 2.40E+12    0.0    10000.0
     Reverse Arrhenius coefficients:             2.40E+12    0.0    10000.0
640. C7H15O2-1+CH3O2=C7H15O-1+CH3O+O2              1.40E+16   -1.6     1860.0
     Warning...all REV parameters are zero...          0.00000E+00 0.00000E+00 0.00000E+00
               this reaction will be treated as irreversible
641. C7H15O2-2+CH3O2=C7H15O-2+CH3O+O2              1.40E+16   -1.6     1860.0
     Warning...all REV parameters are zero...          0.00000E+00 0.00000E+00 0.00000E+00
               this reaction will be treated as irreversible
642. C7H15O2-3+CH3O2=C7H15O-3+CH3O+O2              1.40E+16   -1.6     1860.0
     Warning...all REV parameters are zero...          0.00000E+00 0.00000E+00 0.00000E+00
               this reaction will be treated as irreversible
643. C7H15O2-4+CH3O2=C7H15O-4+CH3O+O2              1.40E+16   -1.6     1860.0
     Warning...all REV parameters are zero...          0.00000E+00 0.00000E+00 0.00000E+00
               this reaction will be treated as irreversible
644. C7H15O2-1+C7H15O2-1=O2+C7H15O-1+C7H15O-1      1.40E+16   -1.6     1860.0
     Warning...all REV parameters are zero...          0.00000E+00 0.00000E+00 0.00000E+00
               this reaction will be treated as irreversible
645. C7H15O2-1+C7H15O2-2=C7H15O-1+C7H15O-2+O2      1.40E+16   -1.6     1860.0
     Warning...all REV parameters are zero...          0.00000E+00 0.00000E+00 0.00000E+00
               this reaction will be treated as irreversible
646. C7H15O2-1+C7H15O2-3=C7H15O-1+C7H15O-3+O2      1.40E+16   -1.6     1860.0
     Warning...all REV parameters are zero...          0.00000E+00 0.00000E+00 0.00000E+00
               this reaction will be treated as irreversible
647. C7H15O2-1+C7H15O2-4=C7H15O-1+C7H15O-4+O2      1.40E+16   -1.6     1860.0
     Warning...all REV parameters are zero...          0.00000E+00 0.00000E+00 0.00000E+00
               this reaction will be treated as irreversible
648. C7H15O2-2+C7H15O2-2=O2+C7H15O-2+C7H15O-2      1.40E+16   -1.6     1860.0
     Warning...all REV parameters are zero...          0.00000E+00 0.00000E+00 0.00000E+00
               this reaction will be treated as irreversible
649. C7H15O2-2+C7H15O2-3=C7H15O-2+C7H15O-3+O2      1.40E+16   -1.6     1860.0
     Warning...all REV parameters are zero...          0.00000E+00 0.00000E+00 0.00000E+00
               this reaction will be treated as irreversible
650. C7H15O2-2+C7H15O2-4=C7H15O-2+C7H15O-4+O2      1.40E+16   -1.6     1860.0
     Warning...all REV parameters are zero...          0.00000E+00 0.00000E+00 0.00000E+00
               this reaction will be treated as irreversible
651. C7H15O2-3+C7H15O2-3=O2+C7H15O-3+C7H15O-3      1.40E+16   -1.6     1860.0
     Warning...all REV parameters are zero...          0.00000E+00 0.00000E+00 0.00000E+00
```

```
              this reaction will be treated as irreversible
652. C7H15O2-3+C7H15O2-4=C7H15O-3+C7H15O-4+O2       1.40E+16   -1.6     1860.0
     Warning...all REV parameters are zero...          0.00000E+00 0.00000E+00 0.00000E+00
              this reaction will be treated as irreversible
653. C7H15O2-4+C7H15O2-4=O2+C7H15O-4+C7H15O-4       1.40E+16   -1.6     1860.0
     Warning...all REV parameters are zero...          0.00000E+00 0.00000E+00 0.00000E+00
              this reaction will be treated as irreversible
654. C7H15O2H-3=C7H15O-3+OH                         1.00E+16    0.0    39000.0
     Reverse Arrhenius coefficients:               9.52E+06    2.0    -6922.0
655. C7H15O-1=CH2O+C6H13-1                          6.02E+20   -2.2    24830.0
     Reverse Arrhenius coefficients:               1.00E+11    0.0    11900.0
656. C7H15O-2=CH3CHO+C5H11-1                        1.48E+22   -2.5    20370.0
     Reverse Arrhenius coefficients:               1.00E+11    0.0    12900.0
657. C7H15O-3=C2H5CHO+PC4H9                         6.57E+17   -1.2    19370.0
     Reverse Arrhenius coefficients:               1.00E+11    0.0    12900.0
658. C7H15O-4=NC3H7CHO+NC3H7                        4.77E+22   -2.6    21820.0
     Reverse Arrhenius coefficients:               1.00E+11    0.0    12900.0
659. C7H14OOH1-3=C7H14O1-3+OH                       7.50E+10    0.0    15250.0
     Warning...all REV parameters are zero...          0.00000E+00 0.00000E+00 0.00000E+00
              this reaction will be treated as irreversible
660. C7H14OOH2-4=C7H14O2-4+OH                       7.50E+10    0.0    15250.0
     Warning...all REV parameters are zero...          0.00000E+00 0.00000E+00 0.00000E+00
              this reaction will be treated as irreversible
661. C7H14OOH4-2=C7H14O2-4+OH                       7.50E+10    0.0    15250.0
     Warning...all REV parameters are zero...          0.00000E+00 0.00000E+00 0.00000E+00
              this reaction will be treated as irreversible
662. C7H14OOH1-3=OH+CH2O+C6H12-1                    2.15E+09    1.2    30370.0
     Warning...all REV parameters are zero...          0.00000E+00 0.00000E+00 0.00000E+00
              this reaction will be treated as irreversible
663. C7H14OOH2-4=OH+CH3CHO+C5H10-1                  1.55E+12    0.6    30090.0
     Warning...all REV parameters are zero...          0.00000E+00 0.00000E+00 0.00000E+00
              this reaction will be treated as irreversible
664. C7H14OOH3-5=OH+C2H5CHO+C4H8-1                  2.66E+13    0.1    30430.0
     Warning...all REV parameters are zero...          0.00000E+00 0.00000E+00 0.00000E+00
              this reaction will be treated as irreversible
665. C7H14OOH4-2=OH+NC3H7CHO+C3H6                   6.19E+13    0.1    30840.0
     Warning...all REV parameters are zero...          0.00000E+00 0.00000E+00 0.00000E+00
              this reaction will be treated as irreversible
666. C7H14OOH1-3O2=C7H14OOH1-3+O2                   1.37E+23   -2.4    37640.0
     Reverse Arrhenius coefficients:               7.54E+12    0.0        0.0
667. C7H14OOH2-4O2=C7H14OOH2-4+O2                   1.39E+23   -2.4    37600.0
     Reverse Arrhenius coefficients:               7.54E+12    0.0        0.0
668. C7H14OOH3-5O2=C7H14OOH3-5+O2                   1.39E+23   -2.4    37600.0
     Reverse Arrhenius coefficients:               7.54E+12    0.0        0.0
669. C7H14OOH4-2O2=C7H14OOH4-2+O2                   6.97E+22   -2.4    37600.0
     Reverse Arrhenius coefficients:               7.54E+12    0.0        0.0
670. C7H14OOH1-3O2=NC7KET13+OH                      2.50E+10    0.0    21000.0
671. C7H14OOH2-4O2=NC7KET24+OH                      1.25E+10    0.0    17450.0
672. C7H14OOH3-5O2=NC7KET35+OH                      1.25E+10    0.0    17450.0
673. C7H14OOH4-2O2=NC7KET42+OH                      1.25E+10    0.0    17450.0
674. NC7KET13=NC4H9CHO+CH2CHO+OH                    1.00E+16    0.0    39000.0
     Warning...all REV parameters are zero...          0.00000E+00 0.00000E+00 0.00000E+00
              this reaction will be treated as irreversible
675. NC7KET24=NC3H7CHO+CH3COCH2+OH                  1.00E+16    0.0    39000.0
     Warning...all REV parameters are zero...          0.00000E+00 0.00000E+00 0.00000E+00
              this reaction will be treated as irreversible
676. NC7KET35=C2H5CHO+C2H5COCH2+OH                  1.00E+16    0.0    39000.0
     Warning...all REV parameters are zero...          0.00000E+00 0.00000E+00 0.00000E+00
              this reaction will be treated as irreversible
677. NC7KET42=CH3CHO+NC3H7COCH2+OH                  1.00E+16    0.0    39000.0
     Warning...all REV parameters are zero...          0.00000E+00 0.00000E+00 0.00000E+00
              this reaction will be treated as irreversible
678. C7H14O1-3+OH=C6H12-1+HCO+H2O                   2.50E+12    0.0        0.0
     Warning...all REV parameters are zero...          0.00000E+00 0.00000E+00 0.00000E+00
              this reaction will be treated as irreversible
679. C7H14O2-4+OH=CH3CO+C5H10-1+H2O                 2.50E+12    0.0        0.0
     Warning...all REV parameters are zero...          0.00000E+00 0.00000E+00 0.00000E+00
              this reaction will be treated as irreversible
680. C7H14O1-3+OH=C2H4+NC4H9CO+H2O                  2.50E+12    0.0        0.0
     Warning...all REV parameters are zero...          0.00000E+00 0.00000E+00 0.00000E+00
              this reaction will be treated as irreversible
681. C7H14O2-4+OH=C3H6+NC3H7CO+H2O                  2.50E+12    0.0        0.0
     Warning...all REV parameters are zero...          0.00000E+00 0.00000E+00 0.00000E+00
              this reaction will be treated as irreversible
682. C7H14O1-3+HO2=C6H12-1+HCO+H2O2                 5.00E+12    0.0    17700.0
     Warning...all REV parameters are zero...          0.00000E+00 0.00000E+00 0.00000E+00
              this reaction will be treated as irreversible
683. C7H14O2-4+HO2=CH3CO+C5H10-1+H2O2               5.00E+12    0.0    17700.0
     Warning...all REV parameters are zero...          0.00000E+00 0.00000E+00 0.00000E+00
              this reaction will be treated as irreversible
684. C7H14O1-3+HO2=C2H4+NC4H9CO+H2O2                5.00E+12    0.0    17700.0
     Warning...all REV parameters are zero...          0.00000E+00 0.00000E+00 0.00000E+00
              this reaction will be treated as irreversible
685. C7H14O2-4+HO2=C3H6+NC3H7CO+H2O2                5.00E+12    0.0    17700.0
     Warning...all REV parameters are zero...          0.00000E+00 0.00000E+00 0.00000E+00
              this reaction will be treated as irreversible
686. CHCHCHO+OH=CH2CHO+HCO                          1.00E+12    0.0        0.0
     Reverse Arrhenius coefficients:               2.72E+11    0.3    36200.0
687. O2+C6H12-1=CH2O+NC4H9CHO                       1.00E+14    0.0    37000.0
     Warning...all REV parameters are zero...          0.00000E+00 0.00000E+00 0.00000E+00
              this reaction will be treated as irreversible
688. C6H12-1=C3H6+C3H6                              4.00E+12    0.0    58000.0
689. PC4H9+C2H3=C6H12-1                             1.00E+13    0.0        0.0
690. SC2H4OH+M<=>CH3CHO+H+M                         1.00E+14    0.0    25000.0
     Reverse Arrhenius coefficients:               2.74E+12    0.5     -470.0
```

```
 691. SC2H4OH+O2<=>CH3CHO+HO2                      3.81E+06    2.0     1641.0
      Reverse Arrhenius coefficients:             2.19E+05    2.4    25040.0
 692. NC3H7O2+C3H8<=>NC3H7O2H+NC3H7                1.70E+13    0.0    20460.0
      Reverse Arrhenius coefficients:             2.09E+13   -0.5     5000.0
 693. C3H6+NC3H7O2<=>C3H5-A+NC3H7O2H               3.24E+11    0.0    14900.0
      Reverse Arrhenius coefficients:             2.00E+10    0.0    15000.0
 694. NC3H7O2+CH2O<=>NC3H7O2H+HCO                  5.60E+12    0.0    13600.0
      Reverse Arrhenius coefficients:             8.00E+11    0.0    10000.0
 695. NC3H7O2+CH3CHO<=>NC3H7O2H+CH3CO             2.80E+12    0.0    13600.0
      Reverse Arrhenius coefficients:             1.00E+12    0.0    10000.0
 696. NC3H7O2+HO2<=>NC3H7O2H+O2                    1.75E+10    0.0    -3275.0
      Reverse Arrhenius coefficients:             3.84E+13   -0.8    33610.0
 697. C2H4+NC3H7O2<=>C2H3+NC3H7O2H                 1.13E+13    0.0    30430.0
      Reverse Arrhenius coefficients:             3.00E+12    0.0    11500.0
 698. CH3OH+NC3H7O2<=>CH2OH+NC3H7O2H               6.30E+12    0.0    19360.0
      Reverse Arrhenius coefficients:             1.00E+09    0.0    10000.0
 699. C2H3CHO+NC3H7O2<=>C2H3CO+NC3H7O2H            2.80E+12    0.0    13600.0
      Reverse Arrhenius coefficients:             1.00E+12    0.0    10000.0
 700. CH4+NC3H7O2<=>CH3+NC3H7O2H                   1.12E+13    0.0    24640.0
      Reverse Arrhenius coefficients:             7.43E+11    0.0     5500.0
 701. H2+NC3H7O2<=>H+NC3H7O2H                      3.01E+13    0.0    26030.0
      Reverse Arrhenius coefficients:             4.80E+13    0.0     7950.0
 702. NC3H7O2+C2H6<=>NC3H7O2H+C2H5                 1.70E+13    0.0    20460.0
      Reverse Arrhenius coefficients:             5.00E+11    0.0     6500.0
 703. NC3H7O2+C2H5CHO<=>NC3H7O2H+C2H5CO           2.00E+11    0.0     9500.0
      Reverse Arrhenius coefficients:             5.00E+09    0.0    10000.0
 704. C4H8-1+NC3H7O2<=>C4H71-3+NC3H7O2H            1.40E+12    0.0    14900.0
      Reverse Arrhenius coefficients:             3.16E+11    0.0    13000.0
 705. IC3H7O2<=>C3H6OOH2-1                         1.80E+12    0.0    29400.0
      Reverse Arrhenius coefficients:             1.12E+10    0.1    11810.0
 706. C3H6OOH2-1<=>C3H6+HO2                        3.24E+18   -2.0    18970.0
      Reverse Arrhenius coefficients:             1.00E+11    0.0    11750.0
 707. C3H6OOH2-1O2<=>C3H6OOH2-1+O2                 5.23E+22   -2.2    37820.0
      Reverse Arrhenius coefficients:             4.52E+12    0.0        0.0
 708. C7H133-1<=>C2H4+C5H91-1                      1.01E+17   -1.3    43990.0
      Reverse Arrhenius coefficients:             1.00E+11    0.0     8300.0
 709. C5H91-1<=>C2H2+NC3H7                         2.76E+15   -0.7    30800.0
      Reverse Arrhenius coefficients:             2.00E+11    0.0     7800.0

UNITS for the preceding reactions (unless otherwise noted):
       A units mole-cm-sec-K, E units cal/mole
```

APPENDIX B: CSU186 NATURAL GAS/DIESEL RCCI MECHANISM

The following is a list of the chemical species and reactions that form the CSU186 reduced chemical kinetic mechanism for natural gas/diesel RCCI combustion, which was discussed in Chapter CHAPTER 7:. The list of reactions contains rate constant information in the Arrhenius form. Some of the reactions include third body efficiencies and Troe [57] pressure dependent reaction rates. More information about the format of the mechanism and expressions for rate constants can be found in the CHEMKIN® theory manual [58]. This reduced mechanism uses a blend of n-dodecane and m-xylene (called P-XYL in the mechanism) to represent diesel fuel kinetics and a surrogate mixture of methane, ethane, and propane to represent the kinetics of natural gas. This mechanism is a combination of reduced forms of the methane through n-pentane mechanism of Healy et al. [37] and the reduced diesel surrogate mechanism of Pei et al. [54]. The detailed mechanisms were reduced using the direct relation graph with error propagation and sensitivity analysis (DRGEPSA), which is described in detail in the CONVERGE™ theory manual [21].

ELEMENTS CONSIDERED	ATOMIC WEIGHT
1. C	12.0112
2. H	1.00797
3. N	14.0067
4. O	15.9994
5. AR	39.9480
6. HE	4.00260

UNITS for the following reactions (unless otherwise noted):
A units mole-cm-sec-K, E units cal/mole

SPECIES CONSIDERED	PHASE	CHARGE	MOLECULAR WEIGHT	TEMPERATURE LOW	TEMPERATURE HIGH	ELEMENT COUNT C	H	N	O	AR	HE
1. H	G	0	1.0080E+00	300	5000	0	1	0	0	0	0
2. H2	G	0	2.0159E+00	300	5000	0	2	0	0	0	0
3. O	G	0	1.5999E+01	300	5000	0	0	0	1	0	0
4. O2	G	0	3.1999E+01	300	5000	0	0	0	2	0	0
5. OH	G	0	1.7007E+01	300	5000	0	1	0	1	0	0
6. H2O	G	0	1.8015E+01	300	5000	0	2	0	1	0	0
7. N2	G	0	2.8013E+01	300	5000	0	0	2	0	0	0
8. HO2	G	0	3.3007E+01	200	3500	0	1	0	2	0	0
9. H2O2	G	0	3.4015E+01	300	5000	0	2	0	2	0	0
10. CO	G	0	2.8011E+01	300	5000	1	0	0	1	0	0
11. CO2	G	0	4.4010E+01	300	5000	1	0	0	2	0	0
12. CH2O	G	0	3.0026E+01	300	5000	1	2	0	1	0	0
13. HCO	G	0	2.9019E+01	300	5000	1	1	0	1	0	0
14. HOCHO	G	0	4.6026E+01	300	5000	1	2	0	2	0	0
15. HOCH2O	G	0	4.7034E+01	300	5000	1	3	0	2	0	0
16. CH3OH	G	0	3.2042E+01	300	5000	1	4	0	1	0	0
17. CH2OH	G	0	3.1034E+01	300	5000	1	3	0	1	0	0
18. CH3O	G	0	3.1034E+01	300	5000	1	3	0	1	0	0
19. CH3O2H	G	0	4.8042E+01	300	5000	1	4	0	2	0	0
20. CH3O2	G	0	4.7034E+01	300	5000	1	3	0	2	0	0
21. CH4	G	0	1.6043E+01	300	5000	1	4	0	0	0	0
22. CH3	G	0	1.5035E+01	300	5000	1	3	0	0	0	0
23. CH2	G	0	1.4027E+01	250	4000	1	2	0	0	0	0
24. CH2(S)	G	0	1.4027E+01	300	4000	1	2	0	0	0	0
25. CH	G	0	1.3019E+01	300	5000	1	1	0	0	0	0
26. C2H6	G	0	3.0070E+01	300	5000	2	6	0	0	0	0
27. C2H5	G	0	2.9062E+01	300	5000	2	5	0	0	0	0
28. C2H4	G	0	2.8054E+01	300	5000	2	4	0	0	0	0
29. C2H3	G	0	2.7046E+01	300	5000	2	3	0	0	0	0
30. C2H2	G	0	2.6038E+01	300	5000	2	2	0	0	0	0
31. C2H	G	0	2.5030E+01	300	5000	2	1	0	0	0	0
32. CH3CHO	G	0	4.4054E+01	300	5000	2	4	0	1	0	0
33. CH3CO	G	0	4.3046E+01	300	5000	2	3	0	1	0	0
34. CH2CHO	G	0	4.3046E+01	300	5000	2	3	0	1	0	0
35. CH2CO	G	0	4.2038E+01	300	5000	2	2	0	1	0	0
36. HCCO	G	0	4.1030E+01	300	4000	2	1	0	1	0	0
37. C2H5O	G	0	4.5062E+01	300	5000	2	5	0	1	0	0
38. C2H5O2	G	0	6.1061E+01	300	5000	2	5	0	2	0	0
39. C2H3O1-2	G	0	4.3046E+01	300	5000	2	3	0	1	0	0
40. CH3COCH2	G	0	5.7073E+01	300	5000	3	5	0	1	0	0
41. CH3COCH2O2	G	0	8.9072E+01	300	5000	3	5	0	3	0	0
42. CH3COCH2O2H	G	0	9.0079E+01	300	5000	3	6	0	3	0	0
43. CH3COCH2O	G	0	7.3072E+01	300	5000	3	5	0	2	0	0
44. C2H3CHO	G	0	5.6065E+01	300	5000	3	4	0	1	0	0
45. C2H3CO	G	0	5.5057E+01	300	5000	3	3	0	1	0	0
46. C2H5CHO	G	0	5.8081E+01	300	5000	3	6	0	1	0	0
47. C3H8	G	0	4.4097E+01	300	5000	3	8	0	0	0	0
48. IC3H7	G	0	4.3089E+01	300	5000	3	7	0	0	0	0
49. NC3H7	G	0	4.3089E+01	300	5000	3	7	0	0	0	0
50. C3H6	G	0	4.2081E+01	300	5000	3	6	0	0	0	0
51. C3H5-A	G	0	4.1073E+01	300	5000	3	5	0	0	0	0
52. C3H4-P	G	0	4.0065E+01	300	4000	3	4	0	0	0	0
53. C3H4-A	G	0	4.0065E+01	300	4000	3	4	0	0	0	0
54. C3H3	G	0	3.9057E+01	300	4000	3	3	0	0	0	0
55. C3H2	G	0	3.8049E+01	150	4000	3	2	0	0	0	0
56. C3H5O	G	0	5.7073E+01	300	5000	3	5	0	1	0	0
57. C3H6OOH1-2	G	0	7.5088E+01	300	5000	3	7	0	2	0	0
58. NC3H7O2	G	0	7.5088E+01	300	5000	3	7	0	2	0	0
59. IC3H7O2	G	0	7.5088E+01	300	5000	3	7	0	2	0	0
60. CH3CHCO	G	0	5.6065E+01	300	5000	3	4	0	1	0	0
61. C4H8-1	G	0	5.6108E+01	300	5000	4	8	0	0	0	0
62. PC4H9	G	0	5.7116E+01	300	5000	4	9	0	0	0	0
63. SC4H9	G	0	5.7116E+01	300	5000	4	9	0	0	0	0
64. C4H71-3	G	0	5.5100E+01	300	5000	4	7	0	0	0	0
65. C4H71-4	G	0	5.5100E+01	300	5000	4	7	0	0	0	0
66. C4H6	G	0	5.4092E+01	300	5000	4	6	0	0	0	0
67. PC4H9O2	G	0	8.9115E+01	300	5000	4	9	0	2	0	0

68. C4H7O	G	0	7.1100E+01	300	5000	4	7	0	1	0	0
69. NC3H7CHO	G	0	7.2108E+01	300	5000	4	8	0	1	0	0
70. C5H11-1	G	0	7.1143E+01	300	5000	5	11	0	0	0	0
71. C5H11-2	G	0	7.1143E+01	300	5000	5	11	0	0	0	0
72. C5H10-1	G	0	7.0135E+01	300	5000	5	10	0	0	0	0
73. C5H91-4	G	0	6.9127E+01	300	5000	5	9	0	0	0	0
74. C5H11O2-1	G	0	1.0314E+02	300	5000	5	11	0	2	0	0
75. C5H10OOH1-3	G	0	1.0314E+02	300	5000	5	11	0	2	0	0
76. C5H10OOH1-3O2	G	0	1.3514E+02	300	5000	5	11	0	4	0	0
77. NC5KET13	G	0	1.1813E+02	300	5000	5	10	0	3	0	0
78. C6H13-1	G	0	8.5171E+01	300	5000	6	13	0	0	0	0
79. C6H13-2	G	0	8.5171E+01	300	5000	6	13	0	0	0	0
80. C6H12-1	G	0	8.4163E+01	300	5000	6	12	0	0	0	0
81. C6H111-5	G	0	8.3155E+01	300	5000	6	11	0	0	0	0
82. C6H13O2-1	G	0	1.1717E+02	300	5000	6	13	0	2	0	0
83. C6H12OOH1-3	G	0	1.1717E+02	300	5000	6	13	0	2	0	0
84. C6H12OOH1-3O2	G	0	1.4917E+02	300	5000	6	13	0	4	0	0
85. NC6KET13	G	0	1.3216E+02	300	5000	6	12	0	3	0	0
86. NC3H7COCH2	G	0	8.5127E+01	300	5000	5	9	0	1	0	0
87. C7H15-1	G	0	9.9198E+01	300	5000	7	15	0	0	0	0
88. C7H14-1	G	0	9.8190E+01	300	5000	7	14	0	0	0	0
89. C7H15O2-1	G	0	1.3120E+02	300	5000	7	15	0	2	0	0
90. C7H14OOH1-3	G	0	1.3120E+02	300	5000	7	15	0	2	0	0
91. C7H14OOH1-3O2	G	0	1.6320E+02	300	5000	7	15	0	4	0	0
92. C7H14O1-3	G	0	1.1419E+02	300	5000	7	14	0	1	0	0
93. NC5H11CHO	G	0	1.0016E+02	300	5000	6	12	0	1	0	0
94. NC5H11CO	G	0	9.9154E+01	300	5000	6	11	0	1	0	0
95. NC4H9COCH2	G	0	9.9154E+01	300	5000	6	11	0	1	0	0
96. C4H7OOH1-4	G	0	8.8107E+01	300	5000	4	8	0	2	0	0
97. C4H7O1-4	G	0	7.1100E+01	300	5000	4	7	0	1	0	0
98. NC12H26	G	0	1.7034E+02	300	5000	12	26	0	0	0	0
99. C12H25-1	G	0	1.6933E+02	300	5000	12	25	0	0	0	0
100. C12H25-2	G	0	1.6933E+02	300	5000	12	25	0	0	0	0
101. C12H25-3	G	0	1.6933E+02	300	5000	12	25	0	0	0	0
102. ISO8	G	0	1.6933E+02	300	5000	12	25	0	0	0	0
103. C10H21-1	G	0	1.4128E+02	300	5000	10	21	0	0	0	0
104. C10H21-2	G	0	1.4128E+02	300	5000	10	21	0	0	0	0
105. C10H21-5	G	0	1.4128E+02	300	5000	10	21	0	0	0	0
106. C9H19-1	G	0	1.2725E+02	300	5000	9	19	0	0	0	0
107. C9H19-4	G	0	1.2725E+02	300	5000	9	19	0	0	0	0
108. C9H19-5	G	0	1.2725E+02	300	5000	9	19	0	0	0	0
109. C8H17-1	G	0	1.1322E+02	300	5000	8	17	0	0	0	0
110. C8H17-4	G	0	1.1322E+02	300	5000	8	17	0	0	0	0
111. C12H24-1	G	0	1.6833E+02	300	5000	12	24	0	0	0	0
112. C12H24-2	G	0	1.6833E+02	300	5000	12	24	0	0	0	0
113. ISO13	G	0	1.6833E+02	300	5000	12	24	0	0	0	0
114. C10H20-1	G	0	1.4027E+02	300	5000	10	20	0	0	0	0
115. C9H18-1	G	0	1.2624E+02	300	5000	9	18	0	0	0	0
116. C12H25O2-2	G	0	2.0133E+02	300	5000	12	25	0	2	0	0
117. ISO4	G	0	2.0133E+02	300	5000	12	25	0	2	0	0
118. ISO3	G	0	2.0133E+02	300	5000	12	25	0	2	0	0
119. C8H17O2-1	G	0	1.4522E+02	300	5000	8	17	0	2	0	0
120. C12OOH2-4	G	0	2.0133E+02	300	5000	12	25	0	2	0	0
121. ISO5	G	0	2.0133E+02	300	5000	12	25	0	2	0	0
122. ISO6	G	0	2.0133E+02	300	5000	12	25	0	2	0	0
123. ISO7	G	0	2.0133E+02	300	5000	12	25	0	2	0	0
124. C8OOH1-3	G	0	1.4522E+02	300	5000	8	17	0	2	0	0
125. C12OOH2-4O2	G	0	2.3333E+02	300	5000	12	25	0	4	0	0
126. ISO1	G	0	2.3333E+02	300	5000	12	25	0	4	0	0
127. ISO2	G	0	2.3333E+02	300	5000	12	25	0	4	0	0
128. C8OOH1-3O2	G	0	1.7722E+02	300	5000	8	17	0	4	0	0
129. C12O2-4	G	0	1.8432E+02	300	5000	12	24	0	1	0	0
130. ISO11	G	0	1.8432E+02	300	5000	12	24	0	1	0	0
131. ISO12	G	0	1.8432E+02	300	5000	12	24	0	1	0	0
132. C12KET2-4	G	0	2.1632E+02	300	5000	12	24	0	3	0	0
133. ISO9	G	0	2.1632E+02	300	5000	12	24	0	3	0	0
134. ISO10	G	0	2.1632E+02	300	5000	12	24	0	3	0	0
135. C8KET1-3	G	0	1.6021E+02	300	5000	8	16	0	3	0	0
136. C8H17COCH2	G	0	1.5526E+02	300	5000	10	19	0	1	0	0
137. C7H15COCH2	G	0	1.4124E+02	300	5000	9	17	0	1	0	0
138. NC8H17CHO	G	0	1.4224E+02	300	5000	9	18	0	1	0	0
139. NC6H13CHO	G	0	1.1419E+02	300	5000	7	14	0	1	0	0
140. NC8H17CO	G	0	1.4124E+02	300	5000	9	17	0	1	0	0
141. NC6H13CO	G	0	1.1318E+02	300	5000	7	13	0	1	0	0
142. C12H23	G	0	1.6732E+02	300	5000	12	23	0	0	0	0
143. C9H17	G	0	1.2524E+02	300	5000	9	17	0	0	0	0
144. C6H5CH3	G	0	9.2142E+01	300	5000	7	8	0	0	0	0
145. C6H5CH2J	G	0	9.1134E+01	200	6000	7	7	0	0	0	0
146. CY13PD	G	0	6.6104E+01	300	5000	5	6	0	0	0	0
147. OXCCXCCXO	G	0	8.4075E+01	300	5000	4	4	0	2	0	0
148. C6H6	G	0	7.8115E+01	300	5000	6	6	0	0	0	0
149. CY13PD5J	G	0	6.5096E+01	300	5000	5	5	0	0	0	0
150. C6H4CH3	G	0	9.1134E+01	300	5000	7	7	0	0	0	0
151. O2C6H4CH3	G	0	1.2313E+02	300	5000	7	7	0	2	0	0
152. RODC6J(C)DO	G	0	1.2313E+02	300	5000	7	7	0	2	0	0
153. OCCXCCXCJC	G	0	9.5122E+01	300	5000	6	7	0	1	0	0
154. P-XYL	G	0	1.0617E+02	300	5000	8	10	0	0	0	0
155. MEC6H3CH3	G	0	1.0516E+02	300	5000	8	9	0	0	0	0
156. PXYLCH2J	G	0	1.0516E+02	300	5000	8	9	0	0	0	0
157. MEC6H4CHO	G	0	1.2015E+02	300	5000	8	8	0	1	0	0
158. MEC6H4CJO	G	0	1.1914E+02	300	5000	8	7	0	1	0	0
159. HOMEC6H3CH3	G	0	1.2217E+02	300	5000	8	10	0	1	0	0
160. OMEC6H3CH3	G	0	1.2116E+02	300	5000	8	9	0	1	0	0
161. O2MEC6H3CH3	G	0	1.3716E+02	300	5000	8	9	0	2	0	0
162. MEC6H4CH2OJ	G	0	1.2116E+02	300	5000	8	9	0	1	0	0

```
163. PXYLCH2OOJ       G  0 1.3716E+02   300   5000          8         9         0         2         0         0
164. AR               G  0 3.9948E+01   300   5000          0         0         0         0         1         0
165. CH3CO2           G  0 5.9045E+01   300   5000          2         3         0         2         0         0
166. C3H6OOH2-1       G  0 7.5088E+01   300   5000          3         7         0         2         0         0
167. C3H6OOH1-2O2     G  0 1.0709E+02   300   5000          3         7         0         4         0         0
168. C3H6OOH2-1O2     G  0 1.0709E+02   300   5000          3         7         0         4         0         0
169. IC3H7O           G  0 5.9089E+01   300   5000          3         7         0         1         0         0
170. C3KET12          G  0 9.0079E+01   300   5000          3         6         0         3         0         0
171. C3KET21          G  0 9.0079E+01   300   5000          3         6         0         3         0         0
172. C2H3COCH3        G  0 7.0092E+01   300   5000          4         6         0         1         0         0
173. PC4H9O           G  0 7.3116E+01   300   5000          4         9         0         1         0         0
174. C4H8OOH1-3       G  0 8.9115E+01   300   5000          4         9         0         2         0         0
175. C3H6OOH1-3       G  0 7.5088E+01   300   5000          3         7         0         2         0         0
176. C3H6OOH1-3O2     G  0 1.0709E+02   300   5000          3         7         0         4         0         0
177. C3KET13          G  0 9.0079E+01   300   5000          3         6         0         3         0         0
178. NC3H7O           G  0 5.9089E+01   300   5000          3         7         0         1         0         0
179. CH3CO3           G  0 7.5044E+01   300   5000          2         3         0         3         0         0
180. CH3CO3H          G  0 7.6052E+01   300   5000          2         4         0         3         0         0
181. NC3H7O2H         G  0 7.6096E+01   300   5000          3         8         0         2         0         0
182. C4H8OOH1-3O2     G  0 1.2111E+02   300   5000          4         9         0         4         0         0
183. NC4KET13         G  0 1.0411E+02   300   5000          4         8         0         3         0         0
184. C2H5CO           G  0 5.7073E+01   300   5000          3         5         0         1         0         0
185. C2H5O2H          G  0 6.2069E+01   300   5000          2         6         0         2         0         0
186. CH2CH2COCH3      G  0 7.1100E+01   300   5000          4         7         0         1         0         0
-------------------------------------------------------------------------------
```

```
                                                    (k = A T**b exp(-E/RT))
   REACTIONS CONSIDERED                                   A        b        E

  1. H+O2<=>O+OH                                       3.55E+15   -0.4    16600.0
     Reverse Arrhenius coefficients:                  1.03E+13    0.0     -133.0
  2. O+H2<=>H+OH                                       5.08E+04    2.7     6292.0
     Reverse Arrhenius coefficients:                  2.64E+04    2.7     4880.0
  3. OH+H2<=>H+H2O                                     2.16E+08    1.5     3430.0
     Reverse Arrhenius coefficients:                  2.29E+09    1.4    18320.0
  4. O+H2O<=>OH+OH                                     2.97E+06    2.0    13400.0
     Reverse Arrhenius coefficients:                  1.45E+05    2.1    -2904.0
  5. H2+M<=>H+H+M                                      4.58E+19   -1.4   104400.0
     Reverse Arrhenius coefficients:                  1.14E+20   -1.7      820.0
     H2              Enhanced by    2.500E+00
     H2O             Enhanced by    1.200E+01
     CO              Enhanced by    1.900E+00
     CO2             Enhanced by    3.800E+00
  6. O2+M<=>O+O+M                                      4.42E+17   -0.6   118900.0
     Reverse Arrhenius coefficients:                  6.16E+15   -0.5        0.0
     H2              Enhanced by    2.500E+00
     H2O             Enhanced by    1.200E+01
     CO              Enhanced by    1.900E+00
     CO2             Enhanced by    3.800E+00
     CH4             Enhanced by    2.000E+00
     C2H6            Enhanced by    3.000E+00
  7. OH+M<=>O+H+M                                      9.78E+17   -0.7   102100.0
     Reverse Arrhenius coefficients:                  4.71E+18   -1.0        0.0
     H2              Enhanced by    2.500E+00
     H2O             Enhanced by    1.200E+01
     CO              Enhanced by    1.500E+00
     CO2             Enhanced by    2.000E+00
     CH4             Enhanced by    2.000E+00
     C2H6            Enhanced by    3.000E+00
  8. H2O+M<=>H+OH+M                                    1.91E+23   -1.8   118500.0
     Reverse Arrhenius coefficients:                  4.50E+22   -2.0        0.0
     H2              Enhanced by    7.300E-01
     H2O             Enhanced by    1.200E+01
     CH4             Enhanced by    2.000E+00
     C2H6            Enhanced by    3.000E+00
  9. H+O2(+M)<=>HO2(+M)                                1.48E+12    0.6        0.0
     Low pressure limit:  0.34820E+17 -0.41100E+00 -0.11150E+04
     TROE centering:      0.50000E+00  0.10000E-29  0.10000E+31  0.10000E+11
     H2              Enhanced by    1.300E+00
     H2O             Enhanced by    1.400E+01
     CO              Enhanced by    1.900E+00
     CO2             Enhanced by    3.800E+00
     CH4             Enhanced by    2.000E+00
     C2H6            Enhanced by    3.000E+00
 10. HO2+H<=>H2+O2                                     1.66E+13    0.0      823.0
     Reverse Arrhenius coefficients:                  3.17E+12    0.3    55510.0
 11. HO2+H<=>OH+OH                                     7.08E+13    0.0      295.0
     Reverse Arrhenius coefficients:                  2.03E+10    0.7    36840.0
 12. HO2+O<=>OH+O2                                     3.25E+13    0.0        0.0
     Reverse Arrhenius coefficients:                  3.22E+12    0.3    53280.0
 13. HO2+OH<=>H2O+O2                                   1.97E+10    1.0     -328.4
     Reverse Arrhenius coefficients:                  3.99E+10    1.2    69250.0
 14. H2O2+O2<=>HO2+HO2                                 1.14E+16   -0.3    49730.0
     Reverse Arrhenius coefficients:                  1.03E+14    0.0    11040.0
     Declared duplicate reaction...
 15. H2O2+O2<=>HO2+HO2                                 2.14E+13   -0.3    37280.0
     Reverse Arrhenius coefficients:                  1.94E+11    0.0    -1409.0
     Declared duplicate reaction...
 16. H2O2(+M)<=>OH+OH(+M)                              2.95E+14    0.0    48430.0
     Low pressure limit:  0.12020E+18  0.00000E+00  0.45500E+05
     TROE centering:      0.50000E+00  0.10000E-29  0.10000E+31  0.10000E+11
     H2              Enhanced by    2.500E+00
     H2O             Enhanced by    1.200E+01
```

```
    CO              Enhanced by    1.900E+00
    CO2             Enhanced by    3.800E+00
    CH4             Enhanced by    2.000E+00
    C2H6            Enhanced by    3.000E+00
17. H2O2+H<=>H2O+OH                                  2.41E+13    0.0     3970.0
    Reverse Arrhenius coefficients:                 1.26E+08    1.3    71410.0
18. H2O2+H<=>H2+HO2                                  2.15E+10    1.0     6000.0
    Reverse Arrhenius coefficients:                 3.72E+07    1.7    22000.0
19. H2O2+O<=>OH+HO2                                  9.55E+06    2.0     3970.0
    Reverse Arrhenius coefficients:                 8.57E+03    2.7    18560.0
20. H2O2+OH<=>H2O+HO2                                2.00E+12    0.0      427.2
    Reverse Arrhenius coefficients:                 3.66E+10    0.6    31320.0
    Declared duplicate reaction...
21. H2O2+OH<=>H2O+HO2                                1.70E+18    0.0    29410.0
    Reverse Arrhenius coefficients:                 3.12E+16    0.6    60300.0
    Declared duplicate reaction...
22. CO+O(+M)<=>CO2(+M)                               1.80E+10    0.0     2384.0
    Low pressure limit:  0.13500E+25 -0.27880E+01  0.41910E+04
    H2              Enhanced by    2.000E+00
    O2              Enhanced by    6.000E+00
    H2O             Enhanced by    6.000E+00
    CO              Enhanced by    1.500E+00
    CO2             Enhanced by    3.500E+00
    CH4             Enhanced by    2.000E+00
    C2H6            Enhanced by    3.000E+00
23. CO+O2<=>CO2+O                                    1.05E+12    0.0    42540.0
    Reverse Arrhenius coefficients:                 8.04E+15   -0.8    51230.0
24. CO+OH<=>CO2+H                                    2.23E+05    1.9    -1158.0
    Reverse Arrhenius coefficients:                 5.90E+11    0.7    24260.0
25. CO+HO2<=>CO2+OH                                  3.01E+13    0.0    23000.0
    Reverse Arrhenius coefficients:                 2.28E+16   -0.5    84970.0
26. HCO+M<=>H+CO+M                                   4.75E+11    0.7    14870.0
    Reverse Arrhenius coefficients:                 3.58E+10    1.0     -457.3
    H2              Enhanced by    2.000E+00
    H2O             Enhanced by    1.200E+01
    CO              Enhanced by    1.500E+00
    CO2             Enhanced by    2.000E+00
    CH4             Enhanced by    2.000E+00
    C2H6            Enhanced by    3.000E+00
27. HCO+O2<=>CO+HO2                                  7.58E+12    0.0      410.0
    Reverse Arrhenius coefficients:                 1.20E+12    0.3    33950.0
28. HCO+H<=>CO+H2                                    7.34E+13    0.0        0.0
    Reverse Arrhenius coefficients:                 2.21E+12    0.7    88230.0
29. HCO+O<=>CO+OH                                    3.02E+13    0.0        0.0
    Reverse Arrhenius coefficients:                 4.72E+11    0.6    86820.0
30. HCO+O<=>CO2+H                                    3.00E+13    0.0        0.0
    Reverse Arrhenius coefficients:                 1.24E+18   -0.6   112200.0
31. HCO+OH<=>CO+H2O                                  1.02E+14    0.0        0.0
    Reverse Arrhenius coefficients:                 3.26E+13    0.6   103100.0
32. HCO+CH3<=>CH4+CO                                 2.65E+13    0.0        0.0
    Reverse Arrhenius coefficients:                 7.29E+14    0.2    89770.0
33. HCO+HO2<=>CH2O+O2                                2.50E+14   -0.1    13920.0
    Reverse Arrhenius coefficients:                 8.07E+15    0.0    53420.0
34. HCO+HO2<=>CO2+H+OH                               3.00E+13    0.0        0.0
    Warning...all REV parameters are zero... 0.0000e+000 0.000 0.000E+00
             this reaction will be treated as irreversible
35. CH2O+CO<=>HCO+HCO                                9.19E+13    0.4    73040.0
    Reverse Arrhenius coefficients:                 1.80E+13    0.0        0.0
36. HCO+HCO<=>H2+CO+CO                               3.00E+12    0.0        0.0
    Warning...all REV parameters are zero... 0.0000e+000 0.000 0.000E+00
             this reaction will be treated as irreversible
37. HCO+H(+M)<=>CH2O(+M)                             1.09E+12    0.5     -260.0
    Low pressure limit:  0.13500E+25 -0.25700E+01  0.14250E+04
    TROE centering:      0.78240E+00  0.27100E+03  0.27550E+04  0.65700E+04
    H2              Enhanced by    2.000E+00
    H2O             Enhanced by    6.000E+00
    CO              Enhanced by    1.500E+00
    CO2             Enhanced by    2.000E+00
    CH4             Enhanced by    2.000E+00
    C2H6            Enhanced by    3.000E+00
38. CO+H2(+M)<=>CH2O(+M)                             4.30E+07    1.5    79600.0
    Low pressure limit:  0.50700E+28 -0.34200E+01  0.84348E+05
    TROE centering:      0.93200E+00  0.19700E+03  0.15400E+04  0.10300E+05
    H2              Enhanced by    2.000E+00
    H2O             Enhanced by    6.000E+00
    CO              Enhanced by    1.500E+00
    CO2             Enhanced by    2.000E+00
    CH4             Enhanced by    2.000E+00
    C2H6            Enhanced by    3.000E+00
39. CH2O+OH<=>HCO+H2O                                7.82E+07    1.6    -1055.0
    Reverse Arrhenius coefficients:                 4.90E+06    1.8    29030.0
40. CH2O+H<=>HCO+H2                                  5.74E+07    1.9     2740.0
    Reverse Arrhenius coefficients:                 3.39E+05    2.2    17930.0
41. CH2O+O<=>HCO+OH                                  6.26E+09    1.1     2260.0
    Reverse Arrhenius coefficients:                 1.92E+07    1.4    16040.0
42. CH2O+CH3<=>HCO+CH4                               3.83E+01    3.4     4312.0
    Reverse Arrhenius coefficients:                 2.06E+02    3.2    21040.0
43. CH2O+HO2<=>HCO+H2O2                              7.10E-03    4.5     6580.0
    Reverse Arrhenius coefficients:                 2.43E-02    4.1     5769.0
44. HOCH2O<=>CH2O+OH                                 2.06E+21   -2.3    25730.0
    Reverse Arrhenius coefficients:                 4.50E+15   -1.1       0.0
45. HOCH2O<=>HOCHO+H                                 1.00E+14    0.0    14900.0
    Reverse Arrhenius coefficients:                 1.12E+15   -0.3    11500.0
46. HOCHO<=>CO+H2O                                   2.45E+12    0.0    60470.0
    Reverse Arrhenius coefficients:                 2.26E+03    2.1    52890.0
```

```
47. HOCHO<=>CO2+H2                                  2.95E+09    0.0    48520.0
    Reverse Arrhenius coefficients:                6.77E+05    1.0    51470.0
48. HOCHO<=>HCO+OH                                  3.47E+22   -1.5   110700.0
    Reverse Arrhenius coefficients:                1.00E+14    0.0        0.0
49. HOCHO+OH<=>H2O+CO2+H                            2.62E+06    2.1      916.0
    Warning...all REV parameters are zero... 0.0000e+000 0.000 0.000E+00
             this reaction will be treated as irreversible
50. HOCHO+OH<=>H2O+CO+OH                            1.85E+07    1.5     -962.0
    Warning...all REV parameters are zero... 0.0000e+000 0.000 0.000E+00
             this reaction will be treated as irreversible
51. HOCHO+H=>H2+CO2+H                               4.24E+06    2.1     4868.0
52. HOCHO+H<=>H2+CO+OH                              6.03E+13   -0.3     2988.0
    Warning...all REV parameters are zero... 0.0000e+000 0.000 0.000E+00
             this reaction will be treated as irreversible
53. HOCHO+CH3<=>CH4+CO+OH                           3.90E-07    5.8     2200.0
    Warning...all REV parameters are zero... 0.0000e+000 0.000 0.000E+00
             this reaction will be treated as irreversible
54. HOCHO+HO2=>H2O2+CO+OH                           1.00E+12    0.0    11920.0
55. HOCHO+O=>CO+OH+OH                               1.77E+18   -1.9     2975.0
56. CH3O(+M)<=>CH2O+H(+M)                           6.80E+13    0.0    26170.0
    Low pressure limit:  0.18670E+26 -0.30000E+01  0.24307E+05
    TROE centering:      0.90000E+00  0.25000E+04  0.13000E+04  0.10000+100
    H2              Enhanced by    2.000E+00
    H2O             Enhanced by    6.000E+00
    CO              Enhanced by    1.500E+00
    CO2             Enhanced by    2.000E+00
    CH4             Enhanced by    2.000E+00
    C2H6            Enhanced by    3.000E+00
57. CH3O+O2<=>CH2O+HO2                              4.38E-19    9.5    -5501.0
    Reverse Arrhenius coefficients:                1.42E-20    9.8    21080.0
58. CH2O+CH3O<=>CH3OH+HCO                           6.62E+11    0.0     2294.0
    Reverse Arrhenius coefficients:                8.39E+10    0.1    17710.0
59. CH4+CH3O<=>CH3+CH3OH                            6.12E+02    2.9     8248.0
    Reverse Arrhenius coefficients:                1.44E+01    3.1     6935.0
60. CH3O+CH3<=>CH2O+CH4                             1.20E+13    0.0        0.0
    Reverse Arrhenius coefficients:                6.75E+13    0.2    82810.0
61. CH3O+H<=>CH2O+H2                                2.00E+13    0.0        0.0
    Reverse Arrhenius coefficients:                1.23E+11    0.7    81270.0
62. CH3O+HO2<=>CH2O+H2O2                            3.01E+11    0.0        0.0
    Reverse Arrhenius coefficients:                1.07E+12    0.0    65270.0
63. CH2O+H(+M)<=>CH2OH(+M)                          5.40E+11    0.5     3600.0
    Low pressure limit:  0.12700E+33 -0.48200E+01  0.65300E+04
    TROE centering:      0.71870E+00  0.10300E+03  0.12910E+04  0.41600E+04
    H2              Enhanced by    2.000E+00
    H2O             Enhanced by    6.000E+00
    CO              Enhanced by    1.500E+00
    CO2             Enhanced by    2.000E+00
    CH4             Enhanced by    2.000E+00
    C2H6            Enhanced by    3.000E+00
64. CH2OH+O2<=>CH2O+HO2                             1.51E+15   -1.0        0.0
    Reverse Arrhenius coefficients:                1.98E+14   -0.6    20060.0
    Declared duplicate reaction...
65. CH2OH+O2<=>CH2O+HO2                             2.41E+14    0.0     5017.0
    Reverse Arrhenius coefficients:                3.15E+13    0.4    25080.0
    Declared duplicate reaction...
66. CH2OH+H<=>CH2O+H2                               6.00E+12    0.0        0.0
    Reverse Arrhenius coefficients:                1.50E+11    0.8    74750.0
67. CH2OH+HO2<=>CH2O+H2O2                           1.20E+13    0.0        0.0
    Reverse Arrhenius coefficients:                1.73E+14    0.1    58750.0
68. CH2OH+HCO<=>CH2O+CH2O                           1.80E+14    0.0        0.0
    Reverse Arrhenius coefficients:                7.60E+14    0.5    59560.0
69. CH2OH+CH3O<=>CH2O+CH3OH                         2.40E+13    0.0        0.0
    Reverse Arrhenius coefficients:                1.28E+13    0.6    74980.0
70. CH2OH+CH2O<=>CH3OH+HCO                          1.88E+04    2.7     4208.0
    Reverse Arrhenius coefficients:                9.63E+03    2.9    13110.0
71. OH+CH2OH<=>H2O+CH2O                             2.40E+13    0.0        0.0
    Reverse Arrhenius coefficients:                6.35E+12    0.7    89640.0
72. O+CH2OH<=>OH+CH2O                               4.20E+13    0.0        0.0
    Reverse Arrhenius coefficients:                5.44E+11    0.7    73340.0
73. CH2O+CH3OH<=>CH2OH+CH2OH                        6.50E+12    0.7    68460.0
    Reverse Arrhenius coefficients:                3.00E+12    0.0        0.0
74. CH2OH+HO2<=>HOCH2O+OH                           1.00E+13    0.0        0.0
    Reverse Arrhenius coefficients:                8.17E+13    0.0    33470.0
75. CH3OH(+M)<=>CH3+OH(+M)                          1.90E+16    0.0    91730.0
    Low pressure limit:  0.29500E+45 -0.73500E+01  0.95460E+05
    TROE centering:      0.41400E+00  0.27900E+03  0.54590E+04  0.10000E+11
76. CH3OH(+M)<=>CH2OH+H(+M)                         2.69E+16   -0.1    98940.0
    Low pressure limit:  0.23400E+41 -0.63300E+01  0.10310E+06
    TROE centering:      0.77300E+00  0.69300E+03  0.53330E+04  0.10000E+11
77. CH3OH+H<=>CH3O+H2                               3.60E+12    0.0     6095.0
    Reverse Arrhenius coefficients:                1.68E+11    0.2     5868.0
78. CH3OH+H<=>CH2OH+H2                              1.20E+06    2.4     2583.0
    Reverse Arrhenius coefficients:                1.39E+04    2.5     8871.0
79. CH3OH+O<=>CH2OH+OH                              3.88E+05    2.5     3080.0
    Reverse Arrhenius coefficients:                2.32E+03    2.6     7956.0
80. CH3OH+OH<=>CH3O+H2O                             5.13E+05    2.1     2450.0
    Reverse Arrhenius coefficients:                2.53E+05    2.2    17120.0
81. CH3OH+OH<=>CH2OH+H2O                            1.44E+06    2.0     -839.0
    Reverse Arrhenius coefficients:                1.76E+05    2.0    20340.0
82. CH3OH+O2<=>CH2OH+HO2                            2.05E+13    0.0    44900.0
    Reverse Arrhenius coefficients:                1.24E+12   -0.2    -3501.0
83. CH3OH+HO2<=>CH2OH+H2O2                          1.08E+04    2.5    10530.0
    Reverse Arrhenius coefficients:                7.20E+04    2.0      819.0
84. CH3OH+CH3<=>CH2OH+CH4                           3.19E+01    3.2     7172.0
    Reverse Arrhenius coefficients:                3.35E+02    2.8    15000.0
```

```
 85. CH3O+CH3OH<=>CH2OH+CH3OH                       3.00E+11    0.0     4074.0
     Reverse Arrhenius coefficients:               7.42E+10   -0.1    10590.0
 86. CH3OH+CH2O<=>CH3O+CH3O                        7.98E+12    0.5    81490.0
     Reverse Arrhenius coefficients:               6.03E+13    0.0        0.0
 87. CH3+H(+M)<=>CH4(+M)                           1.27E+16   -0.6      383.0
     Low pressure limit:  0.24770E+34 -0.47600E+01  0.24440E+04
     TROE centering:      0.78300E+00  0.74000E+02  0.29400E+04  0.69600E+04
     H2              Enhanced by    2.000E+00
     H2O             Enhanced by    6.000E+00
     CO              Enhanced by    1.500E+00
     CO2             Enhanced by    2.000E+00
     CH4             Enhanced by    2.000E+00
     C2H6            Enhanced by    3.000E+00
 88. CH4+H<=>CH3+H2                                6.14E+05    2.5     9587.0
     Reverse Arrhenius coefficients:               6.73E+02    2.9     8047.0
 89. CH4+OH<=>CH3+H2O                              5.83E+04    2.6     2190.0
     Reverse Arrhenius coefficients:               6.78E+02    2.9    15540.0
 90. CH4+O<=>CH3+OH                                1.02E+09    1.5     8600.0
     Reverse Arrhenius coefficients:               5.80E+05    1.9     5648.0
 91. CH4+HO2<=>CH3+H2O2                            1.13E+01    3.7    21010.0
     Reverse Arrhenius coefficients:               7.17E+00    3.5     3468.0
 92. CH4+CH2<=>CH3+CH3                             2.46E+06    2.0     8270.0
     Reverse Arrhenius coefficients:               1.74E+06    1.9    12980.0
 93. CH3+OH<=>CH2O+H2                              8.00E+09    0.5    -1755.0
     Reverse Arrhenius coefficients:               1.07E+12    0.3    68210.0
 94. CH3+OH<=>CH2(S)+H2O                           4.51E+17   -1.3     1417.0
     Reverse Arrhenius coefficients:               1.65E+16   -0.9     1039.0
 95. CH3+OH<=>CH3O+H                               6.94E+07    1.3    11200.0
     Reverse Arrhenius coefficients:               1.50E+12    0.5     -110.0
 96. CH3+OH<=>CH2OH+H                              3.09E+07    1.6     4506.0
     Reverse Arrhenius coefficients:               1.65E+11    0.7     -284.0
 97. CH3+OH<=>CH2+H2O                              5.60E+07    1.6     5420.0
     Reverse Arrhenius coefficients:               9.22E+05    2.1    14060.0
 98. CH3+HO2<=>CH3O+OH                             1.00E+12    0.3     -687.5
     Reverse Arrhenius coefficients:               6.19E+12    0.1    24550.0
 99. CH3+HO2<=>CH4+O2                              1.16E+05    2.2    -3022.0
     Reverse Arrhenius coefficients:               2.02E+07    2.1    53210.0
100. CH3+O<=>CH2O+H                                5.54E+13    0.1     -136.0
     Reverse Arrhenius coefficients:               3.83E+15   -0.1    68410.0
101. CH3+O2<=>CH3O+O                               7.55E+12    0.0    28320.0
     Reverse Arrhenius coefficients:               4.72E+14   -0.5      288.0
102. CH3+O2<=>CH2O+OH                              2.64E+00    3.3     8105.0
     Reverse Arrhenius coefficients:               5.28E-01    3.5    59920.0
103. CH3+O2(+M)<=>CH3O2(+M)                        7.81E+09    0.9        0.0
     Low pressure limit:  0.68500E+25 -0.30000E+01  0.00000E+00
     TROE centering:      0.60000E+00  0.10000E+04  0.70000E+02  0.17000E+04
104. CH3O2+CH2O<=>CH3O2H+HCO                       1.99E+12    0.0    11660.0
     Reverse Arrhenius coefficients:               1.32E+14   -0.9     9259.0
105. CH4+CH3O2<=>CH3+CH3O2H                        1.81E+11    0.0    18480.0
     Reverse Arrhenius coefficients:               2.23E+12   -0.7     -655.0
106. CH3OH+CH3O2<=>CH2OH+CH3O2H                    1.81E+12    0.0    13710.0
     Reverse Arrhenius coefficients:               2.35E+14   -1.0     2404.0
107. CH3O2+CH3<=>CH3O+CH3O                         5.08E+12    0.0    -1411.0
     Reverse Arrhenius coefficients:               1.97E+12    0.2    28070.0
108. CH3O2+HO2<=>CH3O2H+O2                         2.47E+11    0.0    -1570.0
     Reverse Arrhenius coefficients:               5.30E+14   -0.8    35520.0
109. CH3O2+CH3O2<=>CH2O+CH3OH+O2                   3.11E+14   -1.6    -1051.0
     Warning...all REV parameters are zero... 0.0000e+000 0.000 0.000E+00
               this reaction will be treated as irreversible
110. CH3O2+CH3O2<=>O2+CH3O+CH3O                    1.40E+16   -1.6     1860.0
     Warning...all REV parameters are zero... 0.0000e+000 0.000 0.000E+00
               this reaction will be treated as irreversible
111. CH3O2+H<=>CH3O+OH                             9.60E+13    0.0        0.0
     Reverse Arrhenius coefficients:               1.72E+09    1.0    40780.0
112. CH3O2+O<=>CH3O+O2                             3.60E+13    0.0        0.0
     Reverse Arrhenius coefficients:               2.23E+11    0.6    57520.0
113. CH3O2+OH<=>CH3OH+O2                           6.00E+13    0.0        0.0
     Reverse Arrhenius coefficients:               1.54E+13    0.4    59160.0
114. CH3O2H<=>CH3O+OH                              6.31E+14    0.0    42300.0
     Reverse Arrhenius coefficients:               2.51E+06    1.9    -2875.0
115. CH2(S)+M<=>CH2+M                              1.00E+13    0.0        0.0
     Reverse Arrhenius coefficients:               4.49E+12    0.0     9020.0
116. CH2(S)+CH4<=>CH3+CH3                          1.60E+13    0.0     -570.0
     Reverse Arrhenius coefficients:               5.07E+12   -0.1    13160.0
117. CH2(S)+O2<=>CO+OH+H                           7.00E+13    0.0        0.0
     Warning...all REV parameters are zero... 0.0000e+000 0.000 0.000E+00
               this reaction will be treated as irreversible
118. CH2(S)+H2<=>CH3+H                             7.00E+13    0.0        0.0
     Reverse Arrhenius coefficients:               2.02E+16   -0.6    15270.0
119. CH2(S)+H<=>CH2+H                              3.00E+13    0.0        0.0
     Reverse Arrhenius coefficients:               1.35E+13    0.0     9020.0
120. CH2(S)+H<=>CH+H2                              3.00E+13    0.0        0.0
     Reverse Arrhenius coefficients:               6.95E+13   -0.3    12480.0
121. CH2(S)+O<=>CO+H+H                             3.00E+13    0.0        0.0
     Warning...all REV parameters are zero... 0.0000e+000 0.000 0.000E+00
               this reaction will be treated as irreversible
122. CH2(S)+OH<=>CH2O+H                            3.00E+13    0.0        0.0
     Reverse Arrhenius coefficients:               1.15E+18   -0.8    85230.0
123. CH2(S)+CO2<=>CH2O+CO                          3.00E+12    0.0        0.0
     Reverse Arrhenius coefficients:               4.37E+10    0.4    59810.0
124. CH2+H(+M)<=>CH3(+M)                           2.50E+16   -0.8        0.0
     Low pressure limit:  0.32000E+28 -0.31400E+01  0.12300E+04
     TROE centering:      0.68000E+00  0.78000E+02  0.19950E+04  0.55900E+04
     H2              Enhanced by    2.000E+00
     H2O             Enhanced by    6.000E+00
```

```
     CO              Enhanced by    1.500E+00
     CO2             Enhanced by    2.000E+00
     CH4             Enhanced by    2.000E+00
     C2H6            Enhanced by    3.000E+00
125. CH2+O2<=>CH2O+O                                2.40E+12    0.0     1500.0
     Reverse Arrhenius coefficients:               5.96E+14   -0.4    60980.0
126. CH2+O2<=>CO2+H+H                               5.80E+12    0.0     1500.0
     Warning...all REV parameters are zero... 0.0000e+000 0.000 0.000E+00
              this reaction will be treated as irreversible
127. CH2+O2<=>CO+OH+H                               5.00E+12    0.0     1500.0
     Warning...all REV parameters are zero... 0.0000e+000 0.000 0.000E+00
              this reaction will be treated as irreversible
128. CH2+O<=>CO+H+H                                 5.00E+13    0.0        0.0
     Warning...all REV parameters are zero... 0.0000e+000 0.000 0.000E+00
              this reaction will be treated as irreversible
129. CH2+H<=>CH+H2                                  1.00E+18   -1.6        0.0
     Reverse Arrhenius coefficients:               5.16E+18   -1.8     3460.0
     Declared duplicate reaction...
130. CH2+OH<=>CH+H2O                                1.13E+07    2.0     3000.0
     Reverse Arrhenius coefficients:               6.18E+08    1.7    21350.0
131. CH+O2<=>HCO+O                                  3.30E+13    0.0        0.0
     Reverse Arrhenius coefficients:               9.37E+12    0.2    71210.0
132. CH+O<=>CO+H                                    5.70E+13    0.0        0.0
     Reverse Arrhenius coefficients:               2.77E+15    0.0   176000.0
133. CH+OH<=>HCO+H                                  3.00E+13    0.0        0.0
     Reverse Arrhenius coefficients:               5.07E+14    0.0    88110.0
134. CH2+H<=>CH+H2                                  2.70E+11    0.7    25700.0
     Reverse Arrhenius coefficients:               1.90E+11    0.7    28730.0
     Declared duplicate reaction...
135. CH+H2O<=>H+CH2O                                1.71E+13    0.0     -755.0
     Reverse Arrhenius coefficients:               8.37E+14    0.0    57520.0
136. CH+CO2<=>HCO+CO                                1.70E+12    0.0      685.0
     Reverse Arrhenius coefficients:               2.56E+11    0.0    66460.0
137. CH3+CH3(+M)<=>C2H6(+M)                         9.21E+16   -1.2      635.8
     Low pressure limit:  0.11350E+37 -0.52460E+01  0.17050E+04
     TROE centering:      0.40500E+00  0.11200E+04  0.69600E+02  0.10000E+11
     H2              Enhanced by    2.000E+00
     H2O             Enhanced by    6.000E+00
     CO              Enhanced by    1.500E+00
     CO2             Enhanced by    2.000E+00
     CH4             Enhanced by    2.000E+00
     C2H6            Enhanced by    3.000E+00
138. C2H5+H(+M)<=>C2H6(+M)                          5.21E+17   -1.0     1580.0
     Low pressure limit:  0.19900E+42 -0.70800E+01  0.66850E+04
     TROE centering:      0.84200E+00  0.12500E+03  0.22190E+04  0.68820E+04
     H2              Enhanced by    2.000E+00
     H2O             Enhanced by    6.000E+00
     CO              Enhanced by    1.500E+00
     CO2             Enhanced by    2.000E+00
     CH4             Enhanced by    2.000E+00
     C2H6            Enhanced by    3.000E+00
139. C2H6+H<=>C2H5+H2                               1.15E+08    1.9     7530.0
     Reverse Arrhenius coefficients:               1.06E+04    2.6     9760.0
140. C2H6+O<=>C2H5+OH                               3.55E+06    2.4     5830.0
     Reverse Arrhenius coefficients:               1.70E+02    3.1     6648.0
141. C2H6+OH<=>C2H5+H2O                             1.48E+07    1.9      950.0
     Reverse Arrhenius coefficients:               1.45E+04    2.5    18070.0
142. C2H6+O2<=>C2H5+HO2                             6.03E+13    0.0    51870.0
     Reverse Arrhenius coefficients:               2.92E+10    0.3     -593.0
143. C2H6+CH3<=>C2H5+CH4                            1.51E-07    6.0     6047.0
     Reverse Arrhenius coefficients:               1.27E-08    6.2     9817.0
144. C2H6+HO2<=>C2H5+H2O2                           3.46E+01    3.6    16920.0
     Reverse Arrhenius coefficients:               1.85E+00    3.6     3151.0
145. C2H6+CH3O2<=>C2H5+CH3O2H                       1.94E+01    3.6    17100.0
     Reverse Arrhenius coefficients:               2.02E+01    3.2     1734.0
146. C2H6+CH3O<=>C2H5+CH3OH                         2.41E+11    0.0     7090.0
     Reverse Arrhenius coefficients:               4.78E+08    0.5     9547.0
147. C2H6+CH<=>C2H5+CH2                             1.10E+14    0.0     -260.0
     Reverse Arrhenius coefficients:               1.97E+09    0.9    -1490.0
148. CH2(S)+C2H6<=>CH3+C2H5                         1.20E+14    0.0        0.0
     Reverse Arrhenius coefficients:               3.20E+12    0.1    17500.0
149. C2H4+H(+M)<=>C2H5(+M)                          1.08E+12    0.5     1822.0
     Low pressure limit:  0.12000E+43 -0.76200E+01  0.69700E+04
     TROE centering:      0.97500E+00  0.21000E+03  0.98400E+03  0.43740E+04
     H2              Enhanced by    2.000E+00
     H2O             Enhanced by    6.000E+00
     CO              Enhanced by    1.500E+00
     CO2             Enhanced by    2.000E+00
     CH4             Enhanced by    2.000E+00
     C2H6            Enhanced by    3.000E+00
150. H2+CH3O2<=>H+CH3O2H                            1.50E+14    0.0    26030.0
     Reverse Arrhenius coefficients:               1.69E+18   -1.1     8434.0
151. C2H5+C2H3<=>C2H4+C2H4                          6.86E+11    0.1    -4300.0
     Reverse Arrhenius coefficients:               4.82E+14    0.0    71530.0
152. CH3+C2H5<=>CH4+C2H4                            1.18E+04    2.5    -2921.0
     Reverse Arrhenius coefficients:               2.39E+06    2.4    66690.0
153. C2H5+H<=>CH3+CH3                               9.69E+13    0.0      220.0
     Reverse Arrhenius coefficients:               2.03E+09    1.0    10510.0
154. C2H5+H<=>C2H4+H2                               2.00E+12    0.0        0.0
     Reverse Arrhenius coefficients:               4.44E+11    0.4    68070.0
155. C2H5+O<=>CH3CHO+H                              1.10E+14    0.0        0.0
     Reverse Arrhenius coefficients:               1.03E+17   -0.5    77420.0
156. C2H5+HO2<=>C2H5O+OH                            1.10E+13    0.0        0.0
     Reverse Arrhenius coefficients:               9.68E+15   -0.7    27650.0
157. CH3O2+C2H5<=>CH3O+C2H5O                        8.00E+12    0.0    -1000.0
```

```
     Reverse Arrhenius coefficients:              4.40E+14   -0.4    30890.0
158. C2H5O+O2<=>CH3CHO+HO2                         4.28E+10    0.0     1097.0
     Reverse Arrhenius coefficients:              1.32E+08    0.6    34130.0
159. C2H5O<=>CH3+CH2O                             1.32E+20   -2.0    20750.0
     Reverse Arrhenius coefficients:              3.00E+11    0.0     6336.0
160. C2H5O<=>CH3CHO+H                             5.43E+15   -0.7    22230.0
     Reverse Arrhenius coefficients:              8.00E+12    0.0     6400.0
161. C2H5O2<=>C2H5+O2                             1.31E+62  -14.8    49180.0
     Reverse Arrhenius coefficients:              2.88E+56  -13.8    14620.0
162. C2H5+O2<=>C2H4+HO2                           7.56E+14   -1.0     4749.0
     Reverse Arrhenius coefficients:              8.80E+14   -1.0    18130.0
     Declared duplicate reaction...
163. C2H5+O2<=>C2H4+HO2                           4.00E-01    3.9    13620.0
     Reverse Arrhenius coefficients:              4.66E-01    3.9    27000.0
     Declared duplicate reaction...
164. C2H5+O2<=>CH3CHO+OH                          8.26E+02    2.4     5285.0
     Reverse Arrhenius coefficients:              2.25E+03    2.3    65970.0
165. C2H5O2<=>CH3CHO+OH                           2.52E+41  -10.2    43710.0
     Reverse Arrhenius coefficients:              1.50E+36   -9.3    69840.0
166. C2H5O2<=>C2H4+HO2                            1.82E+38   -8.4    37890.0
     Reverse Arrhenius coefficients:              4.63E+32   -7.4    16700.0
167. C2H3O1-2<=>CH3CO                             8.50E+14    0.0    14000.0
     Reverse Arrhenius coefficients:              1.00E+14    0.0    48710.0
168. C2H3O1-2<=>CH2CHO                            1.00E+14    0.0    14000.0
     Reverse Arrhenius coefficients:              1.24E+15   -0.4    44010.0
169. CH3CHO<=>CH3+HCO                             7.69E+20   -1.3    86950.0
     Reverse Arrhenius coefficients:              1.75E+13    0.0        0.0
170. CH3CHO+H<=>CH3CO+H2                          2.37E+13    0.0     3642.0
     Reverse Arrhenius coefficients:              1.64E+10    0.6    17600.0
171. CH3CHO+O<=>CH3CO+OH                          5.94E+12    0.0     1868.0
     Reverse Arrhenius coefficients:              2.13E+09    0.6    14410.0
172. CH3CHO+OH<=>CH3CO+H2O                        3.37E+12    0.0     -619.0
     Reverse Arrhenius coefficients:              2.47E+10    0.5    28230.0
173. CH3CHO+O2<=>CH3CO+HO2                        3.01E+13    0.0    39150.0
     Reverse Arrhenius coefficients:              1.09E+11    0.3    -1588.0
174. CH3CHO+CH3<=>CH3CO+CH4                       7.08E-04    4.6     1966.0
     Reverse Arrhenius coefficients:              4.47E-04    4.8    17460.0
175. CH3CHO+HO2<=>CH3CO+H2O2                      3.01E+12    0.0    11920.0
     Reverse Arrhenius coefficients:              1.20E+12   -0.1     9877.0
176. CH3O2+CH3CHO<=>CH3O2H+CH3CO                  3.01E+12    0.0    11920.0
     Reverse Arrhenius coefficients:              2.34E+13   -0.5     8282.0
177. CH3CHO+OH<=>CH3+HOCHO                        3.00E+15   -1.1        0.0
     Reverse Arrhenius coefficients:              2.37E+16   -1.3    23750.0
178. CH3CHO+OH<=>CH2CHO+H2O                       1.72E+05    2.4      815.0
     Reverse Arrhenius coefficients:              1.33E+05    2.5    24950.0
179. CH3CO(+M)<=>CH3+CO(+M)                       3.00E+12    0.0    16720.0
     Low pressure limit:  0.12000E+16  0.00000E+00  0.12518E+05
180. CH3CO+H<=>CH2CO+H2                           2.00E+13    0.0        0.0
     Reverse Arrhenius coefficients:              1.04E+13    0.2    60560.0
181. CH3CO+O<=>CH2CO+OH                           2.00E+13    0.0        0.0
     Reverse Arrhenius coefficients:              5.38E+12    0.2    59140.0
182. CH3CO+CH3<=>CH2CO+CH4                        5.00E+13    0.0        0.0
     Reverse Arrhenius coefficients:              2.36E+16   -0.2    62100.0
183. CH2CHO<=>CH2CO+H                             4.07E+15   -0.3    50600.0
     Reverse Arrhenius coefficients:              5.00E+13    0.0    12300.0
184. CH2CHO+O2<=>CH2O+CO+OH                       8.95E+13   -0.6    10120.0
     Warning...all REV parameters are zero... 0.0000e+000 0.000 0.000E+00
              this reaction will be treated as irreversible
185. CH2+CO(+M)<=>CH2CO(+M)                       8.10E+11    0.0        0.0
     Low pressure limit:  0.26900E+34 -0.51100E+01  0.70950E+04
     TROE centering:      0.59070E+00  0.27500E+03  0.12260E+04  0.51850E+04
     H2              Enhanced by    2.000E+00
     H2O             Enhanced by    6.000E+00
     CO              Enhanced by    1.500E+00
     CO2             Enhanced by    2.000E+00
     CH4             Enhanced by    2.000E+00
     C2H6            Enhanced by    3.000E+00
186. CH2CO+H<=>CH3+CO                             1.10E+13    0.0     3400.0
     Reverse Arrhenius coefficients:              2.40E+12    0.0    40200.0
187. CH2CO+H<=>HCCO+H2                            2.00E+14    0.0     8000.0
     Reverse Arrhenius coefficients:              1.43E+11    0.5     4520.0
188. CH2CO+O<=>CH2+CO2                            1.75E+12    0.0     1350.0
     Reverse Arrhenius coefficients:              2.85E+09    0.8    49440.0
189. CH2CO+O<=>HCCO+OH                            1.00E+13    0.0     8000.0
     Reverse Arrhenius coefficients:              3.72E+09    0.5     3108.0
190. CH2CO+OH<=>HCCO+H2O                          1.00E+13    0.0     2000.0
     Reverse Arrhenius coefficients:              7.60E+10    0.4    13410.0
191. CH2CO+OH<=>CH2OH+CO                          2.00E+12    0.0    -1010.0
     Reverse Arrhenius coefficients:              8.17E+09    0.5    24530.0
192. CH2(S)+CH2CO<=>C2H4+CO                       1.60E+14    0.0        0.0
     Reverse Arrhenius coefficients:              3.75E+14    0.2   103400.0
193. HCCO+OH<=>H2+CO+CO                           1.00E+14    0.0        0.0
     Warning...all REV parameters are zero... 0.0000e+000 0.000 0.000E+00
              this reaction will be treated as irreversible
194. H+HCCO<=>CH2(S)+CO                           1.10E+13    0.0        0.0
     Reverse Arrhenius coefficients:              4.06E+07    1.6    18540.0
195. HCCO+O<=>H+CO+CO                             8.00E+13    0.0        0.0
     Warning...all REV parameters are zero... 0.0000e+000 0.000 0.000E+00
              this reaction will be treated as irreversible
196. HCCO+O2<=>OH+CO+CO                           4.20E+10    0.0      850.0
     Warning...all REV parameters are zero... 0.0000e+000 0.000 0.000E+00
              this reaction will be treated as irreversible
197. HCCO+M<=>CH+CO+M                             6.50E+15    0.0    58820.0
     Reverse Arrhenius coefficients:              7.60E+22   -1.9        0.0
198. CH+CH2O<=>H+CH2CO                            9.46E+13    0.0     -515.0
```

```
     Reverse Arrhenius coefficients:              1.62E+15    0.0    69060.0
199. CH+HCCO<=>CO+C2H2                             5.00E+13    0.0        0.0
     Reverse Arrhenius coefficients:              1.72E+17    0.0   164600.0
200. C2H3+H(+M)<=>C2H4(+M)                         1.36E+14    0.2      660.0
     Low pressure limit:  0.14000E+31 -0.38600E+01  0.33200E+04
     TROE centering:      0.78200E+00  0.20750E+03  0.26630E+04  0.60950E+04
     H2              Enhanced by    2.000E+00
     H2O             Enhanced by    6.000E+00
     CO              Enhanced by    1.500E+00
     CO2             Enhanced by    2.000E+00
     CH4             Enhanced by    2.000E+00
     C2H6            Enhanced by    3.000E+00
201. C2H4(+M)<=>C2H2+H2(+M)                        8.00E+12    0.4    88770.0
     Low pressure limit:  0.15800E+52 -0.93000E+01  0.97800E+05
     TROE centering:      0.73500E+00  0.18000E+03  0.10350E+04  0.54170E+04
     H2              Enhanced by    2.000E+00
     H2O             Enhanced by    6.000E+00
     CO              Enhanced by    1.500E+00
     CO2             Enhanced by    2.000E+00
     CH4             Enhanced by    2.000E+00
     C2H6            Enhanced by    3.000E+00
202. C2H4+H<=>C2H3+H2                              5.07E+07    1.9    12950.0
     Reverse Arrhenius coefficients:              1.60E+04    2.4     5190.0
203. C2H4+O<=>CH3+HCO                              8.56E+06    1.9      183.0
     Reverse Arrhenius coefficients:              3.30E+02    2.6    26140.0
204. C2H4+O<=>CH2CHO+H                             4.99E+06    1.9      183.0
     Reverse Arrhenius coefficients:              1.54E+09    1.2    18780.0
205. C2H4+OH<=>C2H3+H2O                            1.80E+06    2.0     2500.0
     Reverse Arrhenius coefficients:              6.03E+03    2.4     9632.0
206. C2H4+CH3<=>C2H3+CH4                           6.62E+00    3.7     9500.0
     Reverse Arrhenius coefficients:              1.91E+00    3.8     3280.0
207. C2H4+O2<=>C2H3+HO2                            4.00E+13    0.0    58200.0
     Reverse Arrhenius coefficients:              2.00E+10    0.2    -4249.0
208. C2H4+CH3O<=>C2H3+CH3OH                        1.20E+11    0.0     6750.0
209. C2H4+CH3O2<=>C2H3+CH3O2H                      8.59E+00    3.8    27132.0
210. CH+CH4<=>C2H4+H                               6.00E+13    0.0        0.0
     Reverse Arrhenius coefficients:              3.57E+14    0.0    55480.0
211. CH2(S)+CH3<=>C2H4+H                           2.00E+13    0.0        0.0
     Reverse Arrhenius coefficients:              6.13E+19   -1.2    73050.0
212. C2H2+H(+M)<=>C2H3(+M)                         5.60E+12    0.0     2400.0
     Low pressure limit:  0.38000E+41 -0.72700E+01  0.72200E+04
     TROE centering:      0.75100E+00  0.98500E+02  0.13020E+04  0.41670E+04
     H2              Enhanced by    2.000E+00
     H2O             Enhanced by    6.000E+00
     CO              Enhanced by    1.500E+00
     CO2             Enhanced by    2.000E+00
     CH4             Enhanced by    2.000E+00
     C2H6            Enhanced by    3.000E+00
213. C2H3+O2<=>C2H2+HO2                            2.12E-06    6.0     9484.0
     Reverse Arrhenius coefficients:              1.09E-05    5.9    24030.0
214. C2H3+O2<=>CH2O+HCO                            8.50E+28   -5.3     6500.0
     Reverse Arrhenius coefficients:              3.99E+27   -4.9    93450.0
215. C2H3+O2<=>CH2CHO+O                            5.50E+14   -0.6     5260.0
     Reverse Arrhenius coefficients:              3.00E+18   -1.4    16300.0
216. CH3+C2H3<=>CH4+C2H2                           3.92E+11    0.0        0.0
     Reverse Arrhenius coefficients:              3.50E+14   -0.2    70780.0
217. C2H3+H<=>C2H2+H2                              9.64E+13    0.0        0.0
     Reverse Arrhenius coefficients:              9.43E+13    0.3    69240.0
218. C2H3+OH<=>C2H2+H2O                            5.00E+12    0.0        0.0
     Reverse Arrhenius coefficients:              5.18E+13    0.1    84130.0
219. C2H+H(+M)<=>C2H2(+M)                          1.00E+17    0.0        0.0
     Low pressure limit:  0.37500E+34 -0.48000E+01  0.19000E+04
     TROE centering:      0.64600E+00  0.13200E+03  0.13150E+04  0.55660E+04
     H2              Enhanced by    2.000E+00
     H2O             Enhanced by    6.000E+00
     CO              Enhanced by    1.500E+00
     CO2             Enhanced by    2.000E+00
     CH4             Enhanced by    2.000E+00
     C2H6            Enhanced by    3.000E+00
220. C2H2+O2<=>HCCO+OH                             2.00E+08    1.5    30100.0
     Reverse Arrhenius coefficients:              2.04E+06    1.5    32270.0
221. O+C2H2<=>C2H+OH                               4.60E+19   -1.4    28950.0
     Reverse Arrhenius coefficients:              9.00E+13    0.0        0.0
222. C2H2+O<=>CH2+CO                               6.94E+06    2.0     1900.0
     Reverse Arrhenius coefficients:              4.05E+01    3.2    48360.0
223. C2H2+O<=>HCCO+H                               1.35E+07    2.0     1900.0
     Reverse Arrhenius coefficients:              4.76E+07    1.6    20800.0
224. C2H2+OH<=>C2H+H2O                             3.37E+07    2.0    14000.0
     Reverse Arrhenius coefficients:              4.52E+04    2.7     -428.0
225. C2H2+OH<=>CH2CO+H                             3.24E+13    0.0    12000.0
     Reverse Arrhenius coefficients:              3.06E+17   -0.8    35790.0
226. C2H2+OH<=>CH3+CO                              4.83E-04    4.0    -2000.0
     Reverse Arrhenius coefficients:              3.49E-06    4.6    52120.0
227. CH3COCH2<=>CH2CO+CH3                          1.00E+14    0.0    31000.0
     Reverse Arrhenius coefficients:              1.00E+11    0.0     6000.0
228. CH3COCH2O2<=>CH3COCH2+O2                      2.02E+15   -1.0    24460.0
     Reverse Arrhenius coefficients:              1.20E+11    0.0    -1100.0
229. CH2O+CH3COCH2O2<=>HCO+CH3COCH2O2H             1.29E+11    0.0     9000.0
     Reverse Arrhenius coefficients:              2.51E+10    0.0    10100.0
230. HO2+CH3COCH2O2<=>CH3COCH2O2H+O2               1.00E+12    0.0        0.0
     Warning...all REV parameters are zero... 0.0000e+000 0.000 0.000E+00
              this reaction will be treated as irreversible
231. CH3COCH2O2H<=>CH3COCH2O+OH                    1.00E+16    0.0    43000.0
     Reverse Arrhenius coefficients:              1.00E+15   -0.8        0.0
232. CH3COCH2O<=>CH3CO+CH2O                        3.73E+20   -2.2    17260.0
```

```
     Reverse Arrhenius coefficients:              1.00E+11    0.0    11900.0
233. C2H3CHO<=>C2H3+HCO                            2.00E+24   -2.1   103400.0
     Reverse Arrhenius coefficients:              1.81E+13    0.0        0.0
234. C2H3CHO+H<=>C2H3CO+H2                         1.34E+13    0.0     3300.0
     Reverse Arrhenius coefficients:              3.31E+10    0.6    22680.0
235. C2H3CHO+O<=>C2H3CO+OH                         5.94E+12    0.0     1868.0
     Reverse Arrhenius coefficients:              7.62E+09    0.6    19840.0
236. C2H3CHO+OH<=>C2H3CO+H2O                       9.24E+06    1.5     -962.0
     Reverse Arrhenius coefficients:              2.42E+05    2.0    33310.0
237. C2H3CHO+O2<=>C2H3CO+HO2                       1.00E+13    0.0    40700.0
     Reverse Arrhenius coefficients:              1.30E+11    0.3     5391.0
238. C2H3CHO+HO2<=>C2H3CO+H2O2                     3.01E+12    0.0    11920.0
     Reverse Arrhenius coefficients:              4.30E+12   -0.1    15300.0
239. C2H3CHO+CH3<=>C2H3CO+CH4                      2.61E+06    1.8     5911.0
     Reverse Arrhenius coefficients:              5.88E+06    1.9    26830.0
240. C2H3CHO+C2H3<=>C2H3CO+C2H4                    1.74E+12    0.0     8440.0
     Reverse Arrhenius coefficients:              1.00E+13    0.0    28000.0
241. C2H3CHO+CH3O<=>C2H3CO+CH3OH                   1.00E+12    0.0     3300.0
     Reverse Arrhenius coefficients:              5.30E+10    0.4    22910.0
242. C2H3CHO+CH3O2<=>C2H3CO+CH3O2H                 3.01E+12    0.0    11920.0
     Reverse Arrhenius coefficients:              8.37E+13   -0.5    13710.0
243. C2H3CO<=>C2H3+CO                              1.37E+21   -2.2    39410.0
     Reverse Arrhenius coefficients:              1.51E+11    0.0     4810.0
244. C2H5CHO<=>C2H5+HCO                            1.50E+27   -3.2    87040.0
     Reverse Arrhenius coefficients:              1.81E+13    0.0        0.0
245. C3H8(+M)<=>CH3+C2H5(+M)                       1.29E+37   -5.8    97380.0
     Low pressure limit:  0.56400E+75 -0.15740E+02  0.98714E+05
     TROE centering:      0.31000E+00  0.50000E+02  0.30000E+04  0.90000E+04
     H2              Enhanced by    2.000E+00
     H2O             Enhanced by    6.000E+00
     CO              Enhanced by    1.500E+00
     CO2             Enhanced by    2.000E+00
     CH4             Enhanced by    2.000E+00
     C2H6            Enhanced by    3.000E+00
246. C3H8<=>NC3H7+H                                3.75E+17   -0.4   101200.0
     Reverse Arrhenius coefficients:              1.00E+14    0.0        0.0
247. C3H8<=>IC3H7+H                                2.38E+18   -0.7    98680.0
     Reverse Arrhenius coefficients:              1.00E+14    0.0        0.0
248. C3H8+O2<=>IC3H7+HO2                           2.00E+13    0.0    49640.0
     Reverse Arrhenius coefficients:              1.76E+09    0.6     -169.0
249. C3H8+O2<=>NC3H7+HO2                           6.00E+13    0.0    52290.0
     Reverse Arrhenius coefficients:              3.35E+10    0.3      -59.0
250. H+C3H8<=>H2+IC3H7                             1.17E+07    2.4     4471.0
     Reverse Arrhenius coefficients:              2.19E+01    3.3     9351.0
251. H+C3H8<=>H2+NC3H7                             1.33E+06    2.5     6756.0
     Reverse Arrhenius coefficients:              1.42E+02    3.2     9096.0
252. C3H8+O<=>IC3H7+OH                             5.49E+05    2.5     3140.0
     Reverse Arrhenius coefficients:              4.79E+00    3.4     6608.0
253. C3H8+O<=>NC3H7+OH                             3.71E+06    2.4     5505.0
     Reverse Arrhenius coefficients:              2.05E+02    3.0     6433.0
254. C3H8+OH<=>NC3H7+H2O                           1.05E+10    1.0     1586.0
     Reverse Arrhenius coefficients:              1.19E+07    1.5    18820.0
255. C3H8+OH<=>IC3H7+H2O                           4.67E+07    1.6      -35.0
     Reverse Arrhenius coefficients:              8.33E+03    2.5    19740.0
256. C3H8+HO2<=>IC3H7+H2O2                         5.88E+04    2.5    14860.0
     Reverse Arrhenius coefficients:              5.72E+02    2.8     3742.0
257. C3H8+HO2<=>NC3H7+H2O2                         8.10E+04    2.5    16690.0
     Reverse Arrhenius coefficients:              5.00E+03    2.4     3030.0
258. CH3+C3H8<=>CH4+IC3H7                          6.40E+04    2.2     7520.0
     Reverse Arrhenius coefficients:              9.82E+02    2.7    13940.0
259. CH3+C3H8<=>CH4+NC3H7                          9.04E-01    3.6     7154.0
     Reverse Arrhenius coefficients:              8.79E-02    3.8    11030.0
260. IC3H7+C3H8<=>NC3H7+C3H8                       3.00E+10    0.0    12900.0
     Reverse Arrhenius coefficients:              3.00E+10    0.0    12900.0
261. C2H3+C3H8<=>C2H4+IC3H7                        1.00E+11    0.0    10400.0
     Reverse Arrhenius coefficients:              1.31E+11    0.0    17800.0
262. C2H3+C3H8<=>C2H4+NC3H7                        1.00E+11    0.0    10400.0
     Reverse Arrhenius coefficients:              1.31E+11    0.0    17800.0
263. C2H5+C3H8<=>C2H6+IC3H7                        1.00E+11    0.0    10400.0
     Reverse Arrhenius coefficients:              3.63E+10    0.0     9934.0
264. C2H5+C3H8<=>C2H6+NC3H7                        1.00E+11    0.0    10400.0
     Reverse Arrhenius coefficients:              3.63E+10    0.0     9934.0
265. C3H8+C3H5-A<=>NC3H7+C3H6                      7.94E+11    0.0    20500.0
     Reverse Arrhenius coefficients:              5.37E+16   -1.3    13400.0
266. C3H8+C3H5-A<=>IC3H7+C3H6                      7.94E+11    0.0    16200.0
     Reverse Arrhenius coefficients:              5.37E+16   -1.3     9095.0
267. C3H8+CH3O<=>NC3H7+CH3OH                       3.00E+11    0.0     7000.0
     Reverse Arrhenius coefficients:              1.22E+10    0.0     9182.0
268. C3H8+CH3O<=>IC3H7+CH3OH                       3.00E+11    0.0     7000.0
     Reverse Arrhenius coefficients:              1.22E+10    0.0     9182.0
269. CH3O2+C3H8<=>CH3O2H+NC3H7                     8.10E+04    2.5    16690.0
     Reverse Arrhenius coefficients:              9.72E+04    2.0     1435.0
270. CH3O2+C3H8<=>CH3O2H+IC3H7                     5.88E+04    2.5    14860.0
     Reverse Arrhenius coefficients:              1.11E+04    2.3     2147.0
271. IC3H7<=>H+C3H6                                6.92E+13    0.0    37690.0
     Reverse Arrhenius coefficients:              2.64E+13    0.0     2160.0
272. IC3H7+H<=>C2H5+CH3                            2.00E+13    0.0        0.0
     Reverse Arrhenius coefficients:              4.34E+07    1.2     8620.0
273. IC3H7+O2<=>C3H6+HO2                           4.50E-19    0.0     5020.0
     Reverse Arrhenius coefficients:              2.00E-19    0.0    17500.0
274. IC3H7+OH<=>C3H6+H2O                           2.41E+13    0.0        0.0
     Reverse Arrhenius coefficients:              2.98E+12    0.6    83820.0
275. IC3H7+O<=>CH3CHO+CH3                          4.82E+13    0.0        0.0
     Reverse Arrhenius coefficients:              1.28E+11    0.8    86480.0
276. NC3H7<=>CH3+C2H4                              9.24E+10    0.9    30500.0
```

```
277. NC3H7<=>H+C3H6                                4.14E+12    0.2    35600.0
278. NC3H7+O2<=>C3H6+HO2                           3.00E-19    0.0     3000.0
     Reverse Arrhenius coefficients:              2.00E-19    0.0    17500.0
279. C3H6<=>C2H3+CH3                               2.73E+62  -13.3   123200.0
     Reverse Arrhenius coefficients:              6.82E+53  -11.8    20550.0
280. C3H6<=>C3H5-A+H                               2.01E+61  -13.3   118500.0
     Reverse Arrhenius coefficients:              2.04E+61  -13.5    30610.0
281. C3H6+O<=>C2H5+HCO                             1.58E+07    1.8    -1216.0
     Reverse Arrhenius coefficients:              9.19E+01    2.7    23110.0
282. C3H6+O<=>CH2CO+CH3+H                          2.50E+07    1.8       76.0
     Warning...all REV parameters are zero... 0.0000e+000 0.000 0.000E+00
               this reaction will be treated as irreversible
283. C3H6+O=>CH3CHCO+H+H                           2.50E+07    1.8       76.0
284. C3H6+O<=>C3H5-A+OH                            5.24E+11    0.7     5884.0
     Reverse Arrhenius coefficients:              1.10E+11    0.7    20150.0
285. C3H6+OH<=>C3H5-A+H2O                          3.12E+06    2.0     -298.0
     Reverse Arrhenius coefficients:              1.34E+07    1.9    30270.0
286. C3H6+HO2<=>C3H5-A+H2O2                        2.70E+04    2.5    12340.0
     Reverse Arrhenius coefficients:              6.34E+06    1.8    12010.0
287. C3H6+H<=>C3H5-A+H2                            1.73E+05    2.5     2492.0
     Reverse Arrhenius coefficients:              7.02E+04    2.5    18170.0
288. C3H6+H<=>C2H4+CH3                             2.30E+13    0.0     2547.0
     Reverse Arrhenius coefficients:              7.27E+07    1.3    11200.0
289. C3H6+O2<=>C3H5-A+HO2                          4.00E+12    0.0    39900.0
     Reverse Arrhenius coefficients:              8.51E+12   -0.3      887.0
290. C3H6+CH3<=>C3H5-A+CH4                         2.21E+00    3.5     5675.0
     Reverse Arrhenius coefficients:              8.18E+02    3.1    22890.0
291. C3H6+C2H5<=>C3H5-A+C2H6                       1.00E+11    0.0     9800.0
     Reverse Arrhenius coefficients:              5.37E+05    1.3    16440.0
292. C3H6+CH3O2<=>C3H5-A+CH3O2H                    3.24E+11    0.0    14900.0
     Reverse Arrhenius coefficients:              2.00E+10    0.0    15000.0
293. C3H5-A<=>C2H2+CH3                             2.40E+48   -9.9    82080.0
     Reverse Arrhenius coefficients:              2.61E+46   -9.8    36950.0
294. C3H5-A<=>C3H4-A+H                             4.19E+13    0.2    61930.0
     Reverse Arrhenius coefficients:              2.40E+11    0.7     3007.0
295. C3H5-A+HO2<=>C3H5O+OH                         7.00E+12    0.0    -1000.0
     Reverse Arrhenius coefficients:              1.60E+12    0.1    11660.0
296. C3H5-A+CH3O2<=>C3H5O+CH3O                     7.00E+12    0.0    -1000.0
     Reverse Arrhenius coefficients:              1.99E+15   -0.7    17020.0
297. C3H5-A+H<=>C3H4-A+H2                          1.23E+03    3.0     2582.0
     Reverse Arrhenius coefficients:              2.82E+00    3.8    47220.0
298. C3H5-A+CH3<=>C3H4-A+CH4                       1.00E+11    0.0        0.0
     Reverse Arrhenius coefficients:              4.92E+12    0.1    47780.0
299. C3H5-A+C2H5<=>C2H6+C3H4-A                     4.00E+11    0.0        0.0
     Reverse Arrhenius coefficients:              1.80E+12    0.1    40330.0
300. C3H5-A+C2H5<=>C2H4+C3H6                       4.00E+11    0.0        0.0
     Reverse Arrhenius coefficients:              6.94E+16   -1.3    52800.0
301. C3H5-A+C2H3<=>C2H4+C3H4-A                     1.00E+12    0.0        0.0
     Reverse Arrhenius coefficients:              1.62E+13    0.1    48190.0
302. C3H4-A+C3H6<=>C3H5-A+C3H5-A                   4.75E+08    0.7    28700.0
     Reverse Arrhenius coefficients:              8.43E+10    0.0     -262.0
303. C3H5-A+O2<=>C3H4-A+HO2                        2.18E+21   -2.9    30760.0
     Reverse Arrhenius coefficients:              2.61E+19   -2.4    20710.0
304. C3H5-A+O2<=>CH2CHO+CH2O                       7.14E+15   -1.2    21050.0
     Reverse Arrhenius coefficients:              4.94E+16   -1.4    88620.0
305. C3H5-A+O2<=>C2H3CHO+OH                        2.47E+13   -0.4    23020.0
     Reverse Arrhenius coefficients:              1.99E+13   -0.6    75140.0
306. C3H5-A+O2<=>C2H2+CH2O+OH                      9.72E+29   -5.7    21450.0
     Warning...all REV parameters are zero... 0.0000e+000 0.000 0.000E+00
               this reaction will be treated as irreversible
307. C3H4-A+M<=>C3H3+H+M                           1.14E+17    0.0    70000.0
     Reverse Arrhenius coefficients:              2.00E+17    0.0    -1000.0
308. C3H4-A<=>C3H4-P                               1.20E+15    0.0    92400.0
     Reverse Arrhenius coefficients:              3.22E+18   -1.0    96590.0
309. C3H4-A+O2<=>C3H3+HO2                          4.00E+13    0.0    39160.0
     Reverse Arrhenius coefficients:              3.17E+11   -0.1      311.0
310. C3H4-A+HO2<=>CH2CO+CH2+OH                     4.00E+12    0.0    19000.0
     Reverse Arrhenius coefficients:              1.00E+00    0.0        0.0
311. C3H4-A+OH<=>CH2CO+CH3                         3.12E+12    0.0     -397.0
     Reverse Arrhenius coefficients:              1.81E+17   -1.4    36070.0
312. C3H4-A+OH<=>C3H3+H2O                          1.00E+07    2.0     1000.0
     Reverse Arrhenius coefficients:              1.60E+05    2.2    31730.0
313. C3H4-A+O<=>C2H4+CO                            7.80E+12    0.0     1600.0
     Reverse Arrhenius coefficients:              3.27E+08    1.3   121900.0
314. C3H4-A+O<=>C2H2+CH2O                          3.00E-03    4.6    -4243.0
     Reverse Arrhenius coefficients:              2.32E+02    3.2    81190.0
315. C3H4-A+H<=>C3H3+H2                            2.00E+07    2.0     5000.0
     Reverse Arrhenius coefficients:              3.02E+04    2.3    20840.0
316. C3H4-A+CH3<=>C3H3+CH4                         3.67E-02    4.0     6830.0
     Reverse Arrhenius coefficients:              5.06E-02    3.8    24210.0
317. C3H4-A+C3H5-A<=>C3H3+C3H6                     2.00E+11    0.0     7700.0
     Reverse Arrhenius coefficients:              2.64E+19   -2.7    42140.0
318. C3H4-A+C2H<=>C3H3+C2H2                        1.00E+13    0.0        0.0
     Reverse Arrhenius coefficients:              1.42E+16   -1.4    53820.0
319. C3H4-P+M<=>C3H3+H+M                           1.14E+17    0.0    70000.0
     Reverse Arrhenius coefficients:              2.00E+17    0.0    -1000.0
320. C3H4-P<=>C2H+CH3                              4.20E+16    0.0   100000.0
     Reverse Arrhenius coefficients:              1.02E+12    0.6    -1600.0
321. C3H4-P+O2<=>HCCO+OH+CH2                       1.00E+07    1.5    30100.0
     Reverse Arrhenius coefficients:              1.00E+00    0.0        0.0
322. C3H4-P+O2<=>C3H3+HO2                          2.00E+13    0.0    41600.0
     Reverse Arrhenius coefficients:              6.37E+11   -0.2     1021.0
323. C3H4-P+HO2<=>C2H4+CO+OH                       3.00E+12    0.0    19000.0
     Reverse Arrhenius coefficients:              1.00E+00    0.0        0.0
324. C3H4-P+OH<=>C3H3+H2O                          1.00E+07    2.0     1000.0
```

```
     Reverse Arrhenius coefficients:              6.44E+05    2.0    30000.0
325. C3H4-P+OH<=>CH2CO+CH3                         5.00E-04    4.5    -1000.0
     Reverse Arrhenius coefficients:              1.08E-02    4.1    31280.0
326. C3H4-P+O<=>C2H3+HCO                          3.20E+12    0.0     2010.0
     Reverse Arrhenius coefficients:              2.55E+12   -0.4    32350.0
327. C3H4-P+O<=>HCCO+CH3                          9.60E+08    1.0        0.0
     Reverse Arrhenius coefficients:              1.43E+04    1.8    26990.0
328. C3H4-P+O=>HCCO+CH2+H                         3.20E-19    0.0     2010.0
329. C3H4-P+O<=>C3H3+OH                           7.65E+08    1.5     8600.0
     Reverse Arrhenius coefficients:              2.18E+08    1.3    22470.0
330. C3H4-P+H<=>C3H3+H2                           2.00E+07    2.0     5000.0
     Reverse Arrhenius coefficients:              1.22E+05    2.1    19110.0
331. C3H4-P+CH3<=>C3H3+CH4                        1.50E+00    3.5     5600.0
     Reverse Arrhenius coefficients:              8.31E+00    3.2    21250.0
332. C3H4-P+C2H<=>C3H3+C2H2                       1.00E+12    0.0        0.0
     Reverse Arrhenius coefficients:              5.30E+11   -0.4    49630.0
333. C3H4-P+C2H3<=>C3H3+C2H4                      1.00E+12    0.0     7700.0
     Reverse Arrhenius coefficients:              9.54E+11   -0.4    52450.0
334. C3H4-P+C3H5-A<=>C3H3+C3H6                    1.00E+12    0.0     7700.0
     Reverse Arrhenius coefficients:              4.93E+16   -1.7    37950.0
335. C3H3+O<=>CH2O+C2H                            1.00E+13    0.0        0.0
     Reverse Arrhenius coefficients:              5.45E+14    0.0    31610.0
336. C3H3+OH<=>C3H2+H2O                           1.00E+13    0.0        0.0
     Reverse Arrhenius coefficients:              1.34E+15    0.0    15680.0
337. C3H3+O2<=>CH2CO+HCO                          3.01E+10    0.0     2870.0
     Reverse Arrhenius coefficients:              4.88E+11    0.0    59470.0
338. C3H3+CH3<=>C2H5+C2H                          4.30E+15   -0.8    45630.0
     Reverse Arrhenius coefficients:              1.81E+13    0.0        0.0
339. C3H2+O2<=>HCO+HCCO                           5.00E+13    0.0        0.0
     Reverse Arrhenius coefficients:              2.33E+14   -0.2    77190.0
340. C3H4-A+HO2<=>C2H4+CO+OH                      1.00E+12    0.0    14000.0
     Reverse Arrhenius coefficients:              1.00E+00    0.0        0.0
341. C3H4-A+HO2<=>C3H3+H2O2                       3.00E+13    0.0    14000.0
     Reverse Arrhenius coefficients:              1.55E+16   -1.4    44000.0
342. C2H2+CH3<=>C3H4-P+H                          4.23E+08    1.1    12090.0
     Reverse Arrhenius coefficients:              1.00E+14    0.0     4000.0
343. C2H2+CH3<=>C3H4-A+H                          6.74E+19   -2.1    31590.0
     Reverse Arrhenius coefficients:              6.41E+25   -3.3    21770.0
344. C3H3+H<=>C3H2+H2                             5.00E+13    0.0        0.0
     Reverse Arrhenius coefficients:              6.00E+07    1.4     4110.0
345. C3H2+OH<=>C2H2+HCO                           5.00E+13    0.0        0.0
     Reverse Arrhenius coefficients:              2.28E+16   -0.3    75020.0
346. C3H2+O2<=>HCCO+CO+H                          5.00E+13    0.0        0.0
     Warning...all REV parameters are zero... 0.0000e+000 0.000 0.000E+00
               this reaction will be treated as irreversible
347. CH3CHCO+OH<=>C2H5+CO2                        1.73E+12    0.0    -1010.0
     Warning...all REV parameters are zero... 0.0000e+000 0.000 0.000E+00
               this reaction will be treated as irreversible
348. CH3CHCO+H<=>C2H5+CO                          4.40E+12    0.0     1459.0
     Warning...all REV parameters are zero... 0.0000e+000 0.000 0.000E+00
               this reaction will be treated as irreversible
349. CH3CHCO+O<=>CH3CHO+CO                        3.20E+12    0.0     -437.0
     Warning...all REV parameters are zero... 0.0000e+000 0.000 0.000E+00
               this reaction will be treated as irreversible
350. NC3H7O2<=>NC3H7+O2                           2.40E+20   -1.6    35960.0
     Reverse Arrhenius coefficients:              4.52E+12    0.0        0.0
351. IC3H7O2<=>IC3H7+O2                           3.13E+22   -2.2    38160.0
     Reverse Arrhenius coefficients:              7.54E+12    0.0        0.0
352. NC3H7O2<=>C3H6OOH1-2                         6.00E+11    0.0    26850.0
     Reverse Arrhenius coefficients:              1.12E+08    0.6    11720.0
353. C3H6OOH1-2<=>C3H6+HO2                        7.83E+15   -1.3    15950.0
     Reverse Arrhenius coefficients:              1.00E+11    0.0    11000.0
354. C3H6OOH1-2<=>C2H4+CH2O+OH                    1.31E+33   -7.0    48120.0
     Warning...all REV parameters are zero... 0.0000e+000 0.000 0.000E+00
               this reaction will be treated as irreversible
355. C3H5O<=>C2H3CHO+H                            1.00E+14    0.0    29100.0
     Reverse Arrhenius coefficients:              1.68E+14   -0.2    19690.0
356. C3H5O<=>C2H3+CH2O                            1.46E+20   -2.0    35090.0
     Reverse Arrhenius coefficients:              1.50E+11    0.0    10600.0
357. C3H5O+O2<=>C2H3CHO+HO2                       1.00E+12    0.0     6000.0
     Reverse Arrhenius coefficients:              1.29E+11    0.0    32000.0
358. IC3H7O2<=>C3H6+HO2                           1.01E+43   -9.4    41490.0
     Reverse Arrhenius coefficients:              1.95E+33   -7.3    16670.0
359. NC3H7O2<=>C3H6+HO2                           5.04E+38   -8.1    40490.0
     Reverse Arrhenius coefficients:              1.20E+30   -6.2    20420.0
360. PC4H9<=>C2H5+C2H4                            3.50E+12    0.5    29470.0
     Reverse Arrhenius coefficients:              1.32E+04    2.5     6130.0
361. SC4H9<=>C3H6+CH3                             4.80E+10    1.0    30350.0
     Reverse Arrhenius coefficients:              1.76E+04    2.5     6130.0
362. PC4H9<=>C4H8-1+H                             2.62E+12    0.3    35700.0
     Reverse Arrhenius coefficients:              2.50E+11    0.5     2620.0
363. SC4H9<=>C4H8-1+H                             3.03E+11    0.6    36820.0
     Reverse Arrhenius coefficients:              4.24E+11    0.5     1230.0
364. PC4H9+O2<=>C4H8-1+HO2                        2.00E-18    0.0     5000.0
     Reverse Arrhenius coefficients:              2.00E-19    0.0    17500.0
365. SC4H9+O2<=>C4H8-1+HO2                        2.00E-18    0.0     5000.0
     Reverse Arrhenius coefficients:              2.00E-19    0.0    17500.0
366. C4H8-1<=>C3H5-A+CH3                          5.08E+19   -1.3    76510.0
     Reverse Arrhenius coefficients:              1.35E+13    0.0        0.0
367. C4H8-1<=>C2H3+C2H5                           2.88E+23   -2.0   101600.0
     Reverse Arrhenius coefficients:              9.00E+12    0.0        0.0
368. C4H8-1<=>H+C4H71-3                           3.72E+14   -0.1    85200.0
     Reverse Arrhenius coefficients:              5.00E+13    0.0        0.0
369. C4H8-1+O2<=>C4H71-3+HO2                      2.00E+13    0.0    37190.0
     Reverse Arrhenius coefficients:              4.65E+12    0.1     -168.0
```

370. C4H8-1+H<=>C4H71-3+H2	3.38E+05	2.4	207.0
Reverse Arrhenius coefficients:	4.32E+06	2.1	20330.0
371. C4H8-1+H<=>C4H71-4+H2	6.65E+05	2.5	6756.0
Reverse Arrhenius coefficients:	3.04E+04	2.5	11030.0
372. C4H8-1+OH<=>C4H71-3+H2O	2.76E+04	2.6	-1919.0
Reverse Arrhenius coefficients:	1.53E+06	2.4	33360.0
373. C4H8-1+OH<=>C4H71-4+H2O	5.27E+09	1.0	1586.0
Reverse Arrhenius coefficients:	1.04E+09	1.0	21010.0
374. C4H8-1+CH3<=>C4H71-3+CH4	3.69E+00	3.3	4002.0
Reverse Arrhenius coefficients:	1.23E+03	3.0	24610.0
375. C4H8-1+CH3<=>C4H71-4+CH4	4.52E-01	3.6	7154.0
Reverse Arrhenius coefficients:	5.40E-01	3.6	11910.0
376. C4H8-1+HO2<=>C4H71-3+H2O2	4.82E+03	2.5	10530.0
Reverse Arrhenius coefficients:	1.59E+06	2.0	14350.0
377. C4H8-1+HO2<=>C4H71-4+H2O2	2.38E+03	2.5	16490.0
Reverse Arrhenius coefficients:	2.80E+03	2.2	4460.0
378. C4H8-1+CH3O2<=>C4H71-3+CH3O2H	4.82E+03	2.5	10530.0
Reverse Arrhenius coefficients:	3.30E+06	1.8	11330.0
379. C4H8-1+CH3O2<=>C4H71-4+CH3O2H	2.38E+03	2.5	16490.0
Reverse Arrhenius coefficients:	5.83E+03	2.0	1440.0
380. C4H8-1+CH3O<=>C4H71-3+CH3OH	4.00E+01	2.9	8609.0
Reverse Arrhenius coefficients:	2.47E+02	2.7	27000.0
381. C4H8-1+CH3O<=>C4H71-4+CH3OH	2.17E+11	0.0	6458.0
Reverse Arrhenius coefficients:	4.79E+09	0.0	9002.0
382. C4H8-1+C3H5-A<=>C4H71-3+C3H6	7.90E+10	0.0	12400.0
Reverse Arrhenius coefficients:	1.00E+11	0.0	17500.0
383. C4H8-1+C4H6<=>C4H71-3+C4H71-3	2.35E+12	0.0	46720.0
Reverse Arrhenius coefficients:	1.60E+12	0.0	0.0
384. C4H71-4<=>C2H4+C2H3	8.77E+12	-0.2	36290.0
Reverse Arrhenius coefficients:	2.00E+11	0.0	7800.0
385. C4H71-4<=>C4H6+H	3.00E+13	0.0	35000.0
386. C4H71-3<=>C4H6+H	1.20E+14	0.0	49300.0
Reverse Arrhenius coefficients:	4.00E+13	0.0	1300.0
387. C4H71-3+C2H5<=>C4H8-1+C2H4	2.59E+12	0.0	-131.0
Reverse Arrhenius coefficients:	1.15E+13	0.1	49440.0
388. C4H71-3+CH3O<=>C4H8-1+CH2O	2.41E+13	0.0	0.0
Reverse Arrhenius coefficients:	2.48E+12	0.3	66330.0
389. C4H71-3+O<=>C2H3CHO+CH3	6.03E+13	0.0	0.0
Reverse Arrhenius coefficients:	3.38E+15	-0.8	81630.0
390. C4H71-3+HO2<=>C4H7O+OH	9.64E+12	0.0	0.0
Reverse Arrhenius coefficients:	7.29E+15	-1.1	15530.0
391. C4H71-3+CH3O2<=>C4H7O+CH3O	9.64E+12	0.0	0.0
Reverse Arrhenius coefficients:	7.12E+17	-1.7	20290.0
392. C3H5-A+C4H71-3<=>C3H6+C4H6	6.31E+12	0.0	0.0
Reverse Arrhenius coefficients:	1.00E+10	0.0	50000.0
393. C4H71-3+O2<=>C4H6+HO2	1.00E+09	0.0	0.0
Reverse Arrhenius coefficients:	1.00E+11	0.0	17000.0
394. H+C4H71-3<=>C4H6+H2	3.16E+13	0.0	0.0
Reverse Arrhenius coefficients:	1.07E+13	0.0	56810.0
395. C2H5+C4H71-3<=>C4H6+C2H6	3.98E+12	0.0	0.0
Reverse Arrhenius coefficients:	3.21E+12	0.0	49840.0
396. C2H3+C4H71-3<=>C2H4+C4H6	3.98E+12	0.0	0.0
Reverse Arrhenius coefficients:	1.16E+13	0.0	57710.0
397. C4H71-3+C2H5O2<=>C4H7O+C2H5O	3.80E+12	0.0	-1200.0
Reverse Arrhenius coefficients:	2.00E+10	0.0	0.0
398. C4H7O<=>CH3CHO+C2H3	7.94E+14	0.0	19000.0
Reverse Arrhenius coefficients:	1.00E+10	0.0	20000.0
399. C4H7O<=>C2H3CHO+CH3	7.94E+14	0.0	19000.0
Reverse Arrhenius coefficients:	1.00E+10	0.0	20000.0
400. C4H6<=>C2H3+C2H3	4.03E+19	-1.0	98150.0
Reverse Arrhenius coefficients:	1.26E+13	0.0	0.0
401. C4H6+OH<=>C2H5+CH2CO	1.00E+12	0.0	0.0
Reverse Arrhenius coefficients:	3.73E+12	0.0	30020.0
402. C4H6+OH<=>CH2O+C3H5-A	1.00E+12	0.0	0.0
Reverse Arrhenius coefficients:	3.50E+06	0.0	71060.0
403. C4H6+OH<=>C2H3+CH3CHO	1.00E+12	0.0	0.0
Reverse Arrhenius coefficients:	5.44E+11	0.0	18550.0
404. C4H6+O<=>C2H4+CH2CO	1.00E+12	0.0	0.0
Reverse Arrhenius coefficients:	6.38E+11	0.0	94340.0
405. C4H6+O<=>CH2O+C3H4-A	1.00E+12	0.0	0.0
Reverse Arrhenius coefficients:	1.08E+12	0.0	79050.0
406. C2H3+C2H4<=>C4H6+H	5.00E+11	0.0	7300.0
Reverse Arrhenius coefficients:	1.00E+13	0.0	4700.0
407. PC4H9O2<=>PC4H9+O2	2.85E+20	-1.6	35930.0
Reverse Arrhenius coefficients:	4.52E+12	0.0	0.0
408. PC4H9O2<=>C4H8-1+HO2	5.04E+38	-8.1	40490.0
Reverse Arrhenius coefficients:	1.60E+30	-6.3	20350.0
409. C5H11-1<=>C2H4+NC3H7	3.20E+12	0.5	29430.0
Reverse Arrhenius coefficients:	8.80E+03	2.5	6130.0
410. C5H11-1<=>H+C5H10-1	3.35E+11	0.6	35640.0
Reverse Arrhenius coefficients:	2.50E+11	0.5	2620.0
411. C5H11-1<=>C5H11-2	3.88E+09	0.4	19760.0
Reverse Arrhenius coefficients:	1.60E+08	0.8	22200.0
412. C5H11-2<=>C3H6+C2H5	1.22E+12	0.6	29360.0
Reverse Arrhenius coefficients:	8.80E+03	2.5	6130.0
413. C5H11-2<=>C5H10-1+H	2.35E+10	1.0	36680.0
Reverse Arrhenius coefficients:	4.24E+11	0.5	1230.0
414. C5H10-1<=>C2H5+C3H5-A	9.86E+21	-2.1	75060.0
Reverse Arrhenius coefficients:	4.00E+12	0.0	-596.0
415. C5H10-1+H<=>C5H91-4+H2	1.17E+07	2.4	4471.0
Reverse Arrhenius coefficients:	2.78E+02	3.2	11240.0
416. C5H10-1+O<=>C5H91-4+OH	5.51E+05	2.5	2830.0
Reverse Arrhenius coefficients:	5.17E+01	3.2	7505.0
417. C5H10-1+OH<=>C5H91-4+H2O	4.67E+07	1.6	-35.0
Reverse Arrhenius coefficients:	4.32E+04	2.4	21890.0

```
418. C5H10-1+CH3<=>C5H91-4+CH4                     1.36E+01    3.5     5481.0
     Reverse Arrhenius coefficients:               8.43E-03    4.2    12730.0
419. C5H10-1+O2<=>C5H91-4+HO2                      2.00E+13    0.0    49640.0
     Reverse Arrhenius coefficients:               7.76E+07    1.1    -1072.0
420. C5H10-1+HO2<=>C5H91-4+H2O2                    9.64E+03    2.6    13910.0
     Reverse Arrhenius coefficients:               5.29E+01    3.0     4372.0
421. C5H10-1+CH3O2<=>C5H91-4+CH3O2H                9.64E+03    2.6    13910.0
     Reverse Arrhenius coefficients:               1.10E+02    2.9     1352.0
422. C5H10-1+CH3O<=>C5H91-4+CH3OH                  1.45E+11    0.0     4571.0
     Reverse Arrhenius coefficients:               1.49E+07    0.8     9611.0
423. C5H91-4<=>C3H6+C2H3                           5.81E+11    0.2    35850.0
     Reverse Arrhenius coefficients:               1.00E+11    0.0     7800.0
424. C5H11-1+O2<=>C5H10-1+HO2                      8.37E-01    3.6    11960.0
     Reverse Arrhenius coefficients:               1.31E+00    3.4    27810.0
425. C5H11-2+O2<=>C5H10-1+HO2                      5.35E-01    3.7     9322.0
     Reverse Arrhenius coefficients:               2.02E+01    3.1    22740.0
426. C5H11O2-1<=>C5H11-1+O2                        2.34E+20   -1.6    35830.0
     Reverse Arrhenius coefficients:               4.52E+12    0.0        0.0
427. C5H11O2-1<=>C5H10OOH1-3                       2.50E+10    0.0    20850.0
     Reverse Arrhenius coefficients:               2.60E+09   -0.1     7850.0
428. C5H11O2-1<=>C5H10-1+HO2                       5.04E+38   -8.1    40490.0
     Reverse Arrhenius coefficients:               1.52E+31   -6.7    20510.0
429. C5H10OOH1-3<=>OH+CH2O+C4H8-1                  8.28E+13   -0.2    30090.0
     Warning...all REV parameters are zero... 0.0000e+000 0.000 0.000E+00
               this reaction will be treated as irreversible
430. C5H10OOH1-3O2<=>C5H10OOH1-3+O2                8.04E+22   -2.3    37970.0
     Reverse Arrhenius coefficients:               7.54E+12    0.0        0.0
431. C5H10OOH1-3O2<=>NC5KET13+OH                   2.50E+10    0.0    21000.0
     Reverse Arrhenius coefficients:               1.11E+03    1.5    44740.0
432. NC5KET13<=>C2H5CHO+CH2CHO+OH                  1.05E+16    0.0    41600.0
     Warning...all REV parameters are zero... 0.0000e+000 0.000 0.000E+00
               this reaction will be treated as irreversible
433. C6H13-1+O2<=>C6H12-1+HO2                      3.00E-19    0.0     3000.0
     Reverse Arrhenius coefficients:               2.00E-19    0.0    17500.0
434. C6H13-2+O2<=>C6H12-1+HO2                      4.50E-19    0.0     5020.0
     Reverse Arrhenius coefficients:               2.00E-19    0.0    17500.0
435. C6H13-1<=>C2H4+PC4H9                          6.39E+19   -2.0    30640.0
     Reverse Arrhenius coefficients:               3.30E+11    0.0     7200.0
436. C6H13-1<=>C6H12-1+H                           9.62E+13   -0.3    36000.0
     Reverse Arrhenius coefficients:               1.00E+13    0.0     2900.0
437. C6H13-2<=>C3H6+NC3H7                          1.83E+19   -1.8    30170.0
     Reverse Arrhenius coefficients:               1.50E+11    0.0     7200.0
438. C6H13-2<=>C6H12-1+H                           6.25E+12    0.1    36820.0
     Reverse Arrhenius coefficients:               1.00E+13    0.0     1200.0
439. C6H13-1<=>C6H13-2                             5.48E+08    1.6    38760.0
     Reverse Arrhenius coefficients:               3.56E+07    2.0    41270.0
440. C6H12-1<=>NC3H7+C3H5-A                        1.00E+16    0.0    71000.0
     Reverse Arrhenius coefficients:               1.00E+13    0.0        0.0
441. C6H12-1+OH<=>C5H11-1+CH2O                     1.00E+11    0.0    -4000.0
     Warning...all REV parameters are zero... 0.0000e+000 0.00 0.000E+00
               this reaction will be treated as irreversible
442. C6H12-1+O<=>C5H11-1+HCO                       1.00E+11    0.0    -1050.0
     Warning...all REV parameters are zero... 0.0000e+000 0.00 0.000E+00
               this reaction will be treated as irreversible
443. C6H12-1+H<=>C6H111-5+H2                       1.17E+07    2.4     4471.0
     Reverse Arrhenius coefficients:               3.90E+03    2.7    11250.0
444. C6H12-1+OH<=>C6H111-5+H2O                     4.67E+07    1.6      -35.0
     Reverse Arrhenius coefficients:               6.06E+05    1.9    21900.0
445. C6H12-1+CH3<=>C6H111-5+CH4                    1.36E+01    3.5     5481.0
     Reverse Arrhenius coefficients:               1.18E-01    3.8    12740.0
446. C6H12-1+HO2<=>C6H111-5+H2O2                   9.64E+03    2.6    13910.0
447. C6H12-1+CH3O2<=>C6H111-5+CH3O2H               9.64E+03    2.6    13910.0
     Reverse Arrhenius coefficients:               1.55E+03    2.4     1362.0
448. C6H12-1+CH3O<=>C6H111-5+CH3OH                 1.45E+11    0.0     4571.0
     Reverse Arrhenius coefficients:               2.10E+08    0.4     9621.0
449. C6H13O2-1<=>C6H13-1+O2                        5.15E+20   -1.7    35790.0
     Reverse Arrhenius coefficients:               4.52E+12    0.0        0.0
450. C6H13O2-1<=>C6H12-1+HO2                       5.04E+38   -8.1    40490.0
     Reverse Arrhenius coefficients:               9.64E+29   -6.2    20470.0
451. C6H13O2-1<=>C6H12OOH1-3                       2.50E+10    0.0    20850.0
     Reverse Arrhenius coefficients:               3.00E+09   -0.1     7860.0
452. C6H12OOH1-3<=>OH+CH2O+C5H10-1                 7.70E+13   -0.2    30090.0
     Warning...all REV parameters are zero... 0.0000e+000 0.00 0.000E+00
               this reaction will be treated as irreversible
453. C6H12OOH1-3O2<=>C6H12OOH1-3+O2                8.87E+22   -2.3    37980.0
     Reverse Arrhenius coefficients:               7.54E+12    0.0        0.0
454. C6H12OOH1-3O2<=>NC6KET13+OH                   2.50E+10    0.0    21000.0
     Reverse Arrhenius coefficients:               8.82E+02    1.6    44710.0
455. NC6KET13<=>NC3H7CHO+CH2CHO+OH                 1.00E+16    0.0    39000.0
     Warning...all REV parameters are zero... 0.0000e+000 0.00 0.000E+00
               this reaction will be treated as irreversible
456. NC3H7COCH2<=>NC3H7+CH2CO                      1.23E+18   -1.4    43450.0
     Reverse Arrhenius coefficients:               1.00E+11    0.0    11600.0
457. C7H15-1<=>C5H11-1+C2H4                        1.23E+19   -1.9    31400.0
     Reverse Arrhenius coefficients:               1.00E+11    0.0     8200.0
458. C7H15-1<=>C7H14-1+H                           9.65E+13   -0.3    36010.0
     Reverse Arrhenius coefficients:               1.00E+13    0.0     2900.0
459. C7H15-1+O2<=>C7H14-1+HO2                      3.00E-09    0.0     3000.0
     Reverse Arrhenius coefficients:               6.52E-10    0.2    18760.0
460. C7H14-1+OH<=>CH2O+C6H13-1                     1.00E+11    0.0    -4000.0
     Warning...all REV parameters are zero... 0.0000e+000 0.00 0.000E+00
               this reaction will be treated as irreversible
461. C7H14-1+OH<=>CH3CHO+C5H11-1                   1.00E+11    0.0    -4000.0
     Warning...all REV parameters are zero... 0.0000e+000 0.00 0.000E+00
               this reaction will be treated as irreversible
```

```
462. C7H14-1+O<=>CH2CHO+C5H11-1                    1.00E+11    0.0    -1050.0
     Warning...all REV parameters are zero... 0.0000e+000 0.00 0.000E+00
               this reaction will be treated as irreversible
463. C7H14-1<=>PC4H9+C3H5-A                        3.17E+21   -1.6    75330.0
     Reverse Arrhenius coefficients:              1.00E+13    0.0        0.0
464. C7H15O2-1<=>C7H15-1+O2                        2.66E+20   -1.7    35400.0
     Reverse Arrhenius coefficients:              4.52E+12    0.0        0.0
465. C7H15O2-1<=>C7H14-1+HO2                       4.31E+36   -7.5    39510.0
466. C7H15O2-1<=>C7H14OOH1-3                       2.50E+10    0.0    20450.0
467. C7H14OOH1-3<=>C7H14O1-3+OH                    7.50E+10    0.0    15250.0
     Warning...all REV parameters are zero... 0.0000e+000 0.00 0.000E+00
               this reaction will be treated as irreversible
468. C7H14OOH1-3<=>OH+CH2O+C6H12-1                 2.15E+09    1.2    30370.0
     Warning...all REV parameters are zero... 0.0000e+000 0.00 0.000E+00
               this reaction will be treated as irreversible
469. C7H14OOH1-3<=>C4H7OOH1-4+NC3H7                1.61E+12    0.5    27740.0
     Reverse Arrhenius coefficients:              2.20E+03    2.5     6130.0
470. C7H14OOH1-3O2<=>C7H14OOH1-3+O2                1.37E+23   -2.4    37640.0
     Reverse Arrhenius coefficients:              7.54E+12    0.0        0.0
471. C7H14O1-3+OH<=>C6H12-1+HCO+H2O                2.50E+12    0.0        0.0
     Warning...all REV parameters are zero... 0.0000e+000 0.00 0.000E+00
               this reaction will be treated as irreversible
472. C7H14O1-3+HO2<=>C6H12-1+HCO+H2O2              5.00E+12    0.0    17700.0
     Warning...all REV parameters are zero... 0.0000e+000 0.00 0.000E+00
               this reaction will be treated as irreversible
473. NC5H11CHO+O2<=>NC5H11CO+HO2                   2.00E+13    0.5    42200.0
     Reverse Arrhenius coefficients:              1.00E+07    0.0    40000.0
474. NC5H11CHO+OH<=>NC5H11CO+H2O                   2.69E+10    0.8     -340.0
     Reverse Arrhenius coefficients:              1.74E+10    0.8    31200.0
475. NC5H11CHO+H<=>NC5H11CO+H2                     4.00E+13    0.0     4200.0
     Reverse Arrhenius coefficients:              1.80E+13    0.0    24000.0
476. NC5H11CHO+O<=>NC5H11CO+OH                     5.00E+12    0.0     1790.0
     Reverse Arrhenius coefficients:              1.00E+12    0.0    19000.0
477. NC5H11CHO+HO2<=>NC5H11CO+H2O2                 2.80E+12    0.0    13600.0
     Reverse Arrhenius coefficients:              1.00E+12    0.0    10000.0
478. NC5H11CHO+CH3<=>NC5H11CO+CH4                  1.70E+12    0.0     8440.0
     Reverse Arrhenius coefficients:              1.50E+13    0.0    28000.0
479. NC5H11CHO+CH3O<=>NC5H11CO+CH3OH               1.15E+11    0.0     1280.0
     Reverse Arrhenius coefficients:              3.00E+11    0.0    18000.0
480. NC5H11CHO+CH3O2<=>NC5H11CO+CH3O2H             1.00E+12    0.0     9500.0
     Reverse Arrhenius coefficients:              2.50E+10    0.0    10000.0
481. NC5H11CO<=>C5H11-1+CO                         1.00E+11    0.0     9600.0
     Reverse Arrhenius coefficients:              1.00E+11    0.0        0.0
482. NC4H9COCH2<=>PC4H9+CH2CO                      1.55E+18   -1.4    43140.0
     Reverse Arrhenius coefficients:              1.00E+11    0.0    11600.0
483. C4H7OOH1-4<=>C4H7O1-4+OH                      2.02E+20   -1.5    47040.0
     Reverse Arrhenius coefficients:              2.00E+13    0.0        0.0
484. C4H7O1-4<=>CH2O+C3H5-A                        2.41E+16   -1.1     7550.0
     Reverse Arrhenius coefficients:              1.00E+11    0.0    11900.0
485. C6H12-1<=>C3H6+C3H6                           4.00E+12    0.0    58000.0
486. PC4H9+C2H3<=>C6H12-1                          1.00E+13    0.0        0.0
487. C4H71-4+C2H5<=>C6H12-1                        8.00E+12    0.0        0.0
488. C6H12-1+O2<=>C6H111-5+HO2                     2.00E+13    0.0    49640.0
489. C6H12-1+O<=>C6H111-5+OH                       5.51E+05    2.5     2830.0
490. C3H5-A+C3H6=C6H111-5                          4.00E+11    0.0    16900.0
491. C12H25-1+H=NC12H26                            1.00E+14    0.0        0.0
492. C12H25-2+H=NC12H26                            1.00E+14    0.0        0.0
493. C12H25-3+H=NC12H26                            1.00E+14    0.0        0.0
494. ISO8+H=NC12H26                                1.00E+14    0.0        0.0
     Declared duplicate reaction...
495. ISO8+H=NC12H26                                1.00E+14    0.0        0.0
     Declared duplicate reaction...
496. ISO8+H=NC12H26                                1.00E+14    0.0        0.0
     Declared duplicate reaction...
497. C10H21-1+C2H5=NC12H26                         8.00E+12    0.0        0.0
498. C9H19-1+NC3H7=NC12H26                         8.00E+12    0.0        0.0
499. C8H17-1+PC4H9=NC12H26                         8.00E+12    0.0        0.0
500. C7H15-1+C5H11-1=NC12H26                       8.00E+12    0.0        0.0
501. C6H13-1+C6H13-1=NC12H26                       8.00E+12    0.0        0.0
502. NC12H26+H=C12H25-1+H2                         1.33E+06    2.5     6756.0
503. NC12H26+H=C12H25-2+H2                         2.60E+06    2.4     4471.0
504. NC12H26+H=C12H25-3+H2                         2.60E+06    2.4     4471.0
505. NC12H26+H=ISO8+H2                             2.60E+06    2.4     4471.0
     Declared duplicate reaction...
506. NC12H26+H=ISO8+H2                             2.60E+06    2.4     4471.0
     Declared duplicate reaction...
507. NC12H26+H=ISO8+H2                             2.60E+06    2.4     4471.0
     Declared duplicate reaction...
508. NC12H26+OH=C12H25-1+H2O                       1.06E+10    1.0     1590.0
509. NC12H26+OH=C12H25-2+H2O                       9.40E+07    1.6      -35.0
510. NC12H26+OH=C12H25-3+H2O                       9.40E+07    1.6      -35.0
511. NC12H26+OH=ISO8+H2O                           9.40E+07    1.6      -35.0
     Declared duplicate reaction...
512. NC12H26+OH=ISO8+H2O                           9.40E+07    1.6      -35.0
     Declared duplicate reaction...
513. NC12H26+OH=ISO8+H2O                           9.40E+07    1.6      -35.0
     Declared duplicate reaction...
514. NC12H26+O=C12H25-1+OH                         1.96E+06    2.4     4750.0
515. NC12H26+O=C12H25-2+OH                         1.10E+06    2.5     2830.0
516. NC12H26+O=C12H25-3+OH                         1.10E+06    2.5     2830.0
517. NC12H26+O=ISO8+OH                             1.10E+06    2.5     2830.0
     Declared duplicate reaction...
518. NC12H26+O=ISO8+OH                             1.10E+06    2.5     2830.0
     Declared duplicate reaction...
519. NC12H26+O=ISO8+OH                             1.10E+06    2.5     2830.0
```

```
     Declared duplicate reaction...
520. NC12H26+HO2=C12H25-1+H2O2                 4.08E+01    3.6    17160.0
521. NC12H26+HO2=C12H25-2+H2O2                 3.88E+02    3.3    12300.0
522. NC12H26+HO2=C12H25-3+H2O2                 3.88E+02    3.3    12300.0
523. NC12H26+HO2=ISO8+H2O2                     3.88E+02    3.3    12300.0
     Declared duplicate reaction...
524. NC12H26+HO2=ISO8+H2O2                     3.88E+02    3.3    12300.0
     Declared duplicate reaction...
525. NC12H26+HO2=ISO8+H2O2                     3.88E+02    3.3    12300.0
     Declared duplicate reaction...
526. NC12H26+CH3=C12H25-1+CH4                  9.06E-01    3.6     7154.0
527. NC12H26+CH3=C12H25-2+CH4                  3.02E+00    3.5     5481.0
528. NC12H26+CH3=C12H25-3+CH4                  3.02E+00    3.5     5481.0
529. NC12H26+CH3=ISO8+CH4                      3.02E+00    3.5     5481.0
     Declared duplicate reaction...
530. NC12H26+CH3=ISO8+CH4                      3.02E+00    3.5     5481.0
     Declared duplicate reaction...
531. NC12H26+CH3=ISO8+CH4                      3.02E+00    3.5     5481.0
     Declared duplicate reaction...
532. NC12H26+O2=C12H25-1+HO2                   6.00E+13    0.0    52290.0
533. NC12H26+O2=C12H25-2+HO2                   4.00E+13    0.0    49640.0
534. NC12H26+O2=C12H25-3+HO2                   4.00E+13    0.0    49640.0
535. NC12H26+O2=ISO8+HO2                       4.00E+13    0.0    49640.0
     Declared duplicate reaction...
536. NC12H26+O2=ISO8+HO2                       4.00E+13    0.0    49640.0
     Declared duplicate reaction...
537. NC12H26+O2=ISO8+HO2                       4.00E+13    0.0    49640.0
     Declared duplicate reaction...
538. NC12H26+C2H3=C12H25-1+C2H4                1.00E+12    0.0    18000.0
539. NC12H26+C2H3=C12H25-2+C2H4                8.00E+11    0.0    16800.0
540. NC12H26+C2H3=C12H25-3+C2H4                8.00E+11    0.0    16800.0
541. NC12H26+C2H3=ISO8+C2H4                    8.00E+11    0.0    16800.0
     Declared duplicate reaction...
542. NC12H26+C2H3=ISO8+C2H4                    8.00E+11    0.0    16800.0
     Declared duplicate reaction...
543. NC12H26+C2H3=ISO8+C2H4                    8.00E+11    0.0    16800.0
     Declared duplicate reaction...
544. NC12H26+C2H5=C12H25-1+C2H6                1.00E+11    0.0    13400.0
545. NC12H26+C2H5=C12H25-2+C2H6                1.00E+11    0.0    10400.0
546. NC12H26+C2H5=C12H25-3+C2H6                1.00E+11    0.0    10400.0
547. NC12H26+C2H5=ISO8+C2H6                    1.00E+11    0.0    10400.0
     Declared duplicate reaction...
548. NC12H26+C2H5=ISO8+C2H6                    1.00E+11    0.0    10400.0
     Declared duplicate reaction...
549. NC12H26+C2H5=ISO8+C2H6                    1.00E+11    0.0    10400.0
     Declared duplicate reaction...
550. NC12H26+CH3O<=>C12H25-1+CH3OH             4.34E+11    0.0     6458.0
551. NC12H26+CH3O<=>C12H25-2+CH3OH             2.90E+11    0.0     4571.0
552. NC12H26+CH3O<=>C12H25-3+CH3OH             2.90E+11    0.0     4571.0
553. NC12H26+CH3O<=>ISO8+CH3OH                 2.90E+11    0.0     4571.0
     Declared duplicate reaction...
554. NC12H26+CH3O<=>ISO8+CH3OH                 2.90E+11    0.0     4571.0
     Declared duplicate reaction...
555. NC12H26+CH3O<=>ISO8+CH3OH                 2.90E+11    0.0     4571.0
     Declared duplicate reaction...
556. NC12H26+CH3O2<=>C12H25-1+CH3O2H           1.39E+00    4.0    18280.0
557. NC12H26+CH3O2<=>C12H25-2+CH3O2H           2.04E+01    3.6    14810.0
558. NC12H26+CH3O2<=>C12H25-3+CH3O2H           2.04E+01    3.6    14810.0
559. NC12H26+CH3O2<=>ISO8+CH3O2H               2.04E+01    3.6    14810.0
     Declared duplicate reaction...
560. NC12H26+CH3O2<=>ISO8+CH3O2H               2.04E+01    3.6    14810.0
     Declared duplicate reaction...
561. NC12H26+CH3O2<=>ISO8+CH3O2H               2.04E+01    3.6    14810.0
     Declared duplicate reaction...
562. C12H25-1=C2H4+C10H21-1                    9.12E+11    0.3    27238.0
563. H+C12H24-1=C12H25-1                       2.50E+11    0.5     2620.0
564. C12H25-2=C3H6+C9H19-1                     6.00E+11    0.5    27650.0
565. H+C12H24-1=C12H25-2                       4.24E+11    0.5     1230.0
566. H+C12H24-2=C12H25-2                       2.50E+11    0.5     2620.0
567. C12H25-3=C4H8-1+C8H17-1                   6.00E+11    0.5    27650.0
568. H+C12H24-2=C12H25-3                       2.50E+11    0.5     2620.0
569. H+ISO13=C12H25-3                          2.50E+11    0.5     2620.0
570. ISO8=C5H10-1+C7H15-1                      3.96E+11    0.5    27650.0
571. ISO8=C2H5+C10H20-1                        3.96E+11    0.5    27650.0
572. H+ISO13=ISO8                              1.65E+11    0.5     2620.0
     Declared duplicate reaction...
573. H+ISO13=ISO8                              1.65E+11    0.5     2620.0
     Declared duplicate reaction...
574. ISO8=C6H12-1+C6H13-1                      1.07E+11    0.5    27650.0
575. ISO8=NC3H7+C9H18-1                        1.07E+11    0.5    27650.0
576. H+ISO13=ISO8                              4.47E+10    0.5     2620.0
     Declared duplicate reaction...
577. H+ISO13=ISO8                              4.47E+10    0.5     2620.0
     Declared duplicate reaction...
578. ISO8=C7H14-1+C5H11-1                      9.63E+10    0.5    27650.0
579. H+ISO13=ISO8                              4.01E+10    0.5     2620.0
     Declared duplicate reaction...
580. C10H21-1=C2H4+C8H17-1                     9.12E+11    0.3    27238.0
581. H+C10H20-1=C10H21-1                       2.50E+11    0.5     2620.0
582. C10H21-2=C3H6+C7H15-1                     6.00E+11    0.5    27650.0
583. H+C10H20-1=C10H21-2                       4.24E+11    0.5     1230.0
584. C10H21-5=C6H12-1+PC4H9                    6.00E+11    0.5    27650.0
585. C10H21-5=NC3H7+C7H14-1                    6.00E+11    0.5    27650.0
586. C9H19-1=C2H4+C7H15-1                      9.12E+11    0.3    27238.0
587. H+C9H18-1=C9H19-1                         2.50E+11    0.5     2620.0
```

```
588. C9H19-4=C5H10-1+PC4H9                      6.00E+11    0.5    27650.0
589. C9H19-4=C2H5+C7H14-1                       6.00E+11    0.5    27650.0
590. C9H19-5=C6H12-1+NC3H7                      6.00E+11    0.5    27650.0
591. C8H17-1=C2H4+C6H13-1                       9.12E+11    0.3    27238.0
592. C8H17-4=C5H10-1+NC3H7                      6.00E+11    0.5    27650.0
593. C8H17-4=C2H5+C6H12-1                       6.00E+11    0.5    27650.0
594. C12H25-1=ISO8                              6.92E+00    3.2    16558.0
     Declared duplicate reaction...
595. C12H25-1=ISO8                              1.82E+02    2.5    10960.0
     Declared duplicate reaction...
596. C12H25-1=ISO8                              2.96E+00    3.1    11020.0
     Declared duplicate reaction...
597. C12H25-2=ISO8                              1.42E+00    3.3    16140.0
     Declared duplicate reaction...
598. C12H25-2=ISO8                              1.86E+00    3.3    13200.0
     Declared duplicate reaction...
599. C12H25-2=ISO8                              6.00E-01    3.4    14000.0
     Declared duplicate reaction...
600. C12H25-3=ISO8                              1.42E+00    3.3    16140.0
     Declared duplicate reaction...
     Declared duplicate reaction...
601. C12H25-3=ISO8                              1.86E+00    3.3    13200.0
     Declared duplicate reaction...
602. C12H25-3=ISO8                              6.00E-01    3.4    14000.0
     Declared duplicate reaction...
603. ISO8=ISO8                                  2.28E-01    3.3    16140.0
     Declared duplicate reaction...
604. ISO8=ISO8                                  3.33E-01    3.3    13200.0
     Declared duplicate reaction...
605. C10H21-1=C10H21-5                          1.82E+02    2.5    10960.0
     Declared duplicate reaction...
606. C10H21-1=C10H21-5                          2.96E+00    3.1    11020.0
     Declared duplicate reaction...
607. C10H21-2=C10H21-5                          1.42E+00    3.3    16140.0
     Declared duplicate reaction...
608. C10H21-2=C10H21-5                          1.86E+00    3.3    13200.0
     Declared duplicate reaction...
609. C9H19-1=C9H19-4                            6.92E+00    3.2    16558.0
     Declared duplicate reaction...
610. C9H19-1=C9H19-5                            1.82E+02    2.5    10960.0
611. C9H19-1=C9H19-4                            2.96E+00    3.1    11020.0
     Declared duplicate reaction...
612. C8H17-1=C8H17-4                            6.92E+00    3.2    16558.0
     Declared duplicate reaction...
613. C8H17-1=C8H17-4                            1.82E+02    2.5    10960.0
     Declared duplicate reaction...
614. C12H24-1+HO2<=>C12H23+H2O2                 7.58E+02    3.4    13720.0
615. C12H24-2+HO2<=>C12H23+H2O2                 7.58E+02    3.4    13720.0
616. ISO13+HO2<=>C12H23+H2O2                    2.54E+02    3.4    13720.0
     Declared duplicate reaction...
617. ISO13+HO2<=>C12H23+H2O2                    3.85E+02    3.4    13720.0
     Declared duplicate reaction...
618. ISO13+HO2<=>C12H23+H2O2                    1.19E+02    3.4    13720.0
     Declared duplicate reaction...
619. C12H24-1+OH=C12H23+H2O                     5.62E+07    1.6      -35.0
620. C12H24-2+OH=C12H23+H2O                     5.62E+07    1.6      -35.0
621. ISO13+OH=C12H23+H2O                        1.88E+07    1.6      -35.0
     Declared duplicate reaction...
622. ISO13+OH=C12H23+H2O                        2.85E+07    1.6      -35.0
     Declared duplicate reaction...
623. ISO13+OH=C12H23+H2O                        8.86E+06    1.6      -35.0
     Declared duplicate reaction...
624. C12H24-1+H=C12H23+H2                       1.56E+07    2.4     4471.0
625. C12H24-2+H=C12H23+H2                       1.56E+07    2.4     4471.0
626. ISO13+H=C12H23+H2                          5.22E+06    2.4     4471.0
     Declared duplicate reaction...
627. ISO13+H=C12H23+H2                          7.92E+06    2.4     4471.0
     Declared duplicate reaction...
628. ISO13+H=C12H23+H2                          2.46E+06    2.4     4471.0
     Declared duplicate reaction...
629. C12H24-1+CH3=C12H23+CH4                    1.81E+01    3.5     5481.0
630. C12H24-2+CH3=C12H23+CH4                    1.81E+01    3.5     5481.0
631. ISO13+CH3=C12H23+CH4                       6.05E+00    3.5     5481.0
     Declared duplicate reaction...
632. ISO13+CH3=C12H23+CH4                       9.19E+00    3.5     5481.0
     Declared duplicate reaction...
633. ISO13+CH3=C12H23+CH4                       2.85E+00    3.5     5481.0
     Declared duplicate reaction...
634. C12H24-1+O=C12H23+OH                       6.62E+06    2.5     2830.0
635. C12H24-2+O=C12H23+OH                       6.62E+06    2.5     2830.0
636. ISO13+O=C12H23+OH                          2.21E+06    2.5     2830.0
     Declared duplicate reaction...
637. ISO13+O=C12H23+OH                          3.36E+06    2.5     2830.0
     Declared duplicate reaction...
638. ISO13+O=C12H23+OH                          1.04E+06    2.5     2830.0
     Declared duplicate reaction...
639. C9H18-1+HO2<=>C9H17+H2O2                   5.59E+02    3.4    13720.0
640. C9H18-1+OH=C9H17+H2O                       4.21E+08    1.6      -35.0
641. C9H18-1+H=C9H17+H2                         1.17E+07    2.4     4471.0
642. C9H18-1+CH3=C9H17+CH4                      1.36E+01    3.5     5481.0
643. C9H18-1+O=C9H17+OH                         4.97E+06    2.5     2830.0
644. C12H24-1+OH=CH3CHO+C10H21-1                1.00E+11    0.0    -4000.0
     Warning...all REV parameters are zero... 0.0000e+000 0.00 0.000E+00
               this reaction will be treated as irreversible
645. C12H24-1+O=CH2CHO+C10H21-1                 1.00E+11    0.0    -1050.0
```

```
     Warning...all REV parameters are zero... 0.0000e+000 0.00 0.000E+00
               this reaction will be treated as irreversible
646. C12H24-2+OH=CH3CHO+C10H21-1                    1.00E+11    0.0    -4000.0
     Warning...all REV parameters are zero... 0.0000e+000 0.00 0.000E+00
               this reaction will be treated as irreversible
647. C12H24-2+OH=C2H5CHO+C9H19-1                    1.00E+11    0.0    -4000.0
     Warning...all REV parameters are zero... 0.0000e+000 0.00 0.000E+00
               this reaction will be treated as irreversible
648. C12H24-2+O=CH3CHO+C10H20-1                     1.00E+11    0.0    -1050.0
     Warning...all REV parameters are zero... 0.0000e+000 0.00 0.000E+00
               this reaction will be treated as irreversible
649. ISO13+OH=C2H5CHO+C9H19-1                       3.34E+10    0.0    -4000.0
     Warning...all REV parameters are zero... 0.0000e+000 0.00 0.000E+00
               this reaction will be treated as irreversible
650. ISO13+OH=NC3H7CHO+C8H17-1                      3.34E+10    0.0    -4000.0
     Warning...all REV parameters are zero... 0.0000e+000 0.00 0.000E+00
               this reaction will be treated as irreversible
     Declared duplicate reaction...
651. ISO13+O=C2H5CHO+C9H18-1                        3.34E+10    0.0    -1050.0
     Warning...all REV parameters are zero... 0.0000e+000 0.00 0.000E+00
               this reaction will be treated as irreversible
652. ISO13+OH=NC3H7CHO+C8H17-1                      5.08E+10    0.0    -4000.0
     Warning...all REV parameters are zero... 0.0000e+000 0.00 0.000E+00
               this reaction will be treated as irreversible
     Declared duplicate reaction...
653. ISO13+OH=NC5H11CHO+C6H13-1                     1.58E+10    0.0    -4000.0
     Warning...all REV parameters are zero... 0.0000e+000 0.00 0.000E+00
               this reaction will be treated as irreversible
654. C10H20-1+OH=CH2O+C9H19-1                       1.00E+11    0.0    -4000.0
     Warning...all REV parameters are zero... 0.0000e+000 0.00 0.000E+00
               this reaction will be treated as irreversible
655. C10H20-1+OH=CH3CHO+C8H17-1                     1.00E+11    0.0    -4000.0
     Warning...all REV parameters are zero... 0.0000e+000 0.00 0.000E+00
               this reaction will be treated as irreversible
656. C10H20-1+O=CH2CHO+C8H17-1                      1.00E+11    0.0    -1050.0
     Warning...all REV parameters are zero... 0.0000e+000 0.00 0.000E+00
               this reaction will be treated as irreversible
657. C9H18-1+OH=CH2O+C8H17-1                        1.00E+11    0.0    -4000.0
     Warning...all REV parameters are zero... 0.0000e+000 0.00 0.000E+00
               this reaction will be treated as irreversible
658. C9H18-1+OH=CH3CHO+C7H15-1                      1.00E+11    0.0    -4000.0
     Warning...all REV parameters are zero... 0.0000e+000 0.00 0.000E+00
               this reaction will be treated as irreversible
659. C9H18-1+O=CH2CHO+C7H15-1                       1.00E+11    0.0    -1050.0
     Warning...all REV parameters are zero... 0.0000e+000 0.00 0.000E+00
               this reaction will be treated as irreversible
660. C12H23=C2H3+C10H20-1                           2.50E+13    0.0    35000.0
     Reverse Arrhenius coefficients:               1.00E+11    0.0     9600.0
661. C12H23=C3H5-A+C9H18-1                          2.50E+13    0.0    25000.0
     Reverse Arrhenius coefficients:               1.00E+11    0.0     9600.0
662. C12H23=C9H17+C3H6                              2.50E+13    0.0    30000.0
     Reverse Arrhenius coefficients:               1.00E+11    0.0     9600.0
663. C9H17=C2H3+C7H14-1                             2.50E+13    0.0    35000.0
     Reverse Arrhenius coefficients:               1.00E+11    0.0     9600.0
664. C9H17=C3H5-A+C6H12-1                           2.50E+13    0.0    25000.0
     Reverse Arrhenius coefficients:               1.00E+11    0.0     9600.0
665. C12H24-1=C9H19-1+C3H5-A                        2.50E+16    0.0    71000.0
     Reverse Arrhenius coefficients:               1.00E+13    0.0        0.0
666. C10H20-1=C7H15-1+C3H5-A                        2.50E+16    0.0    71000.0
     Reverse Arrhenius coefficients:               1.00E+13    0.0        0.0
667. C9H18-1=C6H13-1+C3H5-A                         2.50E+16    0.0    71000.0
     Reverse Arrhenius coefficients:               1.00E+13    0.0        0.0
668. C9H18-1=C6H12-1+C3H6                           3.98E+12    0.0    57629.0
669. C10H20-1=C7H14-1+C3H6                          3.98E+12    0.0    57629.0
670. C12H24-1=C9H18-1+C3H6                          3.98E+12    0.0    57629.0
671. ISO13=C7H14-1+C5H10-1                          1.33E+12    0.0    57629.0
     Declared duplicate reaction...
672. ISO13=C6H12-1+C6H12-1                          2.02E+12    0.0    57629.0
673. ISO13=C2H4+C10H20-1                            2.02E+12    0.0    57629.0
674. ISO13=C5H10-1+C7H14-1                          6.27E+11    0.0    57629.0
     Declared duplicate reaction...
675. ISO13=C3H6+C9H18-1                             6.27E+11    0.0    57629.0
676. C12H25-2+O2=C12H25O2-2                         7.54E+12    0.0        0.0
677. C12H25-3+O2=ISO4                               1.97E+12    0.0        0.0
678. ISO8+O2=ISO4                                   5.57E+12    0.0        0.0
679. ISO8+O2=ISO3                                   4.44E+12    0.0        0.0
     Declared duplicate reaction...
680. ISO8+O2=ISO3                                   3.10E+12    0.0        0.0
     Declared duplicate reaction...
681. C8H17-1+O2=C8H17O2-1                           4.52E+12    0.0        0.0
682. C12H25O2-2=C12OOH2-4                           2.50E+10    0.0    20450.0
683. ISO4=ISO5                                      6.52E+09    0.0    20450.0
     Declared duplicate reaction...
684. ISO4=ISO5                                      1.85E+10    0.0    20450.0
     Declared duplicate reaction...
685. ISO4=ISO5                                      1.85E+10    0.0    20450.0
     Declared duplicate reaction...
686. ISO3=ISO6                                      1.47E+10    0.0    20450.0
     Declared duplicate reaction...
687. ISO3=ISO6                                      1.47E+10    0.0    20450.0
     Declared duplicate reaction...
688. ISO3=ISO7                                      1.84E+09    0.0    18650.0
     Declared duplicate reaction...
689. ISO3=ISO6                                      1.03E+10    0.0    20450.0
     Declared duplicate reaction...
```

```
690. ISO3=ISO6                                  1.03E+10    0.0    20450.0
     Declared duplicate reaction...
691. ISO3=ISO7                                  1.28E+09    0.0    18650.0
     Declared duplicate reaction...
692. C8H17O2-1=C8OOH1-3                         2.50E+10    0.0    20450.0
693. C12H25O2-2<=>C12H24-1+HO2                  5.92E+42   -9.4    41530.0
694. C12H25O2-2<=>C12H24-2+HO2                  4.31E+36   -7.5    39510.0
695. ISO4<=>C12H24-2+HO2                        1.12E+36   -7.5    39510.0
696. ISO4<=>ISO13+HO2                           1.12E+36   -7.5    39510.0
     Declared duplicate reaction...
697. ISO4<=>ISO13+HO2                           3.18E+36   -7.5    39510.0
     Declared duplicate reaction...
698. ISO4<=>ISO13+HO2                           3.18E+36   -7.5    39510.0
     Declared duplicate reaction...
699. ISO3<=>ISO13+HO2                           2.54E+36   -7.5    39510.0
     Declared duplicate reaction...
700. ISO3<=>ISO13+HO2                           2.54E+36   -7.5    39510.0
     Declared duplicate reaction...
701. ISO3<=>ISO13+HO2                           1.77E+36   -7.5    39510.0
     Declared duplicate reaction...
702. C12OOH2-4=C12O2-4+OH                       7.50E-40    0.0    15250.0
     Warning...all REV parameters are zero... 0.0000e+000 0.00 0.000E+00
               this reaction will be treated as irreversible
703. ISO5=C12O2-4+OH                            3.05E-40    0.0    15250.0
     Warning...all REV parameters are zero... 0.0000e+000 0.00 0.000E+00
               this reaction will be treated as irreversible
704. ISO5=ISO11+OH                              1.40E+10    0.0    15250.0
     Warning...all REV parameters are zero... 0.0000e+000 0.00 0.000E+00
               this reaction will be treated as irreversible
     Declared duplicate reaction...
705. ISO6=ISO11+OH                              2.17E+10    0.0    15250.0
     Warning...all REV parameters are zero... 0.0000e+000 0.00 0.000E+00
               this reaction will be treated as irreversible
     Declared duplicate reaction...
706. ISO5=ISO11+OH                              3.05E+10    0.0    15250.0
     Warning...all REV parameters are zero... 0.0000e+000 0.00 0.000E+00
               this reaction will be treated as irreversible
     Declared duplicate reaction...
707. ISO6=ISO11+OH                              1.58E+10    0.0    15250.0
     Warning...all REV parameters are zero... 0.0000e+000 0.00 0.000E+00
               this reaction will be treated as irreversible
     Declared duplicate reaction...
708. ISO6=ISO11+OH                              2.17E+10    0.0    15250.0
     Warning...all REV parameters are zero... 0.0000e+000 0.00 0.000E+00
               this reaction will be treated as irreversible
     Declared duplicate reaction...
709. ISO6=ISO11+OH                              1.58E+10    0.0    15250.0
     Warning...all REV parameters are zero... 0.0000e+000 0.00 0.000E+00
               this reaction will be treated as irreversible
     Declared duplicate reaction...
710. ISO7=ISO12+OH                              3.83E+09    0.0     7000.0
     Warning...all REV parameters are zero... 0.0000e+000 0.00 0.000E+00
               this reaction will be treated as irreversible
711. C12OOH2-4=OH+CH3CHO+C10H20-1               1.00E+13    0.0    30000.0
     Warning...all REV parameters are zero... 0.0000e+000 0.00 0.000E+00
               this reaction will be treated as irreversible
712. ISO5=OH+C2H5CHO+C9H18-1                    1.86E+12    0.0    30000.0
     Warning...all REV parameters are zero... 0.0000e+000 0.00 0.000E+00
               this reaction will be treated as irreversible
713. ISO5=OH+C3H6+NC8H17CHO                     4.07E+12    0.0    30000.0
     Warning...all REV parameters are zero... 0.0000e+000 0.00 0.000E+00
               this reaction will be treated as irreversible
714. ISO6=OH+C5H10-1+NC6H13CHO                  2.10E+12    0.0    30000.0
     Warning...all REV parameters are zero... 0.0000e+000 0.00 0.000E+00
               this reaction will be treated as irreversible
715. ISO6=OH+NC5H11CHO+C6H12-1                  2.10E+12    0.0    30000.0
     Warning...all REV parameters are zero... 0.0000e+000 0.00 0.000E+00
               this reaction will be treated as irreversible
716. C8OOH1-3=OH+CH2O+C7H14-1                   1.00E+13    0.0    30000.0
     Warning...all REV parameters are zero... 0.0000e+000 0.00 0.000E+00
               this reaction will be treated as irreversible
717. C12OOH2-4+O2=C12OOH2-4O2                   7.54E+12    0.0        0.0
718. ISO5+O2=ISO1                               1.40E+12    0.0        0.0
     Declared duplicate reaction...
719. ISO5+O2=ISO1                               3.07E+12    0.0        0.0
     Declared duplicate reaction...
720. ISO5+O2=ISO1                               3.07E+12    0.0        0.0
     Declared duplicate reaction...
721. ISO6+O2=ISO2                               2.22E+12    0.0        0.0
     Declared duplicate reaction...
722. ISO6+O2=ISO2                               2.22E+12    0.0        0.0
     Declared duplicate reaction...
723. ISO6+O2=ISO2                               1.54E+12    0.0        0.0
     Declared duplicate reaction...
724. ISO6+O2=ISO2                               1.55E+12    0.0        0.0
     Declared duplicate reaction...
725. C8OOH1-3+O2=C8OOH1-3O2                     7.54E+12    0.0        0.0
726. C12OOH2-4O2=C12KET2-4+OH                   1.25E+10    0.0    17450.0
727. ISO1=ISO9+OH                               2.32E+09    0.0    17450.0
     Declared duplicate reaction...
728. ISO1=ISO9+OH                               5.09E+09    0.0    17450.0
     Declared duplicate reaction...
729. ISO1=ISO9+OH                               5.09E+09    0.0    17450.0
     Declared duplicate reaction...
730. ISO2=ISO10+OH                              3.69E+09    0.0    17450.0
```

```
     Declared duplicate reaction...
731. ISO2=ISO10+OH                                3.69E+09    0.0    17450.0
     Declared duplicate reaction...
732. ISO2=ISO10+OH                                2.56E+09    0.0    17450.0
     Declared duplicate reaction...
733. ISO2=ISO10+OH                                2.57E+09    0.0    17450.0
     Declared duplicate reaction...
734. C8OOH1-3O2=C8KET1-3+OH                       2.50E+10    0.0    21000.0
735. C12KET2-4=OH+CH3COCH2+NC8H17CHO              1.00E+16    0.0    39000.0
     Warning...all REV parameters are zero... 0.0000e+000 0.00 0.000E+00
              this reaction will be treated as irreversible
736. ISO9=OH+CH3CHO+C8H17COCH2                    4.07E+15    0.0    39000.0
     Warning...all REV parameters are zero... 0.0000e+000 0.00 0.000E+00
              this reaction will be treated as irreversible
737. ISO9=OH+NC3H7COCH2+NC6H13CHO                 4.07E+15    0.0    39000.0
     Warning...all REV parameters are zero... 0.0000e+000 0.00 0.000E+00
              this reaction will be treated as irreversible
738. ISO10=OH+C2H5CHO+C7H15COCH2                  2.95E+15    0.0    39000.0
     Warning...all REV parameters are zero... 0.0000e+000 0.00 0.000E+00
              this reaction will be treated as irreversible
739. ISO10=OH+NC4H9COCH2+NC5H11CHO                2.96E+15    0.0    39000.0
     Warning...all REV parameters are zero... 0.0000e+000 0.00 0.000E+00
              this reaction will be treated as irreversible
740. C8KET1-3=OH+CH2CHO+NC5H11CHO                 1.00E+16    0.0    39000.0
     Warning...all REV parameters are zero... 0.0000e+000 0.00 0.000E+00
              this reaction will be treated as irreversible
741. C12O2-4+OH=CH3CO+C10H20-1+H2O                2.50E-38    0.0        0.0
     Warning...all REV parameters are zero... 0.0000e+000 0.00 0.00
              this reaction will be treated as irreversible
742. C12O2-4+OH=C3H6+NC8H17CO+H2O                 2.50E-38    0.0        0.0
     Warning...all REV parameters are zero... 0.0000e+000 0.00 0.00
              this reaction will be treated as irreversible
743. ISO11+OH=C5H10-1+NC6H13CO+H2O                7.81E+11    0.0        0.0
     Warning...all REV parameters are zero... 0.0000e+000 0.00 0.00
              this reaction will be treated as irreversible
744. ISO12+OH=NC3H7COCH2+C7H14-1+H2O              1.09E+12    0.0        0.0
     Warning...all REV parameters are zero... 0.0000e+000 0.00 0.00
              this reaction will be treated as irreversible
745. ISO11+OH=C6H12-1+NC5H11CO+H2O                7.99E+11    0.0        0.0
     Warning...all REV parameters are zero... 0.0000e+000 0.00 0.00
              this reaction will be treated as irreversible
746. C12O2-4+HO2=CH3CO+C10H20-1+H2O2              5.00E-38    0.0    17700.0
     Warning...all REV parameters are zero... 0.0000e+000 0.00 0.00
              this reaction will be treated as irreversible
747. C12O2-4+HO2=C3H6+NC8H17CO+H2O2               5.00E-38    0.0    17700.0
     Warning...all REV parameters are zero... 0.0000e+000 0.00 0.00
              this reaction will be treated as irreversible
748. ISO11+HO2=C5H10-1+NC6H13CO+H2O2              1.56E+12    0.0    17700.0
     Warning...all REV parameters are zero... 0.0000e+000 0.00 0.00
              this reaction will be treated as irreversible
749. ISO12+HO2=NC3H7COCH2+C7H14-1+H2O2            2.17E+12    0.0    17700.0
     Warning...all REV parameters are zero... 0.0000e+000 0.00 0.00
              this reaction will be treated as irreversible
750. ISO11+HO2=C6H12-1+NC5H11CO+H2O2              1.60E+12    0.0    17700.0
     Warning...all REV parameters are zero... 0.0000e+000 0.00 0.00
              this reaction will be treated as irreversible
751. C8H17COCH2=C8H17-1+CH2CO                      2.00E+13    0.0    31000.0
     Reverse Arrhenius coefficients:              2.00E+11    0.0     7350.0
752. C7H15COCH2=C7H15-1+CH2CO                      2.00E+13    0.0    31000.0
     Reverse Arrhenius coefficients:              2.00E+11    0.0     7350.0
753. NC8H17CHO+O2=NC8H17CO+HO2                     2.00E+13    0.5    42200.0
     Reverse Arrhenius coefficients:              1.00E+07    0.0    40000.0
754. NC8H17CHO+OH=NC8H17CO+H2O                     2.69E+10    0.8     -340.0
     Reverse Arrhenius coefficients:              1.74E+10    0.8    31200.0
755. NC8H17CHO+H=NC8H17CO+H2                       4.00E+13    0.0     4200.0
     Reverse Arrhenius coefficients:              1.80E+13    0.0    24000.0
756. NC8H17CHO+O=NC8H17CO+OH                       5.00E+12    0.0     1790.0
     Reverse Arrhenius coefficients:              1.00E+12    0.0    19000.0
757. NC8H17CHO+HO2=NC8H17CO+H2O2                   2.80E+12    0.0    13600.0
     Reverse Arrhenius coefficients:              1.00E+12    0.0    10000.0
758. NC8H17CHO+CH3=NC8H17CO+CH4                    1.70E+12    0.0     8440.0
     Reverse Arrhenius coefficients:              1.50E+13    0.0    28000.0
759. NC8H17CHO+CH3O=NC8H17CO+CH3OH                 1.15E+11    0.0     1280.0
     Reverse Arrhenius coefficients:              3.00E+11    0.0    18000.0
760. NC8H17CHO+CH3O2=NC8H17CO+CH3O2H               1.00E+12    0.0     9500.0
     Reverse Arrhenius coefficients:              2.50E+10    0.0    10000.0
761. NC8H17CO=C8H17-1+CO                           1.00E+11    0.0     9600.0
     Reverse Arrhenius coefficients:              1.00E+11    0.0        0.0
762. NC6H13CHO+O2=NC6H13CO+HO2                     2.00E+13    0.5    42200.0
     Reverse Arrhenius coefficients:              1.00E+07    0.0    40000.0
763. NC6H13CHO+OH=NC6H13CO+H2O                     2.69E+10    0.8     -340.0
     Reverse Arrhenius coefficients:              1.74E+10    0.8    31200.0
764. NC6H13CHO+H=NC6H13CO+H2                       4.00E+13    0.0     4200.0
     Reverse Arrhenius coefficients:              1.80E+13    0.0    24000.0
765. NC6H13CHO+O=NC6H13CO+OH                       5.00E+12    0.0     1790.0
     Reverse Arrhenius coefficients:              1.00E+12    0.0    19000.0
766. NC6H13CHO+HO2=NC6H13CO+H2O2                   2.80E+12    0.0    13600.0
     Reverse Arrhenius coefficients:              1.00E+12    0.0    10000.0
767. NC6H13CHO+CH3=NC6H13CO+CH4                    1.70E+12    0.0     8440.0
     Reverse Arrhenius coefficients:              1.50E+13    0.0    28000.0
768. NC6H13CHO+CH3O=NC6H13CO+CH3OH                 1.15E+11    0.0     1280.0
     Reverse Arrhenius coefficients:              3.00E+11    0.0    18000.0
769. NC6H13CHO+CH3O2=NC6H13CO+CH3O2H               1.00E+12    0.0     9500.0
     Reverse Arrhenius coefficients:              2.50E+10    0.0    10000.0
770. NC6H13CO=C6H13-1+CO                           1.00E+11    0.0     9600.0
```

	Reverse Arrhenius coefficients:	1.00E+11	0.0	0.0
771.	CY13PD=CY13PD5J+H	1.00E+15	0.0	78000.0
772.	CY13PD+O2=CY13PD5J+HO2	5.00E+12	0.0	37150.0
773.	CY13PD+O=C4H6+CO	1.02E+14	-0.3	4674.0
774.	CY13PD+H=H2+CY13PD5J	1.60E+06	2.4	4471.0
775.	CY13PD+O=CY13PD5J+OH	6.03E+10	0.7	7633.0
776.	CY13PD+OH=CY13PD5J+H2O	4.12E+06	2.0	-298.0
777.	CY13PD+HO2=CY13PD5J+H2O2	4.00E+12	0.0	15900.0
778.	CY13PD+HCO=CY13PD5J+CH2O	7.20E+06	1.9	17010.0
779.	CY13PD+CH3=CH4+CY13PD5J	1.80E-01	4.0	0.0
780.	CY13PD+C2H3=CY13PD5J+C2H4	1.20E-01	4.0	0.0
781.	CY13PD+C3H5-A=C3H6+CY13PD5J	6.00E+12	0.0	15000.0
782.	CY13PD+C3H3=CY13PD5J+C3H4-A	6.00E+12	0.0	12000.0
783.	CY13PD+C3H3=CY13PD5J+C3H4-P	6.00E+12	0.0	12000.0
784.	CY13PD+C2H3=C6H6+CH3	2.12E+67	-16.1	42640.0
785.	C3H3+CH3=C4H6	1.00E+14	0.0	0.0
786.	CY13PD5J+C2H3CHO=C2H3CO+CY13PD	1.00E+13	0.0	8843.0
787.	C3H5-A+OH=C3H4-A+H2O	6.03E+12	0.0	0.0
788.	C3H3+C3H3=C6H6	3.89E+50	-11.0	20320.0
789.	C6H5CH2J+C3H4-A=C6H5CH3+C3H3	2.00E+12	0.0	12000.0
790.	C6H5CH2J+CY13PD=CY13PD5J+C6H5CH3	7.90E+10	0.0	12400.0
791.	C6H5CH3=C6H5CH2J+H	2.09E+15	0.0	87463.4
792.	C6H4CH3+H=C6H5CH3	1.00E+14	0.0	0.0
793.	C6H5CH3+H=C6H6+CH3	7.00E+05	2.0	943.0
794.	C6H5CH3+O2=C6H5CH2J+HO2	2.18E+07	2.5	46045.0
795.	C6H5CH3+H=C6H5CH2J+H2	6.47E+00	4.0	3384.0
796.	C6H5CH3+O=C6H5CH2J+OH	6.00E+10	0.7	7632.0
797.	C6H5CH3+OH=C6H5CH2J+H2O	1.77E+05	2.4	-601.8
798.	C6H5CH3+HO2=C6H5CH2J+H2O2	7.00E+02	3.0	12000.0
799.	C6H5CH3+CH3O2=C6H5CH2J+CH3O2H	1.02E+04	2.5	12339.3
800.	C6H5CH3+CH3=C6H5CH2J+CH4	2.21E+00	3.5	5675.0
801.	C6H5CH3+CH3O=C6H5CH2J+CH3OH	2.12E+10	0.0	3000.0
802.	C6H5CH3+C2H3=C6H5CH2J+C2H4	2.21E+00	3.5	4680.0
803.	C6H5CH3+HCO=C6H5CH2J+CH2O	3.77E+13	0.0	23787.4
804.	C6H5CH3+C6H4CH3=C6H5CH2J+C6H5CH3	7.94E+12	0.0	11949.0
805.	C6H5CH2J=CY13PD5J+C2H2	1.00E+13	0.0	70000.0
806.	C6H5CH3+H=C6H4CH3+H2	1.90E+07	2.0	9696.0
807.	C6H5CH3+O=C6H4CH3+OH	2.00E+13	0.0	14700.0
808.	C6H5CH3+OH=C6H4CH3+H2O	2.34E+04	2.7	730.0
809.	C6H5CH3+CH3=C6H4CH3+CH4	1.70E+00	3.7	9500.0
810.	C6H5CH3+HO2=C6H4CH3+H2O2	9.20E+12	0.0	28810.0
811.	C6H4CH3+O2=>O2C6H4CH3	1.00E+13	0.0	0.0
812.	O2C6H4CH3=>C6H4CH3+O2	6.36E+19	-1.4	48700.0
813.	C6H4CH3+O2=RODC6J(C)DO	1.02E+25	-3.5	8780.0
814.	O2C6H4CH3=RODC6J(C)DO	6.64E+46	-10.2	44320.0
815.	C6H4CH3+H=C6H5CH2J+H	1.00E+13	0.0	0.0
816.	C6H4CH3+CH3=P-XYL	1.20E+06	2.0	-3700.0
817.	OCCXCCXCJC+CO=RODC6J(C)DO	1.51E+11	0.0	4810.0
818.	OCCXCCXCJC=>C2H2+HCO+C3H4-P	3.00E+13	0.0	43710.0
819.	OCCXCCXCJC+O2=OXCCXCCXO+CH3CO	5.42E+12	0.0	0.0
820.	PXYLCH2J+H=P-XYL	1.00E+14	0.0	0.0
821.	MEC6H3CH3+H=P-XYL	1.00E+14	0.0	0.0
822.	P-XYL+H=C6H5CH3+CH3	1.40E+06	2.0	943.0
823.	P-XYL+O2=PXYLCH2J+HO2	4.36E+07	2.5	46045.0
824.	P-XYL+H=PXYLCH2J+H2	1.29E+01	4.0	3384.0
825.	P-XYL+O=PXYLCH2J+OH	1.20E+11	0.7	7632.0
826.	P-XYL+OH=PXYLCH2J+H2O	3.54E+05	2.4	-601.8
827.	P-XYL+HO2=PXYLCH2J+H2O2	1.40E+03	3.0	12000.0
828.	P-XYL+CH3O2=PXYLCH2J+CH3O2H	2.04E+04	2.5	12339.3
829.	P-XYL+CH3=PXYLCH2J+CH4	4.42E+00	3.5	5680.0
830.	P-XYL+CH3O=PXYLCH2J+CH3OH	4.24E+10	0.0	3000.0
831.	P-XYL+C2H3=PXYLCH2J+C2H4	4.42E+00	3.5	4680.0
832.	P-XYL+HCO=PXYLCH2J+CH2O	7.54E+13	0.0	23787.4
833.	P-XYL+C6H4CH3=PXYLCH2J+C6H5CH3	1.59E+13	0.0	11949.0
834.	PXYLCH2J=C6H6+C2H2+H	1.00E+13	0.0	70000.0
835.	PXYLCH2J+O2=PXYLCH2OOJ	1.38E+41	-9.4	9020.0
836.	PXYLCH2OOJ=MEC6H4CHO+OH	4.00E+76	-20.0	64725.0
837.	PXYLCH2OOJ+HO2=>MEC6H4CH2OJ+OH+O2	6.30E+10	0.0	-720.0
838.	PXYLCH2OOJ+CH3O2=>MEC6H4CH2OJ+CH3O+O2	6.30E+10	0.0	-720.0
839.	2PXYLCH2OOJ=>2MEC6H4CH2OJ+O2	6.30E+10	0.0	-720.0
840.	PXYLCH2J+O=MEC6H4CH2OJ	2.00E+13	0.0	0.0
841.	PXYLCH2J+O=MEC6H4CHO+H	1.51E+13	0.0	0.0
842.	PXYLCH2J+O=C6H4CH3+CH2O	1.19E+14	0.0	0.0
843.	PXYLCH2J+HO2=MEC6H4CH2OJ+OH	5.00E+12	0.0	0.0
844.	PXYLCH2J+CH3O2=MEC6H4CH2OJ+CH3O	5.00E+12	0.0	0.0
845.	MEC6H4CH2OJ+O2=HO2+MEC6H4CHO	6.60E+10	0.0	2200.0
846.	MEC6H4CH2OJ=MEC6H4CHO+H	1.00E+14	0.0	29100.0
847.	MEC6H4CH2OJ=C6H4CH3+CH2O	1.46E+20	-2.0	35090.0
848.	MEC6H4CH2OJ+H=MEC6H4CHO+H2	4.00E+13	0.0	0.0
849.	MEC6H4CH2OJ+OH=MEC6H4CHO+H2O	2.00E+13	0.0	0.0
850.	MEC6H4CH2OJ+HO2=MEC6H4CHO+H2O2	2.00E+13	0.0	0.0
851.	MEC6H4CH2OJ+CH3=MEC6H4CHO+CH4	2.00E+13	0.0	0.0
852.	MEC6H4CH2OJ+PXYLCH2J=MEC6H4CHO+P-XYL	1.00E+13	0.0	0.0
853.	C6H4CH3+HCO=MEC6H4CHO	5.00E+12	0.0	0.0
854.	MEC6H4CHO+OH=H2O+MEC6H4CJO	3.44E+09	1.2	-447.0
855.	MEC6H4CHO+H=H2+MEC6H4CJO	7.47E+00	4.0	1384.0
856.	MEC6H4CHO=MEC6H4CJO+H	4.00E+15	0.0	83700.0
857.	MEC6H4CHO+O=MEC6H4CJO+OH	6.00E+12	0.0	1800.0
858.	MEC6H4CHO+O2=MEC6H4CJO+HO2	7.00E+11	0.0	39500.0
859.	MEC6H4CHO+HO2=MEC6H4CJO+H2O2	7.00E+02	3.0	10000.0
860.	MEC6H4CHO+CH3=MEC6H4CJO+CH4	2.00E-06	5.6	1500.0
861.	MEC6H4CHO+PXYLCH2J=MEC6H4CJO+P-XYL	1.60E+12	0.0	13100.0
862.	MEC6H4CJO=C6H4CH3+CO	1.37E+21	-2.2	39410.0
863.	MEC6H4CJO+HO2=C6H4CH3+CO2+OH	1.00E+13	0.0	0.0
864.	P-XYL+H=MEC6H3CH3+H2	1.90E+07	2.0	9696.0

```
865. P-XYL+O=MEC6H3CH3+OH                          2.00E+13    0.0    14700.0
866. P-XYL+OH=MEC6H3CH3+H2O                        2.34E+04    2.7      730.0
867. P-XYL+CH3=MEC6H3CH3+CH4                       1.70E+00    3.7     9500.0
868. P-XYL+HO2=MEC6H3CH3+H2O2                      9.20E+12    0.0    28810.0
869. MEC6H3CH3+O2=>O2MEC6H3CH3                     1.00E+13    0.0        0.0
870. O2MEC6H3CH3=>MEC6H3CH3+O2                     6.36E+19   -1.4    48700.0
871. MEC6H3CH3+O2=OMEC6H3CH3+O                     7.27E+29   -4.7    15600.0
872. O2MEC6H3CH3=>OMEC6H3CH3+O                     1.64E+43   -8.8    50880.0
873. OMEC6H3CH3+O=>O2MEC6H3CH3                     2.00E+14    0.0        0.0
874. OMEC6H3CH3=H+C6H5CH3+CO                       7.60E+11    0.0    43800.0
875. MEC6H3CH3+H=PXYLCH2J+H                        1.00E+13    0.0        0.0
876. MEC6H3CH3+O=OMEC6H3CH3                        1.00E+14    0.0        0.0
877. MEC6H3CH3+OH=HOMEC6H3CH3                      3.00E+13    0.0        0.0
878. MEC6H3CH3+HO2=OMEC6H3CH3+OH                   5.00E+12    0.0        0.0
879. OMEC6H3CH3+H=HOMEC6H3CH3                      2.50E+14    0.0        0.0
880. HOMEC6H3CH3+O2=OMEC6H3CH3+HO2                 1.00E+13    0.0    38900.0
881. HOMEC6H3CH3+H=OMEC6H3CH3+H2                   1.20E+14    0.0    12400.0
882. HOMEC6H3CH3+O=OMEC6H3CH3+OH                   1.30E+13    0.0     2900.0
883. HOMEC6H3CH3+OH=OMEC6H3CH3+H2O                 1.40E+08    1.4     -960.0
884. HOMEC6H3CH3+HO2=OMEC6H3CH3+H2O2               1.00E+12    0.0    10000.0
885. HOMEC6H3CH3+CH3=OMEC6H3CH3+CH4                1.80E+11    0.0     7700.0
886. HOMEC6H3CH3+CY13PD5J=OMEC6H3CH3+CY13PD        4.90E+11    0.0     9400.0
887. P-XYL+O=OMEC6H3CH3+H                          2.48E+14   -0.3     4674.0
888. CH3CHO+CH3CO3=CH3CO+CH3CO3H                   3.01E+12    0.0    11920.0
     Reverse Arrhenius coefficients:               1.92E+12    0.0    12650.0
889. CH3CO3=CH3CO+O2                               6.86E+19   -1.9    38530.0
     Reverse Arrhenius coefficients:               1.20E+11    0.0    -1100.0
890. CH3CO3+HO2=CH3CO3H+O2                         1.75E+10    0.0    -3275.0
     Reverse Arrhenius coefficients:               3.08E+12   -0.3    38180.0
891. H2O2+CH3CO3=HO2+CH3CO3H                       2.41E+12    0.0     9936.0
     Reverse Arrhenius coefficients:               3.84E+12    0.1    12710.0
892. CH4+CH3CO3=CH3+CH3CO3H                        1.81E+11    0.0    18480.0
     Reverse Arrhenius coefficients:               1.83E+11   -0.2     3711.0
893. CH2O+CH3CO3=HCO+CH3CO3H                       1.99E+12    0.0    11660.0
     Reverse Arrhenius coefficients:               1.08E+13   -0.4    13620.0
894. C2H6+CH3CO3=C2H5+CH3CO3H                      1.70E+13    0.0    20460.0
     Reverse Arrhenius coefficients:               1.45E+12    0.0     9460.0
895. C3KET21=CH2O+CH3CO+OH                         1.00E+16    0.0    43000.0
     Warning...all REV parameters are zero...          0.00000E+00 0.00000E+00 0.00000E+00
               this reaction will be treated as irreversible
896. CH2CH2COCH3=C2H4+CH3CO                        1.00E+14    0.0    18000.0
     Reverse Arrhenius coefficients:               1.00E+11    0.0        0.0
897. C2H3COCH3+OH=CH3CHO+CH3CO                     1.00E+11    0.0        0.0
     Warning...all REV parameters are zero...          0.00000E+00 0.00000E+00 0.00000E+00
               this reaction will be treated as irreversible
898. C2H3COCH3+HO2=CH2CHO+CH3CO+OH                 6.03E+09    0.0     7949.0
     Warning...all REV parameters are zero...          0.00000E+00 0.00000E+00 0.00000E+00
               this reaction will be treated as irreversible
899. C2H3COCH3+CH3O2=CH2CHO+CH3CO+CH3O             3.97E+11    0.0    17050.0
     Warning...all REV parameters are zero...          0.00000E+00 0.00000E+00 0.00000E+00
               this reaction will be treated as irreversible
900. C2H4+CH3CO3=C2H3+CH3CO3H                      1.13E+13    0.0    30430.0
     Reverse Arrhenius coefficients:               3.30E+12   -0.1     9440.0
901. C2H5CHO+CH3CO3=C2H5CO+CH3CO3H                 3.01E+12    0.0    11920.0
     Reverse Arrhenius coefficients:               1.65E+12    0.0    12630.0
902. C3H8+CH3CO3=IC3H7+CH3CO3H                     2.00E+12    0.0    17000.0
     Reverse Arrhenius coefficients:               3.10E+10    0.3     8650.0
903. C3H8+CH3CO3=NC3H7+CH3CO3H                     1.70E+13    0.0    20460.0
     Reverse Arrhenius coefficients:               1.67E+12    0.0     9570.0
904. NC3H7O2+CH3CHO<=>NC3H7O2H+CH3CO               2.80E+12    0.0    13600.0
     Reverse Arrhenius coefficients:               1.00E+12    0.0    10000.0
905. CH3CO3H=CH3CO2+OH                             5.01E+14    0.0    40150.0
     Reverse Arrhenius coefficients:               3.62E+07    1.8     1338.0
906. CH3CO2+M=CH3+CO2+M                            4.40E+15    0.0    10500.0
     Reverse Arrhenius coefficients:               4.55E+08    1.4    17520.0
907. IC3H7O2+CH3CO3=IC3H7O+CH3CO2+O2               1.40E+16   -1.6     1860.0
     Warning...all REV parameters are zero...          0.00000E+00 0.00000E+00 0.00000E+00
               this reaction will be treated as irreversible
908. PC4H9O2+CH3CO3=PC4H9O+CH3CO2+O2               1.40E+16   -1.6     1860.0
     Warning...all REV parameters are zero...          0.00000E+00 0.00000E+00 0.00000E+00
               this reaction will be treated as irreversible
909. NC3H7O2+CH3CO3=NC3H7O+CH3CO2+O2               1.40E+16   -1.6     1860.0
     Warning...all REV parameters are zero...          0.00000E+00 0.00000E+00 0.00000E+00
               this reaction will be treated as irreversible
910. IC3H7O2<=>C3H6OOH2-1                          1.80E+12    0.0    29400.0
     Reverse Arrhenius coefficients:               1.12E+10    0.1    11810.0
911. C3H6OOH2-1<=>C3H6+HO2                         3.24E+18   -2.0    18970.0
     Reverse Arrhenius coefficients:               1.00E+11    0.0    11750.0
912. C3H6OOH2-1O2<=>C3H6OOH2-1+O2                  5.23E+22   -2.2    37820.0
     Reverse Arrhenius coefficients:               4.52E+12    0.0        0.0
913. C3H6OOH1-2O2=C3H6OOH1-2+O2                    2.39E+25   -2.9    40100.0
     Reverse Arrhenius coefficients:               5.00E+12    0.0        0.0
914. C3H6OOH1-2O2=C3KET12+OH                       6.00E+11    0.0    26400.0
     Reverse Arrhenius coefficients:               9.25E+04    1.3    48920.0
915. C3H6OOH2-1O2=C3KET21+OH                       3.00E+11    0.0    23850.0
     Reverse Arrhenius coefficients:               1.40E+03    1.8    49750.0
916. NC3H7O2+CH3O2=NC3H7O+CH3O+O2                  1.40E+16   -1.6     1860.0
     Warning...all REV parameters are zero...          0.00000E+00 0.00000E+00 0.00000E+00
               this reaction will be treated as irreversible
917. NC3H7O2+C2H5O2=NC3H7O+C2H5O+O2                1.40E+16   -1.6     1860.0
     Warning...all REV parameters are zero...          0.00000E+00 0.00000E+00 0.00000E+00
               this reaction will be treated as irreversible
918. NC3H7O2+NC3H7O2=O2+NC3H7O+NC3H7O              1.40E+16   -1.6     1860.0
     Warning...all REV parameters are zero...          0.00000E+00 0.00000E+00 0.00000E+00
               this reaction will be treated as irreversible
```

```
919. IC3H7O2+NC3H7O2=IC3H7O+NC3H7O+O2              1.40E+16   -1.6     1860.0
     Warning...all REV parameters are zero...          0.00000E+00 0.00000E+00 0.00000E+00
               this reaction will be treated as irreversible
920. NC3H7O2+CH3=NC3H7O+CH3O                       7.00E+12    0.0    -1000.0
     Reverse Arrhenius coefficients:              5.30E+12    0.0    26920.0
921. NC3H7O2+C2H5=NC3H7O+C2H5O                     7.00E+12    0.0    -1000.0
     Reverse Arrhenius coefficients:              7.54E+14   -0.6    29330.0
922. NC3H7O2+IC3H7=NC3H7O+IC3H7O                   7.00E+12    0.0    -1000.0
     Reverse Arrhenius coefficients:              1.29E+15   -0.4    30000.0
923. NC3H7O2+NC3H7=NC3H7O+NC3H7O                   7.00E+12    0.0    -1000.0
     Reverse Arrhenius coefficients:              7.61E+14   -0.6    28000.0
924. NC3H7O2+C3H5-A=NC3H7O+C3H5O                   7.00E+12    0.0    -1000.0
     Reverse Arrhenius coefficients:              1.96E+11    0.2    14340.0
925. NC3H7O2=C3H6OOH1-3                            1.12E+11    0.0    24400.0
     Reverse Arrhenius coefficients:              2.72E+11   -0.5     8936.0
926. NC3H7O2+C4H71-3=NC3H7O+C4H7O                  3.80E+12    0.0    -1200.0
     Reverse Arrhenius coefficients:              2.00E+10    0.0        0.0
927. NC3H7O2+PC4H9=NC3H7O+PC4H9O                   7.00E+12    0.0    -1000.0
     Reverse Arrhenius coefficients:              1.06E+15   -0.6    27680.0
928. PC4H9O2+NC3H7O2=PC4H9O+NC3H7O+O2              1.40E+16   -1.6     1860.0
     Warning...all REV parameters are zero...          0.00000E+00 0.00000E+00 0.00000E+00
               this reaction will be treated as irreversible
929. NC3H7O2+C3H8<=>NC3H7O2H+NC3H7                 1.70E+13    0.0    20460.0
     Reverse Arrhenius coefficients:              2.09E+13   -0.5     5000.0
930. C3H6+NC3H7O2<=>C3H5-A+NC3H7O2H                3.24E+11    0.0    14900.0
     Reverse Arrhenius coefficients:              2.00E+10    0.0    15000.0
931. NC3H7O2+CH2O<=>NC3H7O2H+HCO                   5.60E+12    0.0    13600.0
     Reverse Arrhenius coefficients:              8.00E+11    0.0    10000.0
932. NC3H7O2+HO2<=>NC3H7O2H+O2                     1.75E+10    0.0    -3275.0
     Reverse Arrhenius coefficients:              3.84E+13   -0.8    33610.0
933. C2H4+NC3H7O2<=>C2H3+NC3H7O2H                  1.13E+13    0.0    30430.0
     Reverse Arrhenius coefficients:              3.00E+12    0.0    11500.0
934. CH3OH+NC3H7O2<=>CH2OH+NC3H7O2H                6.30E+12    0.0    19360.0
     Reverse Arrhenius coefficients:              1.00E+09    0.0    10000.0
935. C2H3CHO+NC3H7O2<=>C2H3CO+NC3H7O2H             2.80E+12    0.0    13600.0
     Reverse Arrhenius coefficients:              1.00E+12    0.0    10000.0
936. CH4+NC3H7O2<=>CH3+NC3H7O2H                    1.12E+13    0.0    24640.0
     Reverse Arrhenius coefficients:              7.43E+11    0.0     5500.0
937. H2+NC3H7O2<=>H+NC3H7O2H                       3.01E+13    0.0    26030.0
     Reverse Arrhenius coefficients:              4.80E+13    0.0     7950.0
938. NC3H7O2+C2H6<=>NC3H7O2H+C2H5                  1.70E+13    0.0    20460.0
     Reverse Arrhenius coefficients:              5.00E+11    0.0     6500.0
939. NC3H7O2+C2H5CHO<=>NC3H7O2H+C2H5CO             2.00E+11    0.0     9500.0
     Reverse Arrhenius coefficients:              5.00E+09    0.0    10000.0
940. C4H8-1+NC3H7O2<=>C4H71-3+NC3H7O2H             1.40E+12    0.0    14900.0
     Reverse Arrhenius coefficients:              3.16E+11    0.0    13000.0
941. IC3H7+HO2=IC3H7O+OH                           7.00E+12    0.0    -1000.0
     Reverse Arrhenius coefficients:              1.05E+16   -0.6    27320.0
942. CH3O2+IC3H7=CH3O+IC3H7O                       7.00E+12    0.0    -1000.0
     Reverse Arrhenius coefficients:              6.57E+14   -0.3    31560.0
943. IC3H7O2+CH3O2=IC3H7O+CH3O+O2                  1.40E+16   -1.6     1860.0
     Warning...all REV parameters are zero...          0.00000E+00 0.00000E+00 0.00000E+00
               this reaction will be treated as irreversible
944. IC3H7O2+C2H5O2=IC3H7O+C2H5O+O2                1.40E+16   -1.6     1860.0
     Warning...all REV parameters are zero...          0.00000E+00 0.00000E+00 0.00000E+00
               this reaction will be treated as irreversible
945. IC3H7O2+IC3H7O2=O2+IC3H7O+IC3H7O              1.40E+16   -1.6     1860.0
     Warning...all REV parameters are zero...          0.00000E+00 0.00000E+00 0.00000E+00
               this reaction will be treated as irreversible
946. IC3H7O2+CH3=IC3H7O+CH3O                       7.00E+12    0.0    -1000.0
     Reverse Arrhenius coefficients:              1.14E+11    0.7    26720.0
947. IC3H7O2+C2H5=IC3H7O+C2H5O                     7.00E+12    0.0    -1000.0
     Reverse Arrhenius coefficients:              1.63E+13    0.1    29130.0
948. IC3H7O2+IC3H7=IC3H7O+IC3H7O                   7.00E+12    0.0    -1000.0
     Reverse Arrhenius coefficients:              2.78E+13    0.3    29800.0
949. IC3H7O2+NC3H7=IC3H7O+NC3H7O                   7.00E+12    0.0    -1000.0
     Reverse Arrhenius coefficients:              1.64E+13    0.1    27800.0
950. IC3H7O2+C3H5-A=IC3H7O+C3H5O                   7.00E+12    0.0    -1000.0
     Reverse Arrhenius coefficients:              4.24E+09    0.9    14140.0
951. IC3H7O=CH3+CH3CHO                             5.33E+19   -1.7    17140.0
     Reverse Arrhenius coefficients:              1.00E+11    0.0     9256.0
952. IC3H7O2+C4H71-3=IC3H7O+C4H7O                  3.80E+12    0.0    -1200.0
     Reverse Arrhenius coefficients:              2.00E+10    0.0        0.0
953. IC3H7O2+PC4H9=IC3H7O+PC4H9O                   7.00E+12    0.0    -1000.0
     Reverse Arrhenius coefficients:              2.28E+13    0.1    27480.0
954. PC4H9O2+HO2=PC4H9O+OH+O2                      1.40E-14   -1.6     1860.0
     Warning...all REV parameters are zero...          0.00000E+00 0.00000E+00 0.00000E+00
               this reaction will be treated as irreversible
955. C4H71-3+PC4H9O2=C4H7O+PC4H9O                  7.00E+12    0.0    -1000.0
     Reverse Arrhenius coefficients:              1.19E+14   -0.8    16100.0
956. PC4H9O2+PC4H9O2=O2+PC4H9O+PC4H9O              1.40E+16   -1.6     1860.0
     Warning...all REV parameters are zero...          0.00000E+00 0.00000E+00 0.00000E+00
               this reaction will be treated as irreversible
957. PC4H9O2+IC3H7O2=PC4H9O+IC3H7O+O2              1.40E+16   -1.6     1860.0
     Warning...all REV parameters are zero...          0.00000E+00 0.00000E+00 0.00000E+00
               this reaction will be treated as irreversible
958. PC4H9O2+C2H5O2=PC4H9O+C2H5O+O2                1.40E+16   -1.6     1860.0
     Warning...all REV parameters are zero...          0.00000E+00 0.00000E+00 0.00000E+00
               this reaction will be treated as irreversible
959. PC4H9O2+CH3O2=PC4H9O+CH3O+O2                  1.40E+16   -1.6     1860.0
     Warning...all REV parameters are zero...          0.00000E+00 0.00000E+00 0.00000E+00
               this reaction will be treated as irreversible
960. PC4H9O2+CH3=PC4H9O+CH3O                       7.00E+12    0.0    -1000.0
     Reverse Arrhenius coefficients:              6.20E+12    0.0    26630.0
961. PC4H9O2+C2H5=PC4H9O+C2H5O                     7.00E+12    0.0    -1000.0
```

```
     Reverse Arrhenius coefficients:              8.81E+14   -0.6    29040.0
 962. PC4H9O2+IC3H7=PC4H9O+IC3H7O                  7.00E+12    0.0    -1000.0
     Reverse Arrhenius coefficients:              1.50E+15   -0.5    29710.0
 963. PC4H9O2+NC3H7=PC4H9O+NC3H7O                  7.00E+12    0.0    -1000.0
     Reverse Arrhenius coefficients:              8.90E+14   -0.6    27710.0
 964. PC4H9O2+PC4H9=PC4H9O+PC4H9O                  7.00E+12    0.0    -1000.0
     Reverse Arrhenius coefficients:              1.24E+15   -0.6    27390.0
 965. PC4H9O2+C3H5-A=PC4H9O+C3H5O                  7.00E+12    0.0    -1000.0
     Reverse Arrhenius coefficients:              2.30E+11    0.2    14050.0
 966. PC4H9+HO2=PC4H9O+OH                          7.00E+12    0.0    -1000.0
     Reverse Arrhenius coefficients:              8.63E+15   -0.7    25000.0
 967. CH3O2+PC4H9=CH3O+PC4H9O                      7.00E+12    0.0    -1000.0
     Reverse Arrhenius coefficients:              5.40E+14   -0.4    29240.0
 968. PC4H9O=NC3H7+CH2O                            1.56E+21   -2.4    15230.0
     Reverse Arrhenius coefficients:              5.00E+10    0.0     3457.0
 969. PC4H9O2=C4H8OOH1-3                           2.50E+10    0.0    20850.0
     Reverse Arrhenius coefficients:              3.23E+09   -0.1     7871.0
 970. C3KET12=CH3CHO+HCO+OH                        9.45E+15    0.0    43000.0
     Warning...all REV parameters are zero...          0.00000E+00 0.00000E+00 0.00000E+00
               this reaction will be treated as irreversible
 971. C3H6OOH1-3O2=C3KET13+OH                      7.50E+10    0.0    21400.0
     Reverse Arrhenius coefficients:              4.10E+03    1.5    44740.0
 972. C3KET13=CH2O+CH2CHO+OH                       1.00E+16    0.0    43000.0
     Warning...all REV parameters are zero...          0.00000E+00 0.00000E+00 0.00000E+00
               this reaction will be treated as irreversible
 973. C2H3COCH3+OH=CH2CO+C2H3+H2O                  5.10E+11    0.0     1192.0
     Warning...all REV parameters are zero...          0.00000E+00 0.00000E+00 0.00000E+00
               this reaction will be treated as irreversible
 974. C2H3COCH3+HO2=CH2CO+C2H3+H2O2                8.50E+12    0.0    20460.0
     Warning...all REV parameters are zero...          0.00000E+00 0.00000E+00 0.00000E+00
               this reaction will be treated as irreversible
 975. C2H3COCH3+CH3O2=CH2CO+C2H3+CH3O2H            3.01E+12    0.0    17580.0
     Warning...all REV parameters are zero...          0.00000E+00 0.00000E+00 0.00000E+00
               this reaction will be treated as irreversible
 976. C3H6OOH1-3=OH+CH2O+C2H4                      3.04E+15   -0.8    27400.0
     Warning...all REV parameters are zero...          0.00000E+00 0.00000E+00 0.00000E+00
               this reaction will be treated as irreversible
 977. C3H6OOH1-3O2=C3H6OOH1-3+O2                   2.85E+20   -1.6    35690.0
     Reverse Arrhenius coefficients:              4.52E+12    0.0        0.0
 978. C4H8OOH1-3=OH+CH2O+C3H6                      6.64E+13   -0.2    29900.0
     Warning...all REV parameters are zero...          0.00000E+00 0.00000E+00 0.00000E+00
               this reaction will be treated as irreversible
 979. C4H8OOH1-3O2=C4H8OOH1-3+O2                   5.60E+22   -2.2    37960.0
     Reverse Arrhenius coefficients:              7.54E+12    0.0        0.0
 980. NC3H7+HO2=NC3H7O+OH                          7.00E+12    0.0    -1000.0
     Reverse Arrhenius coefficients:              6.22E+15   -0.7    25310.0
 981. CH3O2+NC3H7=CH3O+NC3H7O                      7.00E+12    0.0    -1000.0
     Reverse Arrhenius coefficients:              3.89E+14   -0.4    29550.0
 982. NC3H7O=C2H5+CH2O                             2.72E+21   -2.4    15700.0
     Reverse Arrhenius coefficients:              1.00E+11    0.0     3496.0
 983. NC3H7O=C2H5CHO+H                             8.90E+10    0.7    19800.0
     Reverse Arrhenius coefficients:              4.00E+12    0.0     6260.0
 984. C3H6+CH3CO3=C3H5-A+CH3CO3H                   3.24E+11    0.0    14900.0
     Reverse Arrhenius coefficients:              2.00E+10    0.0    15000.0
 985. C4H8-1+CH3CO3=C4H71-3+CH3CO3H                1.00E+11    0.0     8000.0
     Reverse Arrhenius coefficients:              2.00E+10    0.0    10000.0
 986. C4H8OOH1-3O2=NC4KET13+OH                     2.50E+10    0.0    21400.0
     Reverse Arrhenius coefficients:              1.44E+03    1.5    44740.0
 987. NC4KET13=CH3CHO+CH2CHO+OH                    1.05E+16    0.0    41600.0
     Warning...all REV parameters are zero...          0.00000E+00 0.00000E+00 0.00000E+00
               this reaction will be treated as irreversible
 988. C2H5CHO+H=C2H5CO+H2                          4.00E+13    0.0     4200.0
     Reverse Arrhenius coefficients:              2.38E+10    0.7    18130.0
 989. C2H5CHO+O=C2H5CO+OH                          5.00E+12    0.0     1790.0
     Reverse Arrhenius coefficients:              1.54E+09    0.6    14310.0
 990. C2H5CHO+OH=C2H5CO+H2O                        2.69E+10    0.8     -340.0
     Reverse Arrhenius coefficients:              1.70E+08    1.3    28480.0
 991. C2H5CHO+CH3=C2H5CO+CH4                       2.61E+06    1.8     5911.0
     Reverse Arrhenius coefficients:              1.41E+06    2.0    21380.0
 992. C2H5CHO+HO2=C2H5CO+H2O2                      2.80E+12    0.0    13600.0
     Reverse Arrhenius coefficients:              9.63E+11    0.0    11530.0
 993. C2H5CHO+CH3O=C2H5CO+CH3OH                    1.00E+12    0.0     3300.0
     Reverse Arrhenius coefficients:              1.28E+10    0.4    17460.0
 994. C2H5CHO+CH3O2=C2H5CO+CH3O2H                  3.01E+12    0.0    11920.0
     Reverse Arrhenius coefficients:              2.01E+13   -0.5     8260.0
 995. C2H5CHO+C2H5=C2H5CO+C2H6                     1.00E+12    0.0     8000.0
     Reverse Arrhenius coefficients:              6.43E+12    0.0    19700.0
 996. C2H5CHO+C2H5O2=C2H5CO+C2H5O2H                3.01E+12    0.0    11920.0
     Reverse Arrhenius coefficients:              2.02E+13   -0.5     8264.0
 997. C2H5CHO+O2=C2H5CO+HO2                        1.00E+13    0.0    40700.0
     Reverse Arrhenius coefficients:              3.13E+10    0.3      -58.0
 998. C2H5CHO+C2H3=C2H5CO+C2H4                     1.70E+12    0.0     8440.0
     Reverse Arrhenius coefficients:              3.20E+12    0.1    30130.0
 999. C2H5CO=C2H5+CO                               2.46E+23   -3.2    17550.0
     Reverse Arrhenius coefficients:              1.51E+11    0.0     4810.0
1000. C2H5CHO+NC3H7=C2H5CO+C3H8                    1.70E+12    0.0     8440.0
     Reverse Arrhenius coefficients:              1.90E+14    0.0    18790.0
1001. C2H5CHO+IC3H7=C2H5CO+C3H8                    1.70E+12    0.0     8440.0
     Reverse Arrhenius coefficients:              1.90E+14    0.0    18790.0
1002. C2H5CHO+C3H5-A=C2H5CO+C3H6                   1.70E+12    0.0     8440.0
     Reverse Arrhenius coefficients:              1.00E+13    0.0    28000.0
1003. H2+C2H5O2=H+C2H5O2H                          1.50E+14    0.0    26030.0
     Reverse Arrhenius coefficients:              1.69E+18   -1.1     8438.0
1004. C2H5O2+CH2O=C2H5O2H+HCO                      1.99E+12    0.0    11660.0
     Reverse Arrhenius coefficients:              1.32E+14   -0.9     9263.0
```

1005.	CH4+C2H5O2=CH3+C2H5O2H	1.81E+11	0.0	18480.0
	Reverse Arrhenius coefficients:	2.24E+12	-0.7	-651.0
1006.	CH3OH+C2H5O2=CH2OH+C2H5O2H	1.81E+12	0.0	13710.0
	Reverse Arrhenius coefficients:	2.35E+14	-1.0	2408.0
1007.	C2H5O2+HO2=C2H5O2H+O2	1.75E+10	0.0	-3275.0
	Reverse Arrhenius coefficients:	3.76E+13	-0.8	33820.0
1008.	C2H6+C2H5O2=C2H5+C2H5O2H	8.60E+00	3.8	17200.0
	Reverse Arrhenius coefficients:	8.96E+00	3.3	1838.0
1009.	C2H5O2H=C2H5O+OH	6.31E+14	0.0	42300.0
	Reverse Arrhenius coefficients:	5.66E+08	1.0	-1705.0
1010.	C2H4+C2H5O2=C2H3+C2H5O2H	2.23E+12	0.0	17190.0
	Reverse Arrhenius coefficients:	7.94E+12	-0.6	-8163.0
1011.	C2H5O2+C3H8=C2H5O2H+NC3H7	1.39E+00	4.0	18280.0
	Reverse Arrhenius coefficients:	1.67E+00	3.5	3028.0
1012.	C2H5O2+C3H8=C2H5O2H+IC3H7	1.02E+01	3.6	14810.0
	Reverse Arrhenius coefficients:	1.93E+00	3.4	2094.0
1013.	C3H6+C2H5O2=C3H5-A+C2H5O2H	3.24E+11	0.0	14900.0
	Reverse Arrhenius coefficients:	2.00E+10	0.0	15000.0
1014.	C4H8-1+C2H5O2=C4H71-3+C2H5O2H	1.40E+12	0.0	14900.0
	Reverse Arrhenius coefficients:	3.16E+11	0.0	13000.0

LIST OF ACRONYMS

AHRR

Apparent heat release rate

AMR

Adaptive mesh refinement

ASOC

After start of combustion

ATDC

After top dead center

BMEP

Brake mean effective pressure

BSFC

Brake specific fuel consumption

BTDC

Before top dead center

CA50

Crank Angle 50%

CCM

Cluster compatibility mode

CFD

Computational fluid dynamics

CFL

Courant-Friedrichs-Lewy

CI

Compression ignition

COV

Coefficient of variation

DI

Direct injection

DOHC

Direct over-head cam

ECU

Electronic controller unit

ECM

Electronic controller module

ECN

Engine combustion network

EGR

Exhaust gas recirculation

EIA

Energy Information Administration

EPA

Environmental protection agency

FID

Flame ionization detector

GHG

Green-house gases

GM

General Motors

HCCI

Homogeneous charge compression ignition

HPMPI

Hewlett Packard message passing interface

HRR

Heat release rate

HTHR

High temperature heat release

IMEP

Indicated mean effective pressure

IVC

Intake valve close

IVO

Intake valve open

KH-ACT

Kelvin-Helmholz, aerodynamics, cavitation, and turbulence

KH-RT

Kelvin-Helmholtz, Rayleigh-Taylor

LLNL

Lawrence Livermore National Laboratories

LTC

Low temperature combustion

LTHR

Low temperature heat release

NUIG

National University of Ireland, Galway

PDE

Partial differential equation

PISO

Pressure implicit with splitting of operators

PM

Particulate matter

PRR

Pressure rise rate

NO_X

Oxides of Nitrogen

NTC

Negative temperature coefficient

RANS

Reynolds averaged Navier-Stokes

RCCI

Reactivity controlled compression ignition

RNG

Renormalization group

ROI

Rate of injection

RPM

Revolutions per minute

SI

Spark ignition

SOI

Start of injection

TDC

Top dead center

TCI

Turbulence-chemistry interactions

THC

Total hydrocarbons

UHC

Unburned hydrocarbons